Vol. 28 No. 2
June 2025

ISSN: 1301-9724
e-ISSN: 2146-1511
https://dergipark.org.tr/tr/pub/ijot

International Journal of Thermodynamics

Abstracting and Indexing:

Chemical Abstracts Services, Copernicus, DOAJ, EBSCO, Emerging Sources Citation Index, Engineering Index, Google Scholar, Scopus, and ULAKBIM

International Centre for Applied Thermodynamics

International Journal of Thermodynamics

https://dergipark.org.tr/tr/pub/ijot

Editor-in-Chief

Associate Editor-in-Chief

Associate Editor

Editorial Board

International Journal of Thermodynamics

https://dergipark.org.tr/tr/pub/ijot

Journal Contacts

Editor-in-Chief

Prof. Dr. Lütfullah Kuddusi
ISTANBUL TECHNICAL UNIVERSITY
kuddusi@itu.edu.tr

Department of Mechanical Engineering
Istanbul Technical University
Gumussuyu, 34437 Istanbul Turkey

Volume: 28

Issue: 2

Web: https://dergipark.org.tr/tr/pub/ijot

International Journal of Thermodynamics (IJoT)

ISSN:1301-9724 / e-ISSN:2146-1511

International Journal of Thermodynamics

https://dergipark.org.tr/tr/pub/ijot

ISSN 1301-9724 / e-ISSN 2146-1511

Volume: 28 / No: 2 – June / 2025

CONTENTS

International Journal of Thermodynamics (IJoT)
ISSN 1301-9724 / e-ISSN 2146-1511
https://dergipark.org.tr/en/pub/ijot

Vol. 28 (No. 2), pp. 035-044, 2025
doi: 10.5541/ijot.1534403

Research Article

Refined Covolume Approach for Heavy Alkanes in Abel-Noble EOS at High Pressures

[1]H. Hachoume, [1,2]*H. Ksibi

[1] LMA3E Laboratory, Campus Universitaire Sidi Ahmed Zarroug – 2112, University of Gafsa, Tunisia
[2] University of Sfax, IPEIS, P.B. 1172 Sfax 3018, Tunisia
E-mail: *hatem.ksibi@ipeis.rnu.tn

Received 18 August 2024, Revised 28 November 2024, Accepted 7 January 2025

Abstract

A novel formulation was developed to accurately model volume behavior at very high pressures for heavy n-alkanes, based on excluded volume theory. This approach is crucial as several cubic equations of state become inadequate at pressures exceeding several thousand bars. The covolume formulation was applied to the Abel-Noble equation of state (EoS) for real gases to accurately model the specific volume of linear long-chain alkanes. It adjusts the compression limit volume of these heavy alkanes by tuning a small dimensionless parameter, epsilon (ε), which establishes a numerical relationship between pressure and excluded volume. At high pressure (from 50 MPa), the molar specific volumes of various aliphatic alkanes (C_nH_{2n+2}) between 30 and 250 °C were carefully calculated. The proposed formulation was undoubtedly improved by comparing it with experimental data from many peer-reviewed studies, keeping a square error limit of 3% for heavy n-alkanes. Additionally, we notice that attempts to use the presented EoS for low-carbon number hydrocarbons seem unreliable until the fluid is set under very high pressure.

Keywords: *Covolume; n-alkanes; high pressure; Abel-Noble EoS.*

1. Introduction

The thermodynamic properties of hydrocarbons, primarily n-alkanes, which simply include carbon and hydrogen, at a certain pressure (P) and temperature (T) are ascertained using equations of state for fluids, which are also used to describe the phase behavior of those substances, thereby allowing the determination of the specific volume (v) at given P and T. In fact, most fluid PvT calculations in petroleum engineering cover reservoir models, well testing, pipeline flow calculations, separator design, and precise phase behavior predictions for various tertiary recovery procedures, such as gas injection, pyrolysis, or in situ combustion [1-2].

Designing engineering processes requires accurate experimental density measurements and trustworthy thermodynamic property estimates due to the rising activity in chemical and petroleum engineering. Moreover, oxidation reactions and hydrogen abstractions (H-abstraction) during the combustion of heavy n-alkanes play a key role in heat production. In petroleum refining, these mechanisms, particularly H-abstractions, are essential for breaking down heavy hydrocarbons into smaller, more useful molecules for fuel production.

Heavy alkane processing is generally carried out at high pressure and elevated temperatures. The auto-ignition and oxidation mechanisms of linear alkanes require a temperature range between 550 and 1100 K as mentioned by Biet et al. [3]. For example, the ignition delay time of such a hydrocarbon can be measured in a shock tube at temperatures above 1000 K, or predicted accurately using numerical simulations [4-5]. Although high temperatures are often preferred for the processing of long-chain alkanes due to their high thermal stability, certain conditions can benefit from lower temperatures as given by Bikas and Peters [6]. These include processes such as thermal and catalytic cracking (between 450°C and 750°C) or hydrocracking and hydrogenation (between 300°C and 450°C).

This paper aims to present a straightforward method for accurately analyzing the state of n-alkanes by correlating pressure with the excluded volume and investigating its effect on the specific volume. Using the main idea of Van

Der Waals, we can ignore repulsive forces under sufficiently high pressure that every material should undergo structural transformations towards denser and tighter atomic arrangements. Since these are input data for the aforementioned calculations, their accuracy is critical. Incorrect PvT properties lead to erroneous calculation results, so the calculation method used must be carefully selected [7]. We emphasize that aliphatic hydrocarbons, which lack double or triple bonds that are highly reactive in organic chemistry, are not entirely unreactive. While they do exhibit some reactivity, their generally low reactivity in most laboratory settings makes them a relatively stable but crucial component of organic chemistry.

2. Model Development

2.1. EoS Theory

Based on experimental observations and well-founded theoretical investigations, a wide range of equations of state (EoS) have been produced. As a result, an EoS has a well-established reputation for adaptability in computing pressure

*Corresponding Author

as a function of density and temperature. To characterize the behavior of fluids under high pressures and temperatures, various models (equations of state) have been developed to date. Indeed, the use of equations of state to characterize the P-v-T properties of materials began in 1873 with van der Waals' introduction of his groundbreaking equation. The EoS Virial, a power series formulation of the fluid compressibility factor density, was proposed in 1901 [8]. Despite being proposed as an empirical form, the Virial equation was eventually proved to be derived from statistical mechanics. This equation's fundamental weakness is that it cannot describe multiphase events.

Both the Redlich-Kwong and Peng-Robinson EoSs offered highly successful equations about fifty years later as mentioned by Liu et al. for compressible alkanes [9]. In fact, cubic equations are most usefully applied at high-pressure levels that cannot exceed the supercritical zone [10]. These cubic EoSs are commonly utilized to predict hydrocarbon phase behavior and volumetric features [11]. In the compressible state, estimating the thermodynamic characteristics of nonpolar fluids such as aliphatic alkanes and their mixes was simple and reasonably accurate. At pressures of several hundred bars, cubic equations such as Peng-Robinson or Redlich-Kwong remain relatively reliable, particularly for gases at moderate temperatures. However, their accuracy decreases when complex phenomena, such as liquefaction or phase formation, occur. These equations often struggle to accurately represent such phenomena in condensed phases (liquid or supercritical), where molecular density is extremely high [4]. Furthermore, structural modifications of molecules in these dense phases are not always adequately accounted for in the formulations of cubic equations, which can lead to inaccurate predictions of alkane behavior under high-pressure conditions.

Additionally, we see in the literature that several formulations of PvT are based on the scaled-particle theory for hard spheres for n-alkanes. Therefore, Vega et al. highlighted several applications for this form of EoS at a low-pressure level [12]. The equation of state for hard spheres is defined using a form factor, also known as a structural factor, which depends on the hard sphere's diameter. Recently, Eslami et al. provided a modified perturbed hard-sphere-chain equation of state that has been used to calculate fluid PvT properties, specifically for C1–C20, where predictions are more accurate than those of the original perturbed hard-sphere–chain equation of state without modification [13].

In general, an EoS, described in these models summarizes two major molecular effects (agitation and repulsion effects) in a simpler formulation. The corresponding parameters are derived using the experimental saturation findings as reference data. Furthermore, a basic EoS model for hydrocarbons has proven to be a useful tool for engineering applications such as petrochemicals. The issue of using a cubic equation technique to determine large-scale correlations, on the other hand, remains an open question. It is especially challenging to transition from the scaled equation of state used in the critical area to practical and well-understood analytical forms, or when the fluid (heavy n-alkane) is in the weakly compressible liquid state.

We cited the empirical model of Orwoll and Flory, which expressed the density of n-alkanes entirely as a function of temperature [14]. We also highlighted other empirical equations used to calculate the densities of n-alkanes and their mixtures, employing a modified version of the Tait equation of state, as reported by Bamgbade et al., whose PvT relationship was valid only at low and moderate pressures [15].

Additionally, the Abel-Noble equation is a simple yet effective tool for modeling the behavior of real fluids under moderate conditions. Its mathematical simplicity and low requirements for adjustable parameters make it practical in many situations. By adding simple correlations, this equation can be kept in its fully analytical form. Studies have evaluated its use with low-carbon-number alkanes under high pressure, often modeling hydrocarbons by eliminating the attraction energy term with minimal precision loss [16].

It is discovered that its deviations from published experimental data at a wide range of pressures and moderate temperatures are slightly higher than those calculated for the same compounds using complicated EoS. Using only experimental data points at reduced pressures of less than 2 for parameter fitting, as is common in most commercial chemical processes, results in smaller deviations from experimental values. While the Noble-Abel equation allows for quick and reasonably accurate specific volume calculations at high densities and temperatures, more developed models are needed for extreme pressure and temperature conditions.

2.2 Covolume Models

Determining the covolume for the equation of state calculations, as proposed by Abel-Noble, is useful when combined with van der Waals theory. Arteca explained that covolume, typically considered constant in cubic equations, represented the molar volume of a liquid near its melting point, including both the excluded molecular volume and inter-molecular voids [17]. It reflects the fluid's inability to be compressed indefinitely at a constant temperature, with volume approaching an incompressible threshold as pressure increases. Studies by Höhne and Blankenhorn and Machado et al. examined the behavior of n-alkane mixtures under high pressures, addressing issues like solid-to-solid transitions that can obstruct process lines [18-19].

Because they are made of a structured long chain, aliphatic n-alkanes have a distinct polarity characteristic. Alkanes are insoluble in aqueous solutions because their molecules are nonpolar and cannot interact with water molecules to disperse. Molecules with similar structures, even non-polar ones, can interact and scatter into one another. Alkanes, for instance, are excellent solvents for each other and for organic compounds in general. As the system gets closer to the volume limit of near incompressibility, at extremely high pressures, the covolume stabilizes at a constant value.

Based on the molecular structure and carbon number of the given n-alkane, we used two different formulations of the covolume required for the EoS calculation in this analysis. The molar covolume is calculated using the Van Der Waals model Eq. (1), the Redlich Kowng model Eq. (2), and the Kumar et al. model Eq. (3), which is only valid for n-alkanes [20]. These formulations will be compared to the new covolume correlation used in the current study.

Firstly, the well-known Van Der Waals covolume model is as follows, where T_c and P_c as shown in table 1, denote the critical temperature and pressure of the given pure compound, respectively:

$$b_{vdw} = \frac{RT_C}{8P_C} \tag{1}$$

Therefore, the corresponding expression for the Redlich-Kwong covolume formula is written as follows:

$$b_{rk} = 0{,}08664 \frac{RT_C}{P_C} \tag{2}$$

For heavy alkanes, most studies highlighted the limitations of cubic equations, particularly at high pressures. Kumar et al. addressed this issue by introducing a relationship between covolume and molar mass [20]. They calculated the covolume b values for n-alkanes as follows, where M_w is the molar weight of the considered n-alkane:

$$b_k = -14.69921 + 0.36977\, M_w - 9.12089\, M_w^2 \,.\, 10^{-5} \tag{3}$$

Table 1. Physical Properties of some n-Alkanes.

n-Alkanes	Carbon number N_C	Hydrogen Number N_h	M_w (g/mol)	Critical Temperature (K)	Critical Pressure (bar)
n-Methane	1	4	16.04	190,5	46,0
n-Propane	3	8	44.09	369,8	42,5
n-butane	4	10	58.12	425,1	37,9
n-pentane	5	12	72.15	407,8	36,4
n-hexane	6	14	86.17	469,7	33,7
n-heptane	7	16	100.20	461,0	34,1
n-octane	8	18	114.22	433,8	32,0
n-nonane	9	20	128.25	507,6	30,2
n-decane	10	22	142.28	497,5	30,1
n-undecane	11	24	156.30	504,4	31,2
n-dodecane	12	26	170.33	488,7	30,8
n-tridecane	13	28	184.35	499,8	31,3
n-tetradecane	14	30	198.38	540,2	27,4
n-heptadecane	17	36	240.46	540,5	28,9
n-eicosane	20	42	282.54	519,7	27,4
n-triacontane	30	62	422.80	553,5	25,6
n-tetracontane	40	82	563.06	567,8	28,7
n-pentacontane	50	102	703.32	617,7	21,1

The primary motivation for this study arises from analyzing molar-specific volume data obtained from experiments at various pressures and temperatures. The covolume is modeled as an exponential function that varies with pressure up to very high values. While the concept of covolume as a state-dependent parameter is not novel—Baibuz et al. previously noted its dependence on very high temperatures for real fluids—the current work proposes a new formulation of covolume for heavy alkanes under extreme pressures [21]. Also, we can underline the work of Chiapolino et al. who have taken the covolume as a function of the specific volume for liquid-gas systems far from the critical point [22]. By applying the Abel-Noble EoS and comparing the results with experimental data and Handbook values, this approach aims to refine the accuracy of the P-v-T relationship for these substances [23]. The Abel-Noble equation is a relatively simple yet effective approach to describe the behavior of real fluids under moderate conditions. Its mathematical simplicity and low requirements for adjustable parameters make it a practical tool in many situations.

In reality, under extremely high pressures, heavy alkanes approach a compressibility limit where their behavior shifts from what is typically expected. Instead of simply experiencing a uniform reduction in volume, the long-chain alkanes undergo a significant reorganization. The pressure causes these chains to become increasingly compact and aligned, leading to a more constrained arrangement of the molecules. At such high pressures, the concept of volume as a simple measure becomes inadequate. Instead, the behavior of these alkanes must be understood in terms of covolume the space that the molecules and their interactions effectively occupy. The chains don't just compress but adapt to a new molecular configuration where their movement is severely restricted.

This calls for a refined model where covolume varies with pressure to accurately reflect the constrained nature of the alkanes' long chains. By developing a model that accounts for this pressure-dependent behavior, we can better capture the complex interactions and spatial arrangements of heavy alkanes under extreme conditions. Such a model provides a more precise description of their properties, accommodating the unique effects of high-pressure environments on their molecular structure.

2.3 Sources of Experimental Data

Our research only looks at the volume measurements of pure alkanes using techniques that have been published lately or in the last several decades.

Table 2. Published data of n-Alkanes density at different ranges of pressure and temperature.

n-Alkanes	Temperature range (°C)	Pressure range (MPa)	Year and ref.
n-methane	-182 – 327	< 100	(1988) [24]
	-183 – 327	< 200	(1987) [25]
n-propane	-187.6 – 327	< 100	(1987) [25]
	-188 – 427	< 70	(1982) [26]
n-butane	-138 – 327	< 70	(1987) [25]
	50 – 170	13- 69	(1992) [27]
	25 – 175	< 30	(2015) [28]
n-pentane	50 – 150	7 - 241	(2000) [29]
	75 – 150	8.1 - 65	(1992) [27]
	52.7 – 247.3	1.8 - 275.5	(2010) [9]
	-178 – 613	< 300	(2004) [30]
n-hexane	38 – 238	0.7 - 66.2	(1954) [31]
	40 – 175	0.2 - 65	(1992) [27]
n-heptane	30 – 300	5- 500	(1964) [32]
	25 – 200	0.1- 202	(2009) [33]
n-octane	25 – 75	0.1 - 480	(1982) [34]
	48.7– 150.2	14.3-276.9	(2010) [9]
n-nonane	30 - 300	5-500	(1964) [32]
	25 – 100	0.1 – 192	(2009) [33]
n-decane	25 – 100	.0.1 – 420	(1982) [34]
	51.3 – 247	14.6 - 274.5	(2010) -[9]
n-undecane	30 – 300	5- 500	(1964) [32]
n-dodecane	25 – 300	0.1-81.1	(2004) [33]
	293 – 433	0.1 - 140	(2003) [35]
n-tridecane	30 –300	5 - 500	(1964) [32]
n-tetradecane	23–60	0.1- 10	(2013) [36]
n-heptadecane	50–300	5 - 500	(1964) [32]
n-eicosane	100–300	5 - 500	(1964) [32]
n-triacontane	150–300	5 -500	(1964) [32]
n-tetracontane	150–300	5 - 500	(1964) [32]
n-Octadecane	50–300	0.1- 41.3	(2004) [33]

As a result, specific molar volumes are calculated using data from linear alkane density and volume at various temperatures and pressure ranges (from 50 to 300 MPa). On the other hand, Lindberg et al. used pure chemicals like n-propane and n-heptane to quantify density up to a temperature of 473 K at low pressures [11]. The behavior of n-alkanes is somewhat compressible in these conditions, and covolume takes a minor role.

3. Results and Discussion

3.1 Model Describing

The presented EoS for heavy hydrocarbons at high pressure might be satisfying for many engineering applications. In fact, this EoS may be effectively included in thermochemical codes to resolve shock tube problems when a sudden, and strong temperature shift occurs, such as in the case of shock tube breakdown of hydrocarbons [5]. Using the equation of state, these algorithms concurrently solve for the state surfaces and the chemical byproducts composition such as n-alkanes. Thus, as long as the equations of state correctly characterize pure and mixed chemicals at various temperature and pressure ranges, it is simple to predict operational parameters throughout a transformation process.

$$b = \frac{M_w \varepsilon^2}{K(1+\varepsilon)}\left(1 - e^{-\frac{\varepsilon P}{P_0}}\right) \tag{4}$$

The use of very small exponents (ε) is often chosen in contexts where subtle modifications to a quantity or function are desired, without significantly altering the overall behavior of the target function. In this context, the exponent epsilon has a moderate effect on the function $b(M_w, P)$, gradually bringing it closer to a limiting value with an almost imperceptible impact. The smaller the exponent epsilon, the more gradual and discrete the effect becomes. This pressure-dependent form illustrates how pure compounds tend to reach the volume limit under very high pressures. This method allows for the adjustment of experimental density data across a wide range of n-alkanes. Here, K represents a dimensional constant (K=8.0), and P_0 is a reference pressure, such as atmospheric pressure. The Abel-Noble equation of state (EoS) can be expressed as follows:

$$v = \frac{1}{M_w}\left(\frac{RT}{P} + b\right) \tag{5}$$

where the gas-specific volume. The covolume *b* compensates for the finite volume occupied by the gas molecules and epsilon an arbitrarily small dimensionless value as ε=0.01.

3.2 Effect of Epsilon

Several n-alkanes were used to evaluate the proposed formulation in equations Eq. (4) and Eq. (5). Figure 1 illustrates the application of the proposed covolume for n-heptane and n-eicosane. At pressures ranging from 1 MPa to 300 MPa and a temperature of 100 °C, the specific volume of n-heptane was calculated, showing good agreement with the epsilon values (0.01, 0.005) presented in Figure 1(a). The analysis reveals that a minimal effect is observed when the epsilon parameter doubles, a principle applicable to the measurement of the specific volume of n-alkanes over a wide range of temperatures and under high pressures.

This study also compares the calculated specific volume data at (P, T) for n-eicosane with existing experimental results, using different epsilon values (0.01, 0.002, 0.005), as shown in Figure 1(b). Comparing these values highlights the refined effect of the exponents, with their impact remaining marginal in the estimation of specific molar volumes, particularly when these volumes deviate slightly from a target limiting value. The ε effect is often observed in chemical reactions or physical processes where small accumulated variations, such as radioactive decay, produce progressive but subtle effects over time.

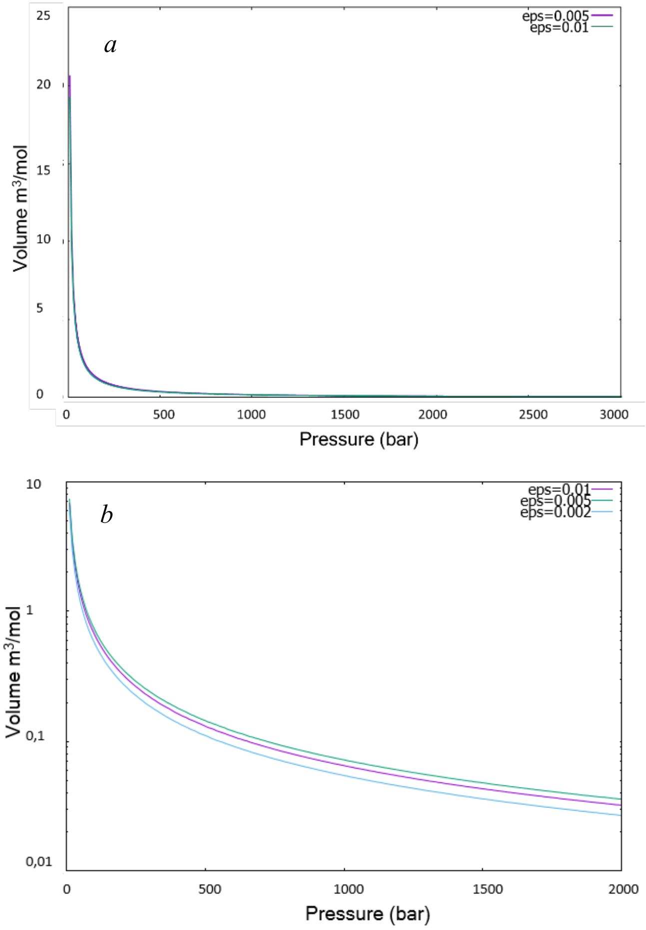

Figure 1. Effect of ε value on the specific volume for both n-heptane (a) and n-eicosane (b) at 100°C.

3.3 Effect of Pressure on Covolume

The covolume parameter has different behavior under the given operating conditions than the bulk of preceding publications, which only provide a single temperature dependence that does not also satisfy the very high-pressure domain. This behavior has been recognized in the literature. The covolume parameter b is given a new pressure-dependent function to prevent thermodynamic inconsistencies at high pressure.

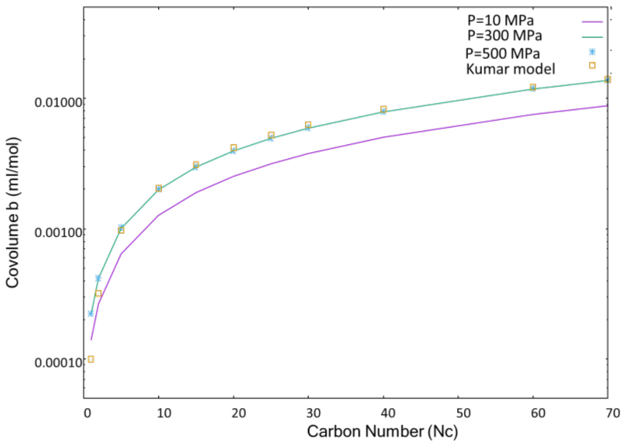

Figure 2. Effect on pressure on the covolume calculated with Eq.(4).

The proposed model shows that the covolume varies with carbon number as pressure gradually increases to thousands of bars, as illustrated in Figure 2, where the covolume is plotted as a function of the carbon number using equation

(4). Even under extremely high pressure, the behavior remains exponential and reaches a constant value. For a given hydrocarbon, the covolume remains stable under high pressure. In this case, the curves for 300 MPa (green) and 500 MPa (*asterisk) are virtually superimposed. When the relation is sufficiently smoothed, it yields satisfactory results compared to the one published by Kumar (Figure 3). In contrast, for the VDW and RK approaches, the covolume estimate remains somewhat imprecise.

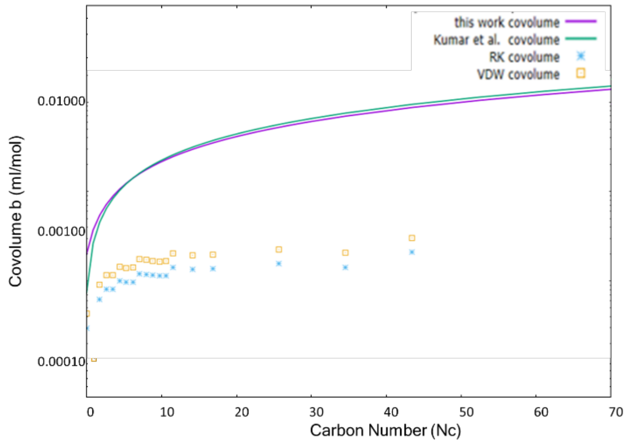

Figure 3. Comparison with covolume correlation of Kumar et al. and those of Van Der Waals and Redlich-Kowng.

We analyzed the correlation between this work at high pressure and that determined from relation Eq. (3) given by Kumar et al., as well as the covolume b in VDW EoS, Eq. (1) and RK EoS Eq. (2). In reality, the covolume curves associated with the suggested techniques exhibit exponential behavior and trend to a constant value as pressure is significantly increased. Additionally, compared to the covolume produced by the current study and supported by Kumar's relation, the link providing the covolume from VDW theory tends to produce a lesser value. In fact, Suceska et al. demonstrate that this influence is related to non-spherical molecules because rotational motion is constrained at high pressures, which emphasizes the current relationship between the covolume and working pressure [37]. Thus, the current equation offers a good and precise correlation for the covolume of heavy aliphatic n-alkanes.

3.4 Specific Volume Calculation for Several n-alkanes

At different temperatures and pressures, the PvT of aliphatic n-alkanes (C1-C50) is estimated using the proposed Abel-Noble EoS-based equation; see Table 2. The experimental data presented here was chosen because it gives precise volumes of both light and heavy n-alkanes at pressures up to 3000 bar. In practice, the volumetric properties of n-alkanes (C1-C50), typical examples of non-polar hydrocarbons, were predicted using the modified Abel-Noble model. In this study, we compared our model to the exact aliphatic n-alkane volumes reported in the literature. To predict the density at higher pressures, only the temperature and molecular weight were employed as input variables. When all necessary experimental data were known, the epsilon term was frequently considered to be a minor constant. Otherwise, a squared average error threshold was used to compare the outcomes to those discussed in the literature.

The specific volume of several pure aliphatic n-alkanes over the high-pressure domain has barely shifted, according to the modified Abel-Noble model. However, even with a specific EoS that is only relevant at low pressure, the density of compressed liquids containing aliphatic alkanes may be predicted with great accuracy [38]. The new study enhances agreement with liquid densities by more precisely characterizing behavior up to 300 MPa and beyond and incorporating the pressure-dependent b into the offered EoS.

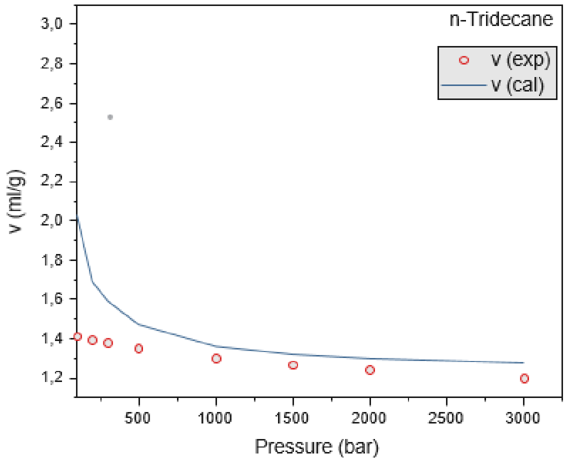

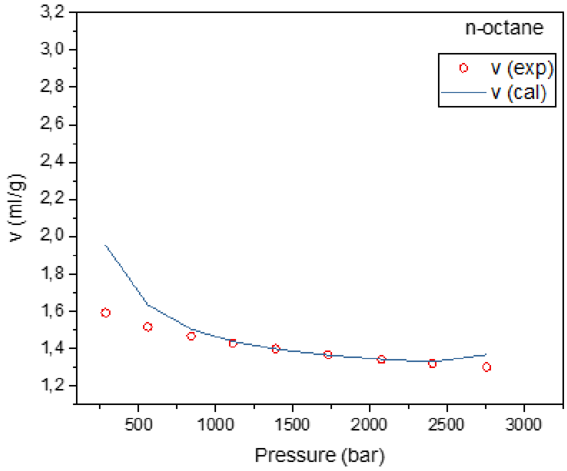

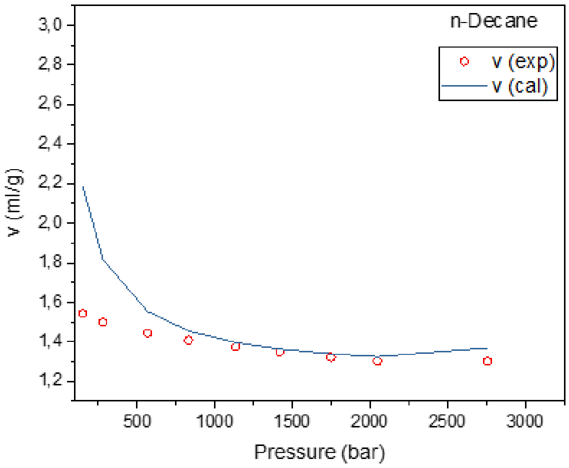

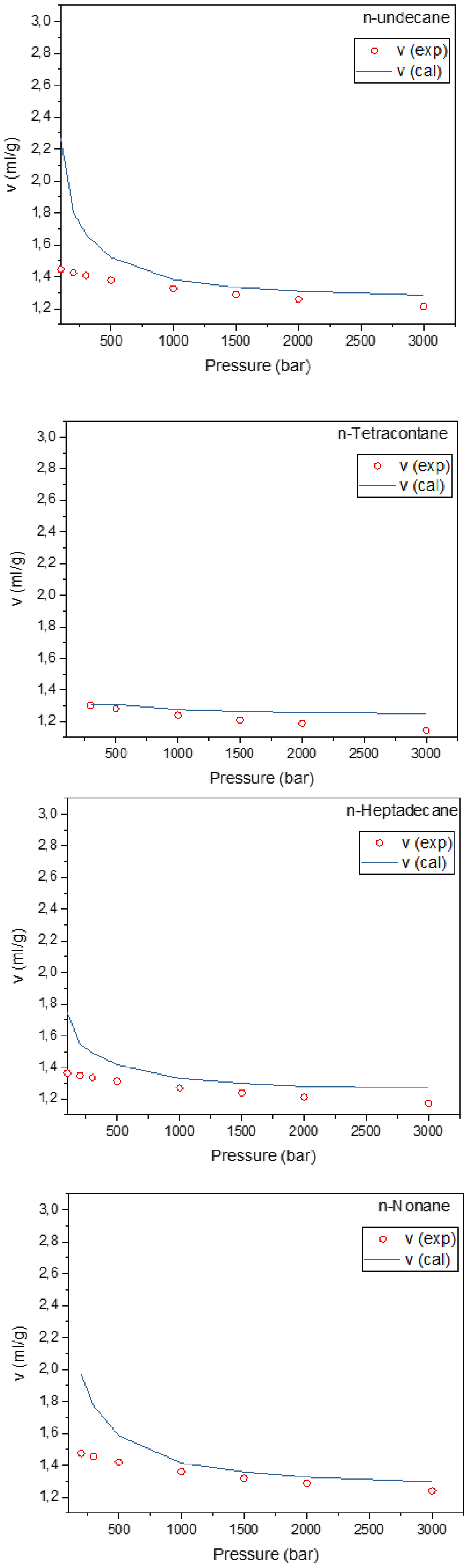

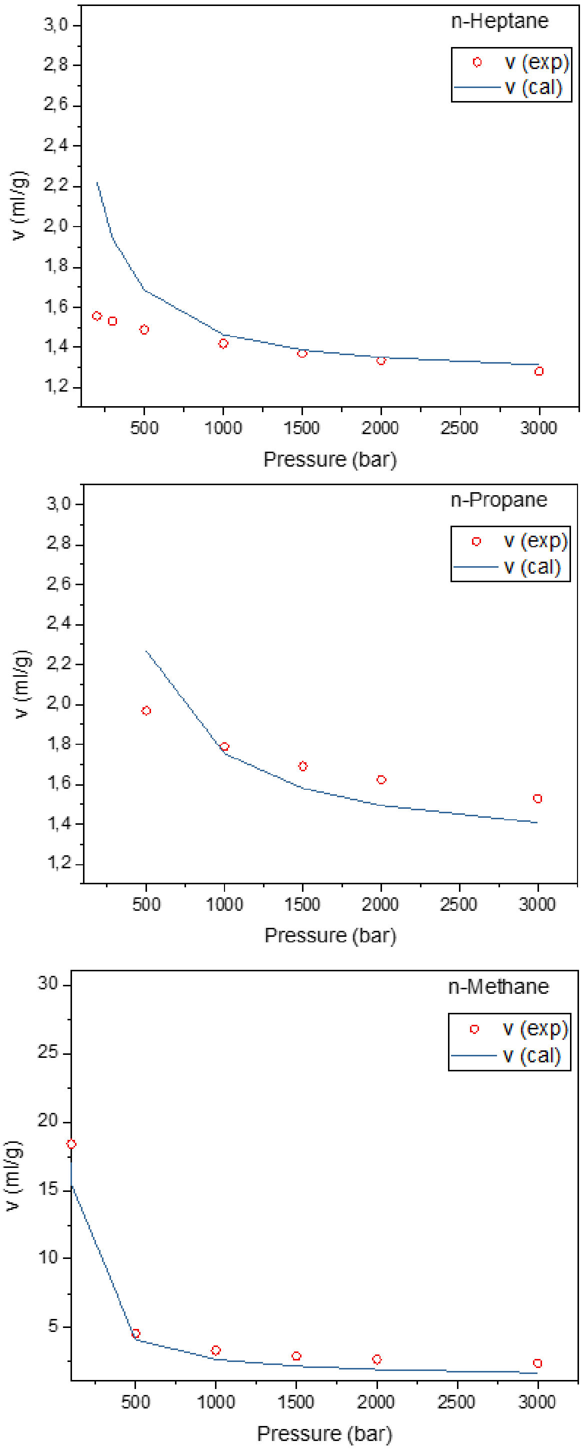

Figures 4. Comparison of experimental and simulated specific volume of listed aliphatic n-alkanes (table 1.) Straight lines depict simulated values through the equation Abel-Noble EoS) and red circles represent experimental data for the considered n-alkane.

Except for n-eicosane and n-heptadecane, which were tested at 250°C, figure 4 compares the specific volumes of the various n-alkanes mentioned in Table 1 were measured at 100 °C, at pressures ranging from a few bars to 300MPa. Three locations that stand out in the majority of the images demonstrate remarkable agreement between the model's (solid line) predictions at high pressure and the data provided in Table 2.

Heavy alkanes, due to their larger molecular size, experience significantly amplified molecular compression effects under high pressures. Typically, the model's validity range is 50 to 300 MPa. Other calculations carried out at various temperatures (50°C, 250°C) with a more precise agreement demonstrate the same tendency. If the n-alkane is heavier, or has a higher carbon number, in the second computation zone, which involves moderate pressures between 100 and 500 bars, the agreement is demonstrated. Our model completely diverges in the final computational region, which is connected to low pressures, where the C_nH_{2n+2} is not always in a fluid condition. For instance, the cases of methane and heptane are presented to illustrate the limitations of the model's applicability.

The modified Abel-Noble EoS modeling specific volumes (in this case, n-triacontane) are reasonably accurate at high pressures, as shown in Figure 5 (up to 50 MPa). The modeling curves display identical exponential behavior and do not cross one another for a given temperature and pressure, indicating thermodynamic consistency. It should be emphasized that all parameter values of the study's component sections are fixed at 0.01, and no attempt is made to alter them as the inquiry develops. Future work will focus on making the optimal value of this little constant even better.

Furthermore, because it propagates in repulsive and chain terms, the pressure-dependent b enables the model to get excellent findings for liquid density. This method is more accurate than cubic EoS in a variety of ways when simulating the precise volume or density for a high-pressure range for a subset of n-alkanes. This equation may also determine the thermodynamic properties of a particular n-alkane with accuracy without the use of a hard-sphere approach or a complicated fluid state description, and it does so without relying on the attracting and repelling components from the traditional cubic EoS. This makes it simpler to write and faster to implement than chemical engineering.

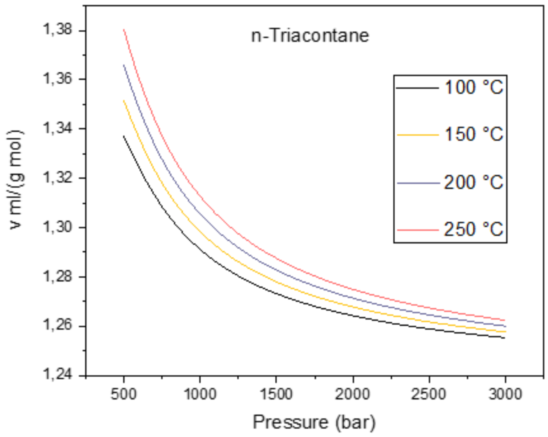

Figure 5. Isotherms of n-triacontane calculated through the modified Abel-Noble EoS (ε=0.01).

However, the covolume Eq. (4) presented in this work has been compared to the standard representation of the Abel-Noble equation for n-heptadecane at room temperature (30°C). Here the pressure was varied from few bars to 3000 bars. The proposed equation accurately reproduces experimental measurements of the specific volume at very high pressure; however the Abel-Noble model equation generates extremely low values that are far from reality, figure 6.

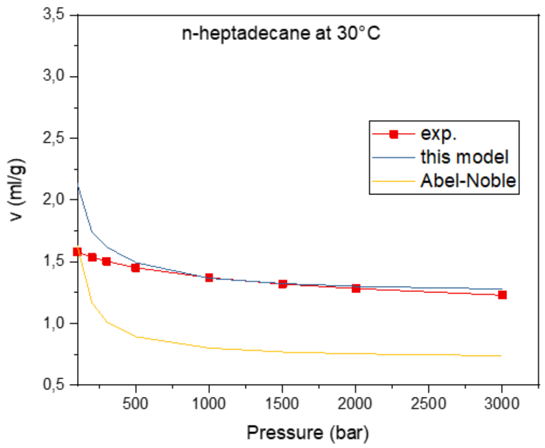

Figure 6. Comparison of Isotherm (30°C) profile of n-heptadecane calculated through Abel-Noble EoS and the presented EoS (ε=0.01).

3.5 Root Mean Square Relative Error Calculation

The mean relative error for the N data points serves as a reference for the EoS prediction's accuracy. The equation is validated in reality by comparing the estimated values to the experimental results using average deviation methodologies. The following are some uses for percent of the root mean square relative error (RMSRE). It was used to evaluate the performance of the model in percent:

$$\%\mathrm{RMSRE} = \sqrt{\frac{1}{N}\sum_{k=1}^{k=N}\left(\frac{v_{exp}-v_{cal}}{v_{exp}}\right)^2} \qquad (6)$$

Figure (7) presents the Root Mean Square Relative Mean Error (RMSRME) for the alkanes studied specifically methane (C1) and propane (C3), alongside heavier alkanes ranging from heptane (C7) to tetracontane (C40). Here, RMSRE is used to illustrate how the covolume formula in Eq. (4) can be used with Abel-Noble EoS to calculate v_{cal} for heavy aliphatic n-alkanes under high pressure. N is the total number of measurements at each temperature, and v_{exp} is based on data from the literature. The data indicate a significant error in the predictions for light alkanes (C1 and C3), where the model demonstrates considerable deviations from experimental results. This substantial error highlights the model's unsuitability for accurately capturing the thermophysical properties of light alkanes, likely due to the dominance of gaseous phase interactions and the reduced molecular complexity of smaller alkanes.

Conversely, the error becomes acceptable for heavier alkanes (C7-C40). This indicates that the model is better equipped to handle the interactions and phase behavior associated with larger molecular structures. Heavier alkanes exhibit more complex intermolecular interactions, including van der Waals forces and enhanced molecular compression effects under high-pressure conditions, which the model appears to capture more effectively.

The results confirm the model’s applicability and reliability within the range of heavier alkanes. This behavior is likely due to the reduced influence of phenomena like gas-phase behavior and liquefaction irregularities, which are more pronounced in light alkanes. Additionally, the denser molecular packing and more predictable structural properties of heavier alkanes may align better with the assumptions underlying the model. Thus, Figure (7) underscores the importance of carefully considering the molecular size and weight range when applying the model to alkanes, ensuring its use is restricted to the domain where its predictions remain valid.

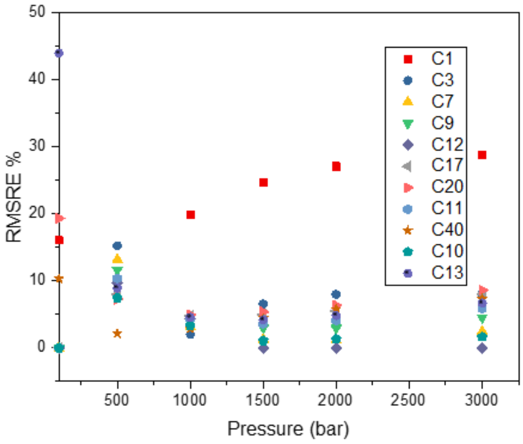

Figure 7. Root mean square relative error from the computation specific volumes for various n-alkanes.

4. Conclusions

This study has enhanced our comprehension of the behavior of aliphatic n-alkanes under high pressure through the use of EoS modeling. To study a new generation equation of state that is created using a numerical approach, the research evaluates the absolute deviation technique. A modified Abel-Noble EoS is employed in this work to accurately reproduce the density of pure aliphatic n-alkanes behavior over a wide pressure range at a moderate temperature. The model uses the classic Abel-Noble model to demonstrate the non-ideality of the state by using the covolume (b) as a function of pressure.

The epsilon term has allowed the model to reliably predict the volume of the (CnH2n+2) throughout a wide variety of high-pressure conditions (from 50 to 300 MPa). This is comparable to the capabilities of actual fluid models.

Nomenclature

b	Covolume or excluded volume (*ml/mol*)
N_c	Carbon number of aliphatic alkane
P_0	Ambient pressure (*MPa*)
ε	Tiny numerical adjustable parameter
T_c	Critical temperature (*K*)
P_c	Critical pressure (*MPa*)
M_w	Molar mass (*g/mol*)
N	Number of data points
P	Pressure (*MPa*)
R	Gas constant (*J/ (K mol)*)
T	Temperature (*K*)
v	Specific volume (*ml/g*)

Abbreviations

EoS	Equation of state
VDW	Van Der Waals
RK	Redlich Kwong

References:

[1] M. Mohsen-Nia, “A modified MMM EOS for high-pressure PVT calculations of heavy hydrocarbons,” *Journal of Petroleum Science and Engineering*, vol. 113, pp. 97–103, Jan. 2014, doi: 10.1016/j.petrol.2013.12.008.

[2] J. C. de Hemptine, P. Mougin, A. Barreau, L. Ruffine, S. Tamouza, and R. Inchekel, “Application to Petroleum Engineering of Statistical Thermodynamics – Based Equations of State,” *Oil & Gas Science and Technology - Rev. IFP*, vol. 61, no. 3, pp. 363–386, May 2006, doi: 10.2516/ogst:2006039a.

[3] J. Biet, M. H. Hakka, V. Warth, P.-A. Glaude, and F. Battin-Leclerc, “Experimental and Modeling Study of the Low-Temperature Oxidation of Large Alkanes,” *Energy & Fuels*, vol. 22, no. 4, pp. 2258–2269, May 2008, doi: 10.1021/ef8000746.

[4] A. B. Moussa and H. Ksibi, “Numerical Simulation of a One-Dimensional Shock Tube Problem at Supercritical Fluid Conditions,” *International Journal of Fluid Mechanics Research*, vol. 35, no. 1, pp. 38–50, Jan. 2008, doi:10.1615/interjfluidmechres.v35.i1.30.

[5] H. Hachoum and H. Ksibi, “On the Generation of an Intense Temperature Gradient Through a Modified Shock Tube Hydrodynamics for a Possible Continuous Sterilization Process,” *Strojnícky časopis/Journal of Mechanical Engineering*, vol. 72, no. 2, pp. 81–92, Nov. 2022, doi: 10.2478/scjme-2022-0018.

[6] G. Bikas and N. Peters, “Kinetic modelling of n-decane combustion and autoignition,” *Combustion and Flame*, vol. 126, no. 1–2, pp. 1456–1475, Jul. 2001, doi: 10.1016/s0010-2180(01)00254-1.

[7] A. I. Rusanov, “Equation of state theory based on excluded volume,” *The Journal of Chemical Physics*, vol. 118, no. 22, pp. 10157–10163, May 2003, doi: 10.1063/1.1572455.

[8] G. M. Kontogeorgis, R. Privat, and J.-N. Jaubert, “Taking Another Look at the van der Waals Equation of State–Almost 150 Years Later,” *Journal of Chemical & Engineering Data*, vol. 64, no. 11, pp. 4619–4637, Aug. 2019, doi: 10.1021/acs.jced.9b00264.

[9] K. Liu, Y. Wu, M. A. McHugh, Hseen Baled, R. M. Enick, and B. D. Morreale, “Equation of state modeling of high-pressure, high-temperature hydrocarbon density data,” *The Journal of Supercritical Fluids*, vol. 55, no. 2, pp. 701–711, Dec. 2010, doi: 10.1016/j.supflu.2010.10.004.

[10] H. Ksibi, “The Solvent-Solute Interaction in Supercritical Solution at Equilibrium: Modeling and Related Industrial Applications,” *International Journal of Thermodynamics*, vol. 7, no. 3, pp. 131–140, Sep. 2004, doi: 10.5541/ijot.1034000134.

[11] G. E. Lindberg, J. L. Baker, J. Hanley, W. M. Grundy, and C. King, “Density, Enthalpy of Vaporization and Local Structure of Neat N-Alkane Liquids,” *Liquids*, vol. 1, no. 1, pp. 47–59, Dec. 2021, doi: 10.3390/liquids1010004.

[12] C. Vega, L. G. MacDowell, and P. Padilla, “Equation of state for hard n-alkane models: Long chains,” *The Journal of Chemical Physics*, vol. 104, no. 2, pp. 701–713, Jan. 1996, doi: 10.1063/1.470867.

[13] H. Eslami, “A perturbed hard-sphere-chain equation of state: prediction from critical point constants,” *Fluid Phase Equilibria*, vol. 216, no. 1, pp. 21–26, Feb. 2004, doi: 10.1016/j.fluid.2003.09.002.

[14] R. A. Orwoll and P. J. Flory, “Equation- of-state parameters for normal alkanes. Correlation with chain length,” *Journal of the American Chemical Society*, vol. 89, no. 26, pp. 6814–6822, Dec. 1967, doi: 10.1021/ja01002a002.

[15] B. A. Bamgbade et al., “Measurements and modeling of high-temperature, high-pressure density for binary mixtures of propane with n-decane and propane with n-eicosane,” *The Journal of Chemical Thermodynamics*, vol. 84, pp. 108–117, May 2015, doi: 10.1016/j.jct.2014.12.015.

[16] P. Longwell, J. Olin, and B. Sage, “Covolumes for a Number of Common Gases.,” Industrial & Engineering Chemistry Chemical & Engineering Data Series, vol. 3, no. 2, pp. 175–180, Oct. 1958, doi: 10.1021/i460004a001.

[17] G. A. Arteca, “Interpretation of covolume in an extension of the Redlich–Kwong equation of state for real gases,” *Journal of Mathematical Chemistry*, vol. 61, no. 9, pp. 1967–1979, Aug. 2023, doi: 10.1007/s10910-023-01497-1.

[18] G.W.H. Höhne and K. Blankenhorn, “High pressure DSC investigations on n-alkanes, n-alkane mixtures and polyethylene,” *Thermochimica acta*, vol. 238, pp. 351–370, Jun. 1994, doi: 10.1016/s0040-6031(94)85219-7.

[19] J. J. B. Machado, Theo, E. Christian Ihmels, K. Fischer, and Jürgen Gmehling, “High pressure solid–solid and solid–liquid transition data for long chain alkanes,” *The Journal of Chemical Thermodynamics*, vol. 40, no. 12, pp. 1632–1637, Jul. 2008, doi: 10.1016/j.jct.2008.07.017.

[20] A. Kumar and R. Okuno, “Direct perturbation of the Peng–Robinson attraction and covolume parameters for reservoir fluid characterization,” *Chemical Engineering Science*, vol. 127, pp. 293–309, May 2015, doi: 10.1016/j.ces.2015.01.032.

[21] V. F. Baibuz, V. Yu. Zitserman, L. M. Golubushkin, and I. G. Malyshev, “The covolume and equation of state of high-temperature real gases,” *Journal of Engineering Physics*, vol. 51, no. 2, pp. 955–956, Aug. 1986, doi: 10.1007/bf00871197.

[22] A. Chiapolino and R. Saurel, “Extended Noble–Abel Stiffened-Gas Equation of State for Sub-and-Supercritical Liquid-Gas Systems Far from the Critical Point,” *Fluids*, vol. 3, no. 3, p. 48, Jul. 2018, doi: 10.3390/fluids3030048.

[23] M. J. Anselme, M. Gude, and A. S. Teja, “The critical temperatures and densities of the n-alkanes from pentane to octadecane,” *Fluid Phase Equilibria*, vol. 57, no. 3, pp. 317–326, Jan. 1990, doi: 10.1016/0378-3812(90)85130-3.

[24] D. G. Friend, J. F. Ely, and H. Ingham, “Thermophysical Properties of Methane,” *Journal of Physical and Chemical Reference Data*, vol. 18, no. 2, pp. 583–638, Apr. 1989, doi: 10.1063/1.555828.

[25] B. A. Younglove and J. F. Ely, “Thermophysical Properties of Fluids. II. Methane, Ethane, Propane, Isobutane, and Normal Butane,” Journal of Physical and Chemical Reference Data, vol. 16, no. 4, pp. 577–798, Oct. 1987, doi: 10.1063/1.555785.

[26] R. D. Goodwin and W. M. Haynes, “Thermophysical properties of propane from 85 to 700 K at pressures to 70 MPa,” OSTI ID: 6402039, Jan. 1982, doi: 10.6028/nbs.mono.170.

[27] E. Kiran and Y. L. Sen, “High-pressure viscosity and density of n-alkanes,” *International Journal of Thermophysics*, vol. 13, no. 3, pp. 411–442, May 1992, doi: 10.1007/bf00503880.

[28] S. Glos, Reiner Kleinrahm, and W. Wagner, “Measurement of the (p,ρ,T) relation of propane, propylene, n-butane, and isobutane in the temperature range from (95 to 340) K at pressures up to 12 MPa using an accurate two-sinker densimeter,” *The Journal of Chemical Thermodynamics*, vol. 36, no. 12, pp. 1037–1059, Dec. 2004, doi: 10.1016/j.jct.2004.07.017.

[29] S. Herrmann and E. Vogel, “Viscosity and Density of Normal Butane Simultaneously Measured at Temperatures from (298 to 448) K and at Pressures up to 30 MPa Incorporating the Near-Critical Region,” *Journal of Chemical & Engineering Data*, vol. 60, no. 12, pp. 3703–3720, Oct. 2015, doi: 10.1021/acs.jced.5b00654.

[30] H.-S. Byun, T. P. DiNoia, and M. A. McHugh, “High-Pressure Densities of Ethane, Pentane, Pentane-d12, 25.5 wt Ethane in Pentane-d12, 2.4 wt Deuterated Poly(ethylene-co-butene) (PEB) in Ethane, 5.3 wt Hydrogenated PEB in Pentane, 5.1 wt Hydrogenated PEB in Pentane-d12, and 4.9 wt Hydrogenated PEB in Pentane-d12+ 23.1 wt Ethane,” *Journal of Chemical & Engineering Data*, vol. 45, no. 5, pp. 810–814, Sep. 2000, doi: 10.1021/je990308+.

[31] A. K. Doolittle, “Specific Volumes of n-Alkanes.,” *Journal of Chemical & Engineering Data*, vol. 9, no. 2, pp. 275–279, Apr. 1964, doi: 10.1021/je60021a048.

[32] D. R. Caudwell, M. Trusler, Velisa Vesovic, and W. A. Wakeham, “Viscosity and Density of Five Hydrocarbon Liquids at Pressures up to 200 MPa and Temperatures up to 473 K,” *Journal of Chemical & Engineering Data*, vol. 54, no. 2, pp. 359–366, Feb. 2009, doi: 10.1021/je800417q.

[33] J. H. Dymond, J. Robertson, and J.D Isdale, “(p, ϱ, T) of some pure n-alkanes and binary mixtures of n-alkanes in the range 298 to 373 K and 0.1 to 500 MPa,” *The Journal of Chemical Thermodynamics*, vol. 14, no. 1, pp. 51–59, Jan. 1982, doi: 10.1016/0021-9614(82)90123-9.

[34] T. S. Khasanshin, A. P. Shchamialiou, and O. G. Poddubskij, “Thermodynamic Properties of Heavy n-Alkanes in the Liquid State: n-Dodecane,” *International Journal of Thermophysics*, vol. 24, no. 5, pp. 1277–1289, Jan. 2003, doi: 10.1023/a:1026199017598.

[35] M. Kariznovi, H. Nourozieh, J. G. James) Guan, and J. Abedi, “Measurement and modeling of density and viscosity for mixtures of Athabasca bitumen and heavy n-alkane,” *Fuel*, vol. 112, pp. 83–95, Oct. 2013, doi: 10.1016/j.fuel.2013.04.071.

[36] Vlastimil Růžička, M. Zábranský, and V. Majer, “Heat capacities of organic compounds in liquid state II. C1 to C18 n-alkanes,” *Journal of Physical and Chemical Reference Data*, vol. 20, no. 2, pp. 405–444, Mar. 1991, doi: 10.1063/1.555883.

[37] M. Suceska, H.-G. Ang, and H. Y. Serene Chan, “Study of the Effect of Covolumes in BKW Equation of State on Detonation Properties of CHNO Explosives,” *Propellants, Explosives, Pyrotechnics*, vol. 38, no. 1, pp. 103–112, Nov. 2012, doi: 10.1002/prep.201100150.

International Journal of Thermodynamics (IJoT)
ISSN 1301-9724 / e-ISSN 2146-1511
https://dergipark.org.tr/en/pub/ijot

Vol. 28 (No. 2), pp. 045-050, 2025
doi: 10.5541/ijot.1395683

Research Article

Quantum thermal engine with spin 1/2 system and geometric phases and interference obtained by unitary transformations of mixed states

*Y. Ben-Aryeh

Physics Department, Technion-Israel Institute of Technology, Haifa, 32000, Israel
E-mail: *phr65yb@physics.technion.ac.il

Received 24 November 2023, Revised 14 February 2024, Accepted 24 March 2024

Abstract

Quantum Carnot engine whose working medium is a two-dimensional spin 1/2 system, with a time-dependent magnetic field in the symmetric *z* direction is described. The dynamic of this engine is obtained by using four steps, where in two steps the system is coupled alternatively to hot and cold heat baths, and in the other two steps the time development is adiabatic and isentropic (with constant entropy). The conditions for getting a reversible Carnot cycle and the role of time duration for its irreversibility are discussed. Since the calculations are made for the expectation values of the Hamiltonian, only dynamical phases are obtained which cannot be used for interference effects. An alternative method is developed for getting geometric phases, which can be used in interferometry. Parallel transport equations for pure states are generalized to mixed states by which dynamical phases are eliminated. The geometric phases are derived by unitary SU(2) transformations, including time-dependent parameters which are a function of the magnetic fields interactions. A special form of the unitary transformation for the mixed thermal states is developed, by which geometric phases are obtained, which are different from those obtained in NMR and neutron interferometry.

Keywords: *Quantum thermodynamics; quantum heat engine; carnot cycle; geometric phases.*

1. Introduction

Quantum thermal engines connected to hot and cold heat baths have been studied extensively in various forms. The studies of such engines are based on Otto [1-4], Carnot, and other engines [5-8] cycles. While quantum properties of time dependent cycles were studied extensively, those studies emphasized the efficiency of such engines. In the present work, we raise the question of whether and how geometric and dynamical phases are involved in such cycles. This question is of much importance as the use of quantum phases in interference experiments may lead to important conclusions about the quantum or classical nature of such systems. The differences between dynamical and geometrical phases are described by following conventional theories [9-11].

A quantum Carnot engine is described, whose working medium is a two-dimensional spin 1/2 system with time dependent magnetic field in the symmetric *z* direction [6,7]. The dynamic of this engine is obtained by using four steps, where in two steps the system is coupled alternatively to hot and cold heat baths, and in the other two steps the time development is adiabatic and isentropic (with constant entropy). The conditions for getting a reversible Carnot cycle, and the role of time duration for its irreversibility are discussed. Since the calculations are made for the expectation of the Hamiltonian, only dynamical phases are obtained which cannot be used for interference effects. We use an alternative method for getting geometric phases which can be used in interferometry [12-15]. Parallel transport equations for pure states are generalized to mixed states by which the dynamical phases are eliminated. The geometric phase is derived by unitary SU(2) transformations, including time-dependent parameters which are a function of the magnetic field interactions. We get a special form of the unitary transformation of the mixed thermal states by which geometric phases are obtained, which are different from those obtained in NMR and neutron interferometry.

The magnetic field $\vec{B}$ is along the positive *z* axis and the Hamiltonian is given by:

$$\hat{H}(t) = 2\mu_B B_z(t)\hat{s}_z \equiv \tilde{\omega}(t)\hat{s}_z ; \\ \tilde{\omega}(t) = 2\mu_B B_z(t). \tag{1}$$

The units are such that $\hbar = 1$, μ_B is the Bohr magneton, $\tilde{\omega}(t)$ is proportional to $B_z(t)$ and $\hat{s}_z$ is the spin operator in the *z* direction. We refer to $\tilde{\omega}(t)$ rather than $B_z(t)$ as “the field”. The mixed density matrix ρ_0 of this system is given by:

$$\rho_0 = P_1 \left|-1/2\right\rangle\left\langle -1/2\right| + P_2 \left|+1/2\right\rangle\left\langle +1/2\right|, \tag{2}$$

where $\{-1/2, +1/2\}$ are the eigenvalues of the spin and the classical probabilities P_1 and P_2 are given, respectively, by statistical mechanics as:

$$P_1 = \frac{e^{\hbar\tilde{\omega}\beta/2}}{e^{\hbar\tilde{\omega}\beta/2} + e^{-\hbar\tilde{\omega}\beta/2}}; \quad P_2 = \frac{e^{-\hbar\tilde{\omega}\beta/2}}{e^{\hbar\tilde{\omega}\beta/2} + e^{-\hbar\tilde{\omega}\beta/2}}; \\ \beta = \frac{1}{k_B T} \tag{3}$$

---

*Corresponding Author

where k_B is the Boltzmann constant, T the absolute temperature, μ_B is the Bohr magneton and $\tilde{\omega}$ was defined in Eq. (1). Based on statistical mechanics, the expectation value of $\hat{s}_z$ is given by:

$$\langle s_z \rangle = -\frac{1}{2}\tanh\left(\tilde{\omega}\beta/2\right); \quad \beta = \frac{1}{k_B T}, \tag{4}$$

and the expectation value of the Hamiltonian is given by:

$$E_0 = \langle H_0 \rangle = \hbar\tilde{\omega}\langle s_z \rangle . \tag{5}$$

H_0 is the zero order Hamiltonian and E_0 is its expectation value.

Such a quantum machine works by different steps in which the energy of the spin1/2 (considered as the working medium) is given by the expectation value of Eq. (5). In each step the temperature or the "frequency" $\hat{\omega} = 2\mu_B B_z$ (or both parameters) are changing. In an alternative approach, we incorporate the geometric phase for mixed states interferometry [12] into the present thermal mixed systems using a general propagator. This two-dimensional spin system is different from the common examples of three-dimensional spin systems described in the Bloch sphere [13].

In the present article, I develop a method by which geometric phases can be obtained in quantum thermal engine systems, leading to interference effects in such systems. This method is applied in my work to a quantum Carnot engine whose working medium is a two-dimensional spin 1/2 system, with a time-dependent magnetic field in the symmetric z axis. Since the general calculations for quantum heat engines, and especially those made in my work for the present quantum system, are made with dynamical phases they do not lead to interference effects. I show by using special unitary transformations of mixed states, which are developed for the present Carnot cycle, the way by which geometric phases are produced. The possibility to obtain geometric phases has not been realized, so far, in the published literature on quantum heat engines. Realization of interference effects by geometric phases for quantum engines can give a new insight into quantum thermodynamics.

The present paper is arranged as follows: In section 2 we obtain the dynamical phases in the present spin 1/2 Carnot quantum engine. The efficiency of such engines under reversible and irreversible conditions is described. In section 3, we apply the geometric phases approach to mixed states as propagators of the quantum engines' thermal states. Results are summarized in Section 4.

2. Methods for reversible and irreversible Carnot cycle with spin 1/2 system

The Carnot engine including its efficiency can be analyzed under different limiting cases. In case A we assume that the parameters of the Carnot cycle are changed infinitely slowly along some path from a certain initial point to a final point. In this case, the Carnot quantum engine is reversible with maximal efficiency, but power is tending to zero. In case B we treat the irreversible Carnot cycle, which gives maximal power but with energy losses. We show in the following analysis that there is a trade between maximum power, and maximum efficiency at which power is zero.

Case A: Reversible Carnot cycle

Carnot quantum engine operates by 4 steps described schematically in Figure 1.

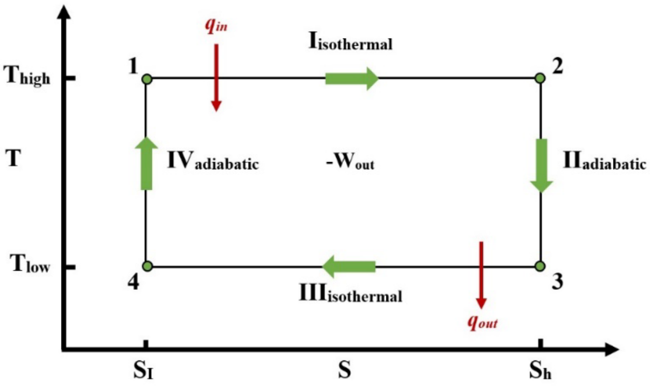

Figure 1. Carnot cycle is described, where the 4 points 1, 2, 3, and 4 denote 4 different states of the system. The transitions between states 1 and 2, and that between states 3 and 4 are described, for the hot isotherm at the temperature T_{high}, and for the cold isotherm at the temperature T_{low}, respectively. The transitions between states 2 and 3, and that between states 4 and 1 are adiabatic with constant entropy S_h and S_l, respectively.

In each of the points 1, 2, 3, and 4 the expectation value of the Hamiltonian of Eq. (5) is given as $\hbar\tilde{\omega}\langle s_z \rangle$ where $\tilde{\omega}(t) = 2\mu_B B_z(t)$, and $\langle s_z \rangle = -(1/2)\tanh\left(\tilde{\omega}\beta/2\right)$ is the expectation value of the spin 1/2 $\hat{s}_z$ operator. In the transitions between consecutive points, the parameter $\tilde{\omega}$ (proportional to the magnetic field) or $\beta = 1/k_B T$ (or both) are changing. The transition between points 1 and 2 describes the hot isotherm (see Fig. 1 as $I_{isothermal}$), where the system is coupled to a hot reservoir at temperature T_{high}. In this step, heat q_{in} is entering into the system. The transition between points 3 and 4 describes the cold isotherm (see Fig. 1 as $III_{isothermal}$), where the system is coupled with the cold reservoir with temperature T_{low}. At this step, heat q_{out} is going out of the system. The transitions between points 2 and 3 are adiabatic and isentropic (described in Fig. 1 as $II_{adiabatic}$ with constant entropy S_h). The transitions between 4 and 1 are adiabatic and isentropic (described in Fig. 1 as $IV_{adiabatic}$ with constant entropy S_l). In these steps (denoted as $II_{adiabatic}$ and $IV_{adiabatic}$), heat is not transferred as the system is isolated from the reservoirs, but work is done by decreasing or increasing the temperature by the difference $\pm\left(T_H - T_C\right)$, respectively. For an ideal Carnot cycle (assuming no losses) the work done by such a thermal machine is given by $q_{in} + q_{out}$ where q_{out} is negative, and its efficiency is given by the limit $\eta = \left(q_{in} + q_{out}\right)/q_{in} = \left(T_{high} - T_{low}\right)/T_{high}$.

The schematic Fig. 1 describes only the physical nature of the present Carnot cycle, but it does not describe quantitatively the experimental values in these steps. Explicit evaluations of the experimental values of the present quantum Carnot engine can be given as follows.

The heat q_{in} by the present spin system is positive and given by:

$$\begin{aligned} & q_{in} = \langle H_2 \rangle - \langle H_1 \rangle = \\ & \frac{\hbar}{2}\left[-\tilde{\omega}_2 \tanh\left(\beta_H \hbar \tilde{\omega}_2\right) + \tilde{\omega}_1 \tanh\left(\beta_H \hbar \tilde{\omega}_1\right)\right]; \\ & \beta_H = 1/k_B T_{high}; \quad \tilde{\omega}_1 = 2\mu_B B_z(1); \\ & \tilde{\omega}_2 = 2\mu_B B_z(2); \quad \tilde{\omega}_1 > \tilde{\omega}_2 \end{aligned} \tag{6}$$

The heat q_{out} of the present spin system is negative and given by:

$$\begin{aligned} & q_{out} = \langle H_4 \rangle - \langle H_3 \rangle = \\ & \frac{\hbar}{2}\left[-\tilde{\omega}_4 \tanh\left(\beta_C \hbar \tilde{\omega}_4\right) + \tilde{\omega}_3 \tanh\left(\beta_C \hbar \tilde{\omega}_3\right)\right]; \\ & \beta_C = 1/k_B T_{low}; \quad \tilde{\omega}_3 = 2\mu_B B_z(3); \\ & \tilde{\omega}_4 = 2\mu_B B_z(4); \quad \tilde{\omega}_4 > \tilde{\omega}_3. \end{aligned} \tag{7}$$

We find by the above equations that while q_{in} is positive q_{out} is negative. Since in the adiabatic transitions between states 2 and 3, and that between states 4 and 1, the entropy is not changed (isentropic transitions), the probabilities P_1 and P_2 are also not changed (as $P_1 + P_2 = 1$ in our system). It follows from Eq. (4) that the expectation value $\langle s_z \rangle = -(1/2)\tanh(\hbar\omega\beta/2)$ is also constant in these transitions. Using these relations, we get:

$$\begin{aligned} & \beta_H \tilde{\omega}_1 = \beta_C \tilde{\omega}_4; \quad \beta_H \tilde{\omega}_2 = \beta_C \tilde{\omega}_3; \\ & \frac{\tilde{\omega}_4}{\tilde{\omega}_1} = \frac{\tilde{\omega}_3}{\tilde{\omega}_2} = \frac{\beta_H}{\beta_C} = \frac{T_{low}}{T_{high}}. \end{aligned} \tag{8}$$

Substituting Eqs. (8) into those of (6) and (7) we get the efficiency of the Carnot reversible cycle as:

$$\eta_{rev} = \frac{q_{in} + q_{0ut}}{q_{in}} = 1 - \frac{T_{low}}{T_{high}}. \tag{9}$$

Case B: Irreversible Carnot cycle

There are various works treating the irreversibility of the Carnot cycle. We refer here to [5] where a simple model (without entering into the detailed interactions) was developed which gives fair comparisons with experimental results under different conditions. We use here the idea that the irreversible heat from the cold (hot) reservoir will decay with time $\tau_C\left(\tau_H\right)$ as:

$$\begin{aligned} & Q_{ir,C} = T_{low}\left(-\Delta S - \frac{C_1}{\tau_C}\right); \\ & Q_{ir,H} = T_{high}\left(\Delta S - \frac{C_2}{\tau_H}\right). \end{aligned} \tag{10}$$

Here ΔS represents the entropy difference $S_h - S_l$, the subscripts H and C refer to the hot and cold reservoir, respectively, C_1 and C_2 are certain constants τ_C and τ_H are decay times and the subscript *ir* represents irreversibility (the reversible regime is approached in times $\tau_C \to \infty$, $\tau_H \to \infty$). We consider the power generated during the Carnot cycle and by using Eq. (10) we get:

$$\begin{aligned} & P = \frac{-W_{out}}{\tau_H + \tau_C} = \\ & \frac{\left(T_{high} - T_{low}\right)\Delta S - T_{low}\left(C_1/\tau_C\right) - T_{high}\left(C_2/\tau_H\right)}{\tau_H + \tau_C}, \end{aligned} \tag{11}$$

where for $-W_{out}$ described in Fig. 1, we inserted the decay times as given by Eq. (11).

The maximum power is found by setting the derivatives of P with respect to τ_H and τ_C equal to zeros. Such a procedure was developed in [5], obtaining different results including the case $C_1 = C_2$ for which Curzon-Ahlborn efficiency [8] was obtained.

There are many other works treating the effects of energy losses on quantum engines' efficiency, but our interest in the present paper is about the possibility to use geometric phases in quantum engines. Since the dynamical phases obtained above for Carnot engine (and similar dynamical phases which can be obtained for other engines) are based on expectation values of the Hamiltonian, they cannot be used for interference experiments. We show in the next section an alternative approach by which geometric phases can be obtained for thermal states which can be applied in interferometers, e.g., in Mach-Zehnder interferometer [12]. The geometric phases obtained for thermal states are different from those obtained in NMR and Neutron interferometry [16-19].

3. Results for geometric phases applied to thermal spin 1/2 states

The density matrix ρ_0 for mixed states includes averaging of thermal fluctuations described by the probabilities P_k. Therefore, unitary transformations cannot operate directly on this density matrix, but they can operate separately on the components of such density matrix composed of pure quantum states. The idea presented in [12] is that the initial density matrix ρ_0 can be developed in time t to a density matrix ρ_t by the unitary transformation operating on the initial vectors $|\tilde{k}\rangle_0$ as:

$$\rho_t = \sum_{k=1}^{N} P_k \left\{ U(t) \left|\tilde{k}\right\rangle_0 \left\langle \tilde{k}\right|_0 U^\dagger(t) \right\} = \sum_{k=1}^{N} P_k \left|\tilde{k}\right\rangle_t \left\langle \tilde{k}\right|_t \tag{12}$$

where $U(t)$ is a unitary matrix of $N \times N$ dimension, $|\tilde{k}\rangle_t = U(t)|\tilde{k}\rangle_0$ are the orthonormal vectors at time t and $|\tilde{k}\rangle_0$ are the initial vectors. The mixed state is described as a mixture of several pure states incoherently weighed by their respective probabilities P_k. For thermal states the eigenvectors in the computational basis are given by:

$$\left|\tilde{1}\right\rangle_0 = \begin{pmatrix} 1 \\ 0 \end{pmatrix}; \left|\tilde{2}\right\rangle_0 = \begin{pmatrix} 0 \\ 1 \end{pmatrix}. \tag{13}$$

corresponding to eigenvalues -1/2 and +1/2 of $\hat{s}_z$. The density matrix of Eq. (2) is transformed to short notation as:

$$\begin{aligned} & \rho_0 = P_1 \left|-1/2\right\rangle\left\langle -1/2\right| + P_2 \left|+1/2\right\rangle\left\langle +1/2\right| \equiv \\ & P_1 \left|\tilde{1}\right\rangle\left\langle \tilde{1}\right| + P_2 \left|\tilde{2}\right\rangle\left\langle \tilde{2}\right|. \end{aligned} \tag{14}$$

The parallel transport of a particular vector $|\tilde{k}\rangle_t$ implies no change in phase when $|\tilde{k}\rangle_t$ evolves into $|\tilde{k}\rangle_{t+dt}$, for some infinitesimal change of the parameter t. Although locally there is no phase change, the system can acquire a geometric phase after completing a closed loop parametrized by t or by the Pancharatnam phase for open cycle. This phase is related to curvature of the parameter space depending only on the geometry of the path. Parallel transport can be satisfied by choosing a suitable $U(t)$ matrix which satisfies the parallel transport conditions, where for the present 1/2 spin system we have such two equations.

The geometric phase γ_{geom} is acquired by a mixed state evolving along a curve Γ under a unitary transformation which satisfies the parallel transport equations and is given by:

$$\begin{aligned}&\gamma_{geom}(\Gamma) = \arg Tr\left[\rho_t U(t)\right] = \\ &= \arg Tr\left[U(t)\rho_0 U^{\dagger}(t)U(t)\right] = \arg Tr\left[U(t)\rho_0\right].\end{aligned} \tag{15}$$

$U(t)$ for thermal states is given by SU(2), a two-dimensional unitary matrix. We choose $U(t)$ to be given by the product of 3 unitary matrices:

$$U(t) = U_1(\tilde{\omega}_1)U_2(\xi)U_3(\tilde{\omega}_2), \tag{16}$$

$$\begin{aligned}&U_1(\tilde{\omega}_1) = \begin{bmatrix}\exp\left[i\tilde{\omega}_1 t/2+\phi\right] & 0 \\ 0 & \exp\left[-i\tilde{\omega}_1 t/2+\phi\right]\end{bmatrix}; \\ &U_3(\tilde{\omega}_2) = \begin{bmatrix}\exp\left[i\tilde{\omega}_2 t/2\right] & 0 \\ 0 & \exp\left[-i\tilde{\omega}_2 t/2\right]\end{bmatrix}\end{aligned} \tag{17}$$

and

$$U_2(\xi) = \begin{bmatrix}\cos\xi & -\sin\xi \\ \sin\xi & \cos\xi\end{bmatrix}. \tag{18}$$

We assume here that $U_1(\tilde{\omega}_1)$ and $U_3(\tilde{\omega}_2)$ operate during time t with Hamiltonians fixed by Eq. (1) as $H_{1z} = \hbar\tilde{\omega}_1\sigma_z/2$ and $H_{2z} = \hbar\tilde{\omega}_2\sigma_z/2$ respectively, where $\tilde{\omega}_1 = 2\mu_B B_{1z}$ and $\tilde{\omega}_2 = 2\mu B_{2z}$, B_{1z} and B_{2z} are constant magnetic fields in the z direction and where ϕ is a certain phase shift between $U_1(\tilde{\omega}_1)$ and $U_3(\tilde{\omega}_2)$. $U_2(\xi)$ is a simple beam-splitter transformation which does not include any time dependence and for simplicity is defined by Eq. (18).

By substituting Eqs. (17-18) into that of (16) we get:

$$U(t) = e^{i\phi}\begin{pmatrix}e^{i\delta t}\cos\xi & -e^{-i\varsigma t}\sin\xi \\ e^{i\varsigma t}\sin\xi & e^{-i\delta t}\cos\xi\end{pmatrix} \tag{19}$$

$$\delta = \frac{\tilde{\omega}_1+\tilde{\omega}_2}{2} \quad ; \quad \varsigma = \frac{\tilde{\omega}_2-\tilde{\omega}_1}{2}. \tag{20}$$

Equation (19) is similar to the SU(2) transformation used in neutron interferometry [19]. But here the parameters δ and ς are multiplied by the time t which leads to a certain dependence of U on time, which is critical for the use of the following analysis.

Realization of the above unitary transformation depends on scales of time. The initial mixed state of Eqs. (2-3) can be produced after a relatively long time in which the system arrives at thermal equilibrium. The operation of the unitary transformation on the initial state is made during time t which is short relative to relaxation times.

We use the above $U(t)$ unitary matrix for obtaining parallel transport equations. Due to the linear relations between $|\tilde{k}\rangle_t$ and $|\tilde{k}\rangle_0$ the two parallel transport equations $\left\langle\tilde{k}\right|_t \dot{U}(t)U^{\dagger}(t)\left|\tilde{k}\right\rangle_t = 0 \quad (k=1,2)$ implies also:

$$\left\langle\tilde{k}\right|_0 \dot{U}(t)U^{\dagger}(t)\left|\tilde{k}\right\rangle_0 = 0 \quad ; \quad k=1,2. \tag{21}$$

We use the eigenvectors of $|\tilde{k}\rangle_0$ in the computational basis given by Eqs. (13). Then we get by using the first Eq. of (21) and that of (19) for

$$\begin{aligned}&(1,0)\begin{pmatrix}(i\delta\cos\xi)e^{i\delta t} & (i\varsigma\sin\xi)e^{-i\varsigma t} \\ (i\varsigma\sin\xi)e^{i\varsigma t} & (-i\delta\cos\xi)e^{-i\delta t}\end{pmatrix}. \\ &\times\begin{pmatrix}\cos\xi e^{-i\delta t} & \sin\xi e^{-i\varsigma t} \\ -\sin\xi e^{i\varsigma t} & \cos\xi e^{i\delta t}\end{pmatrix}\begin{pmatrix}1 \\ 0\end{pmatrix} = 0\end{aligned} \tag{22}$$

Straightforward calculations lead to the result:

$$\begin{aligned}&\left((i\delta\cos\xi)e^{i\delta t} \quad (i\varsigma\sin\xi)e^{-i\varsigma t}\right) \\ &\times\begin{pmatrix}\cos\xi e^{-i\delta t} \\ -\sin\xi e^{i\varsigma t}\end{pmatrix} = i\delta(\cos\xi)^2 - i\varsigma(\sin\xi)^2 = 0\end{aligned} \tag{23}$$

For the second equation of (21) we use calculations from equation (22) in which we exchange $\begin{pmatrix}1 & 0\end{pmatrix}$ to $\begin{pmatrix}0 & 1\end{pmatrix}$ and $\begin{pmatrix}1 \\ 0\end{pmatrix}$ to $\begin{pmatrix}0 \\ 1\end{pmatrix}$.

Then we get:

$$\begin{aligned}&\left(i\varsigma\sin\xi e^{i\varsigma t} \quad -i\delta\cos\xi e^{-i\delta t}\right) \\ &\times\begin{pmatrix}e^{-i\varsigma t}\sin\xi \\ e^{i\delta t}\cos\xi\end{pmatrix} = i\varsigma(\sin\xi)^2 - i\delta(\cos\xi)^2 = 0.\end{aligned} \tag{24}$$

The equivalent equations (23) and (24) lead to a sufficient condition for parallel transport:

$$\begin{aligned}&(\tan\xi)^2 = \frac{\delta}{\varsigma}; \\ &\cos^2\xi\left(1+\frac{\delta^2}{\varsigma^2}\right) = 1 \to \cos\xi = \sqrt{\frac{\varsigma^2}{\delta^2+\varsigma^2}}\end{aligned} \tag{25}$$

Using Eq. (13), and that of (16) for $U(t)$ we get:

$$\begin{aligned}&\left\langle 1\right|_0 U(t)\left|1\right\rangle_0 = \cos\xi e^{i(\delta t+\phi)}; \\ &\left\langle 2\right|_0 U(t)\left|2\right\rangle_0 = \cos\xi e^{-i(\delta t+\phi)}.\end{aligned} \tag{26}$$

The geometric phase γ_{geom} is obtained by the incoherent superposition of two fields produced separately from the two components of the thermal field so that it is given by:

$$\gamma_{geom} = \arg\left[P_1 \cos\xi e^{i(\delta t+\phi)} + P_2 \cos\xi e^{-i(\delta t+\phi)} \right] \tag{27}$$

From Eq. (27) we get the result:

$$\gamma_{geom} = \arctan\left[\left(\frac{P_1 - P_2}{P_1 + P_2} \right) \tan\left(\delta t + \phi\right) \right], \tag{28}$$

where for the present system $P_1 + P_2 = 1$. Radiation intensity is reduced by the factor:

$$\begin{aligned} \tilde{v} &= \left| P_1 \cos\xi e^{i(\delta t+\phi)} + P_2 \cos\xi e^{-i(\delta t+\phi)} \right| = \\ &\cos\xi \sqrt{P_1^2 + P_2^2 + 2P_1P_2 \cos\left(2\delta t + 2\phi\right)}. \end{aligned} \tag{29}$$

The unitary development of the spin 1/2 system was produced by the consecutive interactions of this system with magnetic fields in times which are short relative to relaxation times in this system. Parallel transport equations, which eliminate the dynamical phase, were obtained by assuming the relations of Eq. (25) between the parameters included in the analysis. For the present mixed spin 1/2 system $\delta t + \phi$ represents the Pancharatnam's phase for open cycle and $(P_1 - P_2)/(P_1 + P_2)$ represents the thermal noise parameter.

By using equation (3) the thermal noise term can be transformed to:

$$\left(\frac{P_1 - P_2}{P_1 + P_2} \right) = \tanh\left[\frac{\hbar\tilde{\omega}\beta}{2} \right]. \tag{30}$$

For very low temperatures this term tends to the value 1. For very high temperatures we can use the approximations:

$$\begin{aligned} &\sinh\left[\frac{\hbar\tilde{\omega}\beta}{2}\right] = \frac{\hbar\tilde{\omega}\beta}{2}; \quad \cosh\left[\frac{\hbar\tilde{\omega}\beta}{2}\right] = 1; \\ &\left(\frac{P_1 - P_2}{P_1 + P_2} \right) = \frac{\hbar\tilde{\omega}}{2k_B T} \end{aligned} \tag{31}$$

so that this term is given by the ratio between the quantum vacuum energy $\hbar\tilde{\omega}/2$ and the thermal energy $k_B T$. It is interesting to note that the Pancharatnam phase for open cycle in neutrons experiments [19] was obtained for open cycles.

4. Conclusions

The efficiency of thermal engines and the role of time durations for getting maximum efficiency was analyzed. Two-dimensional Carnot thermal spin 1/2 system with time-dependent magnetic fields in the symmetric z was analyzed. The density matrix ρ_0 obtained for mixed states includes averaging of thermal fluctuations with the probability $P_k\left(k = 1,2\right)$ and therefore it cannot be used in interferometry. The use of unitary transformation of mixed states, including the parallel transport equations to these states, were found to be of special interest, as by their use dynamical phases are eliminated and we remain with geometric phases. We find that the geometric phases obtained by the unitary transformation are Pancharatnam's phases which are gauge invariant and are valid also for open circles. It is interesting to find that geometric phases can be obtained in quantum engine systems, which lead to interference effects, and which are different from the common ones in NMR and neutron interferometry. In conclusion, geometric phases which can be obtained in quantum engines (and which were not observed so far) will lead to new insights in quantum thermodynamics.

Acknowledgements
The present study was supported by Technion-Mossad under grant No. 2007156.

Conflict of interest
The author declares no conflicts of interest, Artificial AI-assisted technology was not used.

Role of the Corresponding Author
The article was obtained by Y. Ben-Aryeh investigation.

References:

[1] R. Kosloff and Y. Rezek, "The Quantum Harmonic Otto Cycle," *Entropy*, vol. 19, no. 4, p. 136, Mar. 2017, doi: 10.3390/e19040136.

[2] H. S. Leff, "Thermal efficiency at maximum work output: New results for old heat engines," *Am J Phys*, vol. 55, no. 7, pp. 602–610, Jul. 1987, doi: 10.1119/1.15071.

[3] J. Roßnagel *et al.*, "A single-atom heat engine," *Science (1979)*, vol. 352, no. 6283, pp. 325–329, Apr. 2016, doi: 10.1126/science.aad6320.

[4] O. Abah *et al.*, "Single-Ion Heat Engine at Maximum Power," *Phys Rev Lett*, vol. 109, no. 20, p. 203006, Nov. 2012, doi: 10.1103/PhysRevLett.109.203006.

[5] M. Esposito, R. Kawai, K. Lindenberg, and C. Van den Broeck, "Efficiency at Maximum Power of Low-Dissipation Carnot Engines," *Phys Rev Lett*, vol. 105, no. 15, Oct. 2010, Art. no. 150603, doi: 10.1103/PhysRevLett.105.150603.

[6] E. Geva and R. Kosloff, "A quantum-mechanical heat engine operating in finite time. A model consisting of spin-1/2 systems as the working fluid," *J Chem Phys*, vol. 96, no. 4, pp. 3054–3067, Feb. 1992, doi: 10.1063/1.461951.

[7] B. Lin and J. Chen, "Optimal analysis of the performance of an irreversible quantum heat engine with spin systems," *J Phys A Math Gen*, vol. 38, no. 1, pp. 69–79, Jan. 2005, doi: 10.1088/0305-4470/38/1/004.

[8] F. L. Curzon and B. Ahlborn, "Efficiency of a Carnot engine at maximum power output," *Am J Phys*, vol. 43, no. 1, pp. 22–24, Jan. 1975, doi: 10.1119/1.10023.

[9] M. V. Berry, "Quantal phase factors accompanying adiabatic changes," *Proceedings of the Royal Society of London. A. Mathematical and Physical Sciences*, vol. 392, no. 1802, pp. 45–57, Mar. 1984, doi: 10.1098/rspa.1984.0023.

[10] Y. Ben-Aryeh, “Berry and Pancharatnam topological phases of atomic and optical systems,” *Journal of Optics B: Quantum and Semiclassical Optics*, vol. 6, no. 4, pp. R1–R18, Apr. 2004, doi: 10.1088/1464-4266/6/4/R01.

[11] Y. Aharonov and J. Anandan, “Phase change during a cyclic quantum evolution,” *Phys Rev Lett*, vol. 58, no. 16, pp. 1593–1596, Apr. 1987, doi: 10.1103/PhysRevLett.58.1593.

[12] E. Sjöqvist *et al.*, “Geometric Phases for Mixed States in Interferometry,” *Phys Rev Lett*, vol. 85, no. 14, pp. 2845–2849, Oct. 2000, doi: 10.1103/PhysRevLett.85.2845.

[13] E. Sjöqvist, “Quantal phase in split-beam interferometry,” *Phys Rev A (Coll Park)*, vol. 63, no. 3, Feb. 2001, Art. no. 035602, doi: 10.1103/PhysRevA.63.035602.

[14] S. Pancharatnam, “Generalized theory of interference, and its applications,” *Proceedings of the Indian Academy of Sciences - Section A*, vol. 44, no. 5, pp. 247–262, Nov. 1956, doi: 10.1007/BF03046050.

[15] A. G. Wagh and V. C. Rakhecha, “On measuring the Pancharatnam phase. I. Interferometry,” *Phys Lett A*, vol. 197, no. 2, pp. 107–111, Jan. 1995, doi: 10.1016/0375-9601(94)00914-B.

[16] Ghosh and A. Kumar, “Experimental measurement of mixed state geometric phase by quantum interferometry using NMR,” *Phys Lett A*, vol. 349, no. 1–4, pp. 27–36, Jan. 2006, doi: 10.1016/j.physleta.2005.08.092.

[17] M. Ericsson, D. Achilles, J. T. Barreiro, D. Branning, N. A. Peters, and P. G. Kwiat, “Measurement of Geometric Phase for Mixed States Using Single Photon Interferometry,” *Phys Rev Lett*, vol. 94, no. 5, Feb. 2005, Art. no. 050401, doi: 10.1103/PhysRevLett.94.050401.

[18] J. Du *et al.*, “Observation of Geometric Phases for Mixed States using NMR Interferometry,” *Phys Rev Lett*, vol. 91, no. 10, Sep. 2003, Art. no. 100403, doi: 10.1103/PhysRevLett.91.100403.

[19] J. Klepp, S. Sponar, Y. Hasegawa, E. Jericha, and G. Badurek, “Noncyclic Pancharatnam phase for mixed state evolution in neutron polarimetry,” *Phys Lett A*, vol. 342, no. 1–2, pp. 48–52, Jul. 2005, doi: 10.1016/j.physleta.2005.05.038.

International Journal of Thermodynamics (IJoT)
ISSN 1301-9724 / e-ISSN 2146-1511
https://dergipark.org.tr/en/pub/ijot

Vol. 28 (No. 2), pp. 051-058, 2025
doi: 10.5541/ijot.1642883

Research Article

Exergetic Efficiency of Coal Gasification Using High-Temperature Mixtures of O_2/N_2 and O_2/CO_2

*I. G. Donskoy

[1]Melentiev Energy Systems Institute, Russia, Irkutsk, Lermontova st. 130
E-mail: *donskoy.chem@mail.ru

Received 19 February 2025, Revised 04 April 2025, Accepted 10 April 2025

Abstract

A search for ways to improve the efficiency of energy technologies requires the selection of appropriate efficiency criteria and a study of the influence of different factors on them. This paper focuses on coal gasification, including hard coals and brown coals, in air and steam media, considering different efficiency criteria for gasification processes: cold gas efficiency, energy efficiency that takes into account the heat of the gasification agent, and exergy efficiency that considers the chemical, thermal, and mechanical energy of reactants and products. The dependence of these efficiency criteria on stoichiometric ratios and air temperature is demonstrated, and the applicability of these criteria in power plant analysis is discussed.

Keywords: *Thermochemical conversion; chemical thermodynamics; optimization; fuel utilization.*

1. Introduction

Solid fuel gasification can be used for various purposes: waste recycling, production of feedstock for chemical syntheses (primarily hydrogen), or fuel gases for gas engines or electrochemical converters, etc. Depending on the purpose, different criteria may be used to evaluate the efficiency of gasification processes [1]. The most frequently used criteria are given in Table 1.

Table 1. Efficiency criteria for gasification processes.

Criteria	Formula	Notation
Cold gas efficiency (chemical efficiency)	$\eta_{chem} = \frac{\sum_i q_i G_i}{QB}$	q_i – heat of combustion of i-th component; G_i – mass flowrate of *i*-th component; *Q* – heating value of fuel; *B* – fuel flowrate
Thermal efficiency	$\eta_{therm} = \frac{\sum_i q_i G_i}{QB + q_{in}}$	q_{in} – energy used for gasification agent heating
Exergetic efficiency	$\eta_{ex} = \frac{\sum_i Ex_i G_i}{Ex_f B + Ex_g G_g}$	Ex_i – specific exergy of *i*-th component; G_g – gasification agent mass flowrate
Carbon conversion efficiency	$\eta_C = \frac{\sum_i y_i^C G_i}{y_f^C B}$	y_C – carbon content
Component yield	$\eta_i = \frac{G_i}{B}$	

Gasification efficiency metrics in the present study are cold gas efficiency, which is a fraction of solid fuel heating value converted into gas heating value; thermal efficiency, which takes into account the physical heat energy of the gasification agent; and exergy efficiency, which weighs input and output exergy flows. It should be noted that chemical exergy is not equal to heating value but is usually very close. Cold gas efficiency does not include the sensible heat of gas and its expansion work.

Gasification technologies allow for the production of multiple products, so it is necessary to have a method for comparing the different outputs of chemicals, heat, and electricity, depending on the conditions. Considering this, exergy analysis can be considered as such a method.

The main difference between energy and exergy analyses lies in the choice of the reference state. For technical thermodynamics, the reference state is absolute zero temperature and vacuum. In exergy analysis, however, the environment serves as the reference state.

Accordingly, a system at rest with the conditions of the environment has zero useful energy, as it cannot serve as a source or sink for heat or matter in any engine, due to the second law of thermodynamics. Thermal, chemical, and mechanical energy stored within a system cannot be completely utilized. These forms of energy, when weighted by their availability, are referred to as exergy.

Following standard definitions [2], we can express the exergy value of a system as follows:

$$Ex = U + P^{env}V - T^{env}S - \sum_j^{N_s} n_i \mu_i^{env} \qquad (1)$$

Here *Ex* is system exergy, *U* is internal energy of the system, index *env* refers to the environment, and *V* is system volume. Using enthalpy instead of internal energy, we can write the expression for exergy as:

$$Ex = H - (P - P^{env})V - T^{env}S - \sum_j^{N_s} n_i \mu_i^{env} \qquad (2)$$

In this form, exergy can be calculated using tables of thermodynamic properties of substances. Standard exergy values for individual substances are tabulated in

*Corresponding Author

corresponding reference datasets. For example, data from references [3] and [4] are used for calculations in this paper. Calculating exergy for solid fuels involves ill-defined estimates of specific entropy. However, there are reference books and recommended formulas available (for example, [5] for materials and [6] for fuels) to assist with this process.

The full exergy of a gasification-based power plant may also include slag, sulfur, and high-purity nitrogen, among other possible products. However, we will not consider these potential outputs in this discussion, as we focus on the raw producer gas leaving the gasifier unit.

In the case of high-temperature gasification, the producer gas contains both chemical energy that can be used for combustion and thermal energy that can be used, for example, for generating steam. Therefore, the presentation of gasification efficiency in terms of cold gas efficiency (Table 1) is not sufficient to evaluate the overall useful energy potential. It should also be noted that integrating a gas cleaning system into the thermal circuits for water-steam heating can significantly improve the efficiency of the entire power plant.

Many works focused on the analysis of exergy flows in energo-technological plants (combined heat and power plants [7], integrated gasification combined cycles [8], Rankine cycles [9], co-gasification of coal and biomass [10], multifuel plants [11]), including multi-product coal-fired plants (hydrogen [12], methanol [13], ammonia [14]) and CO_2 capture systems (including flue gas recycle [15] and cooling-compressing unit [16]). Some studies compare different capture schemes (for example, advantages of the water shift stage are considered in [17] and the choice of absorbent is considered in [18]) and the energy/exergy efficiency of the plant or specific units under different conditions. Of interest is the relationship between the exergy efficiency of gasification units and process parameters, such as the flow rate and temperature of the gasification agent.

Exergy balances for industrial coal gasification processes were developed in [19] for Hygas and in [20] for Lurgi. The main exergy losses are related to oxidation processes, although these are lower than those for traditional combustion processes [21]. The exergy balance for plants that produce liquid fuels from gasification products is discussed in [22], and the reduction of exergy losses through the use of indirect combustion methods for coal, including gasification, is examined from a general perspective in [23]. Similarly, schemes involving heat recirculation between stages of coal conversion are explored in [24] for steam-oxygen gasification and in [25] for air gasification.

The current study aims to compare the energy and exergy efficiency criteria as applied to some coal gasification processes. In relation to the scope of this paper, we are also interested in works related to the study of the spatial distribution of specific exergy in solid fuel conversion reactors. These works include one-dimensional approximations [26] and 2D/3D formulations (for multiphase flows [27] and gaseous fuels [28]). Data obtained through measurements and mathematical modeling allow us to control the destruction of exergy directly in the reaction zone. However, such detailed models usually do not allow full-scale parametric optimization due to high computation costs.

Let us consider the process of coal gasification with the hot air. Usually, high-temperature heating improves the conditions for gasification, increasing the conversion of fuel and improving the quality of producer gas. Thermodynamic analyses show that reducing the temperature difference between the input and output material flows may increase the efficiency of the fuel conversion process (see, for example, works on general theoretical consideration [29] and, specifically, carbon conversion [30]). However, we must consider the heat input required to obtain high-temperature air. Chemical and thermal energy have different qualities: chemical energy can be converted directly into useful products, while thermal energy can be converted into useful work with significant thermodynamic losses only. Therefore, we need the exergy approach to evaluate the efficiency and to compare different approaches.

A feature of the thermodynamics of solid fuel gasification processes in oxygen-containing environments (compared to combustion processes) is the existence of a certain threshold value of the stoichiometric ratio above which a complete conversion of fuel matter to gaseous products occurs (these thresholds were determined for solid carbon in [31] and for biomass in [32]). This threshold value is typically much lower than that corresponding to complete combustion (ranging from 0.25 for biofuels to 0.5 for pure carbon), and the addition of additional gasifying agents such as steam and carbon dioxide can reduce this value even further. However, a purely stoichiometric approach is not sufficient without considering the thermodynamics and kinetics of heterogeneous reactions. In this study, we examine the kinetic constraints on achieving equilibrium in a reactive system, which allow us to identify temperature ranges for thermodynamically efficient coal gasification.

The novelty of the study is the estimation of exergy efficiency for oxyfuel gasification processes. These processes were proposed in several works for both one-stage [33] and two-stage [34] reactors. The advantage of oxyfuel gasification is the lower cost of carbon dioxide capture, although there are crucial changes in heat transfer and produced gas properties. The papers [34, 35] give estimates for the net efficiency of oxy-fuel IGCC plants of about 40-45%, taking into account carbon capture based on available experimental data. Further investigation may lead to an even lower carbon capture penalty. Traditional and promising coal power plants with carbon capture have net efficiency of 30-35% [36]. The advantage of IGCC is very important in the climate change context, when thermal power plants become subject to strict environmental restrictions, including carbon emissions. The use of cheap coal fuel based on new clean technologies will not only improve the environmental situation but also achieve the specified requirements with acceptable economic efficiency.

It is important to evaluate the thermodynamic efficiency of new promising gasification processes with respect to exergy destruction and to compare them with traditional processes. Moreover, instead of considering a single set of parameters, we obtain exergy efficiency in a wide range of stoichiometric ratios and input temperatures, which allows us to optimize coal gasification conditions.

2. Mathematical Model

The calculation of coal gasification processes is carried out using a mathematical model, which is described previously in detail in the paper [37]. These works use a spatially one-dimensional model of the coal dust gasification process in an oxidizer flow, similar to models [38] and [39].

In formulating the mathematical model, the following assumptions are made. The drying rate is limited by external mass exchange with the ambient air, the pyrolysis rate is proportional to the volatile content in the particle and depends on temperature according to the Arrhenius law, the gasification rate of individual particles is described by the diffusion-kinetic theory of carbon combustion, reactor heat losses can be neglected, and the effects of gas recirculation and slag film are not taken into account.

The chemical kinetics of reactions in the gas phase are not taken into account. It is assumed that substances entering the gas phase immediately reach a state of thermodynamic equilibrium. Therefore, chemical transformations are described using a thermodynamic model with macroscopic constraints on the rate of heterogeneous reactions (for example, lumped models [40] and reduced-order models developed for power plant calculations [41]). This approach is suitable for high-temperature processes where the rate of gas-phase reactions is much faster than that of heterogeneous reactions. Validation of this assumption by means of comparison of calculated gas composition with experimental data can be found in previous works [37]. The possible effects of interaction between organic and mineral components of fuels (due to thermal effects or slagging conditions [42]) are not considered. Therefore, gasification efficiency is mainly determined by stoichiometry and fuel heating value.

One-dimensional approximation does not allow capturing all relevant phenomena in high-temperature gasification processes. For example, feeding systems design and gas-wall interaction, including jet formation and destruction, are important topics in gasification technology. However, this approximation allows estimating reaction zone length and output gas composition, which gives the main technical parameters of the gasifier at the level of a power or chemical plant. The reduction of computations from 3D to 1D is crucial, and additional simplifications (such as the equilibrium gas model) allow for full-scale optimization. Some models include several 1D pieces allowing to reproduce mixing and recirculation effects [38, 43]. We do not take into account these features, modeling the flow in the gasifier as uniform.

The model allows estimating the influence of heterogeneous reactions on exergy efficiency. A similar analysis was presented in [44] for the oxygen-fed coal gasification process (Texaco), where authors obtained an exergy efficiency of 87% with 50% of all losses due to heterogeneous reactions. Temperature range was, however, very narrow. In the present work, we consider a wider range of gasification processes.

In calculations, we varied gasification conditions, namely stoichiometric ratio, fuel composition, gasification agent composition, and its temperature. Depending on carbon content, the optimum stoichiometric ratio varies from 0.25 to 0.5 [45]. In our calculations, we used a range from 0.15 to 0.7 to localize the optimum. Brown and hard coals were considered as a fuel (see Table 2). Brown coals contain less carbon, so their heating value is lower, but a higher content of elemental hydrogen and oxygen (including moisture) allows for decreased specific air consumption and obtaining syngas with a higher content of molecular hydrogen. Hard coals have a higher heating value, which allows for a higher conversion temperature but requires the addition of steam to convert this heat to combustible products. In this regard, carbon dioxide may be considered as an alternative to steam.

The properties of a gasification agent are usually the main control parameter in the conversion process. We use a range of temperatures from 300 K to 1400 K. The latter value is quite high and non-typical for industrial processes. Nevertheless, we consider this range in order to investigate the limits of coal gasification caused by physico-chemical features, which are discussed in Sec. 6.

Table 2. Coals' characteristics.

Coal source		Berezovskiy	Mugunskiy	Urtuysky	Kuznetsky
Coal composition, % mass.	W^r	33	22	29.5	2
	A^r	4.7	15.6	8.8	15.4
	S^r	0.2	0.9	0.3	0.9
	C^r	44.2	46	46.9	68.1
	H^r	3.1	3.6	3	4.2
	N^r	0.4	0.9	0.5	1.6
	O^r	14.4	11	11	7.8

3. Air Gasification of Brown Coals without Heating

Let us consider the gasification process in a cylindrical reactor with a diameter of 3 m and a length of 9 m; the working pressure is about 15 atm [46]. The fuel consumption is about 180 t/h, and the average particle size is 0.1 mm. The gasifying agent is a mixture of air and water vapor (temperature 655 K). The variable parameters are the specific air consumption (1-6 kg/kg of fuel) and the specific steam consumption (0-0.1 kg/kg of fuel). The fuel composition is given in Table 2 [47].

Figure 1 shows a comparison of the exergy and cold gas efficiencies of air-steam gasification of brown coals. From a practical point of view, the most interesting region is the vicinity of the maximum efficiency. Before reaching the extremum, both criteria are practically the same: the cold gas efficiency closely characterizes the exergy of the producer gas. However, as the specific consumption of oxidizer increases, the cold gas efficiency decreases at a sharper rate. At high values of stoichiometric ratio, fuel carbon is almost absent, and the excessive oxygen consumes combustible components of the producer gas. Cold gas efficiency is more sensitive to these losses. Exergy efficiency remains at the level of 30-40% even after complete combustion (stoichiometric ratio of 1), due to the high thermal exergy of combustion products. Interestingly, the dependence is similar for different compositions of coal.

Three presented coals are quite similar in composition: Mugunsky coal contains 2-3 times more ash and less moisture; Urtuisky coal contains more carbon in the organic mass and therefore has a higher heating value. The stoichiometric amount of air required for complete combustion varies for the coals in the range of 5.5-6.3 kg/kg. Urtuysky coal is characterized by the highest cold gas efficiency (68.3%), due to its higher heating value. It is followed by Berezovsky coal (67.5%) and, finally, Mugunsky coal (67.3%). The last two coal compositions, however, differ little, and within the accepted assumptions, the characteristics of their gasification can be considered almost equal. Exergy efficiencies are very close to cold gas efficiencies (68.3%, 67% and 67.3% correspondingly).

4. Coal Gasification with Air Heating

Now, let us consider the gasification process in a reactor with a fuel capacity of 100 t/h with an operating pressure of 30 atmospheres [48]. The geometric dimensions of the reactor are as follows. The length of the reaction zone is 15 meters; the internal diameter is 3 meters. The temperature of the fuel entering the reactor is 300 K; the steam temperature is 600 K, and the air temperature varies from 400 to 1300 K (with increments of 100 degrees). The steam consumption ranges from 0 to 0.2 moles per mole of carbon, and the stoichiometric ratio ranges from 0.1 to 0.7 (with increments of 0.05). Kuznetsky coal with characteristics from Table 2 is used as the fuel.

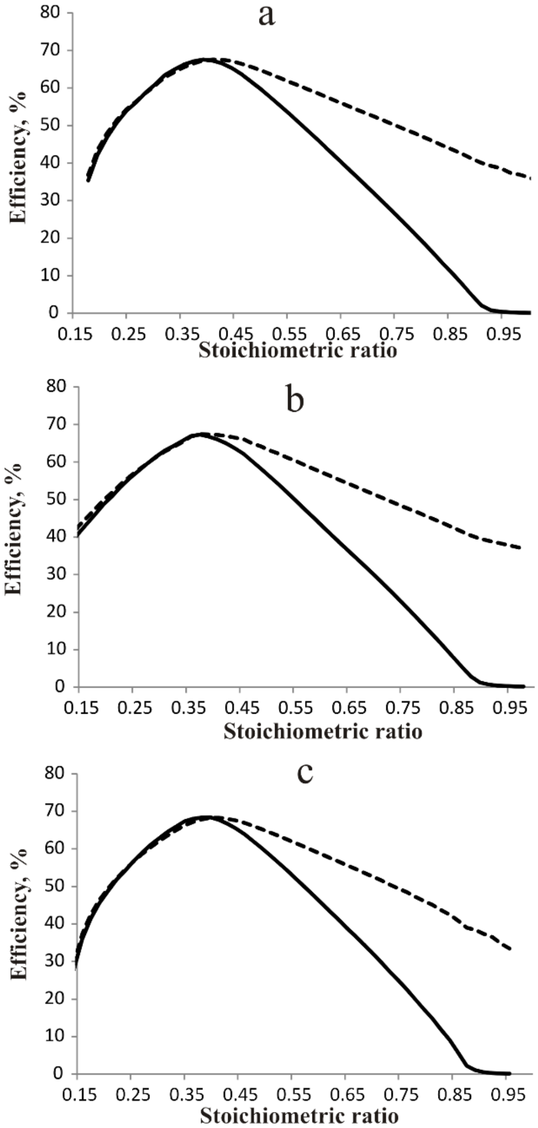

Figure 1. Comparison of cold gas efficiency (solid line) and exergy efficiency (dashed line) of brown coal gasification: Berezovsky (a), Urtuysky (b), Mugunsky (c).

For each parameter set, output gas flow rate and composition were calculated using the mathematical model. Then, criteria presented in Table 1 were estimated. The results are presented below.

A comparison of cold gas, thermal, and exergy efficiencies is presented in Figure 2. The x-axis in each subfigure is the stoichiometric ratio, and the y-axis is the input air temperature. Isolines show surfaces of efficiency criteria dependence on gasification agent parameters for the fixed fuel composition and flow rate. The observed dependences are typical for solid fuel conversion. There is a range of stoichiometric ratios where efficiency achieves its maximum. Qualitatively, these surfaces are similar. However, the optimal conditions for each criterion differ: cold gas efficiency has a relatively flat maximum, with the value above 78% extending along the temperature axis. In contrast, thermal and exergy efficiencies exhibit a more distinct extremum, corresponding to lower temperatures.

Thermal efficiency indicates that high-temperature air heating does not justify an increase in combustible gas yield. Exergy efficiency maximum corresponds to air heating up to 600 K. Cold gas efficiency does not change significantly with increasing temperature, and the thermal exergy of input air included increases. Although the thermal exergy of the gasification products also increases, there is an optimum, marking the point after which the exergy efficiency decreases more slowly than the cold gas efficiency (similarly to the previous section).

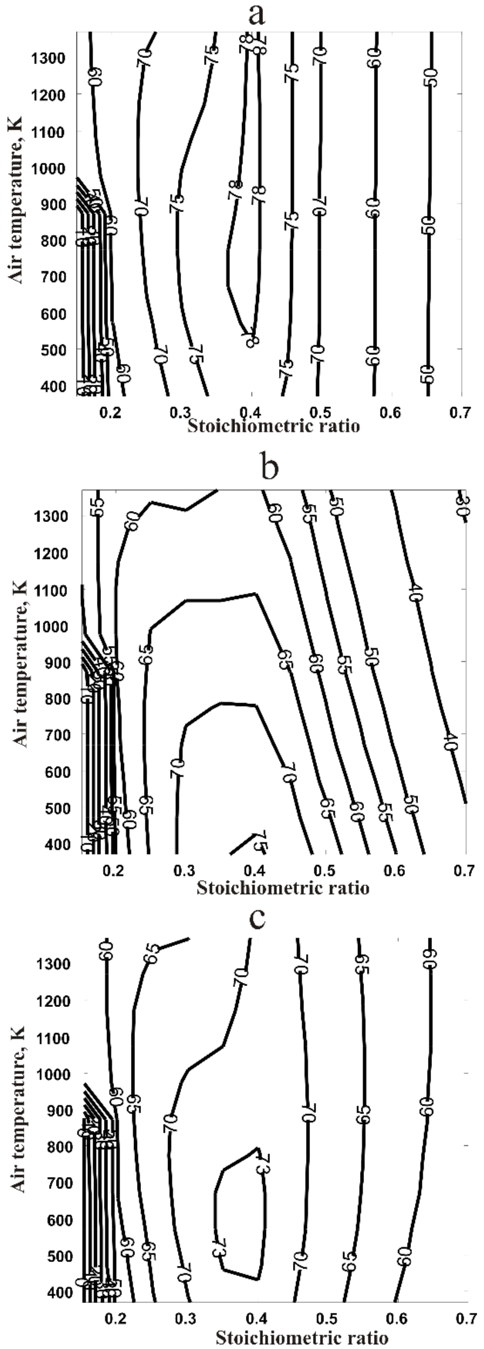

Figure 2. Coal gasification efficiency (%) at a specific steam consumption of 0.1 mol/mol carbon: cold gas efficiency (a), thermal efficiency (b) and exergy efficiency (c).

Kuznetsky coal has a higher heating value compared to brown coals, which results in higher cold gas efficiency. Higher gasification temperature improves conditions for endothermal reactions leading to CO and H_2 formation. The exergy efficiency is lower, although still higher than for brown coals.

5. Coal Gasification with High-Temperature O_2/CO_2 Mixtures

Then let us consider the gasification process under oxy-fuel conditions, when the gasifying agent is a mixture of oxygen with combustion products. By excluding nitrogen, highly concentrated CO_2-H_2O mixtures are obtained after combustion [49]. The extraction of CO_2 for further transportation and disposal is simplified compared to using air.

The higher heat capacity of CO_2 inhibits fuel ignition at low temperatures while also contributing to thermal stability and improved gas quality when using heating [50]. The reactor dimensions and fuel characteristics remain the same as in the previous section. Detailed calculations can be found in [48].

When switching to O_2-CO_2 (ratio is 20/80), increasing the temperature allows for several benefits. Firstly, it expands the range of stable conditions. Secondly, it can result in an increase in cold gas efficiency by up to 20% per 1000 K. The optimal value of the stoichiometric ratio decreases as the gasification agent temperature increases, as CO_2 acts as the gasifying agent in this case.

Figure 3 compares the cold gas, thermal, and exergy efficiency surfaces in the space of stoichiometric ratio and gasification agent temperature as in the previous section. In the vicinity of optimal parameters, all three criteria behave similarly: the maximum efficiency is observed with increasing temperature within a narrow range of stoichiometric ratios. However, the maximum efficiency decreases from 95% for the cold gas efficiency to 88% for the thermal efficiency and 84% for the exergy efficiency.

As the stoichiometric ratio increases, the cold gas efficiency becomes independent of temperature and is only determined by stoichiometric conditions. When taking into account the air heating, the efficiency naturally decreases as temperature increases. In contrast, the exergy efficiency increases with temperature due to the increase in the thermal component of the exergy of the gasification products.

A significant difference between fuel gasification in air and in O_2/CO_2 mixtures is the initial exergy of the gasifying agent: atmospheric air has, by definition, zero chemical exergy; O_2/CO_2 mixtures (even at an oxygen concentration equal to atmospheric) have significant chemical exergy due to the high CO_2 content. In this case, CO_2 is not an inert diluent but a gasification agent, the presence of which improves the conditions of coal conversion and, in some cases, increases the heating value of the producer gas. Therefore, the transition from unstable (low-temperature) gasification conditions to effective high-temperature conversion occurs with a larger jump compared to air gasification.

Authors of [51] noted that the 1D model of the oxy-fuel coal gasification process gives similar results as the equilibrium model. In this regard, our results may be of interest with respect to gasification process characteristics. Cold gas efficiency of 76% was achieved in a laboratory reactor in [35], which is close to the optimum point at the lower temperature boundary (see Figure 3a). The estimated power production efficiency, taking into account carbon capture, is about 40-45%. The presented results show that gasification agent heating can enhance gasification efficiency, allowing to achieve exergy efficiency of 80% at lower stoichiometric ratios. In this regard, the promising power plant needs less oxygen, which is compensated by the CO_2 heating up to 700 K and higher. Thermal energy costs of the heater in some cases are less than power production efficiency increase [52].

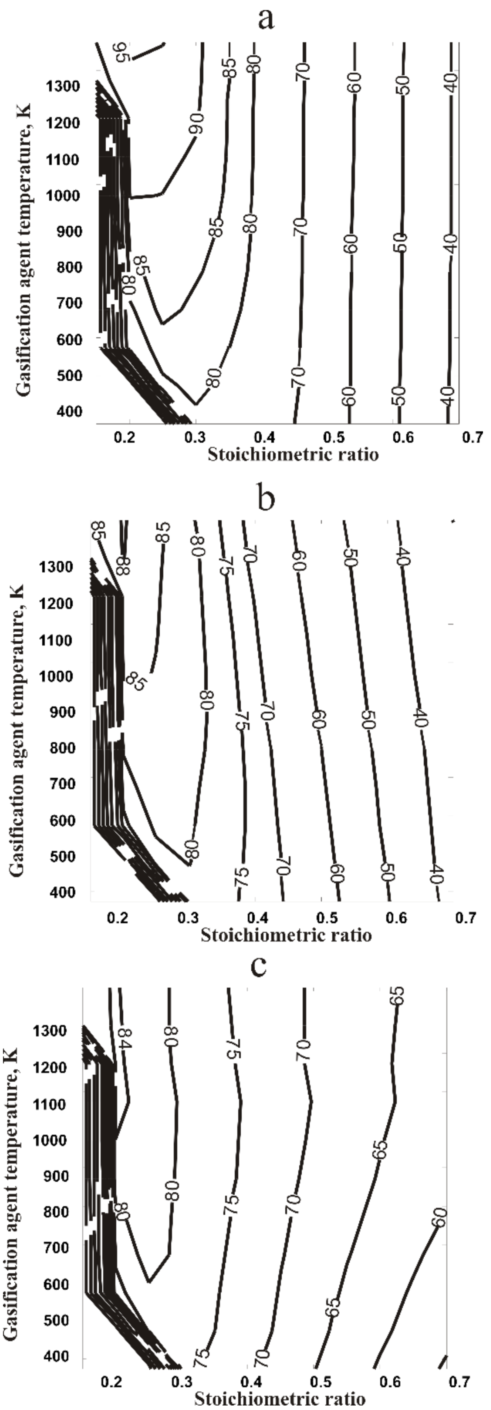

Figure 3. Comparison of coal oxyfuel gasification efficiency criteria (%): cold gas efficiency (a), thermal efficiency (b) and exergy efficiency (c).

6. Discussion

The cold gas and exergy efficiencies of the gasification process are almost equal in the region of low stoichiometric ratios, where the chemical exergy greatly exceeds the thermal exergy. The divergence is observed when the stoichiometric ratio exceeds a value corresponding to the full coal conversion. At this point, oxidation leads to the conversion of the chemical energy of gasification products into thermal energy. The positions of the maximum efficiency are equal for both criteria. The gasification products have significant thermal exergy value after the threshold [31]. In this regard, the conclusion of paper [53], proposing the optimal conditions at stoichiometric ratios slightly above a full conversion threshold, is correct.

Gasification in O_2/CO_2 mixtures allows for higher efficiency due to the utilization of carbon dioxide as a gasification agent in the reaction zone. Full conversion threshold shifts towards lower stoichiometric ratios (which are calculated based on molecular oxygen). In order to maintain high temperatures, internal heating is required (due to the higher heat capacity of CO_2). Nevertheless, the exergy efficiency value for oxyfuel gasification is lower than other efficiency criteria. This is due the higher specific exergy of concentrated CO_2, which increases exergy input in oxyfuel systems but allows simpler carbon capture.

It should also be noted that the efficient use of producer gas thermal exergy is limited due to the requirements for temperature and purity of fuel gas. Harmful impurities, such as sulfur compounds and solid particles, must be removed. A common solution to this is water spray cooling, which reduces the heating value of the producer gas through a water shift reaction and dilution. In some cases, the water shift stage is introduced to enhance the H_2/CO ratio or to capture CO_2 before combustion. The exergy loss during the gas conditioning is estimated to be up to 80% of total exergy losses according to studies [54, 55]. Reducing these exergy losses is possible through hot gas cleaning methods, such as hot filters and sorbent materials [56, 57]. This approach has the potential to improve thermodynamic efficiency, although it may require more expensive materials and more complex equipment to implement.

7. Conclusion

The paper examines the influence of the stoichiometric and heating factors on the efficiency of coal gasification processes. The exergy efficiency of gasification is shown to be similar to the cold gas efficiency when the stoichiometric ratio is below the optimum point, but it exceeds the cold gas efficiency at higher values of the stoichiometric ratio due to the thermal energy of the gas products. When switching to oxyfuel gasification, the initial energy of the gasification agent is higher due to the high CO_2 content, while the higher heat capacity of the mixture can worsen the thermal stability at lower initial temperatures but improve the conditions for high-temperature gasification.

Optimum exergy efficiency is about 73% for air gasification heated to 600-700 K and about 80% for oxyfuel gasification at the same gasification agent temperature. Even higher exergy efficiency is possible at temperatures of O_2/CO_2 mixtures of 1100 K and stoichiometric ratios of about 0.2, but it would be difficult to maintain a stable gasification process in these conditions.

Acknowledgements

The research was carried out under the State Assignment Project (no. FWEU-2021-0005) of the Fundamental Research Program of the Russian Federation 2021-2030 using the resources of the High-Temperature Circuit Multi-Access Research Center.

Nomenclature

Ex – exergy
$IGCC$ – integrated gasification combined cycle
U – internal energy
S – entropy
P – pressure
T – temperature
n – molar quantity
μ – chemical potential
η – efficiency
G – gas mass flowrate
q – gas component heating value
Q – coal heating value
B – coal mass flowrate
y^C – carbon content
W^r – moisture content
A^r – ash content
C^r – carbon content (y^C)
H^r – hydrogen content
O^r – oxygen content
S^r – sulfur content
N^r – nitrogen content
$chem$ – chemical
$therm$ – thermal
eq – equilibrium
in – input
env – environmental

References

[1] T. Duan, C. Lu, S. Xiong, Z. Fu, and B. Zhang, “Evaluation method of the energy conversion efficiency of coal gasification and related applications,” International Journal of Energy Research, vol. 40, no. 2, pp. 168–180, Feb. 2016, doi: 10.1002/er.3444.

[2] M. J. Moran and E. Sciubba, “Exergy Analysis: Principles and Practice,” Journal of Engineering for Gas Turbines and Power, vol. 116, no. 2, pp. 285–290, Apr. 1994, doi: 10.1115/1.2906818.

[3] J. Szargut, “Chemical exergies of the elements,” Applied Energy, vol. 32, no. 4, pp. 269–286, Jan. 1989, doi: 10.1016/0306-2619(89)90016-0.

[4] V. Stepanov, “Chemical energies and exergies of fuels,” Energy, vol. 20, no. 3, pp. 235–242, Mar. 1995, doi: 10.1016/0360-5442(94)00067-D.

[5] C. Michalakakis, J. Fouillou, R. C. Lupton, A. Gonzalez Hernandez, and J. M. Cullen, “Calculating the chemical exergy of materials,” Journal of Industrial Ecology, vol. 25, no. 2, pp. 274–287, Apr. 2021, doi: 10.1111/jiec.13120.

[6] V. S. Stepanov and T. B. Stepanova, The Efficiency of Energy Use. Novosibirsk: Nauka, 1994.

[7] P. A. Shchinninkov, O. V. Borush, and S. V. Zykov, Exergy Research and Optimization of CHPP Operating Modes. Novosibirsk: NSTU Publishing, 2019.

[8] J. C. Lee, H. H. Lee, Y. J. Joo, C. H. Lee, and M. Oh, “Process simulation and thermodynamic analysis of an IGCC (integrated gasification combined cycle) plant with an entrained coal gasifier,” Energy, vol. 64, pp. 58–68, Jan. 2014, doi: 10.1016/j.energy.2013.11.069.

[9] J. Taillon and R. E. Blanchard, “Exergy efficiency graphs for thermal power plants,” Energy, vol. 88, pp. 57–66, Aug. 2015, doi: 10.1016/j.energy.2015.03.055.

[10] A.Thallam Thattai, V. Oldenbroek, L. Schoenmakers, T. Woudstra, and P. V. Aravind, “Experimental model validation and thermodynamic assessment on high percentage (up to 70%) biomass co-gasification at the 253 MW integrated gasification combined cycle power plant in Buggenum, The Netherlands,” Applied Energy, vol. 168, pp. 381–393, Apr. 2016, doi: 10.1016/j.apenergy.2016.01.131.

[11] H.-T. Oh, W.-S. Lee, Y. Ju, and C.-H. Lee, “Performance evaluation and carbon assessment of IGCC power plant with coal quality,” Energy, vol. 188, Dec. 2019, Art. no. 116063, doi: 10.1016/j.energy.2019.116063.

[12] V. E. Nakoryakov, G. v. Nozdrenko, and A. G. Kuzmin, “Investigation of coal fired combined-cycle cogeneration plants for power, heat, syngas, and hydrogen,” Thermophysics and Aeromechanics, vol. 16, no. 4, pp. 515–520, Dec. 2009, doi: 10.1134/S0869864309040027.

[13] W. Wu, L. Zheng, B. Shi, and P.-C. Kuo, “Energy and exergy analysis of MSW-based IGCC power/polygeneration systems,” Energy Conversion and Management, vol. 238, Jun. 2021, Art. no. 114119, doi: 10.1016/j.enconman.2021.114119.

[14] Y. Emre Yuksel, M. Ozturk, and I. Dincer, “Development and assessment of a biomass-gasification based multigenerational plant for production of hydrogen and ammonia fuels,” Fuel, vol. 380, Jan. 2025, Art. no. 133187, doi: 10.1016/j.fuel.2024.133187.

[15] V. Satyam Naidu, P. Aghalayam, and S. Jayanti, “Improving efficiency of CCS-enabled IGCC power plant through the use of recycle flue gas for coal gasification,” Clean Technologies and Environmental Policy, vol. 20, no. 6, pp. 1207–1218, Aug. 2018, doi: 10.1007/s10098-018-1544-0.

[16] B. Jin, H. Zhao, and C. Zheng, “Thermoeconomic cost analysis of CO2 compression and purification unit in oxy-combustion power plants,” Energy Conversion and Management, vol. 106, pp. 53–60, Dec. 2015, doi: 10.1016/j.enconman.2015.09.014.

[17] Y. Cao, B. He, G. Ding, L. Su, and Z. Duan, “Energy and exergy investigation on two improved IGCC power plants with different CO2 capture schemes,” Energy, vol. 140, pp. 47–57, Dec. 2017, doi: 10.1016/j.energy.2017.08.044.

[18] W.-S. Lee, J.-C. Lee, H.-T. Oh, S.-W. Baek, M. Oh, and C.-H. Lee, “Performance, economic and exergy analyses of carbon capture processes for a 300 MW class integrated gasification combined cycle power plant,” Energy, vol. 134, pp. 731–742, Sep. 2017, doi: 10.1016/j.energy.2017.06.059.

[19] S. P. Singh, S. A. Weil, and S. P. Babu, “Thermodynamic analysis of coal gasification processes,” Energy, vol. 5, no. 8–9, pp. 905–914, Aug. 1980, doi: 10.1016/0360-5442(80)90106-1.

[20] C. He, X. Feng, and K. H. Chu, “Process modeling and thermodynamic analysis of Lurgi fixed-bed coal gasifier in an SNG plant,” Applied Energy, vol. 111, pp. 742–757, Nov. 2013, doi: 10.1016/j.apenergy.2013.05.045.

[21] S. C. Kaushik, V. S. Reddy, and S. K. Tyagi, “Energy and exergy analyses of thermal power plants: A review,” Renewable and Sustainable Energy Reviews, vol. 15, no. 4, pp. 1857–1872, May 2011, doi: 10.1016/j.rser.2010.12.007.

[22] S. Qin, X. Zhang, M. Wang, H. Cui, Z. Li, and W. Yi, “Comparison of BGL and Lurgi gasification for coal to liquid fuels (CTL): Process modeling, simulation and thermodynamic analysis,” Energy, vol. 229, Aug. 2021, Art. no. 120697, doi: 10.1016/j.energy.2021.120697.

[23] Q. Yan, T. Lu, J. Luo, Y. Hou, and X. Nan, “Exergy cascade release pathways and exergy efficiency analysis for typical indirect coal combustion processes,” Combustion Theory and Modelling, vol. 23, no. 6, pp. 1134–1149, Nov. 2019, doi: 10.1080/13647830.2019.1639826.

[24] J. Li, W. Han, P. Li, W. Ma, X. Xue, and H. Jin, “High-efficiency power generation system with CO2 capture based on cascading coal gasification employing chemical recuperation,” Energy, vol. 283, Nov. 2023, Art. no. 129153, doi: 10.1016/j.energy.2023.129153.

[25] A. F. Ryzhkov et al., “Development of low-temperature thermochemical conversion reactors for coal power engineering,” Thermal Engineering, vol. 60, no. 12, pp. 895–903, Dec. 2013, doi: 10.1134/S0040601513120100.

[26] L. Feng, G. Zhang, and R. Zhai, “Study on gasification reaction and energy conversion characteristics of the entrained flow coal gasification based on chemical kinetics simulation,” Heliyon, vol. 10, no. 10, May 2024, Art. no. e30997, doi: 10.1016/j.heliyon.2024.e30997.

[27] N. Lior, W. Sarmiento-Darkin, and H. S. Al-Sharqawi, “The exergy fields in transport processes: Their calculation and use,” Energy, vol. 31, no. 5, pp. 553–578, Apr. 2006, doi: 10.1016/j.energy.2005.05.009.

[28] S. K. Som and A. Datta, “Thermodynamic irreversibilities and exergy balance in combustion processes,” Progress in Energy and Combustion Science, vol. 34, no. 3, pp. 351–376, Jun. 2008, doi: 10.1016/j.pecs.2007.09.001.

[29] E. E. Shpil’rain, “Possibility of enhancing efficiency of thermal power schemes by means of chemical regeneration of heat,” Izvestiya AN SSSR. Energetika I transport, no. 6, pp. 115–123, 1985.

[30] G. S. Aslanyan, I. Yu. Ginevskaya, and E. E. Shpil’rain, “Influence of oxygen-steam blast parameters on carbon gasification,” Khimiya tverdogo topliva, no. 1, pp. 90–98, 1984.

[31] M. J. Prins, K. J. Ptasinski, and F. J. J. G. Janssen, “Thermodynamics of gas-char reactions: first and second law analysis,” Chemical Engineering Science, vol. 58, no. 3–6, pp. 1003–1011, Feb. 2003, doi: 10.1016/S0009-2509(02)00641-3.

[32] M. J. Prins and K. J. Ptasinski, “Energy and exergy analyses of the oxidation and gasification of carbon,” Energy, vol. 30, no. 7, pp. 982–1002, Jun. 2005, doi: 10.1016/j.energy.2004.08.010.

[33] G. Donskoy, “How water vapor and carbon dioxide additives affect oxygen gasification of pulverized coal fuel,” Bulletin of the South Ural State University series “Power Engineering,” vol. 21, no. 1, pp. 21–28, 2021, doi: 10.14529/power210102.

[34] Y. Oki et al., “Development of High-efficiency Oxy-fuel IGCC System,” Energy Procedia, vol. 63, pp. 471–475, 2014, doi: 10.1016/j.egypro.2014.11.050.

[35] H. Ishii, H. Tada, R. Takashima, J. Yamamoto, and K. Yokohama, “Verification Test Results of 50 t/d O2/CO2-blown Two-stage Entrained Flow Coal Gasifier and Development into Commercial Scale Gasifier,” Journal of the Japan Institute of Energy, vol. 98, no. 7, pp. 165–170, Jul. 2019, doi: 10.3775/jie.98.165.

[36] V. Tola and A. Pettinau, “Power generation plants with carbon capture and storage: A techno-economic comparison between coal combustion and gasification technologies,” Applied Energy, vol. 113, pp. 1461–1474, Jan. 2014, doi: 10.1016/j.apenergy.2013.09.007.

[37] G. Donskoy, V. A. Shamansky, A. N. Kozlov, and D. A. Svishchev, “Coal gasification process simulations using combined kinetic-thermodynamic models in one-dimensional approximation,” Combustion Theory and Modelling, vol. 21, no. 3, pp. 529–559, May 2017, doi: 10.1080/13647830.2016.1259505.

[38] R. F. D. Monaghan and A. F. Ghoniem, “A dynamic reduced order model for simulating entrained flow gasifiers,” Fuel, vol. 91, no. 1, pp. 61–80, Jan. 2012, doi: 10.1016/j.fuel.2011.07.015.

[39] A. V. Messerle, V. E. Messerle, and A. B. Ustimenko, “Plasma thermochemical preparation for combustion of pulverized coal,” High Temperature, vol. 55, no. 3, pp. 352–360, May 2017, doi: 10.1134/S0018151X17030142.

[40] X. Kong, W. Zhong, W. Du, and F. Qian, “Three Stage Equilibrium Model for Coal Gasification in Entrained Flow Gasifiers Based on Aspen Plus,” Chinese Journal of Chemical Engineering, vol. 21, no. 1, pp. 79–84, Jan. 2013, doi: 10.1016/S1004-9541(13)60444-9.

[41] M. Pérez-Fortes, A. D. Bojarski, E. Velo, J. M. Nougués, and L. Puigjaner, “Conceptual model and evaluation of generated power and emissions in an IGCC plant,” Energy, vol. 34, no. 10, pp. 1721–1732, Oct. 2009, doi: 10.1016/j.energy.2009.05.012.

[42] Kim, H. Oh, S. Lee, and Y.-S. Yoon, “Advanced One-Dimensional Entrained-Flow Gasifier Model Considering Melting Phenomenon of Ash,” Energies, vol. 11, no. 4, Apr. 2018, Art. no. 1015, doi: 10.3390/en11041015.

[43] M. H. Sahraei, M. A. Duchesne, R. W. Hughes, and L. A. Ricardez-Sandoval, “Dynamic reduced order modeling of an entrained-flow slagging gasifier using a new recirculation ratio correlation,” Fuel, vol. 196, pp. 520–531, May 2017, doi: 10.1016/j.fuel.2017.01.079.

[44] H. Wu, X. Chen, M. Aziz, Z. Huang, and Y. Zhang, “Exergy destruction analysis of coal gasification with O2-H2O combined with chemical kinetics,” Fuel, vol. 384, p. 134014, Mar. 2025, doi: 10.1016/j.fuel.2024.134014.

[45] E. Biagini, “Study of the equilibrium of air-blown gasification of biomass to coal evolution fuels,” Energy Conversion and Management, vol. 128, pp. 120–133, Nov. 2016, doi: 10.1016/j.enconman.2016.09.068.

[46] G. Donskoy, “Simulation and Optimization of Entrained-Flow Air-Steam Gasification of Brown Coals,” Energy Systems Research, vol. 5, no. 1, pp. 31–37, 2022, doi: 10.38028/esr.2022.01.0003.

[47] V. S. Vdovenko, M. I. Martynova, N. V. Novitskiy, and G. D. Yushina, Energy fuels of USSR (coals, oil shales, peats, oils, natural gas). Moscow: Energoatomizdat, 1991.

[48] G. Donskoy, “Analysis of efficiency of pulverized coal gasification in high-temperature flow of O2/N2 and O2/CO2 using mathematical modeling,” Bulletin of the Tomsk Polytechnic University Geo Assets Engineering, vol. 332, no. 11, pp. 127–140, Nov. 2021, doi: 10.18799/24131830/2021/11/2575.

[49] C. Yin and J. Yan, “Oxy-fuel combustion of pulverized fuels: Combustion fundamentals and modeling,” Applied Energy, vol. 162, pp. 742–762, Jan. 2016, doi: 10.1016/j.apenergy.2015.10.149.

[50] Deng, Y. Zhao, S. Sun, D. Feng, and W. Zhang, “Review on thermal conversion characteristics of coal in O2/H2O atmosphere,” Fuel Processing Technology, vol. 232, Jul. 2022, Art. no. 107266, doi: 10.1016/j.fuproc.2022.107266.

[51] H. Ishii, T. Hayashi, H. Tada, K. Yokohama, R. Takashima, and J. Hayashi, “Critical assessment of oxy-fuel integrated coal gasification combined cycles,” Applied Energy, vol. 233–234, pp. 156–169, Jan. 2019, doi: 10.1016/j.apenergy.2018.10.021.

[52] A. F. Ryzhkov, S. I. Gordeev, and T. F. Bogatova, “Selecting the process arrangement for preparing the gas turbine working fluid for an integrated gasification combined-cycle power plant,” Thermal Engineering, vol. 62, no. 11, pp. 796–801, Nov. 2015, doi: 10.1134/S0040601515110075.

[53] D. Svishchev, “Thermodynamic Analysis of Air-Blown Staged Gasification of Coal in a Flow,” Energy Systems Research, no. 3(15), pp. 38–43, Nov. 2021, doi: 10.38028/esr.2021.03.0004.

[54] C. Kunze, K. Riedl, and H. Spliethoff, “Structured exergy analysis of an integrated gasification combined cycle (IGCC) plant with carbon capture,” Energy, vol. 36, no. 3, pp. 1480–1487, Mar. 2011, doi: 10.1016/j.energy.2011.01.020.

[55] A. Wahid, R. Mustafida, and A. Husnil, “Exergy Analysis of Coal-Fired Power Plants in Ultra Supercritical Technology versus Integrated Gasification Combined Cycle,” Evergreen, vol. 7, no. 1, pp. 32–42, Mar. 2020, doi: 10.5109/2740939.

[56] Giuffrida, M. C. Romano, and G. Lozza, “Efficiency enhancement in IGCC power plants with air-blown gasification and hot gas clean-up,” Energy, vol. 53, pp. 221–229, May 2013, doi: 10.1016/j.energy.2013.02.007.

[57] Y. A. Kagramanov, V. G. Tuponogov, A. F. Ryzhkov, and A. D. Nikitin, “Multiple Gas–Solid Reactions in a Porous Sorbent Applied to Warm Gas Desulfurization,” Industrial & Engineering Chemistry Research, vol. 59, no. 29, pp. 12943–12954, Jul. 2020, doi: 10.1021/acs.iecr.0c01389.

International Journal of Thermodynamics (IJoT)
ISSN 1301-9724 / e-ISSN 2146-1511
https://dergipark.org.tr/en/pub/ijot

Vol. 28 (No. 2), pp. 059-068, 2025
doi: 10.5541/ijot.1627719

Research Article

Optimization of Intermittent Drying of Rehydrated Dates

[1,2]I. Hasrane, [2*]A. Benseddik, [1]A. Boubekri, [2]D. Daoud [2]S. Bouhoun, [2,3]M. A. Kherrafi,
[2,4]A. Badji, [1,2]C. Nettari

[1] Laboratory of New and Renewable Energies Development in Arid Zones (LENREZA), Kasdi Merbah University,
B.P. 511, Ouargla 30000, Algeria.
[2] Unité de Recherche Appliquée en Energies Renouvelables, URAER, Centre de Développement des Energies
Renouvelables, CDER, 47133, Ghardaïa, Algeria.
[3] Applied Energy and Thermal Laboratory (ETAP), Department of Mechanical Engineering, Faculty of Technology,
Abou Bekr Belkaid University, B.P 119, Tlemcen, 13000, Algeria.
[4] Instrumentation Laboratory Faculty of Electronics and Computers University of Sciences and
Technology Houari Boumediene, Algiers, Algeria.
E-mail: [2*]abdelouahabbenseddik@gmail.com

Received 30 January 2025, Revised 14 March 2025, Accepted 4 April 2025

Abstract

The intermittent drying of dates remains a neglected area in academic research, primarily due to factors such as varying cultivation patterns across regions and limited attention to the valorization of overdried dates. This study investigates the impact of drying parameters: air temperature, air velocity, and intermittency ratio, on the drying time and energy consumption of rehydrated dates using hot air drying. Employing Response Surface Methodology with a Central Composite Design and a desirability function, experiments were conducted within specific ranges of air temperatures (40–70 °C), air velocities (0.5–5 m/s), and intermittency ratios (0.2–1). Results show that while air velocity minimally affects drying time, it negatively influences energy efficiency. Conversely, air temperature is significant for both responses. Reducing the intermittency ratio from 1 to 0.3 resulted in a decrease in total energy consumption by up to 60%, particularly at lower temperatures, with negligible impact on total drying time. The study identifies optimal conditions for minimizing both drying time and energy consumption as an inlet temperature of 66 °C, air velocity of 2.5 m/s, and an intermittency ratio of 0.7. The experimental data were fitted to 7 mathematical drying models, the results indicated that Midilli-Kucuk model gave better performance to define the drying kinetics of intermittent drying of rehydrated dates.

Keywords: *Intermittent drying; hot air dryer; response surface methodology; rehydrated dates.*

1. Introduction

The Phoenix dactylifera L., commonly known as date palm, is an essential crop in arid regions located in Middle East and North Africa. It provides vital nutrients and health-enhancing elements, making it a significant contributor to maintaining nutritional security worldwide. In 2022, the global production of dates has increased about 18% and surpassed 8.53 million tons [1], owing to their high carbohydrate and dietary fiber content, as well as essential minerals and vitamins [2]. One of the most popular dates in North Africa is ‘Deglet Nour’ dates. Algeria and Tunisia are currently the dominant producers and exporters of this particular cultivar [3], it is highly prized due to its semi-soft texture, transparent hue, and overall clarity, which make it a valuable commodity in the global market. Deglet Nour dates is classified into many categories depending on its maturation and sugar content after harvesting, among these categories the ‘freeza’ dates category which represents a state of incomplete maturation where the dates have been overdried on the palm tree, this category is distinguished by a hard texture and very low moisture content which make it undesirable for consumption. Many studies have been carried out in order to valorize this dates category [3, 4], the common process in order to achieve a softer texture is a rehydration treatment which induce an increase in moisture content leading to sugar inversion and thus a complementary maturation of the fruit, followed by a drying in order to achieve a desired moisture content as recommended by the international standards (CEE/ONU DF-08) for a safe storage and preservation.

Drying is a crucial method for preserving food products. It involves removing water from the product to prevent microbial or enzymatic reactions and fungus growth. Additionally, it decreases the product's weight, making it easier to transport and store. One of the most commonly used drying methods is convective hot air drying, which is convenient for industries as it is easy to handle and saves time. However, it is energy-intensive and consumes approximately 10-25% of the total energy [5], Excessive heat exposure during the drying process can also degrade the final product's quality [6]. To overcome these issues, intermittent drying can be a viable solution [7-9], this method involves non-continuous drying, where the product is allowed to rest during tempering periods once the surface is already dried.

*Corresponding Author

This allows moisture to migrate from the center to the surface, leading to full water distribution and homogeneity, as well as surface rewetting. Consequently, the product can avoid many qualities degradation issues, while requiring no energy consumption during the tempering period, resulting in overall energy savings. Intermittent drying has been the subject of many research studies, Pan et al. [7] experimented drying of squash slices in a fluidized bed dryer, it was proven that intermittent drying reduced degradation of β-carotene of about 25% in comparison with conventional continuous drying. Md Saleh et al. [10] investigated the effect of intermittent drying on the quality of organic carrots. They observed that drying at 60°C with a 3-hour tempering period at 30% moisture content resulted in superior retention of total carotenoids (76.9%), minimal color change (8.1), and an optimal rehydration ratio (0.4) compared to continuous drying methods. Additionally, intermittent drying led to a reduction in energy consumption by up to 25%. Continuous and intermittent drying of rough rice were compared at temperatures of 50°C and 70°C by Pereira et al. [11], with intermittent drying showing up to 32.2% reduction in effective drying time, leading to energy savings. The intermittency ratio and tempering period significantly influenced drying kinetics, particularly at 50°C, with both methods reducing operation time by about 30.0% compared to continuous drying. The one-dimensional diffusion model accurately described the drying process, with intermittent drying resulting in increased mass diffusivity, accelerating drying and reducing energy consumption.

Studies regarding the intermittent drying of dates are notably absent in academic literature. This absence can be attributed to several factors. Firstly, the geographical distribution and cultivation of dates vary widely, with certain regions having limited access to this fruit. Consequently, the lack of widespread cultivation may lead to a dearth of academic interest and research initiatives focused on date processing techniques such as intermittent drying. Additionally, the valorization of overdried dates has received relatively little attention in academic research, contributing to the scarcity of studies on this subject. This gap in research reflects broader limitations in the exploration of date processing techniques and their applications. Therefore, while the intermittent drying of dates may seem underrepresented in academic literature, it is more a consequence of these underlying factors rather than an indication of the fruit's insignificance or lack of potential for further exploration. Hence, recognizing the need to address this research gap, the aim of this study is to investigate the effect of different drying parameters including air temperature, air velocity and intermittency ratio on drying time and energy consumption of rehydrated dates in a hot air dryer and to determine the optimum drying conditions using response surface methodology.

2. Material and Methods

2.1 Sample Preparation

For the experiments, Deglet Nour dates were selected as the subject of investigation. These dates were harvested from Toggourt city, located in southern Algeria, renowned for its date production. To ensure proper preservation, the dates were stored in a plastic bag and kept in a refrigerator set at a temperature of 4°C throughout the entire duration of the experiments. This controlled storage condition was maintained to prevent any unwanted changes in the dates' characteristics. According to the method of AOAC (1990), the initial moisture content of the sample was determined to be 17.5% wet basis.

2.2 Rehydration Process

To initiate the rehydration process, 10 pieces of dates, each weighing approximately 75 grams, were placed in a beaker. Distilled water was added to the beaker until it reached a volume of 250 ml, ensuring that the dates were fully submerged. The beaker was then carefully transferred to a water bath, specifically a "Memmert" model, set at a constant temperature of 45 °C for about 6 hours to ensure a complete maturation through sugar inversion [3] which increases the water content inside the dates up to 33 (% w.b).

The samples were removed and wiped gently with a paper towel then placed in an airtight glass storage jar for 7 hours to assure the homogenization of the moisture inside the samples and to maintain the same humidity. The weight was measured again after the rehydration process before placing the samples on the tray in the drying chamber to begin the drying process in order to decrease the moisture content above the standard water content required for safe storage (<26 % w.b) according to The UNE CE DF-08 norm [3].

2.3 Drying Experiments

2.3.1 Description of the dryer

The drying experiments were conducted in a custom air conditioning laboratory unit provided by P.A. Hilton Ltd., bearing the serial number A573 / 53621. The unit was specifically modified and tailored to meet our testing

Figure 1. Experimental hot air dryer.

requirements. For the drying chamber, we utilized a section salvaged from an old refrigerator which ensure a good isolation, with dimensions measuring 60 cm in length, 26 cm in width, and 45 cm in depth (see Figure 1.). Within the drying chamber, we incorporated a perforated tray designed to hold the product being dried. This tray was positioned 30 cm away from the air inlet. The drying chamber and the air conditioning unit were connected using a PVC pipe with a diameter of 125 mm and a length of 160 cm. The modified air conditioning unit composed of: Five heating electrical resistances, totaling 5 kW of power, which provided the high temperatures necessary for the drying experiments. An electrical fan, coupled with a potentiometer to regulate the airflow effectively and manually. The control unit, which was based on an Arduino Mega 2560 board, allowing precise control and monitoring of the drying process.

Temperature control

To maintain a constant drying air temperature in the drying chamber during each experiment, a PID (proportional-integral-derivative) control has been installed in the Arduino. The temperature is measured with a type K thermocouple, it has 0.05 mm in diameter, 3 m of length, and can withstand temperatures up to 1370 K and provide an accuracy of 0.1 °C. The temperature is displayed on the Arduino, which can be controlled by sending commands to the solid-state relay-25DA a type FQFER to adjust the electrical resistances, and thus can increase or decrease the temperature accordingly.

Velocity control

The drying air velocity is measured using an Anemometer (EMC-9400SD) positioned on the tray inside the drying chamber before each experiment. The airflow is regulated by manually adjusting the potentiometer, which controls the power supply to the fan.

Energy consumption

In this study, the energy consumption of each drying experiment was monitored using an electric meter from the brand Energical. This specific energy meter, designed for precision and reliability, played a crucial role in quantifying the electrical energy usage throughout the experimental processes. Notably, the meter operates at a frequency of 50 Hertz, ensuring accurate measurements and providing valuable insights into the energy dynamics of the drying system.

Weight measurement

The weight of samples was measured using a balance KERN ABT 220-4M and recorded every 30 min during the drying. The average time required using a digital balance for weight registration was about 10 s.

2.3.1 Instrumentations

During the experiments, the temperature, the airflow through the dryer, moisture content levels, energy consumption, and mass of dates were monitored throughout the drying process. The measurements were conducted using specific instruments for each parameter.

The inaccuracies in the measurements determine the level of uncertainty in the results. Using appropriate equipment, all parameters were measured during the drying tests. The result I is obtained from the measured values y_1, y_2,.... y_n, where each y_i represents an individual parameter recorded during the experiment. The uncertainty of I, denoted as U_I, is determined by the uncertainties u_1, u_2, ..., u_n, where each u_i corresponds to the uncertainty associated with its respective measured parameter y_i.
U_I [12] is expressed by:

$$U_I = \left[\left(\frac{\partial I}{\partial y_1} u_1\right)^2 + \left(\frac{\partial I}{\partial y_2} u_2\right)^2 + \cdots + \left(\frac{\partial I}{\partial y_n} u_n\right)^2\right]^{1/2} \tag{1}$$

Errors occurred when measuring and calculating the variables are addressed by:

$$E_I = (U_I/I) \times 100 \tag{2}$$

2.3.2 Experimental procedure

Hot air drying was performed under the controlled conditions of airflow temperature, velocity and intermittency ratio. The coded values of these process variables and their ranges used in the hot air drying of dates are presented in Table 2, these coded values were determined when using the Central Composite Design (CCD) for the response surface methodology, which implies five levels assigned to each factor: ($-\alpha$, -1, 0, +1, and $+\alpha$), Where level 0 corresponds to the central points, levels -1 and + 1 correspond to the low and high levels, respectively, and $-\alpha$ and $+\alpha$ correspond to the axial points, the distance between the axial points and the central points is calculated using $\alpha = [2^n]^{1/4}$, where n is the number of process variables[13].

The required temperature of drying air in the heater were adjusted by the PID temperature controller on Arduino. The velocity of air was measured manually by the Anemometer. Total time taken by the system to attain the required air temperature and velocity were about 5 min. Approximately 105 g of dates (10 pieces) on a tray was placed perpendicularly to the hot airflow uniformly distributed.

An intermittent drying approach was implemented in this study. This involved periodically turning off completely the drying system for a specific duration, referred to as tempering period after a specific duration of drying. This cyclic pattern repeats hourly ($t_{on} + t_{off}$=60 minutes), forming a systematic alternation between the 'on' and 'off' states of the drying system until the desired moisture content was achieved. The length of each tempering period was determined by the intermittency ratio assigned to each experiment which can be written as follows:

$$\alpha = \frac{t_{on}}{t_{on} + t_{off}} \tag{3}$$

Table 1. Ranges and uncertainties of measuring instruments.

Independent variables	Instruments	Model	Range	Total uncertainty	Tolerance
Temperature	Thermocouple	K-type	-50 – 1300 C	0.287 °C	±1,5°C
Velocity	Digital anemometer	EMC-9400SD	0.4 – 25 m/s	0.173 m/s	± (2% + 0.2 m/s)
Mass measurement	Balance for moisture determination	KERN ABT 220-4M	0 – 220 g	0.224 g	± 0,0002 g

Table 2. Independent variables and their levels for central composite design.

Independent variable	Coded levels				
	-α	-1	0	1	+α
Temperature (°C) (X_1)	40	46.08	55	64	70
Velocity (m/s) (X_2)	0.5	1.4	2.75	4	5
Intermittency ratio (X_3)	0.2	0.36	0.6	0.84	1

2.4 Moisture Ratio and Mathematical Modelling Procedure

The reduction in mass was documented at 30-minute intervals throughout the drying until the desired moisture content was achieved 26% (w.b). The moisture ratio (MR) was calculated using the equation:

$$\mathrm{MR} = \frac{\mathrm{M_t} - \mathrm{M_d}}{\mathrm{M_0} - \mathrm{M_d}} \tag{4}$$

With M_t, M_d, and M_0 are the water content values respectively at time t, at desired moisture content and at initial moisture content (t = 0). To enhance comprehension, prediction, and optimization of the drying process, mathematical modelling is employed in this study. By applying mathematical models, researchers can effectively translate experimental findings to industrial-scale operations. These models aid in managing and optimizing performance within specified operational parameters. Moreover, they facilitate the identification of empirical or semi-empirical models that best fit experimental results. We used seven common models to analyze the experimental moisture data in drying agriculture products. These models provide safe and straightforward explanations for the drying process characteristics, as listed in Table 3**.**

The most suitable model was chosen from the seven equations proposed by previous researchers, as detailed in Table 3. We conducted regression analyses using the OriginPro 8.0 program. A 3 number of coefficients are important in this assessment procedure. One basic metric that shows how much of the variability in the data the model can explain is the coefficient of determination (R2). A better fit is indicated by a higher R2. Furthermore, the goodness of fit is revealed by the reduced chi-square (χ2), where lower values correspond to a more accurate depiction of the experimental data[13]. The root mean square error (RMSE) gives the deviation between the predicted and experimental values and it must reach zero [14]. These coefficients can be calculated as follows [15, 16]:

$$R^2 = 1 - \frac{\sum_{i=1}^{N}\left(MR_{exp,i} - MR_{pré,i}\right)^2}{\sum_{i=1}^{N}\left(\overline{MR_{exp}} - MR_{exp,i}\right)^2} \tag{5}$$

$$\chi^2 = \frac{\sum_{i=1}^{N}\left(MR_{exp,i} - MR_{pré,i}\right)^2}{N - n} \tag{6}$$

$$RMSE = \sqrt{\frac{1}{N}\sum_{i=1}^{N}\left(MR_{pré,i} - MR_{exp,i}\right)^2} \tag{7}$$

with:

$$\overline{MR_{exp}} = \frac{\sum_{i=1}^{N} MR_{exp,i}}{N} \tag{8}$$

where, $MR_{exp,i}$ is the moisture ratio the experimentally observed, $MR_{pré,i}$ is the predicted moisture ratio obtained by modelling, N and n are the number of observations and the number of constants respectively.

2.5 Response Surface Analysis

Response surface methodology (RSM) is an effective statistical technique for optimizing complex processes. The main advantage of RSM is the reduced number of experimental trials needed to evaluate multiple parameters and their interactions [17]. In this study, (RSM) served as a powerful tool to delve into the primary effects of key process variables, namely drying temperature (X_1), air velocity (X_2), and intermittency ratio (X_3), on both drying time and energy consumption. The optimization factors ranges were thoughtfully selected based on insights gained from previous studies focusing on the drying of dates [3, 4, 18, 19].

For the experimental design, model construction, and data analysis, we have employed Statgraphics Centurion 18, a robust statistical software developed by Statpoint Technologies Inc. located in Warrenton, Virginia, USA. The design of experiments adopted a five-level strategy, employing The Central Composite Design (CCD) which has been chosen for its efficacy, which aligns with that discussed in a prior work [13], where detailed information on the design methodology and parameters can be found. This experimental design comprised 18 trials as shown in Table 4, strategically including four replicates at the central point to estimate experimental error accurately. Experimental data were fitted to a quadratic polynomial model and regression coefficients have been obtained. The quadratic polynomial model applied in the response surface analysis took the following form:

$$y = a_0 + \sum_{i=1}^{3} a_i x_i + \sum_{i=1}^{3} a_i x_i^2 + \sum_{i=1}^{3}\sum_{j>i}^{3} a_{ij} x_i x_j \tag{9}$$

Here, a_0, a_i and a_{ij}(coefficients) denote the intercept, linear, quadratic, and interaction terms, respectively. x_i and x_j stand for the coded independent variables. All model coefficients were established through multiple regression analysis, and the significance of these coefficients was scrutinized using analysis of variance (ANOVA).

To ensure a comprehensive exploration of the parameter space and minimize potential biases, trials were conducted in a random order, this systematic approach aimed at enhancing the reliability and validity of the experimental results. Fitting the response surface involved the application of a generalized quadratic polynomial model tailored for a three-factor analysis. This model effectively and significantly shows how the important factors and their effects are connected [20, 21] providing a detailed insight into the drying process. An optimization was undertaken to minimize both drying time and energy consumption, Results were explained through Pareto charts general trends, 3D response surface, and empirical mathematical model.

3. Results and Discussion

18 trials were carried out based on the experimental design as shown in Table 4, according to different independent variables: Temperature (X_1), velocity (X_2) and intermittency ratio (X_3), the response variables: Time and energy consumption, obtained of each trial are also presented.

Table 3. Mathematical models given by various authors for the drying curves.

N°	Models	Equations	References
01	Newton (Lewis, Exponential, single exponential) Model	$MR = \exp(-kt)$	[22]
02	Page Model	$MR = \exp(-k(t)^{n})$	[23]
03	Modified Page Model	$MR = \exp(-(kt)^{n})$	[24]
04	Henderson and Pabis (single term, generalized exponential) Model	$MR = a \exp(-kt)$	[25]
05	Logarithmic (Asymptotic,Yagcioglu et al.) Model	$MR = a \exp(-kt) + b$	[26]
06	Midilli-Kucuk (Midilli, Midilli et al.) Model	$MR = a \exp(-kt^{n}) + bt$	[24]
07	Approximation of Diffusion (Diffusion Approach) Model	$MR = a \exp(-kt) + (1-a) \exp(-kbt)$	[27]

3.1.1 Analysis of variance (ANOVA) and estimated regression of each response

ANOVA is utilized to evaluate the accuracy and statistical significance of the quadratic model by examining the coefficients of determination ($R^2 = 0.9087$) for time and ($R^2 = 0.8934$) for energy consumption as responses, along with the associated P-values. The obtained P-values, which are both less than 0.05 (0.0027 for time and 0.0048 for energy consumption), indicate statistical significance. Thus, it can be concluded that the model significantly accounts for the variability observed in the responses, additionally diagnostic plots as shown in Figure 2, guarantee the accuracy of the model and illustrate the relationship between observed and predicted outcomes. The data points closely align with the straight line on the plot, indicating a strong agreement between the two datasets. Additionally, the data were normally distributed, affirming the statistical validity of the model. The experimental data was subjected to multiple linear regression analysis, resulting in the development of second-order polynomial equations to analyze the input variables data and correlate response function to coded variables and thus ascertain the notable impacts of process variables on each response [28]

To demonstrate the collective impact of two factors on a given response, response surface and contour plots were created for each fitted model, showcasing the relationship between two independent variables while holding the other constant at its central value. Three distinct response surface plots were presented, and the effects of variables on responses were analyzed through the interpretation of these plots.

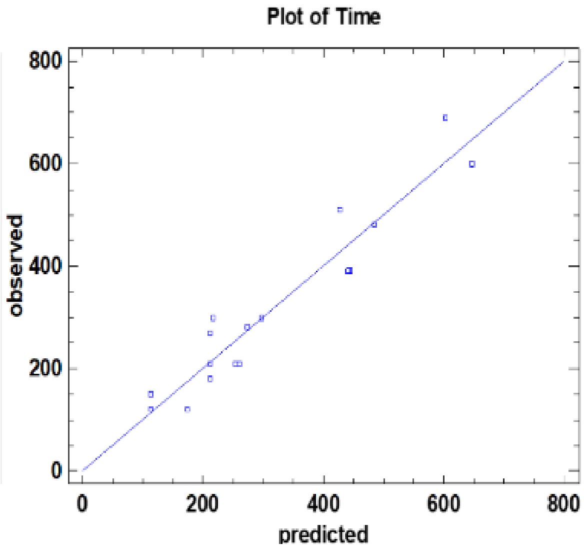

Figure 2.a. Diagnostic plots of energy consumption as response.

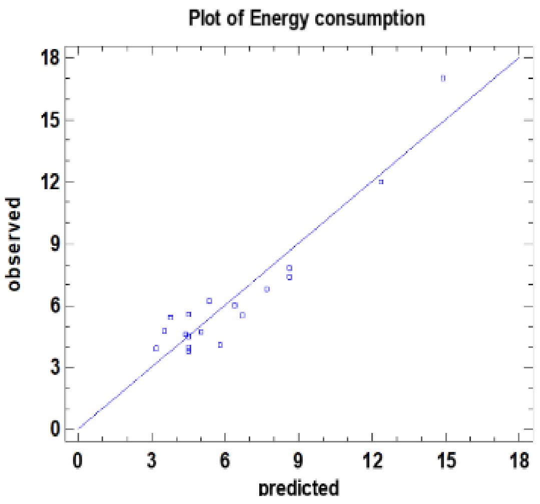

Figure 2.b. Diagnostic plots of energy consumption as response.

Table 4. The matrix of central composite design (CCD) and responses obtained from experimental tests.

Run	Independent variables			Responses	
	X_1 (°C)	X_2 (m/s)	X_3	Energy (kwh)	Time(min)
1	46	1.4	0.36	5.4	690
2	64	1.4	0.36	4.1	210
3	46	4	0.36	7.8	480
4	64	4	0.36	6.2	300
5	46	1.4	0.84	6	390
6	64	1.4	0.84	4.8	150
7	46	4	0.84	17	510
8	64	4	0.84	5.5	120
9	40	2.7	0.6	7.4	600
10	70	2.7	0.6	3.9	120
11	55	0.5	0.6	4.7	300
12	55	5	0.6	12	210
13	55	2.7	0.2	4.6	390
14	55	2.7	1	6.8	280
15	55	2.7	0.6	5.6	270
16	55	2.7	0.6	3.8	180
17	55	2.7	0.6	4.5	210
18	55	2.7	0.6	4	180

3.1.2 Effect of independent factors on drying time

The drying time is an important metric to consider when evaluating the effectiveness of a drying process. It has a substantial influence on the final product's quality attributes in addition to its function in process evaluation, even though this study does not specifically address the quality attributes of the dried dates, it is reasonable to assume that shorter exposure to heat during the drying process preserves the product's quality and minimizes the risk of quality degradation [29]. In other words, reducing the intermittency ratio leads to less effective drying time, which is favorable for quality and thus reducing the amount of time a product is exposed to heat, which is consistent with one of the objectives of improving both product quality and customer satisfaction. The ANOVA analysis of rehydrated dates samples shows that the linear terms: drying temperature and intermittency ratio and their square terms had a significant effect on drying time (P-value <0.05), however the velocity was not significant as presented in Table 5, moreover it can be seen from the table that for all the interaction terms and square term of velocity, the P-values are greater than 0.05 which indicate their insignificancy. The regression analysis yielded the following actual equation representing the relationship between drying time and the input variables:

$$\begin{aligned} Time\ [min] = {} & 4168{,}95 - 95{,}7787X_1 \\ & - 219{,}601\, X_2 - 1645{,}65\, X_3 \\ & + 0{,}671208\, X_1^2 + 1{,}60256X_1\, X_2 \\ & + 1{,}73611\, X_1\, X_3 + 12{,}9856\, X_2^2 \\ & + 84{,}1346\, X_2\, X_3 + 924{,}905\, X_3^2 \end{aligned} \tag{10}$$

Three dimensional response surface plots have been demonstrated to interpret the effect of drying factors on drying time, Figure 3 illustrates the effect of temperature, intermittency ratio and velocity on drying time, it can be seen that changes in velocity have negligible impact, if any, on the drying time, similar results have been found in literature [30], When the moisture content in the food sample is high, the effect of air velocity on the drying rate becomes notable [31] and vice versa as is the case in this study since the initial moisture content for the rehydrated dates is low (33% w.b). When the moisture content is low, the dominant mechanism in drying is the transfer of water from the center of the sample to its surface, neglecting the influence of external factors such as air velocity. Increasing the velocity of the drying air may seem intuitive for accelerating drying through enhanced evaporation, but in this scenario, it would have little to no effect. The figures illustrate that reducing the intermittency ratio to a moderate level (0.55-0.85) can slightly decrease drying time as depicted more clearly in Figure 4. This reduction, although minor, is favorable. As previously discussed, minimizing heat exposure time enhances product quality [32]. Therefore, the key observation here is that decreasing the intermittency ratio does not lengthen drying time, except for low ratios. The critical factor here is temperature, as its increase significantly reduces drying time as shown in Figure 3.

Figure 5 displays the Pareto chart generated for drying time as the response variable. It is evident that both the linear and squared terms of temperature and intermittency ratio surpass the reference line, set at 2.365, indicating their significance in influencing drying time. Notably, temperature emerges as the most influential parameter.

Table 5. Analysis of variance for drying time and coefficients of predicted model.

Source	**Coef estimate**	**Sum of squares**	**Df**	**Mean square**	**F-value**	**P-value**
Model	4168,95		9			**0,0027**
A:Temperature (°C)	-95,7787	306629	1	306629	56,65	**0,0001**
B: Velocity (m/s)	-219,601	2749,42	1	2749,42	0,51	0,4963
C:Intermitteny ratio	-1645,65	35438,0	1	35438,0	6,55	**0,0337**
AA	0,671208	40303,5	1	40303,5	7,45	**0,0259**
AB	1,60256	2812,5	1	2812,5	0,52	0,4915
AC	1,73611	112,5	1	112,5	0,02	0,8889
BB	12,9856	6667,82	1	6667,82	1,23	0,2993
BC	84,1346	5512,5	1	5512,5	1,02	0,3425
CC	924,905	34574,4	1	34574,4	6,39	**0,0354**
Total error		43304,8	8	5413,11		
Total (corr.)		474494	17			

R-squared = 90,8735 percent

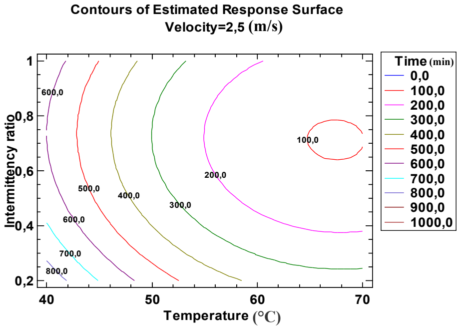

Figure 3. Contour plot showing the effect of intermittency ratio and temperature on dying time.

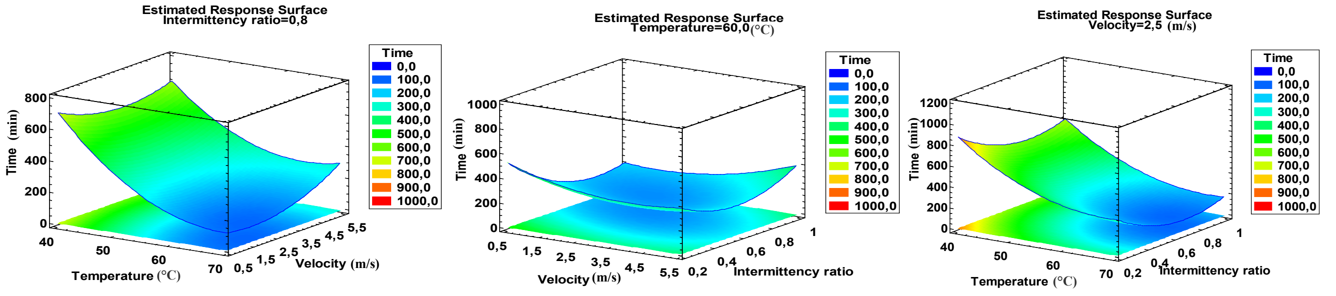

Figure 4. Response surface plot showing the effect of different parameters on drying time.

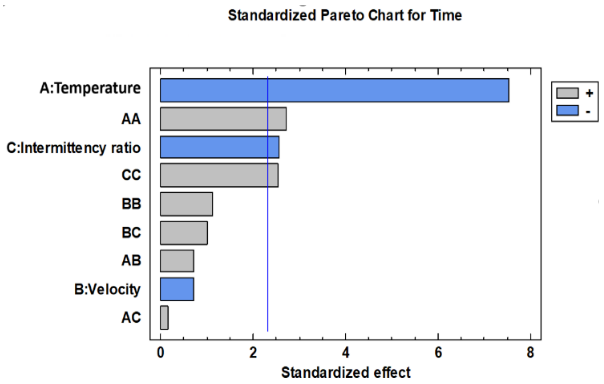

Figure 5. Pareto chart of the standardized effects on drying time.

3.1.3 Effect of independent factors on energy consumption

The ANOVA analysis of rehydrated date samples for energy consumption as a response is presented in Table 6, showing that all the drying parameters significantly ($p < 0.05$) influenced the energy consumption in linear terms, velocity influenced energy consumption in both square position and interaction term with temperature. Regression analysis yielded the following actual equation representing the relationship between energy consumption and the input variables:

$$\begin{aligned} Energy\,[kwh] = {} & 2{,}40312 - 0{,}131673X_1 \\ & + 1{,}6813\,X_2 + 15.931\,X_3 \\ & + 0{,}00552558\,X_1^2 + 0.113248\,X_1 \\ & + 0.56713\,X_1\,X_3 + 0.808506\,X_2^2 \\ & + 2.88462\,X_2\,X_3 + 9{,}67664\,X_3^2 \end{aligned} \tag{11}$$

The effect of interaction of the drying parameters on energy consumption are illustrated in Figure 6. At constant intermittency ratio, the lowest energy consumption is observed when the inlet temperature is high and the air velocity is low, similar results were obtained by Majdi et al, [30] and Beigi [33], when air velocity is high, heaters consume more energy to maintain the desired temperature additionally to energy consumed by the fan which lead to maximum energy consumption. At constant moderate velocity, decreasing intermittency ratio from 1 to 0.3 with low temperatures reduces the total energy consumption up to 60%, this result is consistent with what found by Hajji et al [34] where increasing tempering periods (thus decreasing intermittency ratio) at 40°C led to energy consumption savings.

However, when drying at high temperatures, the effect of intermittency ratio becomes negligible, and energy consumption reaches its minimum value. This phenomenon may be attributed to the relatively small range of moisture content present in the samples studied, which accelerates the drying process, thereby limiting the opportunity for intermittent drying cycles to have a significant impact. In such cases, the rapid removal of moisture content at high temperatures may overshadow the potential energy savings that could be achieved through intermittent drying strategies.

Table 6. Analysis of variance for energy consumption and coefficients of predicted model.

Source	Coefficient estimate	Sum of squares	Df	Mean square	F-value	P-value
Model	2,40312		9			**0,0048**
A: Temperature (°C)	-0,131673	32,2525	1	32,2525	13,03	**0,0069**
B: Velocity (m/s)	1,6813	56,3298	1	56,3298	22,76	**0,0014**
C:Intermittency ratio	15,931	13,2317	1	13,2317	5,35	**0,0495**
AA	0,00552558	2,73139	1	2,73139	1,10	0,3242
AB	-0,113248	14,045	1	14,045	5,67	**0,0444**
AC	-0,56713	12,005	1	12,005	4,85	0,0588
BB	0,808506	25,8479	1	25,8479	10,44	**0,0120**
BC	2,88462	6,48	1	6,48	2,62	0,1443
CC	9	3,78451	1	3,78451	1,53	0,2513
Total error		19,8009	8	2,47512		
Total (corr.)		185,783	17			

R-squared = 89,3419 percent

3.2 Optimum Drying Conditions

The optimum conditions were estimated using Statgraphics 18 software. The software simulation suggested a combination of drying variables that would provide minimum values for total drying time, and energy consumption. Product quality was not assessed in this study, but we assume that decreasing intermittency ratio thus minimizing heat exposure periods leads to better quality retention. Therefore, in the present study, the optimal intermittent drying parameters were determined as temperature of 66°C (X_1), velocity of 2.5 m/s (X_2), and intermittency ratio of 0.7 (X_3). The values of drying time and energy consumption for final dried dates dried at these conditions were predicted as 96 minutes and 3 kwh respectively. These are best results in terms of achieving efficient drying, reducing drying time, and minimizing energy consumption. By carefully controlling and maintaining these optimal conditions, the drying process can be carried out effectively and with optimal efficiency. Figure 7 illustrates the desirability plot showcasing the performance of combined temperature and intermittency ratio at the

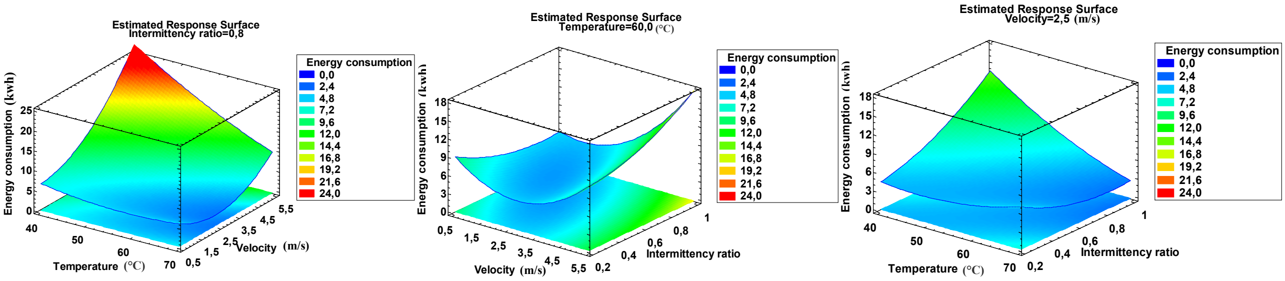

Figure 6. Response surface plot showing the effect of different parameters on energy consumption.

Table 7. Validation tests for predicted and experimental values of response surface model.

	Validation test 1		Validation test 2	
Drying parameters	$X_1 = 60°C$, $X_2=2$ m/s, $X_3=0.7$		$X_1 = 70°C$, $X_2=4$ m/s, $X_3=0.5$	
Response's result	Predicted	Experimental	Predicted	Experimental
Drying time (min)	135	150	168	150
Energy consumption (kwh)	3.51	3.8	4.51	4.3

optimum air velocity. This plot offers a comprehensive overview of the desirability values ranging from 0 to 1, representing the degree of fulfillment of multiple criteria simultaneously. By analyzing the desirability values across various combinations of temperature and intermittency ratio at the optimal air velocity, we can discern the most favorable conditions that strike the best balance between conflicting objectives. This visualization aids in identifying the optimal parameter settings that maximize performance and efficiency in the drying process.

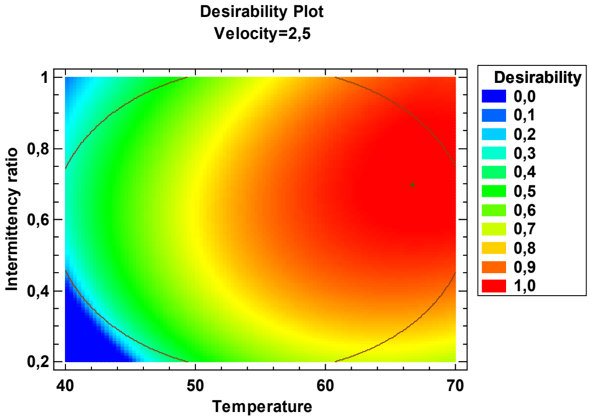

Figure 7. Contour plot illustrating optimal conditions for desirability as function of temperature and intermittency ratio at the optimum velocity.

3.3 Validation Tests

Validation tests was performed in order to validate the adequacy of response surface models by running other tests with random drying conditions and compare it with the predicted responses, two experiments were carried out under different drying conditions as mentioned in Table 7, the differences between the predicted and experimental values are not extreme indicating that the response surface models for the response were acceptable.

3.4 Modeling of Drying Kinetics of Rehydrated Dates

Figure 8 illustrates the variations in moisture ratio over time during intermittent drying of dates. A notable common feature observed in the depicted curves is their tendency towards a declining drying rate, indicative of the falling rate period of the drying curve. This characteristic can be attributed to the relatively low initial moisture content of rehydrated dates used in the experiments.

Seven drying models were employed to characterize drying curves, with their respective model numbers, constants or coefficients, and correlation coefficients presented in Table 3. Model selection was based on the criterion of the highest coefficient of determination (R^2), the lowest reduced chi-square (χ^2), and root mean square error (RMSE). In comparison with other models, the Midilli-Kucuk model, the Algorithmic model, and the approximation of diffusion model, respectively, gave the best agreement between the experimental and predicted moisture ratio.

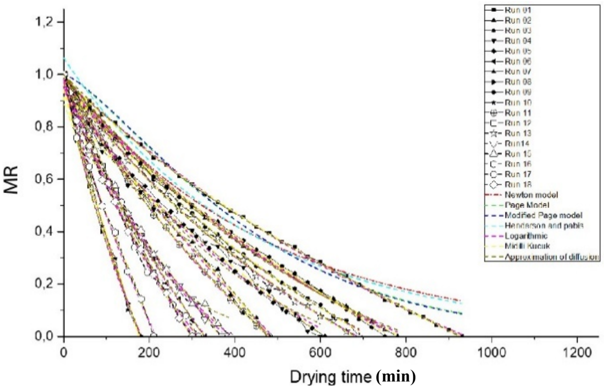

Figure 8. Moisture ratio removed variation under different drying conditions using Midilli-Kucuk, algorithmic and the approximation of diffusion models.

4. Conclusion

The rehydrated dates were dried from an initial moisture content of approximately 33% w.b to a target moisture content of 25% w.b for safe storage using the convective drying method. The experiments were conducted within the range of air temperatures of 40–70 °C, air velocities ranging from 0.5 to 5 m/s, and intermittency ratios spanning from 0.2 to 1, utilizing Response Surface Methodology (RSM) with a Central Composite Design and employing a desirability function. The responses targeted for optimization were drying time and energy consumption. While air velocity did not significantly impact drying time, it negatively affected energy efficiency. Conversely, air temperature played a crucial role in all responses; increasing tempering periods resulted in energy savings, especially at lower temperatures with minimal impact on total drying time. Overall, the findings suggest that energy savings and improved product quality can be achieved without extending total drying time.

The optimal conditions for minimizing both drying time and energy consumption were identified as an inlet temperature of 66 °C, air velocity of 2.5 m/s, and an intermittency ratio of 0.7.

The Midilli-Kucuk model demonstrated superior performance when compared to other models in characterizing the drying kinetics of intermittently dried rehydrated dates.

Nomenclature

α	Intermittency ratio
t_{on}	Time when drying is on (s)
t_{off}	Tempering period (s)
MR	Moisture ratio
w.b	Wet basis (%)

References:

[1] K. D. Alotaibi et al., "Date palm cultivation: A review of soil and environmental conditions and future challenges," Land Degradation & Development, vol. 34, no. 9, pp. 2431-2444, May. 2023, doi: https://doi.org/10.1002/ldr.4619.

[2] Z.-X. Tang, L.-E. Shi, and S. M. Aleid, "Date fruit: chemical composition, nutritional and medicinal values, products," Journal of the Science of Food and Agriculture, vol. 93, no. 10, pp. 2351-2361, Aug. 2013, doi: https://doi.org/10.1002/jsfa.6154.

[3] A. Boubekri, H. Benmoussa, F. Courtois, and C. Bonazzi, "Softening of Overdried 'Deglet Nour' Dates to Obtain High-Standard Fruits: Impact of Rehydration and Drying Processes on Quality Criteria," Drying Technology, vol. 28, no. 2, pp. 222-231, 2010, doi: 10.1080/07373930903526764.

[4] D. Mennouche, B. Bouchekima, A. Boubekri, S. Boughali, H. Bouguettaia, and D. Bechki, "Valorization of rehydrated Deglet-Nour dates by an experimental investigation of solar drying processing method," Energy Conversion and Management, vol. 84, pp. 481-487, 2014, doi: 10.1016/j.enconman.2014.04.067.

[5] K. J. Chua, A. S. Mujumdar, S. K. Chou, M. N. A. Hawlader, and J. C. Ho, "Convective Drying of Banana, Guava and Potato Pieces : Effect of Cyclical Variations of Air Temperature on Drying Kinetics and Color Change," Drying Technology, vol. 18, no. 4-5, pp. 907-936, 2000, doi: 10.1080/07373930008917744.

[6] A. Mukhtar, S. Latif, A. Salvatierra-Rojas, and J. Müller, "Catalase Activity in Hot-Air Dried Mango as an Indicator of Heat Exposure for Rapid Detection of Heat Stress," Applied Sciences, vol. 12, no. 3, doi: 10.3390/app12031305.

[7] Y. K. Pan, L. J. Zhao, and W. B. Hu, "The Effect of Tempering-Intermittent Drying on Quality and Energy of Plant Materials," Drying Technology, vol. 17, no. 9, pp. 1795-1812, 1998, doi: 10.1080/07373939908917653.

[8] A. Singh, J. Sarkar, and R. R. Sahoo, "Experimentation and Performance Analysis of Solar-Assisted Heat Pump Dryer for Intermittent Drying of Food Chips," Journal of Solar Energy Engineering, vol. 144, no. 2, 2021, doi: 10.1115/1.4052549.

[9] N. Ben Mustapha, I. Boumnijel, and D. Mihoubi, "Tempering Drying and Energy Consumption," Journal of Heat Transfer, vol. 144, no. 10, 2022, doi: 10.1115/1.4055045.

[10] R. Md Saleh, B. Kulig, A. Emiliozzi, O. Hensel, and B. Sturm, "Impact of critical control-point based intermittent drying on drying kinetics and quality of carrot (Daucus carota var. laguna)," Thermal Science and Engineering Progress, vol. 20, 2020, doi: 10.1016/j.tsep.2020.100682.

[11] J. C. Alves Pereira et al., "Continuous and Intermittent Drying of Rough Rice: Effects on Process Effective Time and Effective Mass Diffusivity," Agriculture, vol. 10, no. 7, 2020, doi: 10.3390/agriculture10070282.

[12] M. A. Kherrafi et al., "Performance enhancement of indirect solar dryer with offset strip fins: Experimental investigation and comparative analysis," Solar Energy, vol. 266, p. 112158, Dec 2023, doi: 10.1016/j.solener.2023.112158.

[13] A. Benseddik, A. Azzi, M. N. Zidoune, and K. Allaf, "Mathematical empirical models of thin-layer airflow drying kinetics of pumpkin slice," Engineering in Agriculture, Environment and Food, vol. 11, no. 4, pp. 220-231, 2018, doi: 10.1016/j.eaef.2018.07.003.

[14] S. Rafiee, "Thin Layer Drying Properties of Soybean (Viliamz Cultivar)," Journal of Agricultural Science and Technology, (in eng), vol. 11, no. 3, pp. 301-308, 2009. [Online]. Available: http://jast.modares.ac.ir/article-23-1698-en.html.

[15] H. Toğrul, "Suitable drying model for infrared drying of carrot," Journal of Food Engineering, vol. 77, no. 3, pp. 610-619, 2006, doi: 10.1016/j.jfoodeng.2005.07.020.

[16] T. Gunhan, V. Demir, E. Hancioglu, and A. Hepbasli, "Mathematical modelling of drying of bay leaves," Energy Conversion and Management, vol. 46, no. 11-12, pp. 1667-1679, 2005, doi: 10.1016/j.enconman.2004.10.001.

[17] G. Zhanyong, J. Shaohua, L. Ting, P. Jinhui, Z. Libo, and J. Feng, "Optimization on Drying of CuCl Residue by Hot-Air Using Response Surface Methodology," in Drying, Roasting, and Calcining of Minerals, T. P. Battle et al. Eds. Cham: Springer International Publishing, 2016, pp. 73-80. doi: 10.1007/978-3-319-48245-3_9.

[18] S. Chouicha et al., "Valorization Study of Treated Deglet-nour Dates by Solar Drying Using Three Different Solar Driers," Energy Procedia, vol. 50, pp. 907-916, 2014, doi: 10.1016/j.egypro.2014.06.109.

[19] K. O. Falade and E. S. Abbo, "Air-drying and rehydration characteristics of date palm (Phoenix dactylifera L.) fruits," Journal of Food Engineering, vol. 79, no. 2, pp. 724-730, 2007, doi: 10.1016/j.jfoodeng.2006.01.081.

[20] G. J. Swamy and K. Muthukumarappan, "Optimization of continuous and intermittent microwave extraction of pectin from banana peels," Food Chemistry, vol. 220, pp. 108-114, Apr. 2017, doi: 10.1016/j.foodchem.2016.09.197.

[21] N. Aghilinategh, S. Rafiee, S. Hosseinpur, M. Omid, and S. S. Mohtasebi, "Optimization of intermittent microwave-convective drying using response surface methodology," Food Sci Nutr, vol. 3, no. 4, pp. 331-41, Jul. 2015, doi: 10.1002/fsn3.224.

[22] W. K. Lewis, "The Rate of Drying of Solid Materials," Journal of Industrial & Engineering Chemistry, vol. 13, no. 5, pp. 427-432, May. 1921, doi: 10.1021/ie50137a021.

[23] G. Xanthopoulos, G. Lambrinos, and H. Manolopoulou, "Evaluation of Thin-Layer Models for Mushroom (Agaricus bisporus) Drying," Drying Technology, vol. 25, no. 9, pp. 1471-1481, Sep. 2007, doi: 10.1080/07373930701537179.

[24] A. Midilli, H. Kucuk, and Z. Yapar, "A New Model For Single-Layer Drying," Drying Technology, vol. 20, no. 7, pp. 1503-1513, Jul. 2002, doi: 10.1081/DRT-120005864.

[25] Q. Zhang and J. B. Litchfield, "An Optimization Of Intermittent Corn Drying In A Laboratory Scale Thin Layer Dryer," Drying Technology, vol. 9, no. 2, pp. 383-395, Mar. 1991, doi: 10.1080/07373939108916672.

[26] O. Yaldýz and C. Ertekýn, "Thin Layer Solar Drying Of Some Vegetables," vol. 19, pp. 583 - 597, 2001, doi : doi: 10.1081/DRT-100103936.

[27] O. Yaldiz, C. Ertekin, and H. I. Uzun, "Mathematical modeling of thin layer solar drying of sultana grapes," Energy, vol. 26, no. 5, pp. 457-465, May. 2001, doi: 10.1016/S0360-5442(01)00018-4.

[28] M. H. Masud, M. U. H. Joardder, A. A. Ananno, and S. Nasif, "Feasibility study and optimization of solar-assisted intermittent microwave–convective drying condition for potato," European Food Research and Technology, vol. 248, no. 5, pp. 1335-1349, May. 2022, doi: 10.1007/s00217-022-03957-5.

[29] M. Kaveh, Y. Abbaspour-Gilandeh, H. Fatemi, and G. Chen, "Impact of different drying methods on the drying time, energy, and quality of green peas," Journal of Food Processing and Preservation, vol. 45, no. 6, 2021, doi: 10.1111/jfpp.15503.

[30] H. Majdi, J. A. Esfahani, and M. Mohebbi, "Optimization of convective drying by response surface methodology," Computers and Electronics in Agriculture, vol. 156, pp. 574-584, 2019, doi: 10.1016/j.compag.2018.12.021.

[31] S. P. Ong, C. L. Law, and C. L. Hii, "Optimization of Heat Pump–Assisted Intermittent Drying," Drying Technology, vol. 30, no. 15, pp. 1676-1687, 2012, doi: 10.1080/07373937.2012.703741.

[32] W. Hajji and S. Bellagha, "New Emerging Technique to Intensify Convective Air Drying Process: Impact of Interval Starting Accessibility Drying (ISAD) on Quality Attributes of Strawberries Fruits," International Journal of Innovative Approaches in Agricultural Research, vol. 7, no. 3, pp. 252-259, 2023, doi: 10.29329/ijiaar.2023.602.1.

[33] M. Beigi, "Energy efficiency and moisture diffusivity of apple slices during convective drying," Food Science and Technology, vol. 36, 2016, doi: 10.1590/1678-457X.0068.

[34] W. Hajji, S. Bellagha, and K. Allaf, "Energy-saving new drying technology: Interval starting accessibility drying (ISAD) used to intensify dehydrofreezing efficiency," Drying Technology, vol. 40, no. 2, pp. 284-298, 2020, doi: 10.1080/07373937.2020.1788072.

International Journal of Thermodynamics (IJoT)
ISSN 1301-9724 / e-ISSN 2146-1511
https://dergipark.org.tr/en/pub/ijot

Vol. 28 (No. 2), pp. 069-078, 2025
doi: 10.5541/ijot.1587174

Research Article

Exergy Analysis of Oxy-Biogas Combustion with Different Rates of the CO_2 Content

[1]*M. Yıldız, [2]S. Özarslan

[1] Iğdır University, Faculty of Engineering, Department of Mechanical Engineering, Iğdır, Türkiye
[2] Amasya University, Technical Sciences Vocational School, Automotive Program, Amasya, Türkiye
E-mail: [1]*melih.yildiz@igdir.edu.tr

Received 18 November 2024, Revised 9 April 2025, Accepted 18 April 2025

Abstract

This work presents the exergetic evaluations of the oxy-biogas combustion process in an adiabatic furnace for the cases of biogas involving different carbon dioxide (CO_2) concentrations. A three-dimensional steady-state computational fluid dynamics model was developed for combustion simulation. The model was first verified with the data of oxy-natural gas and showed good agreement with the data. Thus, simulation studies were performed for the oxy-biogas combustion with different CO_2 concentrations of biogas fuel, from 10 vol% to 40 vol% with a 10% increment, at a constant input power capacity. The results show that the sum of specific thermo-mechanical and chemical exergy of combustion products has a decreasing trend with increasing CO_2 content in biogas. However, the exergy flow rates of the combustion products increased with the increase in CO_2 due to the increasing mass flow rates. Increasing the CO_2 level in biogas led to an increase in the chemical exergy fraction of the combustion products. Thus, the exergy loss fractions resulting from incomplete combustion varied increasingly from 5.8 % to 13.8 % in the range from 10 % CO_2 to 40 % CO_2 contents of biogas.

Keywords: *Biogas; oxy-combustion; chemical exergy; exergy destruction; computational fluid dynamics.*

1. Introduction

The growing global need for energy, the depletion of fossil fuels, and environmental damage have led to increased interest in the use of renewable energy sources. Among green energy sources, biogas is an energy source that can be produced from a wide variety of organic wastes such as municipal waste, agricultural and industrial waste, and sewage sludge. In response to the search for inexhaustible, sustainable, and clean energy, which is one of today's important problems, biogas is a strong candidate because it can be used as a renewable electricity and heat source when needed, stored, and produced from organic waste. Biogas, consisting of combustible methane-CH_4 (50-75%), non-combustible carbon dioxide-CO_2 (25-50%) and small amounts of other gases, and water vapour, is a valuable energy source with a capacity of 5.5-7 kWh m^{-3} [1, 2]. Methane becomes a harmful greenhouse gas when released into the atmosphere, but it directly affects the amount of energy in biogas and is also an important component for reducing harmful emissions and fossil fuel use. For example, it is known that biogas, when used as vehicle fuel, emits less carbon monoxide, hydrocarbon, and nitrogen oxide emissions than gasoline or diesel engines [3].

According to research, the design of the biogas production process and the type of substrate used determine the composition of the gas. Depending on the type of raw material, methane yield varies between 51% and 65%. For example, the methane efficiency of grass silage is 54%, cattle manure is 60%, liquid pig manure is 65%, forage beet is 51%, and corn silage is 52%. However, depending on the feedstock, biogas may contain contaminants including halogenated compounds, sulphur compounds, nitrogen, and organic silicon species [4]. As can be understood, the high and pure methane content of biogas is an important parameter in energy conversion by burning. The methane content determines the calorific value of biogas. The average calorific value of biogas is quite low, at about 21.5 MJ/m^3, compared to the calorific value of natural gas, which is 36 MJ/m^3. By removing non-flammable CO_2 from the biogas composition, higher calorific values of biogas can be obtained when the amount of methane increases [5].

Some cleaning technologies, such as cryogenic process, water cleaning, and membrane, can be used to improve biogas and increase its efficiency. However, gradual clean-up and upgrade processes increase costs. Another solution to improve the biogas combustion process is to reduce CO_2 concentration by blending biogas with different fuels [6, 7]. It is possible to come across examples of blending various fuels and biogas used for this purpose in the literature. Methane, oxygen, propane, hydrogen, microalgae biofuels supported by nanoparticles, and biodiesel are examples of these fuels [8-11].

Another strategy is an oxygen-enriched or oxy-fuel combustion process to improve biogas combustion. Oxygen-enriched biogas combustion has been investigated in the literature, although it is not at a sufficient level. The studies

*Corresponding Author

performed by Yılmaz et al. [12] and Safe et al. [13] show that the stability limits of biogas are improved, and flame temperature increases with oxygen enrichment. In addition to oxygen-enriched and oxy-fuel combustion of biogas, blending of biogas with different fuels under oxygen-enriched and oxy-fuel combustion studies are also available in the literature, such as the use of diesel-biogas blend with oxygen-enriched in an engine [14], biogas/kerosene mixture with oxygen enrichment in a mini gas turbine engine [15], and biogas-propane-oxygen enrichment [16]. In these studies, it was concluded that oxygen enrichment had a significant effect on the entire reaction process and that enrichment of air with O_2 caused an increase in the laminar combustion rates of both fuels examined, respectively. As a summary of the studies in the literature, it was determined that hydrogen addition and oxygen enrichment have positive effects in reducing combustion instability. In biogas combustion studies using hydrogen and oxygen, it was found that CO emissions decreased, and NOx emissions increased with O_2 enrichment, the net heat release rate of the biogas flame increased with the increase in the net reaction rate of the biogas, and more stable combustion was achieved [17-19].

However, the evaluation of these strategies is a critical issue to determine which strategy is more useful and its improvement potential for sustainable energy solutions in such combustion systems. In this regard, exergy flow analyses, sometimes referred to as the second law analysis, become crucial in the evaluation of systems [20, 21]. Exergy analysis is a useful tool for increasing a system's overall efficiency because it can indicate the origins, extent, and locations of thermodynamic inefficiencies [22]. Therefore, researchers have pointed out that the second law of thermodynamics should be used to make a better evaluation of the systems they examine to reveal the destruction of exergy in the systems [23].

Terhan and Comakli [24] performed the exergy analysis of a natural gas-fuelled boiler used for district heating. They reported that the maximum exergy destruction occurred in the combustion chamber, and the exergy efficiency of the boiler was 32.77% while energy efficiency was 82.21%. Costa et al. [25] carried out an exergy analysis of a thermal power plant with a 50 MW capacity using residual forest biomass fuel. They stated that the main irreversibility occurred in the combustion chamber, and the potential for enhancing the system efficiency is by reducing the moisture content in the biomass. Zueco et al. [26] conducted the exergy analysis of a power plant using different fuels, n-octane, methane, propane, and soybean-based biodiesel. Similarly, they concluded that the main source of the exergy destruction stems from the combustion process in the boiler. Besides, it is stated that the fuel with a simple molecular structure and oxygen will reduce the exergy destruction, although exergy efficiencies were reported at about 31% for all fuels used in the study.

Along with the exergy analyses for boiler and power plant combustion systems, much research is also available on the exergy analyses on internal combustion engines for different combustion strategies and fuels [27-29]. Li et al. [30] studied the exergy analysis of three different combustion modes in internal combustion engines, namely conventional diesel combustion (CDC), homogeneous charge compression ignition (HCCI), and reactivity controlled compression ignition (RCCI). Wang et al. [31] performed an extensive study on a turbocharged hydrogen engine to map exergy efficiencies for varying engine speed and load. They reported that the hydrogen-fuelled engine is limited theoretically by 59% exergy efficiency. In general, many of these studies reported that most of the exergy loss occurs during the combustion process.

Literature survey shows that there are numerous studies performed exergy analyses of systems involving the combustion process. However, the exergy analysis of oxy-biogas combustion in a chamber is missing in the literature, which is a research gap in this field. Besides, no studies have evaluated the effect of CO_2 content on oxy-biogas combustion in terms of exergy. The current study aimed, therefore, to investigate the exergy analysis of oxy-biogas combustion in a furnace designed for natural gas system oxy-combustion presented in the study of Yin et al. [32], to reveal the effect of CO_2 content of biogas during oxy-fuel combustion considering both thermo-mechanical and chemical exergy, to determine the exergy loss due to incomplete combustion by varying CO_2 content. Thus, the current study contributes to the literature in this field by presenting findings based on exergy analyses of oxy-biogas combustion, which is a proposed strategy to overcome drawbacks, such as the lower calorific value of biogas and combustion stability encountered during the combustion process.

2. Materials and Methods

In the present work, combustion modeling of biogases consisting of different rates of CO_2 content was numerically carried out under oxy-fuel conditions in a furnace. The combustion model was simulated using the ANSYS-Fluent CFD software tool, which employs the control volume method. Thus, the combustion characteristics and exergetic investigations were performed by the simulated results. The detailed model development and exergy analysis procedure are given in the following sections.

2.1 Geometric Model and Model Formulation

A three-dimensional furnace model was created to simulate the oxy-combustion by considering the dimensions of a 0.8 MW oxy-natural gas flame furnace in the reference [32]. The furnace has a horizontal design, a square cross-section with 1.05 m x 1.05 m, and a 3.44 m length. The furnace has a burner consisting of a fuel inlet with a 16 mm diameter and two annulus having 28mm and 36mm outer diameters for air entrance. An exhaust line with a 500 mm diameter and a 740 mm length was also designed for the exhaust gas exit. The furnace was modeled in its quarter segment to reduce the computational time since the model can be defined by symmetry boundaries. Thus, the model was meshed with the hexahedral elements for the computational domain as shown in Figure 1.

The model formulations consist of conservation equations of mass, momentum, energy, and transport equations in three-dimensional cartesian coordinates. The equations were solved in the computational domain in which flow with chemical reactions takes place, to estimate the flow field, thermal, and combustion products. The conservation equations and transport equations are expressed for steady-state and Newtonian fluids as follows [33]:

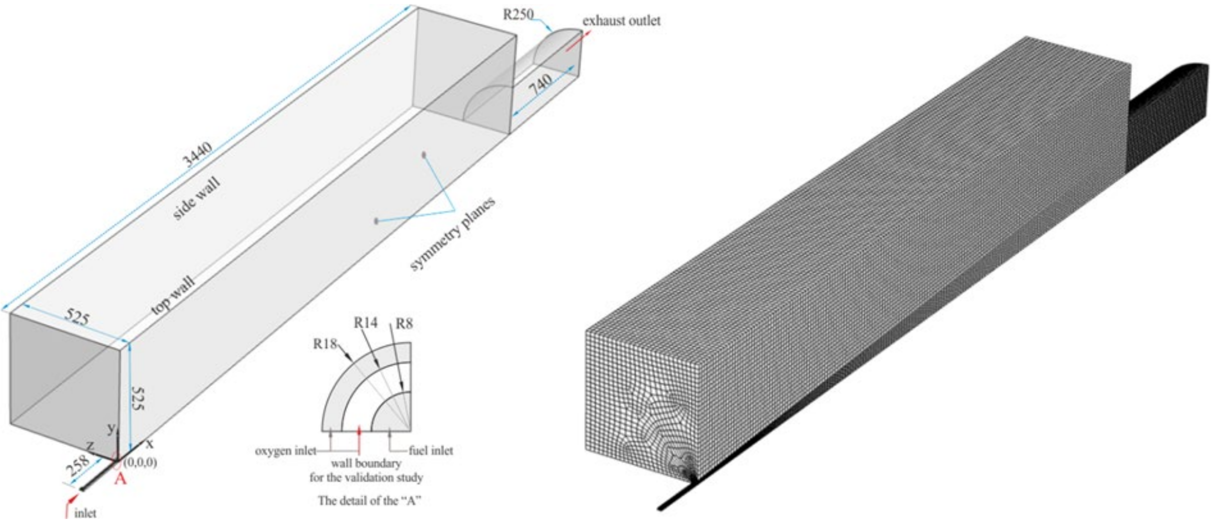

Figure 1. The modelled furnace and its grid structure.

Continuity equation

$$\nabla(\rho\vec{V}) = 0 \tag{1}$$

Momentum equation

$$\nabla(\rho\vec{V}\vec{V}) = -\nabla p + \nabla.(\tau) + \rho\vec{g} + \vec{F} \tag{2}$$

where, $\vec{V}$ is the velocity vector, ρ is the density of the fluid. In Eq. (4), p and τ represent the static pressure and stress tensor, respectively. $\vec{F}$ denotes the external body forces, and $\rho\vec{g}$ is the gravitational force.

Energy equation

$$\nabla\cdot\left[\vec{V}(\rho E + p)\right] = \nabla\cdot\left[k_{eff}\nabla T - \sum h_i\vec{J}_i + \left(\tau_{eff}\cdot\vec{\vartheta}\right)\right] + S \tag{3}$$

where, T is temperature and k_{eff} is defined as the effective conductivity. $\vec{J}_i$ is the diffusion flux of species i, E is total energy, h is sensible enthalpy, and S is the energy source due to the combustion reaction. The total energy is defined as:

$$E = h - \frac{p}{\rho} + \frac{v^2}{2} \tag{4}$$

The enthalpy for ideal gas mixture is expressed as:

$$h = \sum x_i h_i \tag{5}$$

In Eq. (5), x_i is the mass fraction of i th species in a mixture.

The mass fraction of the species in combustion reactions is determined by the species transport equations, and the conservation equation becomes in the following form [34]:

$$\nabla.\left(\rho\vec{V}x_i\right) = -\nabla.\vec{J}_i + R_i \tag{6}$$

where R_i and $\vec{J_\iota}$ are the net production rate and the diffusion flux of i th species in chemical reaction, $\vec{J_\iota}$ is defined as follows:

$$\vec{J}_i = -\left(\rho D_{i,m} + \frac{\mu_t}{Sc_t}\right)\nabla x_i \tag{7}$$

where $D_{i,m}$ represents the diffusion coefficient for species i, and Sc_t is the turbulent Schmidt number, which is set to 0.7 [35].

The present work employs the Eddy-Dissipation-Concept (EDC) model, incorporating chemical kinetic mechanisms, to determine the term R_i in Eq. (6) [36]. In the EDC model, chemical reaction occurs in small turbulent scales defined by the fine scales; the length fraction of the fine scales and the volume fraction of the fine scales. They are calculated as follows [37]:

$$\gamma^* = C_\gamma\left(\frac{\nu\epsilon}{k^2}\right)^{1/4} \tag{8}$$

where, * indicates the quantities of the fine scales. ν, ϵ, and k are the kinematic viscosity, the dissipation rate, and turbulent kinetic energy, respectively. C_γ is a time scale constant. The volume fraction of the scales is estimated as γ^{*3}. A variety of species react in the fine structures across the time scale calculated by Eq. (9).

$$\tau^* = C_\tau\left(\frac{\nu}{\epsilon}\right)^{1/2} \tag{9}$$

The C_τ is a time scale constant. The constants, C_γ and C_τ were set to 1.0 and 3.0 [38] for the current study.

The present work used the modified 4-step global combustion mechanism of Jones and Lindstedt [32, 39]. The mechanisms with Arrhenius equation parameters, which determine the related reaction rate, are given in Table 1. The Arrhenius expression is given by Eq. (10).

$$k_r = A\,T^\beta \exp\left(-\frac{E}{RT}\right) \tag{10}$$

In Eq. (10), k_r represents the reaction rate constant of reaction r. A and β are the pre-exponential factor and temperature exponent, respectively. E and R denote the activation energy for the relevant reaction and the universal gas constant, respectively

The flow field and temperature distribution in the combustion environment are essential to well predict the species since reactions occurring interact with turbulent and heat transfer mechanisms [40]. Therefore, the turbulence and radiation effects were considered by the models; the standard k-ϵ turbulence model and the P1 radiation model in the present study.

Table 1. The modified global mechanism of Jones and Lindstedt (JL_modified).

No	Reactions	Rate exponent	A	β	E [j/kmol]
R1	$CH_4 + 0.5O_2 \rightarrow CO + 2H_2$	$[CH_4]^{0.5}$ $[O_2]^{1.25}$	4.4 10^{11}	0	1.26 10^{8}
R2	$CH_4 + H_2O \rightarrow CO + 3H_2$	$[CH_4]$ $[H_2O]$	3.0 10^{8}	0	1.26 10^{8}
R3	$H_2 + 0.5O_2 \leftrightarrow H_2O$	$[H_2]$ $[O_2]^{0.5}$	5.69 10^{11}	0	1.465 10^{8}
R4	$CO + H_2O \leftrightarrow CO_2 + H_2$	$[CO]$ $[H_2O]$	2.75 10^{9}	0	8.36 10^{8}

The standard k- ϵ model has two transport equations for the turbulence kinetic energy (k) and the dissipation rate (ϵ), which are expressed in Eq. (11) and (12) [34, 41].

$$\frac{\partial}{\partial x_i}(\rho k V_i) = \frac{\partial}{\partial x_j}\left[\left(\mu + \frac{\mu_t}{\sigma_k}\right)\frac{\partial k}{\partial x_j}\right] + G_k + G_b - \rho\epsilon - Y_M \qquad (11)$$

$$\frac{\partial}{\partial x_i}(\rho\epsilon V_i) = \frac{\partial}{\partial x_j}\left[\left(\mu + \frac{\mu_t}{\sigma_\epsilon}\right)\frac{\partial \epsilon}{\partial x_j}\right]$$
$$+ C_{1\epsilon}\frac{\epsilon}{k}(G_k + C_{3\epsilon}G_b) - C_{2\varepsilon}\rho\frac{\epsilon^2}{k} - R_\epsilon + S_\epsilon \qquad (12)$$

In Eq. (11) and (12), G_κ *and* G_b represent the turbulence kinetic energy generation due to the mean velocity gradients and buoyancy, respectively. Y_M is the component of the total dissipation rate attributed to the fluctuating dilatation. σ_κ and σ_ε denote the turbulent Prandtl numbers of k and ε , respectively. $C_{1\varepsilon}$, $C_{2\varepsilon}$, and $C_{3\varepsilon}$ are model constants.

The P-1 radiation model is expressed as in Eq. (13) for radiation flux, q_r, which can be considered in the energy equation for the heat source [34].

$$-\nabla q_r = aG - 4a\sigma T^4 \qquad (13)$$

In Eq. (13), G is the incident radiation, σ is the Stefan-Boltzmann constant, and a represents the absorption coefficient.

2.2 Solving Process

The combustion model was simulated for biogas fuel under stoichiometric oxy-fuel combustion at a constant power capacity of 0.5 MW supplied from the fuel. Biogases were regarded as a mixture composed of CH_4 and CO_2 components [14, 17, 42]. The fuels used for simulation are summarized in Table 2.

Table 2. The fuel components and lower heating values.

Definition	Components (by volume)	*LHV[MJ/kg]
M60C40	60%CH_4 + 40% CO_2	17.6471
M70C30	70%CH_4 + 30% CO_2	22.9508
M80C20	80%CH_4 + 20% CO_2	29.6296
M90C10	90%CH_4 + 10% CO_2	38.2979

* The values were calculated as given in Reference [7].

Considering the fuel components and the lower heating values, the fuel mass flow rates were calculated corresponding to a power of 0.5 MW from fuel input. Thus, the oxygen mass flow rates were determined for a stoichiometric mixture for each fuel component. The pressure and temperature of the fuel and oxygen inputs are considered at atmospheric pressure and 298.15 K, respectively. Besides, the walls of the modelled furnace were subjected to adiabatic boundary conditions, meaning no heat transfer on the walls. The equations were solved with the pressure-based solver and SIMPLE algorithm scheme for pressure-velocity coupling. The second-order upwind schemes were employed for spatial discretization of the equations. Thus, the equations were solved with the convergence criteria of 10^{-7} for the energy and P1 model equations and 10^{-3} for the continuity equation and others.

With the CFD model study, temperature distribution and combustion products were attained for combustion characteristics and exergy analysis for each fuel stated in Table 2.

2.3 Exergy Analysis

Exergy analysis is critical to an assessment of the combustion process since it provides valuable insight into irreversibility and reveals potential being able to be further utilized in a thermodynamic system or process [20]. Therefore, the present work focused on the exergy evaluation of oxy-biogas combustion for different CO_2 contents. Considering the combustion system in the current study, the system is a steady-flow combustion process without exergy input/output by both heat and work. Therefore, the exergy balance equation is expressed as follows:

$$\dot{Ex}_r - \dot{Ex}_p - \dot{Ex}_d = 0 \qquad (14)$$

where, *r, p*, and *d* indicate reactant, products, and destruction, respectively. The reactants in the combustion process are fuel and oxygen. Thus;

$$\dot{Ex}_r = \dot{m}_f ex_f + \dot{m}_{O2} ex_{O2} \qquad (15)$$

where, ex_f and ex_{O2} are the specific exergy (kJ/kg) of fuel and oxygen, respectively. The $\dot{m}_f$ and $\dot{m}_{O2}$ denote the mass flow rates of fuel and oxygen in the reactant.

Similarly, the exergy of the product mixture consisting of six species (O_2, CO_2, CO, H_2O, H_2, and CH_4) in the current study is calculated by the following equation.

$$\dot{Ex}_p = \dot{m}_p ex_p \qquad (16)$$

In Eq. (16), ex_p represents the specific exergy of products. The $\dot{m}_p$ is the mass flow rate of the products, which equals the sum of the mass flow rates of fuel and oxygen.

The exergy in the combustion process can be divided into two parts, thermo-mechanical exergy (ex_{tm}) and chemical exergy (ex_{ch}). Therefore, exergy expression can be written as follows:

$$ex = ex_{tm} + ex_{ch} \qquad (17)$$

By eliminating the contribution of kinetic and potential energy, the specific thermo-mechanical exergy for an ideal gas can be expressed as follows [43]:

$$ex_{tm} = (h - h_0) - T_o\left(c_p ln\frac{T}{T_o} - Rln\frac{P}{P_0}\right) \qquad (18)$$

where, h is the specific enthalpy of the mixture of reactants or products. c_p and R are the specific heat capacity and the gas constant, respectively. The notation "o" indicates the dead state where the system is in thermo-mechanical equilibrium with its surrounding.

The chemical exergy of an ideal gas mixture is calculated as follows [44]:

$$ex_{ch} = \frac{1}{MW_{mix}}\left(\sum y_i\, ex^{o}_{ch,i} + R_u T_o \sum y_i ln y_i\right) \qquad (19)$$

where, MW_{mix} is the molecular weight of the mixture of reactants or products. y_i is the mole fraction of species i in the mixture. R_u is the universal gas constant. $ex^{o}_{ch,i}$ is the standard molar chemical exergy of the species i. The standard molar chemical exergy is calculated by considering the mole fraction of each species at the reference environment, which is presented in Table 3 [45], as given by:

$$ex^{o}_{ch,i} = -RT_o \ln\left(y_{i,o}\right) \qquad (20)$$

As shown in Table 2, the mole fraction of CH_4 is not present in the reference environment. Therefore, it was determined by utilizing the formation reaction of CH_4 and the standard Gibbs free energy of the species in the reaction, as in the reference [46]. Table 3 also summarizes the calculated standard molar chemical exergy.

Table 3. The reference molar fraction of the species and its standard molar exergy.

Species	Mole Fraction ($y_{i,o}$)	Std. Molar ChemicalExergy ($ex^{o}_{ch,i}$) (kJ/mol)
N_2(g)	0.7567	0.6917
O_2(g)	0.2035	3.9465
CO_2(g)	0.000345	19.7611
CO(g)	0.000007	29.4226
H_2O(g)	0.0303	8.6675
H_2(g)	0.0000005	35.9643
CH_4(g)	-	829.9431

Thus, the exergy destruction in combustion process for each fuel was calculated using Eq. (14) as given in Eq. (21).

$$\dot{Ex}_d = \dot{Ex}_r - \dot{Ex}_p \qquad (21)$$

Finally, incomplete combustion exergy loss fraction ($f_{E,ic}$) was determined as follows [47]:

$$f_{E,ic} = \frac{\dot{Ex}_{ch,p}}{\dot{Ex}_{ch,r}} x100 \qquad (22)$$

where, the notations "*ch,p*", "*ch,r*" denote the chemical exergy fractions of the products (exhaust gas) and reactants in the combustion process.

2.4 Mesh Dependency

The grid structures were created meshed with hexahedral cells by considering flow characteristics and the near-wall treatment model, which is the standard wall function in the present study. Hence, adequately fine mesh structures were created in the region of fuel and air streams in which strain flows may occur. On the other hand, course mesh structures were created on the near walls of the furnace to provide $30 < y^{+} < 300$ of which the near-wall model requires. To determine the grid effect on the result, the simulation was performed in different grid structures for oxy-methane combustion with the JL_modified mechanism. The effect of the grid structures is given in Table 4. Since the further increase in the cell number did not change the results considerably, the simulation in the current study was performed on the grid structure with 169605 cells.

Table 4. The effect of the grid structure on the exhaust gas parameters.

	Cell number	T_{exh} [K]	Mole Fraction			
			CO_2	CO	O_2	H_2O
Mesh1	93897	1933.487	0.3195	5.795e-6	0.0412	0.6285
Mesh2	169605	1933.399	0.3106	5.892e-6	0.0406	0.6221
Mesh3	214263	1931.824	0.3187	5.874e-6	0.0409	0.6202

3. Validation

The model was validated by comparing with the data of the temperature and velocity distribution obtained at a 0.8 MW furnace capacity with the JL_modified reaction mechanism presented by Yin et al. [32]. As in the reference, the validated simulation was carried out using the same mass flow rates of the fuel and oxygen inputs for oxy-fuel combustion. Besides, the boundary condition on the walls was subject to a varying temperature profile with respect to axial distance. Figure 2 shows the combustion temperature and x-velocity variations at 142 cm from the burner inlet. The simulation results are compatible with those of Reference 32. Thus, the simulation model can predict reliable results for the evaluation of oxy-biogas combustion.

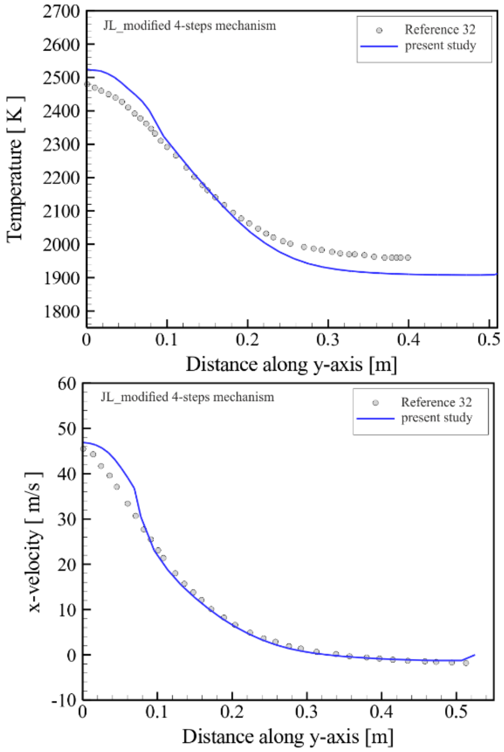

Figure 2. Comparison of the simulation results at 142 cm from the burner in the furnace with a 0.8 MW capacity.

4. Results

4.1 Temperature Development

In Figure 3, axial temperatures are given comparatively in combustion processes using M60C40, M80C20, M70C30, and M90C10 fuel types. Accordingly, it is seen that the maximum temperature is obtained with the M90C10 fuel type. The lowest temperature was recorded in the M60C40 fuel type. It was determined that the temperature is directly proportional to the CH_4 content of the fuel and inversely proportional to the CO_2 content. This can be explained by inert gases such as CO_2 absorbing heat from the combustion process and acting as flame inhibitors. The presence of CO_2 therefore reduces the speed of the flame burning and the combustion rate (the rate at which reactants are converted to combustion products) [48].

Similarly, Sivri et al. [49] tested biogas mixtures containing different amounts of CO_2 in their study on the combustion characteristics of biogas mixtures. They found that high CO_2 concentration decreased the combustion rate and caused lower axial temperature values. Ghenai and Janajreh [50] also argued that the dilution of CH_4-containing fuels with CO_2 and nitrogen reduces the flame temperature. Furthermore, the decreases in temperature can also be attributed to the reduction in the calorific value of the fuel with the increasing CO_2 content.

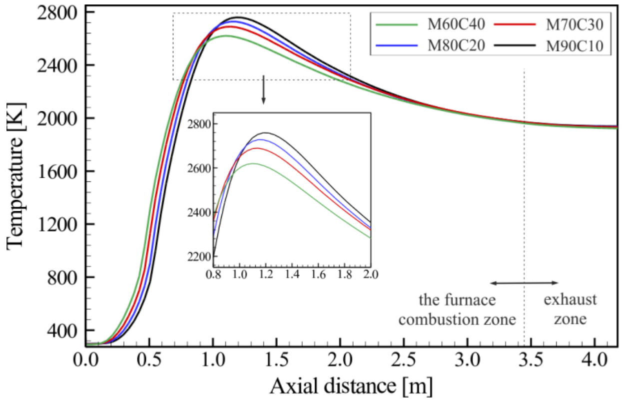

Figure 3. Comparison of the axial temperature values for different fuels.

The velocity changes along the x-axis in the combustion chamber for different fuels are given in Figure 4. Velocity profiles for the fuels show similar trends. As seen in the figure, velocity values in the combustion chamber are high at x=0.

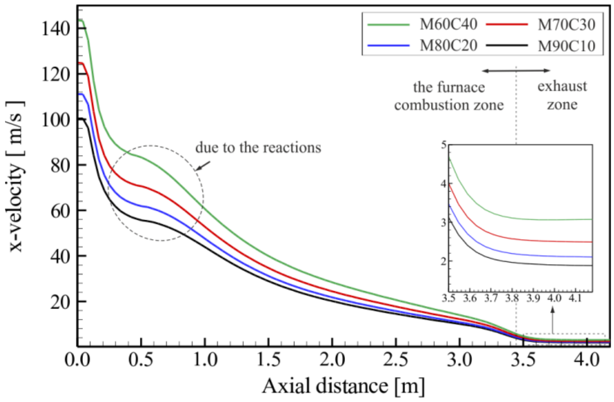

Figure 4. Comparison of x-velocity values through axial distance for different fuels.

After the fuel and oxygen entered the combustion chamber, the velocities have decreasing trends. However, the velocities partially increased between 0.5 m and 1.0 m of the axial distance due to the reaction heat. Afterward, the velocity values along the axis slowed down as the effect of the reaction heat decreased and exited the exhaust region with low velocities. Comparing the velocity values, the velocity values in the case of M60C40 fuel are the highest among the others, and the velocity values decrease with decreasing CO_2 content of biogas. This is due to a decrease in mass flow rate at the same furnace capacity (see Table 5).

Figure 5 illustrates the temperature distributions along the y-axis at x=1.1 m, where the maximum axial temperature occurs approximately (see Figure 3). It is observed that the axial temperature distribution increases with the decrease of the CO_2 ratio in the fuel. Therefore, the highest temperature values were obtained in the M90C10 fuel, while the lowest were in the M60C40 fuel. The reaction zones have high-temperature gradients [51]. Therefore, it can be stated that the change in temperature values after roughly y=0.3 m remains nearly constant, which corresponds to the flame radius at the x=1.1 m.

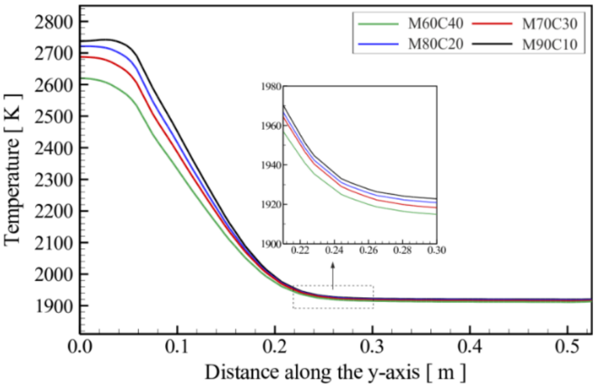

Figure 5. Comparison of temperature values with the y- axis at x=1.1 m.

Figure 6 shows the x-velocity variations in the y-axis direction at the x=1.1 m point for each fuel. As shown in the figure, the velocities are the highest in the center of the combustion chamber due to the highest flame temperature. The x-velocities decrease away from the center of the combustion chamber due to the decreasing or completing reactions, as compatible with the trends in temperature variation given in Figure 5.

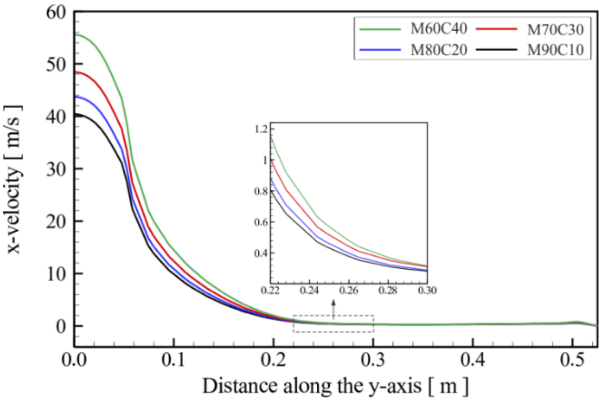

Figure 6. Comparison of x-velocity values with the y-axis at x=1.1 m.

Furthermore, the velocity gradients with the y-axis are nearly zero after x=0.3 m, which is similar to temperature variations. Generally, it is seen that the highest velocity profile belongs to M60C40 fuel. As mentioned above, the mass flow rate at the same furnace capacity gets bigger with the increasing CO_2 content of biogas, which elevates the velocity values.

Figure 7 illustrates the obtained maximum temperature values in the combustion zone and the exhaust temperature variation versus CO_2 content in biogas. It is seen that the increasing CO_2 content brings about a decrease in both the maximum temperature and exhaust temperature. The increasing carbon dioxide with high heat capacity gives rise to decreasing combustion temperature, which in turn decreases the average exhaust temperature [52]. The maximum temperature values were obtained from about 2765 K to 2625 K by varying the CO_2 content. Besides, the exhaust temperatures varied between 1926 K and 1938 K, meaning the average temperature drop is approximately 12 K between M90C10 and M60C40 fuels. A similar trend in the drop in exhaust temperature at a constant power was reported by Bastani et al. [53].

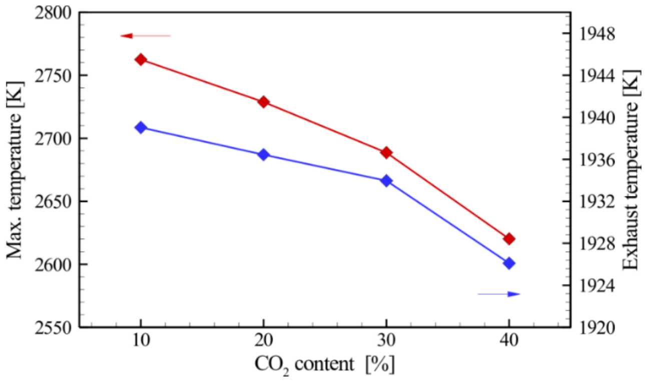

Figure 7. The variation of maximum temperature and exhaust temperature with CO_2 content in biogas.

4.2 Exergetic Evaluation

The section is dedicated to presenting the exergy analysis results. As stated in Section 2.3, the combustion chamber exergy input is provided by reactants consisting of biogas and oxygen at atmospheric pressure and ambient temperature. Therefore, the part of its chemical exergy is only considered by neglecting thermo-mechanical exergy. The calculated specific exergy and exergy flow rates are presented in Table 5 for each fuel. As expected, the maximum specific exergy belongs to M90C10 since it has the highest concentration of CH_4 which has a higher standard molar chemical exergy than that of CO_2 (see Table 3).

Table 5. The specific exergy values and exergy flow rates of the reactants for the fuels.

Fuels	Specific Exergy [kJ/kg]		Mass Flow Rate [kg/s]		Exergy Flow Rate [kW]
	ex_f	ex_{o2}	$\dot{m}_f$	$\dot{m}_{O2}$	$\dot{Ex}_r$
M90C10	39793.5680	123.3281	0.0131	0.04	524.4602
M80C20	30864.1802		0.0169		525.7661
M70C30	23990.7491		0.0218		527.5887
M60C40	18536.8392		0.0283		530.1435

Besides, the exergy flow rates for each fuel are calculated by the sum of the exergy flow rates of the fuels and oxygen as given in Eq. (15). As shown in the table, the exergy flow rates of the reactant relatively increase by increasing CO_2 content due to the increasing mass flow rate calculated by considering the same energy flow rate, 0.5 MW.

Generally, exergy values of fuels are determined by multiplying the lower heating value of fuel (LHV) and the coefficient ϕ which is the ratio of the specific exergy to the lower heating value and calculated depending on the related fuel content [54]. Similar manner, the correlation developed in the current study for biogas fuel for different CO_2 contents (f_{co2} -by volume) is presented below:

$$0 < f_{co2} \leq 0.4$$
$$\phi = 1.0374 + 0.056012(f_{co2})^{1.60193}$$
$$ex_{f,biogas} = \phi x LHV \tag{23}$$

The exergy of the exhaust gases was determined by considering the exhaust gas temperature values (given in Figure 7) and combustion products for each fuel. The obtained mass fractions of each species are given in Table 6. The specific exergy values of the exhaust gas are illustrated in Figure 8. M90C10 shows the highest specific exergy value by 6753.6 kJ/kg, consisting of 91.7 % thermo-mechanical exergy part and 8.3 % chemical exergy. On the other hand, the lowest specific exergy of the exhaust gas was attained at M60C40 by 5985.5 kJ/kg, including 82.3 % thermo-mechanical exergy and 17.7 % chemical exergy fractions.

Table 6. Mass fraction of the combustion products.

Fuels	Species					
	CO_2	CO	H_2O	H_2	O_2	CH_4
M90C10	0.5857	1.44e-5	0.4027	0.0099	0.00121	0.00051
M80C20	0.6064	1.56e-5	0.3767	0.0153	0.00096	0.00063
M70C30	0.6260	1.95e-5	0.3474	0.0247	0.00089	0.00091
M60C40	0.6407	2.91e-5	0.3189	0.0379	0.00077	0.00164

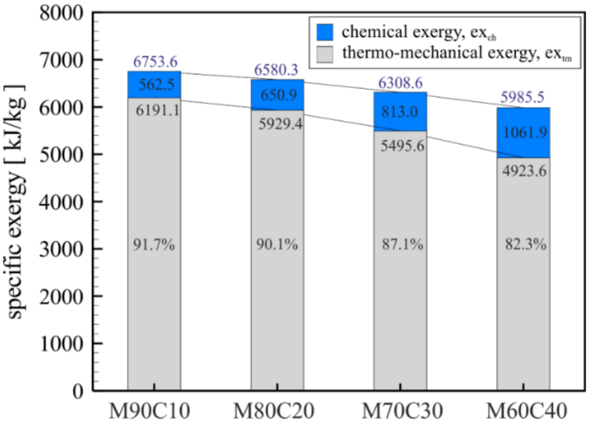

Figure 8. The specific exergy values of exhaust gas mixtures.

Figure 9 shows the exergy flow rates in the furnace. As understood in the figure, the highest exergy destruction ($\dot{Ex}_d$) occurred in M90C10 fuel with 166.14 kW, while the lowest is in M60C40 with 121.14 kW.

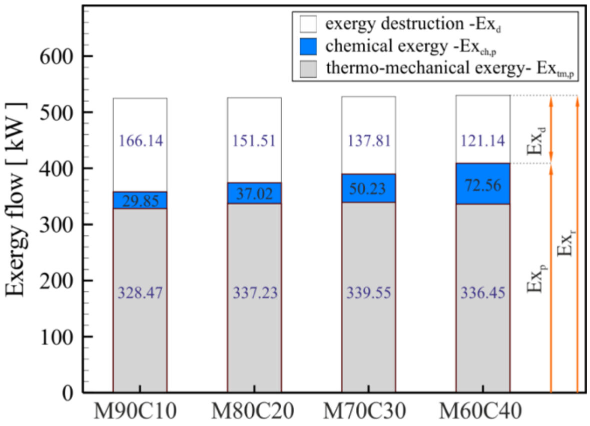

Figure 9. Exergy flow rates for biogas combustion with varying CO_2 content in the furnace.

As a general result, the reduction of CO_2 in biogas causes an increase in the exergy destruction flow in the current combustion system. Another significant result is that the chemical exergy flow of exhaust gas ($\dot{Ex}_{ch,p}$) rises with increasing CO_2 content in biogas. Therefore, the chemical exergy flow in the exhaust reached 72.56 kW in the case of M60C40.

The chemical exergy flow in the exhaust gives an insight into the incomplete combustion exergy loss. Therefore, the chemical exergy flow fractions due to incomplete combustion ($f_{E,ic}$) are shown in Figure 10 for different CO_2 contents. As can be seen, the increasing CO_2 concentration influences considerable incomplete combustion, and the $f_{E,ic}$ value reached about 13.8 % at 40 % CO_2 content (M60C40) while it is about 5.8 % at 10 % CO_2 (M90C10).

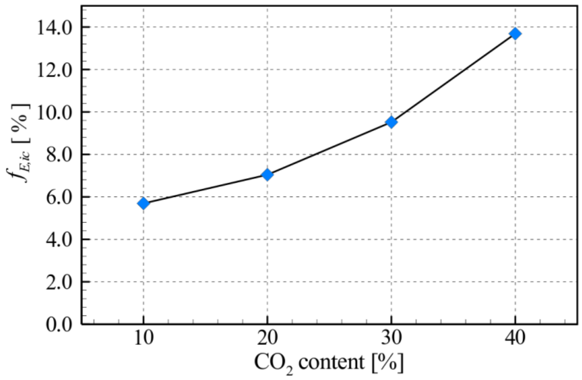

Figure 10. Exergy loss ratio due to incomplete combustion, $f_{e,ic}$.

5. Conclusion

This study investigates the exergy analysis of oxy-biogas combustion in the furnace with a 0.5 MW input power capacity and the adiabatic condition. The focus is on how the varied biogas content with CO_2 ratio influences the exergy flow rates involving thermo-mechanical exergy and chemical exergy. Therefore, the specific exergy and exergy flow rates of reactants and products in the combustion process were calculated for each biogas content varying from 10% CO_2 to 40% CO_2 with a 10% increment, and the obtained results were compared to each other. Additionally, the exergy loss ratios due to incomplete combustion were evaluated considering the chemical exergy flow in the exhaust.

The main findings based on the results are the following:

- The increasing CO_2 concentration in biogas reduced the maximum temperature values in the combustion zone due to its high heat capacity and lowering O_2 concentrations in reaction zones.
- Lowering calorific values with the increase in CO_2 in biogas led to an increase in the mass flow rates to maintain the input power constant, which resulted in the increasing exergy flow rates of the reactants.
- With increasing CO_2 content, the specific exergy of the combustion products decreased while the exergy flow rates increased due to the mass flow rates.
- The chemical exergy fractions of the combustion products increased with elevating CO_2 content in biogas, and the chemical exergy fraction was found to be 17.7% in biogas with 40% CO_2 content while 8.3% at 10% CO_2 content.
- The exergy destruction decreased with increasing CO_2 content in biogas in the current combustion system
- The increasing CO_2 gave rise to an increase in the exergy loss due to incomplete combustion. Thus, the exergy loss fraction due to incomplete combustion was found to be 13.8% in biogas with 40% CO_2 while 5.8% at 10% CO_2 content.

It should be mentioned that one possible limitation of the study is related to the EDC model constant values. These values may differ somewhat depending on the mixture properties in the combustion chamber, which may cause uncertainties in the findings. For future work, further analysis can be performed with different burner and combustion chamber designs, which are also significant factors along with fuel content. These attempts are needed to establish more efficient combustion systems for sustainability.

References:

[1] C. M. Plugge, “Biogas,” *Microbial Biotechnology,* vol. 10, no. 5, pp. 1128-1130, Sep. 2017, doi: 10.1111/1751-7915.12854.

[2] N. Scarlat, J. -F. Dallemand, and F. Fahl, “Biogas: Developments and perspectives in Europe,” *Renewable Energy,* vol. 129, pp. 457-472, Dec. 2018, doi: 10.1016/j.renene.2018.03.006.

[3] S. Rasi, A. Veijanen, and J. Rintala, “Trace compounds of biogas from different biogas production plants,” *Energy,* vol. 32, no. 8, pp. 1375-1380, Aug. 2007, doi: 10.1016/j.energy.2006.10.018.

[4] A. Rafiee, K. R. Khalilpour, J. Prest, and I. Skryabin, “Biogas as an energy vector,” *Biomass and Bioenergy,* vol 144, Jan. 2021, Art. no. 105935, doi: 10.1016/j. biombioe.2020.105935.

[5] S. E. Hosseini and M. A. Wahid, “Development of biogas combustion in combined heat and power generation,” *Renewable and Sustainable Energy Reviews,* vol. 40, pp. 868-875, Dec. 2014, doi: 10.1016/j.rser.2014.07.204.

[6] S. E. Hosseini, G. Bagheri, and M. A. Wahid, “Numerical investigation of biogas flameless combustion,” *Energy Conversion and Management,* vol. 81, pp. 41-50, May 2014, doi: 10.1016/j.enconman. 2014.02.006.

[7] M. Yıldız, “Chemical equilibrium based combustion model to evaluate the effects of H2 addition to biogases with different CO2 contents,” *International Journal of Hydrogen Energy,* vol. 52, pp. 1334-1344, Jan. 2024, doi: 10.1016/j.ijhydene.2023.06.077.

[8] J. P. Gómez Montoya, A. A. Amell, and D. B. Olsen, “Prediction and measurement of the critical compression ratio and methane number for blends of biogas with methane, propane and hydrogen,” *Fuel,* vol. 186, pp. 168-175, Dec. 2016, doi: 10.1016/j.fuel.2016 .08.064.

[9] S. Benaissa, B. Adouane, S. M. Ali, S. S. Rashwan, and Z. Aouachria, “Investigation on combustion characteristics and emissions of biogas/hydrogen blends in gas turbine combustors,” *Thermal Science and Engineering Progress,* vol. 27, Jan. 2022, Art. no.

101178, doi: 10.1016/j.tsep.2021.101178.

[10] A. Sharma, Y. Singh, N. Ahmet Ansari, A. Pal, and S. Lalhriatpuia, "Experimental investigation of the behaviour of a DI diesel engine fuelled with biodiesel/diesel blends having effect of raw biogas at different operating responses," *Fuel,* vol. 279, 2020, Art. no. 118460, doi: 10.1016/j.fuel.2020.118460.

[11] M. Sekar, M. YE. Selim, and M. Elgendi, "Improving the performance of a diesel engine using nanomaterials and chlorella vulgaris microalgae blends assisted with biogas," *International Journal of Hydrogen Energy,* vol. 49, pp. 496-506, Jan. 2024, doi: 10.1016/j.ijhydene. 2023.09.171.

[12] İ. Yilmaz, B. Alabaş, M. Taştan, and G. Tunç, "Effect of oxygen enrichment on the flame stability and emissions during biogas combustion: An experimental study," *Fuel,* vol. 280, Nov. 2020, Art. no. 118703, doi: 10.1016/j.fuel.2020.118703.

[13] K. Safer, M. Safer, F. Tabet, and A. Ouadha, "A numerical investigation of oxygen-enriched biogas counter-flow diffusion flames," *Combustion Science and Technology,* vol. 196, no. 8, pp. 1207-1226, Jun. 2024, doi: 10.1080/00102202.2022.2112955.

[14] K. Cacua, A. Amell, and F. Cadavid, "Effects of oxygen enriched air on the operation and performance of a diesel-biogas dual fuel engine," *Biomass and Bioenergy,* vol. 45, pp. 159-167, Oct. 2012, doi: 10.1016/j.biombioe.2012.06.003.

[15] H. A. Alabaş and B. Albayrak Çeper, "Effect of oxygen enrichment on the combustion characteristic and pollutant emissions of kerosene-biogas mixtures on a mini jet engine combustion chamber," *Journal of the Energy Institute,* vol. 111, Dec. 2023, Art. no. 101420, doi: 10.1016/j.joei.2023.101420.

[16] X. Wang et al., "Effect of propane addition and oxygen enrichment on the flame characteristics of biogas," *Energy & Fuels,* vol. 35, no. 6, pp. 5015-5025, Mar. 2021, doi: 10.1021/acs.energyfuels.1c00113.

[17] B. Alabaş, G. Tunç, M. Taştan, and İ. Yilmaz, "Effect of oxygen enrichment of Biogas-Hydrogen mixtures in a premixed combustor on the combustion instability and emissions," *Fuel,* vol. 340, May 2023, Art. no. 127498, doi: 10.1016/j.fuel.2023.127498.

[18] J. Li et al., "Combustion and heat release characteristics of biogas under hydrogen-and oxygen-enriched condition," *Energies (Basel),* vol. 10, no. 8, p. 1200, 2017, doi: 10.3390/en10081200.

[19] N. Striūgas, R. Paulauskas, R. Skvorčinskienė, and A. Lisauskas, "Investigation of waste biogas flame stability under oxygen or hydrogen-enriched conditions," *Energies (Basel),* vol. 13, no. 18, pp. 4760, Sep. 2020, doi: 10.3390/en13184760.

[20] M. Elwardany, "Enhancing steam boiler efficiency through comprehensive energy and exergy analysis: A review," *Process Safety and Environmental Protection,* vol. 184, pp. 1222-1250, Apr. 2024, doi: 10.1016/j.psep .2024.01.102.

[21] M. Parvez, T. Ahamad, S. Lal, O. Khan, F. Khalid, and Z. Yahya, "Energy, Exergy, Economic, and environmental assessment of a trigeneration system for combined power, cooling, and water desalination system driven by solar energy," *International Journal of Thermofluids,* vol. 22, May 2024, Art. no. 100694, doi: 10.1016/j.ijft.2024.100694.

[22] J. Galindo, S. Ruiz, V. Dolz, and L. Royo-Pascual, "Advanced exergy analysis for a bottoming organic rankine cycle coupled to an internal combustion engine," *Energy Conversion and Management,* vol. 126, pp. 217-227, Oct. 2016, doi: 10.1016/j.enconman. 2016.07.080.

[23] D.-C. Sue and C.-C. Chuang, "Engineering design and exergy analyses for combustion gas turbine based power generation system," *Energy,* vol. 29, no. 8, pp. 1183-1205, Jun. 2004, doi: 10.1016/j.energy.2004.02. 027.

[24] M. Terhan and K. Comakli, "Energy and exergy analyses of natural gas-fired boilers in a district heating system," *Applied Thermal Engineering,* vol. 121, pp. 380-387, Jul. 2017, doi: 10.1016/j.applthermaleng. 2017.04.091.

[25] V. A. F. Costa, L.A.C. Tarelho, and A. Sobrinho, "Mass, energy and exergy analysis of a biomass boiler: A portuguese representative case of the pulp and paper industry," *Applied Thermal Engineering,* vol. 152, pp. 350-361, Apr. 2019, doi: 10.1016/j.applthermaleng. 2019.01.033.

[26] J. Zueco, D. López-Asensio, F.J. Fernández, and L. M. López-González, "Exergy analysis of a steam-turbine power plant using thermocombustion," *Applied Thermal Engineering,* vol. 180, Nov. 2020, Art. no. 115812, doi: 10.1016/j.applthermaleng.2020.115812.

[27] H. Mahabadipour, S. R. Krishnan, and K. K. Srinivasan, "Investigation of exhaust flow and exergy fluctuations in a diesel engine," *Applied Thermal Engineering,* vol. 147, pp. 856-865, Jan. 2019, doi: 10.1016/j.applthermal eng.2018.10.109.

[28] M. N. Nabi and M.G.Rasul, "Influence of second generation biodiesel on engine performance, emissions, energy and exergy parameters," *Energy Conversion and Management,* vol. 169, pp. 326-333, Aug. 2018, doi: 10.1016/j.enconman.2018.05.066.

[29] S. Sarıkoç, İ. Örs, and S. Ünalan, "An experimental study on energy-exergy analysis and sustainability index in a diesel engine with direct injection diesel-biodiesel-butanol fuel blends," *Fuel,* vol. 268, May 2020, Art. no. 117321, doi:10.1016/j.fuel.2020.117321.

[30] Y. Li, M. Jia, Y. Chang, S. L. Kokjohn, and R. D. Reitz, "Thermodynamic energy and exergy analysis of three different engine combustion regimes," *Applied Energy*, vol. 180, pp. 849-858, Oct. 2016, doi: 10.1016/j.apenergy.2016.08.038.

[31] X. Wang, B. Sun, and Q. Luo, "Energy and exergy analysis of a turbocharged hydrogen internal combustion engine," *International Journal of Hydrogen Energy,* vol. 44, no. 11, pp. 5551-5563, Feb. 2019, doi: 10.1016/j.ijhydene.2018.10.047.

[32] C. Yin, L. A. Rosendahl, S. K. Kær, "Chemistry and radiation in oxy-fuel combustion: a computational fluid

dynamic modeling study," *Fuel,* vol. 90, no. 7, pp. 2519-2529, Jul. 2011, doi: 10.1016/j.fuel.2011.03.023.

[33] Wardach-Święcicka, S. Polesek-Karczewska, and D. Kardaś, "Biomass Combustion in the Helically Coiled Domestic Boiler Combined with the Equilibrium/Chemical Kinetics CFD Approach," *Applied Mechanics,* vol. 4, no. 2, pp. 779-802, Jun. 2023, doi: 10.3390/applmech4020040.

[34] Fluent User's Guide*, Centerra Resource Park,10. Cavendish Court, Lebanon, NH 03766, USA.*

[35] M. A. Nemitallah and M. A. Habib, "Experimental and numerical investigations of an atmospheric diffusion oxy-combustion flame in a gas turbine model combustor," *Applied Energy,* vol. 111, pp. 401-415, Nov. 2013, doi: 10.1016/j.apenergy.2013.05.027.

[36] M. Farokhi and M. Birouk, "Application of Eddy dissipation concept for modeling biomass combustion, Part 1: Assessment of the model coefficients," *Energy & Fuels,* vol. 30, no. 12, pp. 10789-10799, Dec. 2016, doi: 10.1021/acs.energyfuels.6b01947.

[37] E.-M. Wartha, M. Bösenhofer, and M. Harasek, "Characteristic chemical time scales for reactive flow modeling," *Combustion Science and Technology,* vol. 193, no. 16, pp. 2807-2832, Dec. 2021, doi: 10.1080/00102202.2020.1760257.

[38] M. J. Evans, P.R. Medwell, and Z.F. Tian, "Modeling lifted jet flames in a heated coflow using an optimized eddy dissipation concept model," *Combustion Science and Technology,* vol. 187, no. 7, pp. 1093-1109, Jul. 2015, doi: 10.1080/00102202.2014.1002836.

[39] J. P. Kim, U. Schnell, and G. Scheffknecht, "Comparison of different global reaction mechanisms for MILD combustion of natural gas," *Combustion Science and Technology,* vol. 180, no. 4, pp. 565-592, Feb. 2008, doi: 10.1080/00102200701838735.

[40] S. Mazumder, and S. P. Roy, "Modeling thermal radiation in combustion environments: progress and challenges," *Energies (Basel),* vol. 16, no. 10, p. 4250, May 2023, doi: 10.3390/en16104250.

[41] J. Gorman, S. Bhattacharyya, L. Cheng, and J. P. Abraham, "Turbulence models commonly used in CFD," in *Applications of Computational Fluid Dynamics Simulation and Modeling*: IntechOpen, 2021, doi: 10.5772/intechopen.99784.

[42] C. A. Cardona and A. A. Amell, "Laminar burning velocity and interchangeability analysis of biogas/C_3H_8/H_2 with normal and oxygen-enriched air," *International Journal of Hydrogen Energy,* vol. 38, no. 19, pp. 7994-8001, Jun. 2013, doi: 10.1016/j.ijhydene.2013.04.094.

[43] M. A. Boles, Y. A. Cengel, Thermodynamics: an engineering approach, 8 th ed. New York: McGraw-Hill Education, 2014.

[44] Y. Kalinci, A. Hepbasli, and I. Dincer, "Exergoeconomic analysis and performance assessment of hydrogen and power production using different gasification systems," *Fuel*, vol. 102, pp. 187-198, Dec. 2012, doi: 10.1016/j.fuel.2012.06.040.

[45] H. Caliskan, M. E. Tat, and A. Hepbasli, "Performance assessment of an internal combustion engine at varying dead (reference) state temperatures," *Applied Thermal Engineering,* vol. 29, no. 16, pp. 3431-3436, Nov. 2009, doi: 10.1016/j.applthermaleng.2009.05.021.

[46] R. Pal, "Chemical exergy of ideal and non-ideal gas mixtures and liquid solutions with applications," *International Journal of Mechanical Engineering Education,* vol. 47, no. 1, pp. 44-72, Jan. 2019, doi: 10.1177/030641901774958.

[47] D. Liu et al., "Theoretical analysis on the exergy destruction mechanisms and reduction under LTC relevant conditions," *Proceedings of the Combustion Institute,* vol. 37, no. 4, pp. 4797-4804, 2019, doi: 10.1016/j.proci.2018.08.012.

[48] O. Razbani, N. Mirzamohammad, and M. Assadi, "Literature review and road map for using biogas in internal combustion engines," in *3 th Int. Conference on Applied Energy*, Perugia, Italy, 2011.

[49] I. Sivri, H. Yilmaz, O. Cam, and I. Yilmaz, "Combustion and emission characteristics of premixed biogas mixtures: An experimental study," *International Journal of Hydrogen Energy,* vol. 47, no. 24, pp. 12377-12392, Mar. 2022, doi: 10.1016/j.ijhydene.2021.08.119.

[50] C. Ghenai and I. Janajreh, "Combustion of renewable biogas fuels," *Journal of Energy and Power Engineering,* vol. 9, no. 10, pp. 831-843, 2015, doi:10.17265/19348975/2015.010.001.

[51] S. K. Som and A. Datta, "Thermodynamic irreversibilities and exergy balance in combustion processes," *Progress in Energy and Combustion science,* vol. 34, no. 3, pp. 351-376, June 2008, doi: 10.1016/j.pecs.2007.09.001.

[52] X. Tian, J. Yang, Y. Gong, Q. Guo, X. Wang, and G. Yu, "Experimental study on OH*, CH*, and CO_2* chemiluminescence diagnosis of CH_4/O_2 diffusion flame with CO_2-diluted fuel," *ACS Omega,* vol. 7, no. 45, pp. 41137-41146, Nov. 2022, doi: 10.1021/acsomega.2c04689.

[53] M. Bastani, S. Tabejamaat, M. Mani, and H. Ashini, "Numerical and experimental investigation of microturbine combustion chamber performance and emissions through biogas consumption with varied component ratios," *Fuel,* vol. 380, Jan. 2025, Art. no. 133234, doi: 10.1016/j.fuel.2024.133234.

[54] T.J. Kotas, Y.R. Mayhew, and R.C. Raichura, "Nomenclature for exergy analysis," *Proceedings of the Institution of Mechanical Engineers, Part A: Journal of Power and Energy,* vol. 209, no. 4, pp. 275-280, Nov. 1995, doi: 10.1243/PIME_PROC_1995_209_006_01.

International Journal of Thermodynamics (IJoT)
ISSN 1301-9724 / e-ISSN 2146-1511
https://dergipark.org.tr/en/pub/ijot

Vol. 28 (No. 2), pp. 079-088, 2025
doi: 10.5541/ijot.1590723

Research Article

Revolutionizing Potato Drying: Performance Insights from Hybrid Solar Drying Systems

[1]*A. D. Balpande, [1]P. B. Maheshwary, [2]P. N. Belkhode

[1] Department of Mechanical Engineering, Rashtrasant Tukdoji Maharaj University, Nagpur, MH, India
[2] Department of Mechanical Engineering, Laxminarayan Institute of Technology, Nagpur, MH, India
E-mail: [1]*ankitabalpande88@gmail.com

Received 25 November 2024, Revised 10 January 2025, Accepted 23 January 2025

Abstract

This study investigates the performance of a hybrid solar dryer designed for the efficient drying of potato slices, aiming to address the challenges associated with conventional drying methods. The primary objectives were to evaluate the moisture removal rate (MRR) of the hybrid solar dryer and compare its effectiveness with traditional solar drying techniques. Through a series of experiments conducted from May to December 2024, the hybrid dryer demonstrated an impressive average MRR of 182.8 g/h, significantly outperforming both conventional (typically 150–180 g/h) and indirect solar dryers. The findings revealed that the hybrid system not only reduced drying time but also preserved the quality of the dried products, ensuring minimal nutrient loss. The MRR ranged from 158.4 g/h in December to 198.3 g/h in May, showcasing stable performance despite climatic fluctuations. Comparative analyses highlighted the superior efficiency of the hybrid design, making it a viable solution for food preservation, particularly in regions with ample sunlight. Additionally, the study emphasizes the importance of sustainable food processing technologies in enhancing food security and reducing agricultural waste. This research contributes valuable insights into the development of innovative drying solutions that can be effectively implemented in various agricultural settings, promoting better utilization of solar energy for food preservation. Future studies could explore further optimizations and integrations to enhance the performance of solar drying systems.

Keywords: *Hybrid solar dryer; moisture removal rate; potato; solar energy; sustainable food preservation.*

1. Introduction

Food drying is an ancient and vital method for preserving agricultural products, extending their shelf life, and reducing post-harvest losses. The process involves removing moisture from food items, thereby inhibiting the growth of microorganisms that cause spoilage. By reducing water activity, drying effectively preserves the nutritional value, flavor, and texture of the food while making it lighter and more compact for storage and transportation [1].

In many developing countries, including India, a significant portion of harvested produce is lost due to inadequate post-harvest handling and preservation techniques. Traditional methods such as open sun drying, although cost-effective, often lead to significant quality degradation due to exposure to contaminants, insects, and unpredictable weather conditions [2]. Consequently, there is a pressing need for efficient, reliable, and hygienic drying technologies to ensure food security and reduce waste.

1.1 Importance of Renewable Energy in Food Preservation

The use of renewable energy in food preservation has gained substantial attention in recent years due to the growing concerns over energy consumption and environmental sustainability. Conventional drying methods, such as mechanical dryers powered by electricity or fossil fuels, contribute to greenhouse gas emissions and incur high operational costs. In contrast, solar energy is a sustainable, eco-friendly alternative that can be harnessed to effectively dry agricultural products [3].

Solar drying systems utilize the abundant and free energy from the sun, making them particularly suitable for regions with high solar insolation. By integrating solar energy with supplementary electrical heating, hybrid solar dryers can overcome the limitations of weather dependency, providing a consistent drying environment. This combination not only reduces the reliance on non-renewable energy sources but also lowers the carbon footprint associated with food preservation.

1.2 Overview of Existing Drying Technologies

Several drying technologies have been developed to enhance the efficiency and quality of dried food products, primarily categorized into open sun drying, conventional mechanical drying, and advanced solar drying systems.

Open sun drying is the most traditional and widely used method, particularly in rural areas. In this approach, food items are spread out under the sun and left to dry naturally. Although it is cost-free and straightforward to implement, this method relies heavily on weather conditions, and exposure to contaminants can compromise the quality and safety of the dried products [4].

Conventional mechanical drying employs electrical or fuel-based heaters to provide the necessary heat for drying.

*Corresponding Author

These systems offer better control over drying conditions, resulting in more consistent and higher-quality dried products. However, they tend to be energy-intensive and expensive to operate, making them less accessible for small-scale farmers and producers.

Advanced solar drying systems encompass various designs, including direct, indirect, and mixed-mode dryers. Direct solar dryers expose food directly to sunlight within an enclosed chamber, which reduces contamination and accelerates the drying process compared to open sun drying. Indirect solar dryers, on the other hand, involve a heat collector that absorbs solar radiation, with the heated air subsequently circulated through the drying chamber, thus avoiding direct exposure of food to sunlight. Mixed-mode solar dryers combine both direct and indirect methods to optimize the drying process [5, 6]. Additionally, hybrid solar dryers integrate solar energy with auxiliary electrical heating to maintain a stable drying environment, ensuring efficient operation even during cloudy or rainy periods and providing a continuous drying process.

1.3 Objectives of the Study

The primary objective of this study is to design, develop, and evaluate the performance of a hybrid solar dryer specifically tailored for drying agricultural products such as potato slices. This study aims to address the limitations of traditional drying methods by integrating renewable solar energy with electrical heating to create an efficient, reliable, and hygienic drying system.

The specific objectives are as follows:

- To create a hybrid solar dryer system that utilizes both solar and electrical energy to provide a consistent and controlled drying environment for various agricultural products.
- To conduct a series of drying experiments over a defined period, collecting data on temperature, humidity, mass before and after drying, and battery percentage. The experiments will be conducted under controlled conditions to assess the dryer's efficiency in removing moisture from potato slices.
- To calculate and analyze the moisture removal rate (MRR) and drying efficiency, and to evaluate the performance of the battery and photovoltaic system in providing consistent power for the drying process.
- To compare the performance of the hybrid solar dryer with traditional open sun drying and conventional mechanical drying methods in terms of drying efficiency, energy consumption, and product quality.

By achieving these objectives, the study aims to demonstrate the feasibility and advantages of using hybrid solar drying technology for food preservation, providing a sustainable solution that can be adopted by small-scale farmers and producers to enhance food security and reduce post-harvest losses.

2. Related Works

The exploration of solar dryers has advanced significantly over the years, addressing various challenges associated with drying agricultural products. Amer et al. [7] evaluated the performance of an automated hybrid solar system dryer (HSSD) for drying aromatic herbs such as lemongrass, thyme, marjoram, and lavender. Their study highlighted the efficiency of HSSD in retaining the physicochemical properties of these herbs, emphasizing its potential for energy savings and reduced carbon footprint. The findings showed that HSSD could save between 19-36% of energy consumption while delivering high-quality dried products.

Kherrafi et al. [8] provided a comprehensive review of solar drying technologies, discussing design variations, hybrid systems, storage materials, and numerical analysis. They emphasized the importance of optimizing the design and performance of solar drying systems through numerical analyses and CFD simulations, which can lead to more efficient and reliable solar drying solutions.

Kalita et al. [9] investigated the performance of a hybrid solar dryer with electric and biogas backup air heaters for drying red chili. They found that the Biogas Hybrid Mode Solar Dryer (BHMSD) was more efficient than the Electric Hybrid Mode Solar Dryer (EHMSD), offering higher moisture diffusivity and energy savings. The study concluded that BHMSD is a more sustainable and eco-efficient alternative to traditional electric-based systems.

Saha et al. [10] reviewed the constructional features and techno-economic-environmental aspects of solar hybrid dryers for fruits, vegetables, and fish. They discussed the advancements in communication and sensing technologies that have enabled real-time control and automation in SHDs, making them competitive with fossil-fueled dryers. The review also highlighted the economic and environmental benefits of SHDs, despite certain techno-economic barriers that need to be addressed through incentives and regulations.

Behera et al. [11] conducted an experimental investigation of a hybrid solar dryer for vegetable drying, incorporating phase change materials (PCMs) for improved efficiency. Their study demonstrated that using PCMs increased collector efficiency, drying efficiency, and drying rate, making the process more suitable for cloudy weather and nighttime drying. This approach showed significant potential for sustainable food preservation.

Lehmad et al. [12] assessed the environmental, economic, and quality aspects of hybrid solar-electric drying of black soldier fly larvae (BSFL). The study highlighted the short payback period and substantial economic savings of the HSED system, along with the superior protein content of the dried larvae compared to conventional methods. This research underscores the potential of HSED systems in ensuring food security and sustainability.

Mahajan et al. [13] detailed the design and analysis of a solar biomass hybrid dryer for drying turmeric. Their design, validated through ANSYS simulations, demonstrated consistent temperature distribution and effective drying under hygienic conditions. This development is particularly beneficial for small-scale turmeric processors, enhancing product value and marketability.

2.1 Challenges in Drying Agricultural Products

Drying agricultural products efficiently and effectively presents several challenges. Direct sunlight can degrade the quality of sensitive herbs and vegetables, as discussed by Amer et al. [7]. Maintaining the desired physicochemical properties while minimizing energy consumption is a significant hurdle.

Traditional drying methods, such as open sun drying (OSD), are often inefficient and time-consuming, as highlighted by Kalita et al. [9]. They found that OSD required twice the drying time compared to hybrid solar dryers and was less effective in reducing moisture content.

Additionally, OSD is susceptible to environmental contamination, leading to quality and hygiene issues.

The integration of auxiliary heating units, such as those in SHDs, can mitigate some of these challenges. However, as Saha et al. [10] pointed out, the high initial costs and operational complexity of these systems can be barriers to widespread adoption, particularly for small-scale farmers [4].

2.2 Technological Advancements in Hybrid Drying Systems

Technological advancements have significantly improved the performance and reliability of hybrid drying systems. Hybrid solar dryers (HSSD, SHD, BHMSD, etc.) combine solar energy with auxiliary heating sources, such as electricity, biogas, or biomass, to provide continuous and efficient drying. These systems, as demonstrated, offer higher drying rates, better moisture diffusivity, and improved energy efficiency compared to traditional methods.

The use of phase change materials (PCMs) in hybrid solar dryers, represents a significant advancement. PCMs enhance thermal storage capacity, allowing for effective drying even during cloudy weather and nighttime. This technology improves overall drying efficiency and makes the process more sustainable.

Advancements in real-time monitoring and control systems, have also played a crucial role in enhancing the performance of hybrid dryers. These systems enable precise control over drying parameters, ensuring consistent product quality and reducing energy consumption.

2.3 Gaps Identified in Existing Literature

Despite the significant advancements in solar drying technologies, several gaps remain. There is a need for more comprehensive studies on the long-term performance and durability of hybrid drying systems under various climatic conditions. Most studies, focus on short-term performance metrics.

Additionally, the economic feasibility and scalability of these technologies for small-scale farmers require further investigation. While Saha et al. [10] and Lehmad et al. [12] provided insights into the economic benefits of hybrid dryers, more studies are needed to evaluate their cost-effectiveness in different agricultural settings.

There is also a gap in the literature regarding the environmental impact of hybrid drying systems over their entire lifecycle. While the potential for energy savings and reduced CO_2 emissions, more detailed life cycle assessments are necessary to fully understand the environmental benefits and trade-offs.

Table 1. Summary of Related Works.

Author	Year	Method	Limitations
Amer et al. [7]	2024	Automated hybrid solar system dryer	Short-term performance metrics
Kherrafi et al. [8]	2024	Review of solar drying technologies	Lack of long-term performance studies
Kalita et al. [9]	2024	Hybrid solar dryer with electric and biogas heaters	Economic feasibility for small-scale farmers
Saha et al. [10]	2024	Review of solar hybrid dryers	High initial costs and operational complexity
Behera et al. [11]	2024	Hybrid solar dryer with PCMs	Limited environmental impact analysis
Lehmad et al. [12]	2024	Hybrid solar-electric drying of BSFL	Need for detailed lifecycle assessments
Mahajan et al. [13]	2024	Solar biomass hybrid dryer for turmeric	Validation needed for large-scale applications

3. Materials and Methods

This section provides a comprehensive overview of the materials and methods employed in designing and constructing the hybrid solar dryer, including detailed descriptions of the components, the experimental setup, and the calculations necessary to evaluate performance metrics.

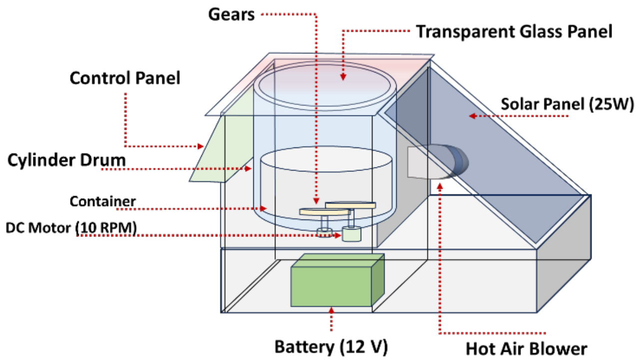

Figure 1. Schematic diagram of the hybrid solar dryer.

3.1 Design of the Hybrid Solar Dryer

The hybrid solar dryer is designed to maximize drying efficiency through the use of solar energy combined with electrical heating. The key components include:

Steel Cabinet: The main body of the dryer is constructed from a steel cylinder with a diameter of $D_c = 0.5$ and height $H_c = 1.2\,m$. The cylinder's role is to provide structural integrity and insulation to maintain internal temperatures [14].

The surface area A_c of the cylinder can be calculated using the formula for the lateral surface area of a cylinder:

$$A_c = \pi D_c H_c \tag{1}$$

Substituting the dimensions:

$$A_c = \pi(0.5)(1.2) \approx 1.88 m^2$$

Glass Lid: The glass lid serves as a transparent barrier allowing solar radiation to penetrate while trapping heat inside. The lid is made of tempered glass with a thickness of $t_g = 0.01\,m$ and a surface area A_g equal to that of the top surface of the cylinder, calculated as follows [15]:

$$A_g = \pi\left(\frac{D_c}{2}\right)^2 \approx \pi(0.25)^2 \approx 0.196\ m^2 \tag{2}$$

Rotating Disk: Inside the dryer, a rotating disk helps to uniformly distribute heat and improve airflow. The disk has a radius $R_d = 0.24$ and a thickness of $t_d = 0.02\,m$. The area of the disk A_d can be calculated as [16]:

$$A_d = \pi R_d^2 \approx \pi(0.24)^2 \approx 0.180\ m^2 \tag{3}$$

Gear System: A gear system is employed to convert the high-speed rotation of the motor to the lower speed required for the rotating disk. The gear ratio G is determined by the number of teeth on the motor gear (T_m) and the disk gear (T_d) [17]:

$$G = \frac{T_m}{T_d} \tag{4}$$

High Torque 12V DC Motor: The motor selected for the dryer operates at 12V with a torque of $T = 1\ Nm$. The power P_m of the motor can be calculated using the formula [18]:

$$P_m = T \cdot \omega \tag{5}$$

where ω is the angular velocity in rad/s. Assuming a speed of N=30 rpm:

$$\omega = \frac{2\pi N}{60} \approx \frac{2\pi(30)}{60} = \pi \frac{rad}{s} \tag{6}$$

Then from Eq. (5):

$$P_m = 1 \cdot \pi \approx 3.14\ W \tag{7}$$

Inlet Hot Air Blower: The inlet hot air blower is crucial for maintaining the desired temperature within the dryer. The blower's specifications include a flow rate $Q_b = 0.1 \frac{m^3}{s}$ The heating power required can be estimated using [19]:

$$Q = \frac{kA \cdot \Delta T}{\Delta t} \tag{8}$$

where Q is the heat transfer rate (W), k is the thermal conductivity (W/m·K), A is the cross-sectional area (m²), ΔT is the temperature difference (K), Δt is the time interval (s).

Air Blower DC Fan: An additional DC fan is integrated to enhance airflow. The fan's specifications are $12V$ with an airflow capacity of $0.05\ m^3/s$.

12V 14Ah Battery and 24W PV Panel: The energy storage system comprises a 12V, 14Ah battery connected to a 24W photovoltaic (PV) panel. The capacity of the battery can be computed as [20]:

$$E_b = V_b \cdot C_b = 12 \cdot 14 = 168\ Wh \tag{9}$$

Control Board with Temperature and Humidity Sensors: The control board includes sensors to monitor internal conditions. The data collected allows for adjustments to the heating and drying processes, enhancing the overall efficiency of the drying operation [21].

3.2 Experimental Setup

The experimental setup is crucial for testing the efficiency of the hybrid solar dryer under various conditions.

The experiments were conducted in a location with direct sunlight exposure from 10 AM to 3 PM. The environmental conditions, including temperature and humidity, were monitored using calibrated sensors. The average temperature during experiments was $T_{avg} = 35°C$ with relative humidity ranging from 30% to 50%.

Fruits were prepared by slicing potatoes into uniform pieces of approximately 2 mm thickness to ensure consistent drying. The initial mass of the samples was recorded before drying. A schematic diagram of a hybrid solar dryer is illustrated in Figure 1.

Duration and Schedule of Drying Experiments: The drying experiments were conducted in a controlled manner from 10 AM to 3 PM, resulting in a total drying duration of $T_d = 5\ hours$.

Data Collection Methods: Data collection was systematic, recording: Temperature and humidity at regular intervals, Mass before and after drying to evaluate moisture removal rates, and battery percentage to assess energy consumption, the data was logged using a digital control board.

Table 2. Data collection parameters.

Parameter	Value
Average temperature	35 °C
Average humidity	30-50 %
Duration of drying	4 hours
Initial mass (potato)	1000 g

3.3 Evaluation

The performance of the hybrid solar dryer is evaluated using various metrics.

Moisture Removal Rate (MRR): The moisture removal rate (MRR) can be calculated using the formula [22]:

$$MRR = \frac{M_i - M_f}{T_d} \tag{10}$$

where: M_i = Initial mass (g), M_f = Final mass (g), T_d = Duration of drying (h).

Drying Efficiency: Drying efficiency (η) is determined by [23]:

$$\eta = \frac{Energy\ used\ for\ drying}{Energy\ input\ from\ solar\ and\ electrical\ sources} \times 100 \tag{11}$$

where energy can be calculated as [18]:

$$Energy\ used = (M_i - M_f) \times L_v \tag{12}$$

L_v is the latent heat of vaporization, approximately $2260 \frac{kJ}{kg}$ commonly accepted value for water at 100°C under standard atmospheric pressure (1 atm).

Battery Efficiency: Battery efficiency (η_b) can be computed as follows [24]:

$$\eta_b = \frac{Energy\ delivered\ to\ load}{Energy\ Supplied\ by\ PV\ panel} \times 100 \tag{13}$$

Assuming energy delivered can be represented as:

$$Energy\ delivered = Battery\ capacity \times discharge\ percentage \tag{14}$$

And energy supplied by the PV panel over the duration of T_d:

$$Energy\ supplied = P_{PV} \times T_d \tag{15}$$

where, $P_{PV} = 24\ W$.

The hybrid solar dryer integrates various components and technologies to enhance drying efficiency while leveraging renewable energy sources. Through precise design and systematic experiments, the performance metrics, including MRR, drying efficiency, and battery efficiency, can be accurately assessed using the methods outlined above. This section serves as the foundation for analyzing the dryer's operational effectiveness in practical applications [25].

4. Results and Discussion

The performance of the hybrid solar dryer was evaluated from May 2024 to January 2025, focusing on drying potato slices. Key parameters assessed include Moisture Removal Rate (MRR), drying efficiency, and energy efficiency. The study aimed to demonstrate the dryer's effectiveness across varying climatic conditions, providing valuable insights for improving solar drying technologies for agricultural products.

4.1 Moisture Removal Rate (MRR)

The Moisture Removal Rate (MRR) for potato slices was evaluated from May to December 2024, showcasing significant variations in drying performance across the months. In May, the average MRR was 198.3 g/h, peaking at 204.038 g/h, indicating efficient moisture extraction. June followed with an average MRR of 195.0 g/h, reaching up to 207.232 g/h. In July, the MRR averaged 197.2 g/h, while August showed stable performance with an average of 197.5 g/h as listed in Table 3. As the climatic conditions shifted in September and December, average MRR values remained steady with minor fluctuations. This consistent performance despite changing environmental conditions reflects the effectiveness of the hybrid solar dryer in optimizing moisture removal across various months as shown in the Figure 2.

Table 3: Average Monthly Moisture Removal Rate (MRR) for Potato Slices (May 2024 – December 2024).

Month	Average MRR (g/h)	Range (g/h)
May 2024	198.3	192.5 – 204.0
June 2024	195.0	190.1 – 207.2
July 2024	197.2	191.5 – 203.4
August 2024	197.5	192.3 – 201.8
September 2024	182.5	175.8 – 189.9
October 2024	174.8	168.4 – 180.3
November 2024	165.3	160.2 – 171.0
December 2024	158.4	152.9 – 164.1

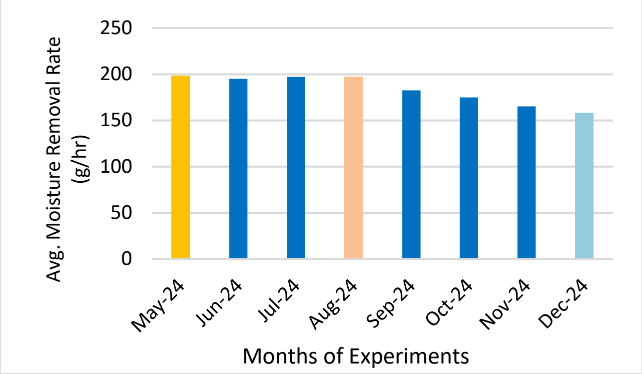

Figure 1. Monthly Average Moisture Removal Rate (MRR) from May 2024 to December 2024.

4.2 Drying Efficiency

Drying efficiency was assessed monthly, showing fluctuations in response to varying climatic conditions. May exhibited the highest average drying efficiency of 68.31%, with values ranging from 67.04% to 70.96%. June followed closely with an average of 68.56%, and the efficiency ranged from 64.31% to 73.92%. By July and August, the drying efficiency decreased, reaching averages of 64.60% and 60.98%, respectively. This reduction can be attributed to higher humidity and lower solar radiation during these months. The gradual decline in efficiency continued into September and December, emphasizing the impact of environmental conditions. Despite these variations, the solar dryer maintained relatively consistent performance, demonstrating its potential to adapt to diverse weather conditions while optimizing energy usage for drying.

Table 4. Average Monthly Drying Efficiency (May 2024 – December 2024).

Month	Average Drying Efficiency (%)	Range (%)
May 2024	68.31	67.0 – 70.9
June 2024	68.56	64.3 – 73.9
July 2024	64.60	62.0 – 67.0
August 2024	60.98	59.3 – 63.3
September 2024	58.40	56.2 – 61.0
October 2024	55.32	53.1 – 58.8
November 2024	52.12	50.5 – 54.9
December 2024	50.45	48.9 – 52.7

As shown in Table 4, May exhibited the highest average drying efficiency at 68.31%, followed by June at 68.56%. In contrast, July and August showed a decrease in drying efficiency, with averages of 64.60% and 60.98%, respectively and so on the winter month from October to December. The variations in drying efficiency can be attributed to changes in environmental conditions, such as increased humidity and lower solar radiation during the later months. Drying efficiency for all four month per day per hour is illustrated in Figure 3.

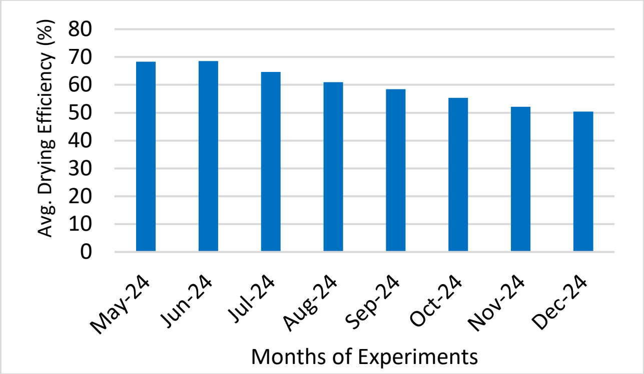

Figure 2. Monthly Average Drying Efficiency from May 2024 to December 2024.

4.3 Energy Efficiency Analysis

Energy efficiency analysis revealed the relationship between energy consumption and moisture removal across the months. In May, the energy efficiency was 4.17 kWh/kg, with a moisture removal of 0.30 kg. June's efficiency was 4.00 kWh/kg, reflecting a slight decrease in performance. July and August saw a marked increase in energy consumption, reaching 6.00 kWh/kg and 7.75 kWh/kg, respectively, despite lower moisture removal shown in Table 5. This increase in energy usage correlates with lower solar radiation and higher humidity during the later months. From September to December, energy efficiency continued to fluctuate with varying climate conditions, highlighting the solar dryer's performance dynamics. These results suggest that while energy efficiency can be affected by environmental factors, the solar dryer remains effective in utilizing energy for moisture extraction across multiple months.

Table 5. Energy Efficiency (kWh/kg) from May to December 2024.

Month	Energy Consumption (kWh)	Moisture Removed (kg)	Energy Efficiency (kWh/kg)
May 2024	1.25	0.30	4.17
June 2024	1.40	0.35	4.00
July 2024	1.50	0.25	6.00
August 2024	1.55	0.20	7.75
September 2024	1.60	0.18	8.89
October 2024	1.70	0.15	11.33
November 2024	1.80	0.12	15.00
December 2024	1.90	0.10	19.00

The energy efficiency (kWh/kg) peaked in December at 19 kWh/kg, demonstrating effective energy utilization despite minimal moisture removal (0.10 kg). In contrast, May and June 2024 showed lower energy efficiencies of 4.17 kWh/kg and 4.00 kWh/kg, respectively, influenced by higher moisture removal (0.30 kg and 0.35 kg) and varying environmental conditions.

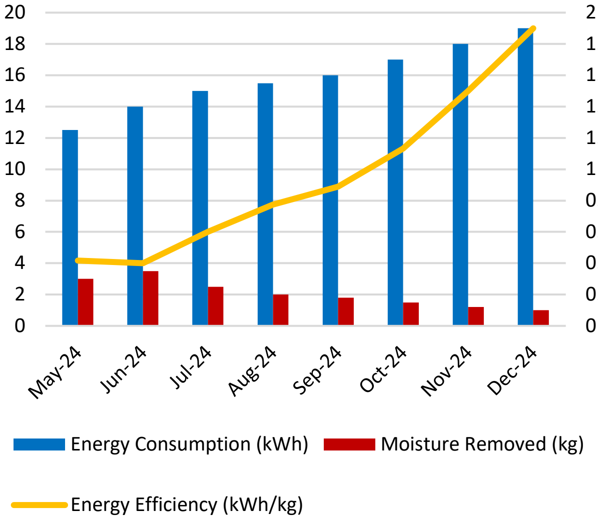

Figure 3. Energy efficiency vs. moisture removal rate and energy efficiency across months.

The solar dryer's performance, significantly affected by seasonal changes in temperature and humidity, achieved optimal drying during peak sunlight. However, lower drying efficiency in July (6.00 kWh/kg) and August (7.75 kWh/kg) emphasizes the need for improved dryer design and parameter adjustments to accommodate climatic variations. Future research should target better energy efficiency while sustaining moisture removal for enhanced sustainability and broader agricultural applications. Energy efficiency vs. moisture removal rate and energy efficiency across months are shown in Figure 4.

A detailed comparison of energy efficiency, moisture removal rate (MRR), and relative humidity (RH) reveals clear seasonal patterns. Energy efficiency steadily increased from May (4.17 kWh/kg) to December (19.00 kWh/kg), with the highest value in January. However, moisture removal decreased progressively, from 0.30 kg in May to just 0.10 kg in December. This inverse trend indicates that higher energy efficiency corresponds to reduced moisture removal, primarily due to lower ambient humidity during cooler months, enhancing energy use while limiting evaporation rates.

4.4 The Uncertainty Analysis of the Results

Uncertainty analysis was conducted to assess the reliability of the experimental data, particularly concerning moisture removal rates, temperature, relative humidity, and air velocity. The measurement uncertainties were determined using standard error propagation formulas, with moisture removal rate (MRR) uncertainty at ±2.5%, temperature accuracy at ±1.2°C, and humidity accuracy at ±3%. These values highlight the precision of the experimental setup while accounting for potential errors in measurements. Over the study period, sensor accuracy remained consistent despite fluctuating environmental conditions. The results offer a confidence interval for key parameters, reinforcing the robustness of the study. This uncertainty analysis assures the validity of the drying performance data, enabling more accurate conclusions about the solar dryer's efficiency. Uncertainty analysis with error bar can be seen in the Figure 5 according to the average monthly moisture removal rate (MMR) with the Table 6.

Table 6: Measurement Uncertainty for Key Parameters.

Parameter	Measurement Range	Accuracy	Uncertainty (%)
Temperature (°C)	25 - 60	±1.0	±1.2
Relative Humidity (%)	30 - 70	±2.0	±3.0
Moisture Removal Rate (g/h)	150 - 210	±5.0	±2.5
Air Velocity (m/s)	0.05 - 1.0	±0.02	±2.0

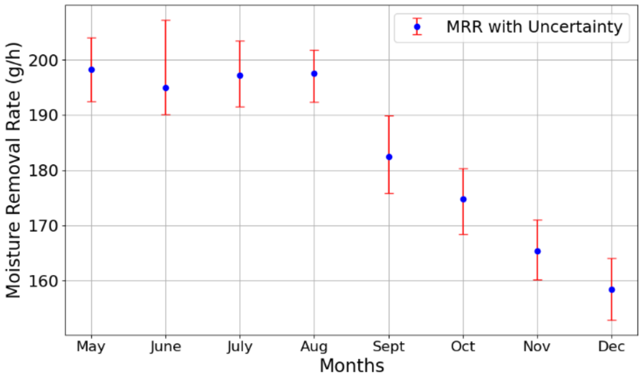

Figure 4. Uncertainty Analysis of Moisture Removal Rate (MRR).

4.5 Cost Analysis

The economic feasibility of the hybrid solar dryer is evaluated by comparing its initial investment, operational costs, and energy savings against conventional and indirect solar dryers. Although the initial installation cost of the hybrid solar dryer is higher, it offers significant savings over time due to lower operational costs, especially in areas with abundant sunlight [26].

Table 7: Comparison of cost parameters between hybrid and conventional solar dryers.

Cost Parameter	Hybrid Solar Dryer	Conventional Solar Dryer	Indirect Solar Dryer
Initial Investment (USD)	2,500	1,200	2,000
Operational Cost (per month)	40	90	70
Energy Savings (per month)	50	20	30
Maintenance Cost (per year)	120	200	150
Drying Time Reduction (%)	38%	N/A	N/A

Based on experimental results, the hybrid system provides enhanced efficiency, reducing drying time by 38% compared to traditional solar drying methods, resulting in lower energy consumption for extended drying periods. Below is the cost breakdown for all three systems, based on average data for such systems in agricultural applications [27, 28].

4.6 Discussion

The hybrid solar dryer demonstrated significant advantages over traditional solar drying methods in terms of moisture removal rates (MRR). Throughout the months, the average MRR ranged from 188.428 g/h to 207.232 g/h, surpassing the performance of conventional solar dryers, which typically exhibit MRR values between 150 g/h and 180 g/h. The hybrid design, integrating solar energy with enhanced airflow and thermal efficiency, maintained optimal drying conditions even under varying climatic conditions. While the dryer's performance showed slight fluctuations in energy consumption and drying efficiency, the overall drying process remained highly effective, especially during peak sunlight hours. Future advancements in dryer design, such as incorporating particulate filters and optimizing operational parameters, could further enhance drying efficiency and product quality.

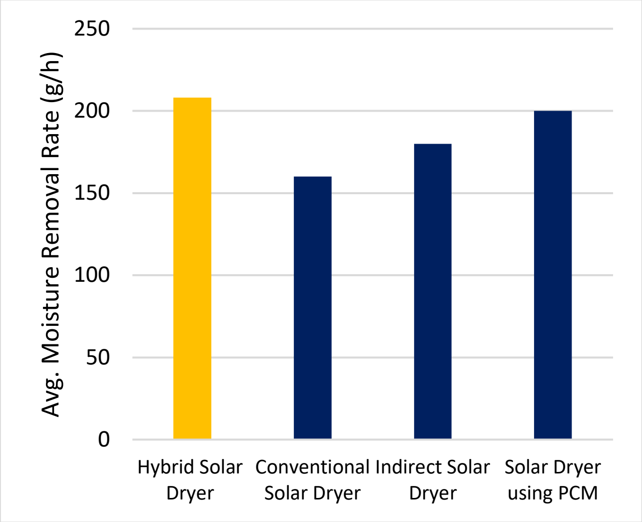

Figure 5. Comparison of hybrid solar dryer with the other traditional solar dryers.

Moreover, while other dryers may require extended drying times, our approach yields high-quality dried products in a shorter duration, which is critical for preserving nutrient content and preventing spoilage. We have compared the moisture removal rate of our hybrid solar dryer with previous techniques [29]. Figure 6 illustrates the comparison of Average Moisture Removal Rate (MMR) for Various Solar Drying Techniques [30, 31]. This comparison highlights the advantages of our hybrid solar dryer in terms of efficiency, effectiveness, and product quality, suggesting its potential for broader applications in agricultural processing and food preservation.

For our dryer, the air used in the dryer was ambient with a relative humidity range of 33.1% to 67.3%. Filtering was not employed, as the environmental conditions were monitored to remain within acceptable levels for drying efficiency. Future iterations may incorporate particulate filters to enhance product quality.

Lifecycle Environmental Footprint: The lifecycle environmental footprint of the hybrid solar dryer, encompassing the manufacturing, operational phase, and end-of-life disposal, is crucial in evaluating its sustainability. The following analysis outlines the environmental impact based on realistic industry data.

The production of solar panels and energy-efficient systems typically has a moderate carbon footprint. According to studies, the production of one kilogram of solar panel material generates approximately 0.2 kg of CO_2 [32, 33]. The material and component manufacturing for the hybrid dryer (solar panels, PCM, energy-efficient components) is considered to have an embodied carbon of approximately 50 kg CO_2. This is a one-time impact during the manufacturing phase.

The hybrid solar dryer operates primarily on solar energy, which significantly reduces operational carbon emissions. According to the U.S. Environmental Protection Agency (EPA), the average grid electricity emits about 0.4 kg CO_2 per kWh. A conventional electric dryer could consume around 1.5 kWh/day during the drying season (approximately 180 days of use per year). In contrast, the hybrid solar dryer, relying mostly on solar energy, has a reduced grid energy requirement, consuming only 0.2 kWh/day from the grid due to its integrated energy-efficient components. This results in a substantial reduction in carbon emissions. Assuming that the dryer operates for 180 days, this reduction can be quantified [34].

At the end of its lifecycle, the system components are recyclable. Solar panels have a recycling rate of about 80% for their materials, and metal parts like copper and aluminum are 90% recyclable. The disposal of the system, therefore, generates minimal waste, and the environmental impact during disposal is low compared to traditional drying technologies that may involve non-recyclable materials [35, 36].

Carbon Footprint Estimation: The operational carbon footprint of the hybrid system is estimated as follows:

Conventional Dryer: Assuming a conventional electric dryer consumes 270 kWh/year (1.5 kWh/day for 180 days) and emits approximately 0.4 kg CO_2/kWh, the annual carbon footprint of a conventional dryer is approximately [37]:

$$270kWh\ /\ year \times 0.4kg\ \ CO^2\ /\ kWh = 108kg\ CO^2/year$$

Hybrid Solar Dryer: The hybrid dryer uses 36 kWh/year from the grid (0.2 kWh/day for 180 days). Its carbon footprint is therefore [38]:

$$36kWh\ /\ year \times 0.4kg\ \ CO^2\ /\ kWh = 14.4kg\ CO^2/year$$

For Carbon Savings, the hybrid system saves approximately [39]:

$$108\,kg\ CO^2/year - 14.4\,kg\ CO^2/year = 93.6\,kg\ CO^2/year$$

Comparison with Conventional Drying Methods: In contrast to the hybrid solar dryer, traditional dryers powered by electricity or fossil fuels result in higher carbon emissions, energy consumption, and environmental impact. Conventional dryers have a carbon footprint of approximately 108 kg CO_2 per year, whereas the hybrid dryer's operational carbon footprint is much lower, at 14.4 kg CO_2 per year, highlighting the significant environmental advantage of the hybrid system shown in Table 8 [40].

Table 8: Comparison of lifecycle environmental footprint for hybrid and conventional solar dryers.

Environmental Impact	Hybrid Solar Dryer	Conventional Solar Dryer	Indirect Solar Dryer
Carbon Footprint (kg CO_2)	14.4	108	90
Energy Consumption (kWh/year)	36	270	230
Water Usage (liters/year)	50	150	120
Recyclability (percentage)	90%	70%	80%

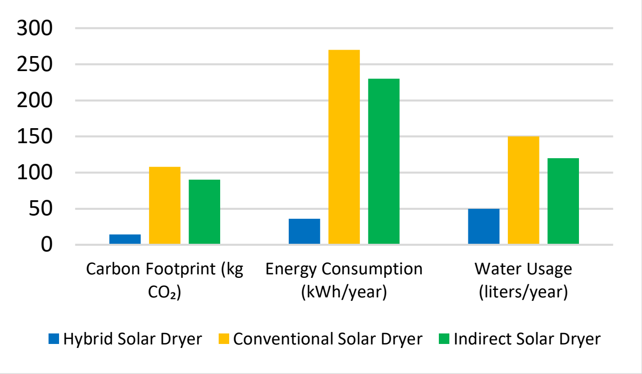

Figure 6. Lifecycle Environmental Footprint Comparison.

The environmental benefits of the hybrid solar dryer compared to conventional and indirect solar dryers is shown in the Figure 7. The hybrid dryer demonstrates a significantly lower carbon footprint, reduced energy consumption, and less water usage, confirming its superiority in terms of sustainability and environmental impact.

5. Conclusion

In conclusion, the experimental evaluation of the hybrid solar dryer over the months from May to December 2024 reveals promising results, with a clear improvement in the average moisture removal rate (MRR) for potato slices when compared to conventional drying methods. The hybrid dryer achieved an average MRR of 182.8 g/hour across the eight months, with the highest performance recorded in May (198.3 g/h) and the lowest in December (158.4 g/h). This system demonstrated consistent efficiency despite fluctuations in climatic conditions. Notably, the average MRR was higher than that of traditional direct and indirect solar dryers, reflecting the hybrid system's superior temperature regulation and energy optimization. The uncertainty analysis revealed an average uncertainty of ±2.5% for MRR, further confirming the reliability of the results. The hybrid system's performance, especially in off-sunshine hours, provides a sustainable solution for food preservation, offering reduced drying times, enhanced product quality, and energy-efficient operation. The results highlight the potential of this technology in contributing to improved food security and reduced agricultural waste. Future research may focus on optimizing the system further and expanding its applicability across different regions and climatic conditions.

Nomenclature

A: *Area (m^2)*
E: *Drying Efficiency (%)*
I: *Current (A)*
k: *Thermal Conductivity ($W / m \cdot K$)*
M: *Moisture Content (%)*
P: *Power (W)*
Q: *Heat Flux (W/m^2)*
RH: *Relative Humidity (%)*
T: *Temperature (°C)*
t: *Time (h)*
ΔT: *Temperature Difference (°C or K)**
Δt: *Time Interval (s)*
V: *Voltage (V)*
η: *Efficiency (%)*

References:

[1] S. Pandey, A. Kumar, and A. Sharma, "Sustainable solar drying: Recent advances in materials, innovative designs, mathematical modeling, and energy storage solutions," *Energy*, vol. 308, Nov. 2024, Art. no. 132725, doi: 10.1016/j.energy.2024.132725.

[2] L. Tang *et al*, "Drying hot red chilies: A comparative study of solar-gas-fired, tunnel, and conventional dryers," *Processes*, vol. 12, no. 10, p. 2104, Sep. 2024, doi: 10.3390/pr12102104.

[3] M. Das and E. K. Akpinar, "Investigation of the effects of solar tracking system on performance of the solar air dryer," *Renewable Energy*, vol. 167, pp. 907–916, Apr. 2021, doi: 10.1016/j.renene.2020.12.010.

[4] X. Li, M. Liu, L. Duanmu, and Y. Ji, "The optimization of solar heating system with seasonal storage based on a real project," *Procedia Engineering*, vol. 121, pp. 1341–1348, Oct. 2015, doi: 10.1016/j.proeng.2015.09.017.

[5] A. Lingayat, V. P. Chandramohan, and V. R. K. Raju, "Design, development and performance of indirect type solar dryer for banana drying," *Energy Procedia*, vol. 109, pp. 409–416, Mar. 2017, doi: 10.1016/j.egypro.2017.03.041.

[6] D. Wang, J. Liu, Y. Liu, Y. Wang, B. Li, and J. Liu, "Evaluation of the performance of an improved solar air heater with 'S' shaped ribs with gap," *Solar Energy*, vol. 195, pp. 89–101, Jan. 2019, doi: 10.1016/j.solener.2019.11.034.

[7] A. Amer, A. Ibrahim, A. Shahin, I. Elsebaee, R. Saad, M. F. Hassan, and Z. Hassan, "Performance evaluation of an automated hybrid solar system dryer for drying some aromatic herbs," *Drying Technology*, vol. 42, no. 4, pp. 728–747, Jan. 2024, doi: 10.1080/07373937.2024.2308607.

[8] M. A. Kherrafi, A. Benseddik, R. Saim, A. Bouregueba, A. Badji, C. Nettari, and I. Hasrane, "Advancements in solar drying technologies: Design variations, hybrid systems, storage materials and numerical analysis: A review," *Solar Energy*, vol. 270, Mar. 2024, Art. no. 112383, doi: 10.1016/j.solener.2024.112383.

[9] N. Kalita, P. Muthukumar, and A. Dalal, "Performance investigation of a hybrid solar dryer with electric and biogas backup air heaters for chilli drying," *Thermal Science and Engineering Progress*, vol. 52, Jul. 2024, Art. no. 102646, doi: 10.1016/j.tsep.2024.102646.

[10] C. K. Saha, N. K. Roy, J. Khatun, N. Tasnim, and M.S. Alam, "Solar hybrid dryers for fruits, vegetables, and fish: A comprehensive review on constructional features and techno-economic-environmental analysis," *Sustainable Energy Technologies and Assessments*, vol. 68, Aug. 2024, Art. no. 103878, doi: 10.1016/j.seta.2024.103878.

[11] D. D. Behera, R.C. Mohanty, and A.M. Mohanty, “Experimental investigation of a hybrid solar dryer for vegetable drying with and without phase change material,” *J. Braz. Soc. Mech. Sci. Eng.*, vol. 46, p. 303, Apr. 2024, doi: 10.1007/s40430-024-04876-0.

[12] M. Lehmad, N. Hidra, P. Lhomme, S. Mghazli, Y. EL Hachimi, and N. Abdenouri, “Environmental, economic and quality assessment of hybrid solar-electric drying of black soldier fly (Hermetia illucens) larvae,” *Renewable Energy*, vol. 226, May. 2024, Art. no. 120401, doi: 10.1016/j.renene.2024.120401.

[13] K.M. Mahajan, V.H. Patil, and T.A. Koli, "Design analysis of an innovative solar biomass hybrid dryer for drying turmeric," *Interactions*, vol. 245, p. 145, July 2024, doi: 10.1007/s10751-024-01965-3.

[14] L. Kumar and O. Prakash, "Optimal simulation approach for tomato flakes drying in hybrid solar dryer," *Energy Sources, Part A: Recovery, Utilization, and Environmental Effects*, vol. 46, no. 1, pp. 5867–5887, Apr. 2024, doi: 10.1080/15567036.2024.2333983.

[15] R. Pawar, S. Santara, A. Sircar, *et al.*, “Design and development of hybrid solar–biomass drying system: An innovative approach,” *MRS Energy & Sustainability*, vol. 11, pp. 409–433, Apr. 2024, doi: 10.1557/s43581-024-00083-5.

[16] M. Yazici and R. Kose, “Energy, exergy and economic investigation of novel hybrid dryer, indirect solar dryer and traditional shade drying,” *Thermal Science and Engineering Progress*, vol. 49, Mar. 2024, Art. no. 102502, doi: 10.1016/j.tsep.2024.102502.

[17] G. Yuan, L. Hong, X. Li, L. Xu, W. Tang, and Z. Wang, “Experimental investigation of a solar dryer system for drying carpet,” *Energy Procedia*, vol. 70, pp. 626–633, May 2015, doi: 10.1016/j.egypro.2015.02.170.

[18] R.S. Gill, S. Singh, and P.P. Singh, “Low cost solar air heater,” *Energy Conversion and Management*, vol. 57, pp. 131–142, May. 2012, doi: 10.1016/j.enconman.2011.12.019.

[19] V.P. Katekar and S.S. Deshmukh, “A review of the use of phase change materials on performance of solar stills,” *Journal of Energy Storage*, vol. 30, Aug. 2020, Art. no. 101398, doi: 10.1016/j.est.2020.101398.

[20] S.M. Salih, J.M. Jalil, and S.E. Najim, “Double-Pass Solar Air Heater (DP-SAH) utilizing Latent Thermal Energy Storage (LTES),” *IOP Conference Series: Materials Science and Engineering*, vol. 518, no. 3, May. 2019, Art. no. 032038, doi: 10.1088/1757-899X/518/3/032038.

[21] S. Haldorai, S. Gurusamy, and M. Pradhapraj, “A review on thermal energy storage systems in solar air heaters,” *International Journal of Energy Research*, vol. 43, no. 12, pp. 6061–6077, Apr. 2019, doi: 10.1002/er.4379.

[22] W. P. Missana, E. Park, and T. T. Kivevele, “Thermal performance analysis of solar dryer integrated with heat energy storage system and a low-cost parabolic solar dish concentrator for food preservation,” *Journal of Energy*, vol. 2020, Jul. 2020, Art. no. 9205283, doi: 10.1155/2020/9205283.

[23] O. Ojike and W. I. Okonkwo, “Study of a passive solar air heater using palm oil and paraffin as storage media,” *Case Stud. Therm. Eng.*, vol. 14, Sep. 2019, Art. no. 100454, doi: 10.1016/j.csite.2019.100454.

[24] D. K. Yadav, S. Malakar, V. K. Arora, et al., “Evacuated Tube Solar Collector-Based Drying System: Analytical Modeling, Influencing Factors, and Recent Progress in Drying of Agri-Commodities,” *Food Eng. Rev.*, vol. 16, pp. 567–594, Dec. 2024, doi: 10.1007/s12393-024-09382-6.

[25] M. A. Eltawil, M. M. Azam, and A. O. Alghannam, “Solar PV powered mixed-mode tunnel dryer for drying potato chips,” *Renewable Energy*, vol. 116, Part A, pp. 594–605, Feb. 2018, doi: 10.1016/j.renene.2017.10.007.

[26] S. Chouicha, A. Boubekri, D. Mennouche, and M. H. Berrbeuh, “Solar drying of sliced potatoes: An experimental investigation,” *Energy Procedia*, vol. 36, pp. 1276–1285, Aug. 2013, doi: 10.1016/j.egypro.2013.07.144.

[27] P. P. Tripathy and S. Kumar, “Influence of sample geometry and rehydration temperature on quality attributes of potato dried under open sun and mixed-mode solar drying,” *Int. J. Green Energy*, vol. 6, no. 2, pp. 143–156, Apr. 2009, doi: 10.1080/15435070902784863.

[28] A. Djebli, S. Hanini, O. Badaoui, B. Haddad, and A. Benhamou, “Modeling and comparative analysis of solar drying behavior of potatoes,” *Renewable Energy*, vol. 145, pp. 1494–1506, Jan. 2020, doi: 10.1016/j.renene.2019.07.083.

[29] S. Kesavan, T.V. Arjunan, and S. Vijayan, “Thermodynamic analysis of a triple-pass solar dryer for drying potato slices,” *J. Therm. Anal. Calorim.*, vol. 136, pp. 159–171, Apr. 2019, doi: 10.1007/s10973-018-7747-0.

[30] M. Y. Nasri and A. Belhamri, “Effects of the climatic conditions and the shape on the drying kinetics, application to solar drying of potato-case of Maghreb's region,” *J. Clean. Prod.*, vol. 183, pp. 1241–1251, May 2018, doi: 10.1016/j.jclepro.2018.02.103.

[31] D. Aydin, S. E. Ezenwali, M. Y. Alibar, and X. Chen, “Novel modular mixed-mode dryer for enhanced solar energy utilization in agricultural crop drying applications,” *Energy Sources, Part A: Recovery, Utilization, and Environmental Effects*, vol. 43, no. 16, pp. 1958–1974, Sep. 2019, doi: 10.1080/15567036.2019.1663306.

[32] A. Fudholi, K. Sopian, M. H. Ruslan, M. A. Alghoul, and M. Y. Sulaiman, “Review of solar dryers for agricultural and marine products,” *Renewable and Sustainable Energy Reviews*, vol. 14, no. 1, pp. 1–30, Jan. 2010, doi: 10.1016/j.rser.2009.07.032.

[33] H.-H. Chen, C. E. Hernandez, and T.-C. Huang, “A study of the drying effect on lemon slices using a closed-type solar dryer,” *Solar Energy*, vol. 78, no. 1,

pp. 97–103, Jan. 2005, doi: 10.1016/j.solener.2004.06.011.

[34] P. R. Olivkar, V. P. Katekar, S. S. Deshmukh, and S. V. Palatkar, “Effect of sensible heat storage materials on the thermal performance of solar air heaters: State-of-the-art review,” *Renewable and Sustainable Energy Reviews*, vol. 157, Apr. 2022, Art. no. 112085, doi: 10.1016/j.rser.2022.112085.

[35] M. A. Eltawil, M. M. Azam, and A. O. Alghannam, “Energy analysis of hybrid solar tunnel dryer with PV system and solar collector for drying mint (MenthaViridis),” *Journal of Cleaner Production*, vol. 181, pp. 352–364, Apr. 2018, doi: 10.1016/j.jclepro.2018.01.229.

[36] G. Srinivasan, D. K. Rabha, and P. Muthukumar, “A review on solar dryers integrated with thermal energy storage units for drying agricultural and food products,” *Solar Energy*, vol. 229, pp. 22–38, Nov. 2021, doi: 10.1016/j.solener.2021.07.075.

[37] N. K. S. Gowda, R. U. Suganthi, V. Malathi, and A. Raghavendra, “Efficacy of heat treatment and sun drying of aflatoxin-contaminated feed for reducing the harmful biological effects in sheep,” *Animal Feed Sci. Technol.*, vol. 133, no. 1–2, pp. 167–175, Feb. 2007, doi: 10.1016/j.anifeedsci.2006.08.009.

[38] D. K. Rabha and P. Muthukumar, “Performance studies on a forced convection solar dryer integrated with a paraffin wax–based latent heat storage system,” *Solar Energy*, vol. 149, pp. 214–226, Jun. 2017, doi: 10.1016/j.solener.2017.04.012.

[39] E. L. Rulazi, J. Marwa, B. Kichonge, and T. Kivevele, “Development and Performance Evaluation of a Novel Solar Dryer Integrated with Thermal Energy Storage System for Drying of Agricultural Products,” *ACS Omega*, vol. 8, no. 45, pp. 43304–43317, Nov. 2023, doi: 10.1021/acsomega.3c07314.

International Journal of Thermodynamics (IJoT)
ISSN 1301-9724 / e-ISSN 2146-1511
https://dergipark.org.tr/en/pub/ijot

Vol. 28 (No. 2), pp. 089-102, 2025
doi: 10.5541/ijot.1665595

Research Article

Numerical Analysis of Bubble Formation Mechanism in Nucleate Pool Boiling

*[1]E. Koç, [1]İ. Y. Uralcan

[1] Istanbul Technical University, Department of Mechanical Engineering, Istanbul, Turkey
E-mail: *esraunver@itu.edu.tr

Received 23 March 2025, Revised 20 April 2025, Accepted 8 May 2025

Abstract

This study comprehensively investigates nucleate pool boiling by focusing on bubble formation, growth, and detachment mechanisms. A numerical analysis of saturated nucleate pool boiling of water on a heated surface, specifically emphasizing a single cavity, was conducted and compared with experimental results documented in the literature. Accurate modeling of boiling phenomena is crucial, particularly in effectively capturing the mass transfer and phase change processes between the liquid and vapor phases. The dynamic separation of these phases through a moving interface presents a significant challenge when simultaneously applying the Navier–Stokes equations to both phases, as it complicates the continuity conditions at the interface. Various numerical methods, incorporating implicit and explicit schemes, have been developed to address these challenges for two-phase flow simulations. Interface tracking techniques such as the Volume of Fluid (VOF), Level-Set, and Lattice Boltzmann methods are commonly employed. This study used Ansys Fluent software to perform a detailed boiling model analysis. Based on the findings from detailed literature reviews, the Volume of Fluid (VOF) method is considered the most suitable simulation approach for modeling pool boiling. After establishing an appropriate computational domain, a two-dimensional simulation of single bubble formation on a microscale heated surface was carried out using a custom-developed User Defined Function (UDF). The objective was to analyze the bubble's geometric characteristics and diameter evolution throughout the boiling process. The accuracy of the numerical model was evaluated by comparing simulation results with experimental observations reported in the literature, showing a high degree of agreement.CFD analyses were conducted for both a flat copper surface and a surface with a single cavity. The results showed that, due to nucleate boiling, the copper surface's superheat values were higher than those on the surface with a cavity. This indicates improved heat transfer performance on the structured surface. These findings suggest that in processes where boiling-induced heat transfer is applied, surfaces that are roughened either through etching or coating methods may yield enhanced thermal performance compared to smooth surfaces, in line with observations reported in the literature.

Keywords: *Nucleate pool boiling; bubble dynamics; two-phase simulation; VOF; UDF; CFD.*

1. Introduction

Numerical modeling is a powerful tool that complements and accelerates experimental investigations in boiling heat transfer. This study numerically examines bubble formation, growth, and detachment within a single cavity during saturated nucleate pool boiling on a heated surface. The simulation results are compared with experimental data to validate the numerical approach. Boiling-induced phase change at the heated surface results in substantial heat flux, making it a critical process in thermal systems. Although several semi-empirical models have been developed to describe the underlying physical mechanisms of boiling, many aspects remain inadequately understood, limiting their applicability to specific conditions.

Boiling heat transfer is widely utilized across various industries due to its capacity to achieve high heat transfer rates with relatively low temperature differences. Pool Boiling Heat Transfer (PBHT) is critical in multiple industrial applications due to its high heat transfer efficiency. These include energy systems, electronics cooling, nuclear reactors, and waste heat recovery units. The morphological characteristics and wettability of heating surfaces directly affect the efficiency of such systems. In recent years, research on surface modification to enhance boiling performance has gained considerable momentum [1]. Over the years, numerous experimental and computational studies have been conducted to unravel the complex nature of boiling phenomena at microscopic and macroscopic scales. These efforts have focused on fundamental processes such as nucleation, bubble growth and collapse, oscillation, detachment, and interactions among adjacent bubbles. Recent efforts have focused on enhancing pool boiling heat transfer by modifying surface structures and using advanced working fluids [2]. Enhancing nucleate pool boiling is crucial for improving thermal system efficiency, and one promising approach involves using nanofluids, base fluids enhanced with nanoparticles to improve thermal conductivity and boiling performance [3].

A central theme in boiling research is the detailed analysis of the complete life cycle of individual vapor bubbles and their interactions, as these significantly influence overall heat transfer performance. In particular,

---

*Corresponding Author

bubble coalescence has been identified as a significant factor affecting fluid motion and thermal transport during pool boiling. The merging of bubbles promotes the evaporation of the liquid layer entrapped between their bases, thereby enhancing heat transfer [4], [5].

Despite extensive research, the physical mechanisms governing boiling have not yet been fully elucidated, and a comprehensive theoretical model has yet to be developed. For theoretical approaches, both analytical and numerical, to be reliable, these mechanisms must be clearly defined and accurately represented.

2. Literature Review

Boiling is the evaporation process at the solid–liquid interface [6]. It is initiated when the temperature of the heated surface (T_w) exceeds the saturation temperature (T_{sat}) of the liquid at a given pressure. Newton's law of cooling commonly expresses the heat flux per unit area during boiling as the following equation [6]:

$$q^{''} = h(T_w - T_{sat}) = h\Delta T_e \tag{1}$$

Where $q^{''}$ is the heat flux, h is the convective heat transfer coefficient, and ΔT_e is the excess temperature or superheat, representing the temperature difference between the heated surface and the saturated liquid. The boiling process encompasses several fundamental mechanisms, including nucleation, bubble growth, coalescence, and detachment, which significantly influence heat transfer performance.

Hsu [7] contributed to understanding these mechanisms by identifying four distinct stages in the bubble emission cycle during nucleate boiling. In the first stage, a vapor bubble initiates growth at a nucleation site due to localized superheating, overcoming surface tension forces that initially inhibit phase change. This is followed by forming a microlayer- a thin liquid film beneath the growing bubble-critical in enhancing heat transfer through rapid evaporation. As the bubble grows, surface tension governs its shape while buoyancy drives its upward movement. Finally, bubble departure occurs when the buoyant force exceeds the adhesive forces anchoring the bubble to the surface, determining its detachment size and concluding the growth cycle.

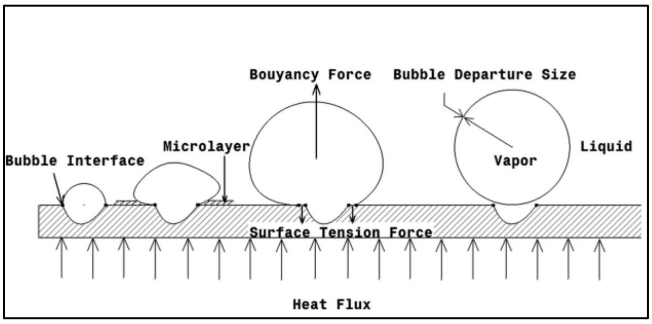

Figure 1. Stages of bubble formation and growth [8].

These sequential stages define the bubble life cycle in nucleate boiling and serve as a foundational framework for analyzing heat transfer dynamics in such systems. Figure 1 illustrates the stages of bubble formation and growth, depicting the progression from initial nucleation to final bubble detachment, as detailed [8].

According to Kenning [9], the bubble detaches from the heated surface following the growth phase, disrupting the thermal boundary layer and allowing cooler liquid from the surrounding bulk to replenish the vacated space. Once the thermal boundary layer recovers, a new nucleation cycle is initiated. The time required for the thermal boundary layer to re-establish itself is called the *holding time*.

Paruya et al. [10] developed a model that incorporates the effects of the microlayer, utilizing the Young–Laplace equation for both low and high superheat conditions. Their model was compared with Computational Fluid Dynamics (CFD) results from existing literature and their experimental data. The comparison demonstrated strong agreement, indicating that the proposed model accurately captures the bubble growth and detachment dynamics.

Petrović et al. [11] introduced the Grid-Resolved Wall Boiling Model (GRWBM) as an enhancement over traditional CFD methods for simulating nucleate boiling. In contrast to the commonly used Subgrid Wall Boiling Model (SWBM), GRWBM explicitly differentiates between bubble growth sites and the remaining heated wall surface during conjugate heat transfer to the liquid. Validation against detailed experimental datasets showed that GRWBM offers improved predictions under high heat flux conditions, particularly in capturing transient wall temperature fluctuations, average wall superheat, void fraction distribution along the pool height, and the swelling behavior of the two-phase mixture.

Iyer et al. [12] proposed a comprehensive pool boiling model encompassing the entire bubble life cycle from nucleation to detachment. The model comprises three interrelated components: heat transfer, force acting on bubbles, and evolution of bubble shape. A novel feature of this approach is the representation of bubbles as truncated spheres atop conical bottlenecks. Validation through CFD simulations and experimental observations confirmed the model's reliability, with good agreement observed regarding bubble lift-off time, wall temperature, bubble morphology, and microlayer thickness, as reported in existing literature.

Mahmoud et al. [13] conducted an experimental investigation to measure the bubble growth rate during saturated pool boiling of deionized water on a smooth copper surface at atmospheric pressure. A smooth surface was intentionally selected to minimize uncertainties arising from surface microstructure effects on bubble dynamics. The measurements were restricted to the isolated bubble regime, and comparisons with existing bubble growth models revealed that the bubble growth rate and exit diameter increased with rising wall superheat.

In the Al-Nagdy et al. [1] study, microchannels with widths ranging from 200 to 1000 µm were fabricated on stainless steel surfaces using laser processing and tested under heat fluxes between 10 and 150 kW/m². Results showed that narrower microchannels notably enhanced the heat transfer coefficient (HTC), with a maximum improvement of 94.3% at 200 µm width. Response Surface Methodology (RSM) was employed to optimize the system parameters, identifying an optimal HTC of 43.93 kW/m²K at a 217 µm channel width and 146 kW/m² heat flux. These findings demonstrate the effectiveness of laser-textured surfaces and statistical modeling in improving nucleate pool boiling performance.

Eid et al.'s study [2] investigates the effects of laser-fabricated micro-cavities, cylindrical, cubic, and pentagonal, on the heat transfer performance of brass heating surfaces. Furthermore, the impact of aluminum oxide (Al_2O_3) nanoparticles suspended in water is analyzed to evaluate combined enhancement techniques. Experimental results demonstrate that geometric cavity design significantly improves heat transfer coefficients (HTC), with pentagonal cavities achieving up to 123.4% enhancement in pure water and 140.5% in nanofluid at low concentrations. These findings confirm that surface structuring and nanofluid additives boost nucleate boiling performance.

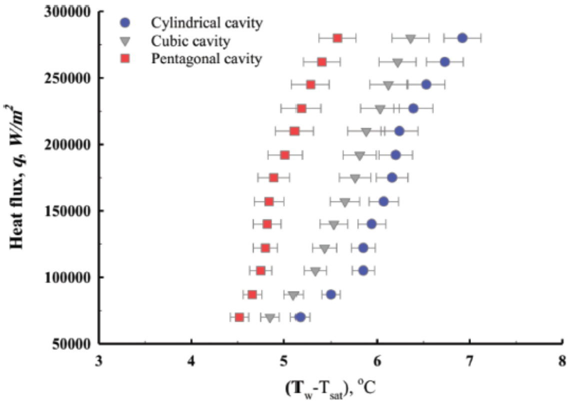

Figure 2. Pool boiling curve of pure water for different structured surfaces [2].

Figure 2 illustrates the variation of wall superheat temperature as a function of the applied heat flux for different micro-cavity geometries. In this context, the heat flux is calculated based on each micro-structured heating surface's projected (planar) area. Wall superheat, denoted as the temperature difference between the actual surface temperature at the top of the micro-cavity and the saturation temperature of water under atmospheric pressure, is a key parameter in evaluating boiling performance. A noticeable leftward shift in the boiling curves for the modified surfaces indicates a substantial reduction in wall superheat, which directly correlates with improved boiling heat transfer characteristics. Specifically, the cylindrical, cubic, and pentagonal micro-cavity surfaces exhibited reductions in wall superheat of 45.4%, 48.5%, and 55.2%, respectively, compared to the smooth (mirror-finished) reference surface. These reductions confirm that modifying the surface geometry with precise micro-cavities can significantly enhance nucleation activity and reduce the thermal resistance at the liquid–solids interface, thereby promoting more efficient phase change heat transfer [2].

Eid et al.'s study [3] focuses on the influence of aluminum oxide (Al_2O_3) nanoparticles suspended in refrigerant R-134a on pool boiling heat transfer. Experiments were conducted using a stainless-steel cylindrical heater with varying surface roughness, nano concentrations, and operating pressures. The results demonstrate that incorporating Al_2O_3 nanoparticles significantly enhances the heat transfer coefficient (HTC), particularly at lower concentrations and higher surface roughness levels. The maximum HTC enhancement reached 167.7%, while higher nanoparticle concentrations led to a performance decline due to surface deposition effects. An empirical correlation was also proposed to predict HTC based on key parameters, including pressure, heat flux, particle concentration, and surface texture. These findings highlight the effectiveness of nanofluids and surface engineering in advancing boiling heat transfer applications [3].

Alsaati et al. [14] developed a mechanical model to predict the Critical Heat Flux (CHF) during narrow-range boiling in a separate study. The model is based on the irreversible growth of the dry spot, driven by the interplay of vapor recoil, surface tension, and hydrostatic forces. CHF initiation occurs when the vapor recoil force from intense evaporation counterbalances the combined effects of surface tension and hydrostatic pressure, leading to sustained dry spot expansion. The model, called the predictive trapped CHF model, incorporates parameters such as confinement geometry, operating temperatures, and CHF characteristics. Although it does not strictly align with traditional CHF conditions in near-evaporation cooling gaps, it effectively estimates the threshold range for pool boiling CHF, offering a practical tool for prediction and control.

Qiu et al. [15] investigated microlayer evaporation in nucleate pool boiling under varying pressure conditions. They developed an analytical method for estimating initial microlayer thickness and validated it through experiments at different pressures. For cases involving multiple bubbles, a nucleation site tracking approach was applied. The complete multi-bubble evaporation model was compared with high-pressure pool boiling experiments, yielding strong agreement with experimental data. Their findings underscore the crucial role of the microlayer in vapor generation and reveal that increasing pressure significantly reduces microlayer evaporation, highlighting the sensitivity of interfacial phase change to operating conditions.

Kumar et al. [16] introduced a physics-based model to improve predictions of bubble departure diameter in nucleate pool boiling. The model employs a force balance analysis, accounting for buoyancy, surface tension, and pressure differential forces. A new coefficient specific to water is introduced, enabling more accurate estimation of departure diameter based on the Jacob number and contact angle. The model was validated against five experimental datasets and compared with five existing models. Results demonstrated superior predictive accuracy, with maximum and minimum average absolute deviations of 30% and 14%, respectively, and 90% of literature data falling within a ±25% error margin.

Kim and Kim [17] proposed a mechanistic nucleate pool boiling heat transfer model incorporating the influence of bubble coalescence. They analyzed transient temperature and heat flux distributions across the boiling surface using high-speed infrared imaging, categorizing surface regions into natural convection, quenching, and evaporation zones. While bubble coalescence was found not to alter heat flux values significantly, it did affect the area fraction of each region. A new heat flux correlation was formulated and validated using experimental data for water and FC-72. The model demonstrated improved predictive accuracy, particularly in capturing the heat flux change rate with wall superheat, reducing error by 94% compared to models that neglect coalescence effects.

Yuan et al. [18] conducted a numerical investigation utilizing the phase-change Lattice Boltzmann Method (LBM) to simulate the spontaneous nucleation and interaction of individual vapor bubbles, with the model incorporating an equation of state to capture phase change phenomena. As stated in their study, the simulation setup involved two identical micro-heaters with a specified wall superheat of 5 °C and a separation distance of 28 lattice units. This configuration enabled the generation of two identical bubbles and allowed for a detailed examination of their growth and coalescence dynamics. The results were compared against experimental observations reported by

Mukherjee and Dhir [19], providing a means of qualitative validation.

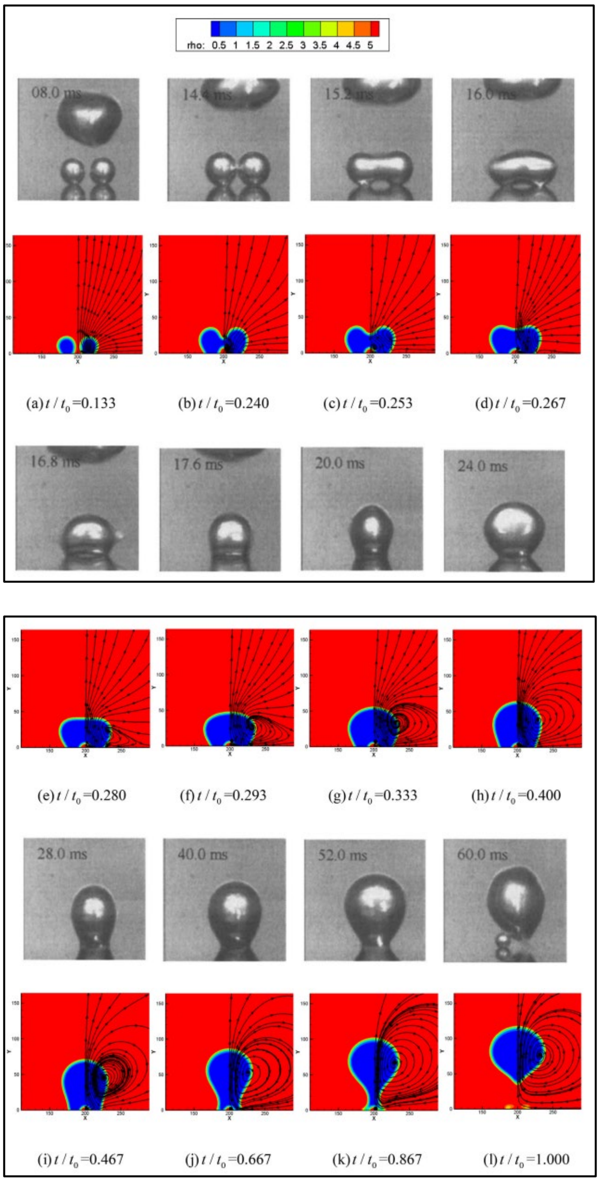

(a) t/t_0=0.133 (b) t/t_0=0.240 (c) t/t_0=0.253 (d) t/t_0=0.267

(e) t/t_0=0.280 (f) t/t_0=0.293 (g) t/t_0=0.333 (h) t/t_0=0.400

(i) t/t_0=0.467 (j) t/t_0=0.667 (k) t/t_0=0.867 (l) t/t_0=1.000

Figure 3. Numerical simulation results and corresponding experimental observations of a representative ebullition cycle involving bubble coalescence during nucleate boiling at a wall superheat of 5 °C [19].

The computational domain was designed to be symmetrical, and the right half of the flow field was visualized over the simulated density distribution. Initially, bubble nuclei emerged at the centers of the two micro-heaters and underwent gradual growth (Figure 3a). As the bubbles expanded and their interfaces came into contact, coalescence was initiated (Figure 3b). This contact led to the rupture of the interface and the formation of a vapor bridge connecting the two bubbles (Figure 3c). A supplementary microlayer was observed forming beneath this vapor bridge (Figure 3c and 3d), which significantly enhanced local heat transfer at the wall due to its relatively lower temperature.

The presence of this microlayer led to the generation of strong vortices beneath the bubble structure. Additionally, surface tension forces acting on the vapor bridge pulled the two bubbles together, eventually resulting in a single, merged bubble (Figure 3e). At this stage, the supplementary microlayer was seen to be trapped within the bubble, and a pair of vortices formed symmetrically on either side. Following coalescence, the merged bubble exhibited oscillatory deformation: it first elongated vertically along the Y-direction due to inertial effects and then expanded laterally in the X-direction as surface tension took over (Figure 3f–3i). Eventually, the bubble necked and detached from the heated surface under the influence of buoyant forces (Figure 3j- 3l), with the associated vortices rising alongside it. Overall, the predicted bubble behavior closely matched experimental observations, capturing all major phases of a typical ebullition cycle involving coalescence: nucleation and individual growth, bubble coalescence, post-coalescence oscillation and expansion, and final detachment. The study notably highlighted the key roles of microlayer dynamics and vortex formation in the heat transfer and bubble departure.

In light of all these studies, simulations were conducted on a single-cavity copper plate, designed as smooth and etched surfaces under varying heat flux conditions. In this way, results regarding bubble growth rate and diameter at different heat flux levels were obtained, which can be compared with findings reported in the literature.

3. Numerical Model

The modeling process in this study is guided by a set of assumptions to simplify and accurately represent the physical phenomena involved. The system consists of two interacting phases, liquid water and water vapor, where bubble formation occurs at a conical cavity on the heated surface.

Table 1. Thermophysical properties of liquid water and vapor at 373.15 K.

Property	**Unit**	**Water**	
		Liquid	**Vapor**
Density, ρ	kg/m³	958	0.597
Specific heat, Cp	J/kg·K	4220	2030
Thermal conductivity, k	W/m·K	0.679	0.025
Viscosity, μ	Pa·s	2.77×10^{-4}	1.30×10^{-5}
Latent heat of vaporization, h_{fg}	kJ/kg	2256	
Surface tension, σ	N/m	0.059	
Saturation temperature, T_{sat}	K	373.15	
Pressure, P	MPa	1.013	

The liquid in the pool is assumed to remain at the saturation temperature throughout the boiling process, ensuring thermal equilibrium in the bulk fluid. Boiling is initiated and sustained by constant heat flux to the heated surface. These assumptions establish a controlled environment for analyzing the fundamental mechanisms of nucleate boiling, particularly the dynamics of bubble formation, growth, and departure under idealized thermal and geometric conditions.

The pool initially contains water at a temperature of 373.15 K; the thermophysical properties are given in Table 1. During the simulation, the thermophysical properties of both liquid water and water vapor, such as specific heat, thermal conductivity, and viscosity, are assumed to vary with temperature. Additionally, surface tension forces and buoyancy forces resulting from the density difference between phases are included in the model. These forces are critical for accurately representing dynamic processes such as bubble detachment from the surface and its upward motion [3].

Table 2 presents the thermophysical properties of copper, which is the solid material used in the constant heat flux boundary condition.

Table 2. Thermophysical properties of copper at 373.15 K.

Property	Unit	Copper
Density, ρ	kg/m³	8920
Specific heat, Cp	J/kg·K	385
Thermal conductivity, k	W/m·K	391

In Figure 4, the ANSYS Fluent model employed in this study is a two-dimensional axisymmetric representation of the experimental setup designed to simulate a single cavity. The computational domain comprises two distinct regions: a solid region representing copper and a fluid region representing water.

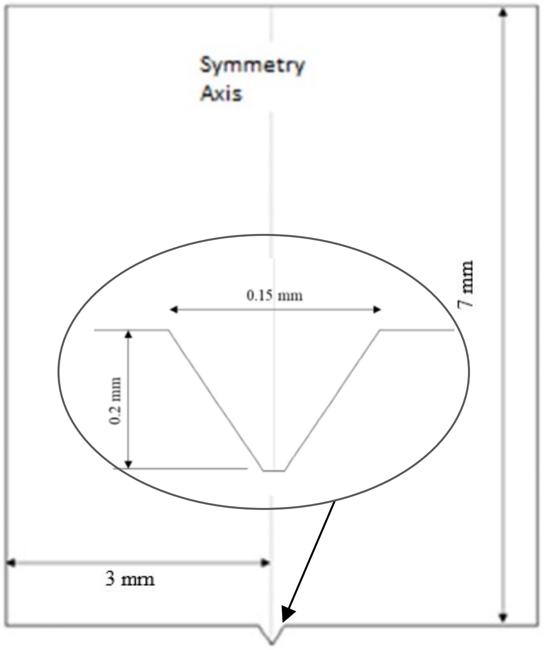

Figure 4. The geometry and dimensions of the cavity where the analyses are conducted.

Material properties corresponding to copper are assigned to the solid domain, while the thermophysical properties of water are specified for the fluid domain. A conical cavity, with a mouth diameter of 150 µm and a depth of 200 µm, is incorporated into the boiling surface to serve as the nucleation site. Bubble formation is confined to this cavity, and the complete bubble nucleation cycle encompassing growth and departure is analyzed over time to investigate the dynamics of nucleate boiling under controlled conditions.

In Figure 5a, the boundary conditions of the CFD model are given. The flow domain was modeled as axisymmetric, with the axis of symmetry selected as the centerline of the domain. An adiabatic boundary condition was applied to the sidewalls of the pool. The inlet and outlet boundary conditions were defined as constant heat flux and atmospheric pressure (pressure outlet), respectively. The mesh model of the cavity is shown in Figure 5b a cylindrical region with a diameter of 1.2 mm was defined above the cavity, and hexagonal elements with a side length of 0.025 mm were used throughout the flow domain. In regions near the cavity where all three phases coexist, the mesh was refined using hexagonal elements with a size of 0.01 mm. To reduce computational time, quadrilateral and hexagonal elements with a size of 0.05 mm were employed in the remaining areas.

In the mesh quality evaluation, highly favorable results were obtained according to various quality criteria. The Jacobian value was measured as 0.98, which is very close to the ideal value of 1, indicating a high-quality mesh structure. The aspect ratio was 1.01, also near the ideal value of 1, suggesting that the mesh cells are proportionally distributed. The orthogonal quality value was recorded at 0.994, which is considered nearly perfect and reflects that the cells are connected at almost orthogonal angles. Regarding skewness, the minimum value was found to be 1.9e-6, which is excellent, while the maximum value was 0.515, slightly above the commonly accepted threshold. However, this suggests that only a few cells exhibit minor distortion and that the mesh structure remains unaffected. Overall, the mesh is of high quality and is suitable and reliable for numerical analysis [20].

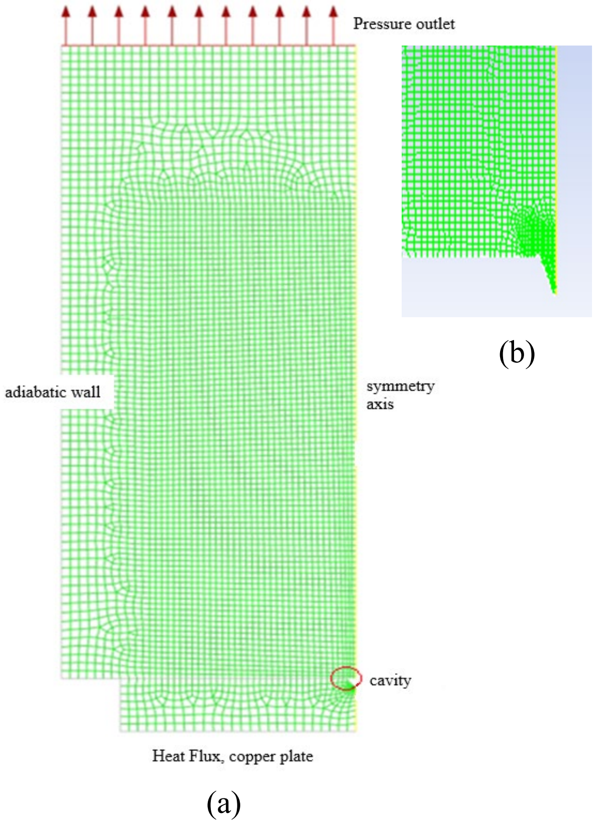

Figure 5.a) Boundary condition of the CFD model, b) Mesh model at the cavity.

In numerical modeling studies, it is essential to ensure that the results are independent of the mesh structure and consistent with experimental data to develop reliable models. Mesh independence tests are conducted by altering the number, size, and geometry of mesh elements to evaluate whether the resulting outputs fall within acceptable error margins [21].

In this study, three different mesh structures were generated by varying the number of nodes and elements, and analyses were conducted for the equivalent diameter of bubble growth. The number of nodes and cells for each mesh structure is presented in Table 3.

The equivalent diameter is a spherical diameter determined solely based on the vapor volume, independent of the actual geometry of the bubble, and is expressed by the following relation [22]:

$$D_{eq} = \left(\frac{6 \cdot V_{vapor}}{\pi}\right)^{\frac{1}{3}} \tag{2}$$

where, D_{eq} equivalent diameter of the bubble, V_{vapor} vapor volume.

Table 3. Mesh structures are used in the computational domain.

Mesh Structure	Number of Nodes	Number of Cells
1	5752	5602
2	12847	12651
3	23121	22953

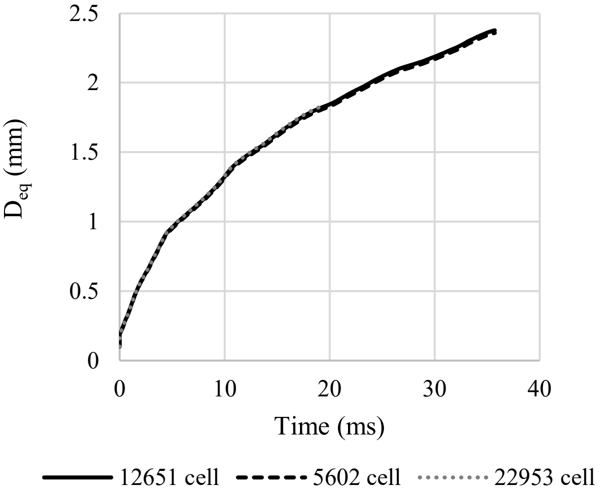

Figure 6. Mesh independence test.

Since the maximum difference in equivalent bubble growth diameters is released in Figure 6, all curves almost overlap entirely, indicating minimal variation. As shown in Table 4, the difference between the mesh configurations is less than 1%, highlighting the negligible impact of mesh size on the equivalent diameter. The simulations were continued using Mesh Structure 2 to optimize computational load and processing time.

Table 4. The % variation in the equivalent diameter of the bubble across different mesh structures.

Mesh Structure	D_{eq} (mm)	Variation (%)
12651 cells	1,825	0
5602 cells	1,811	-0,8
22953 cells	1,837	0,5

It is well established in nucleate pool boiling processes that the heat transfer mechanism is primarily governed by natural convection. In line with this, previous studies have reported that the avarage flow velocity within the system can reach approximately 0.5 m/s [22]. It can be seen in Figure 7, which presents the CFD results of the velocity distribution from the copper plate surface to the atmospheric boundary, that the flow behavior is consistent with findings from the literature.

For the accuracy and stability of numerical solutions, the Courant number (Co), a critical parameter, was set to 0.5 in this study. This value lies within a commonly accepted safe range for selecting the time step in transient simulations [24]. Considering that the minimum cell size around the cavity was 10 micrometers (10^{-5} m), the time step (Δt) was initially estimated using the following relation [6]:

$$\Delta t = \frac{Co \cdot \Delta x}{u_{max}} = \frac{0.5 \times 10^{-5}}{3.5} = 1.47 \times 10^{-6} \tag{3}$$

However, to enhance the numerical stability of the solution, the time step was increased by one order of magnitude and applied as $\Delta t = 1 \times 10^{-5}$ s. This value is consistent with those used in the literature for low Reynolds number boiling problems [24]

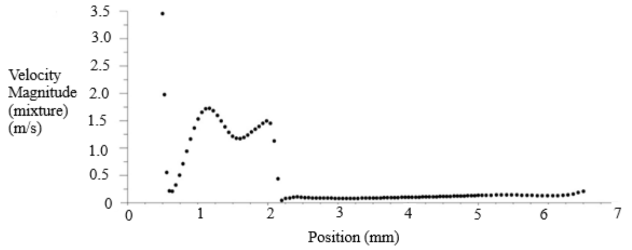

Figure 7. Velocity distribution from the copper plate surface to atmospheric pressure.

3.1. Governing Equations

The fluid flow analysis in this study is based on a series of simplifying assumptions and numerical methods designed to make the computational model both manageable and effective. Initially, the flow is assumed to be stagnant and at saturation temperature, providing a baseline for understanding the boiling dynamics. A two-dimensional axisymmetric model is employed using cylindrical coordinates, which reduces computational complexity while capturing the essential physics of the problem. The assumption of axial symmetry further streamlines the analysis by allowing focus on radial and axial components of the flow. Due to the relatively low velocities, the flow is modeled as laminar, eliminating the need to account for turbulence. The working fluids, water and vapor, are treated as Newtonian and incompressible, while their thermophysical properties are modeled as temperature-dependent to reflect realistic behavior. Surface tension effects and lift forces resulting from density gradients are also considered, enhancing the model's fidelity [21], [25].

Georgoulas and Marengo's study [26] contributes to understanding saturated pool boiling by developing and validating a diabatic CFD model based on the VOF method. This model accurately accounts for phase change due to evaporation and shows strong agreement with analytical and experimental data. It is further used to analyze the impact of key parameters on bubble growth, particularly on detachment diameter and time. The enhanced VOF interface-capturing approach is shown to be a promising and reliable tool for simulating various phase-change phenomena In light of these findings, the present study the Volume of Fluid (VOF) method is adopted for tracking the liquid–vapor interface in the two-phase flow, and a User Defined Function (UDF) is integrated to represent heat input and boundary conditions more accurately. The CLSVOF method is employed to improve interface capturing further. This approach leverages the strengths of both VOF and Level Set methods by reconstructing the interface through vectors perpendicular to it, derived from both functions. This reconstruction ensures improved mass conservation while maintaining an accurate and smooth interface representation. Although these assumptions and methods introduce certain limitations, they are essential for maintaining computational tractability and achieving meaningful, predictive insights into the boiling process.

According to Mudawar et al. [27], mass conservation for each phase is formulated by considering both the time-dependent variation and the convective transport (advection) of the phase's volume fraction. This conservation is balanced by the net mass exchange resulting from phase change processes, specifically the mass entering or leaving a computational cell. In this context, each phase's continuity is governed by fluid motion and interfacial mass transfer mechanisms such as evaporation and condensation, which directly affect the evolution of the volume fraction field. Here are the equations [27],

$$\frac{\partial \alpha_f}{\partial t} + \nabla \cdot \left(\alpha_f \overrightarrow{u_f}\right) = \frac{1}{\rho_f} \sum (\dot{m}_{gf} - \dot{m}_{fg}) \tag{4}$$

$$\frac{\partial \alpha_g}{\partial t} + \nabla \cdot \left(\alpha_g \overrightarrow{u_g}\right) = \frac{1}{\rho_g} \sum (\dot{m}_{fg} - \dot{m}_{gf}) \tag{5}$$

In this formulation, α represents the volume fraction of the phase, t denotes time, and $\vec{u}$ is the velocity vector describing fluid motion. The symbol ρ corresponds to the density of the phase, while $\dot{m}$ indicates the mass transfer rate associated with phase change processes. Specifically, $\dot{m}_{fg}$ refers to the mass transfer rate from liquid to vapor during evaporation, and $\dot{m}_{gf}$ represents the reverse process, condensation, where vapor converts back to liquid.

A distinctive feature of the CLSVOF method is its explicit incorporation of surface tension forces directly into the momentum equation, distinguishing it from the conventional VOF approach. Despite this enhancement, the CLSVOF method, similar to the VOF method, solves a single momentum equation for the entire fluid domain by treating the system as a mixture. This is achieved through effective (pseudo-mixture) fluid properties, such as density and viscosity, which are calculated based on the local volume fractions of the involved phases. The resulting momentum equation governs the flow behavior across the interface and within both phases, ensuring a unified treatment of the multiphase domain. The equation is shown below [27],

$$\frac{\partial}{\partial t}(\rho \vec{u}) + \nabla \cdot (\rho \vec{u}\, \vec{u}) = -\nabla \mathrm{P} + \nabla \cdot [\mu\, (\nabla \vec{u} + \nabla \vec{u}^T)] - \sigma \kappa \delta(\varphi) \nabla \varphi + \vec{S}_M \tag{6}$$

In this formulation, σ denotes the surface tension coefficient, κ represents the interface curvature, and φ refers to the Level-Set function used to track the interface position. The symbol P stands for pressure, μ is the dynamic viscosity, and $\vec{S}_M$ denotes the momentum source term accounting for interfacial forces such as surface tension. As the current study is conducted under zero-gravity (microgravity) conditions, the gravitational body force term is omitted from the momentum equation, simplifying the force balance on the fluid.

Similarly, the energy conservation equation employed in the CLSVOF method follows the same formulation as the conventional VOF approach. It governs the thermal transport within the multiphase system and accounts for both convection and conduction and latent heat effects due to phase change. The equation regarding effective mixture properties is expressed and ensures energy conservation across the liquid-vapor interface during evaporation and condensation processes. Here is the equation [27],

$$\frac{\partial}{\partial t}(\rho E) + \nabla \cdot \left(\vec{u}\,(\rho E + P)\right) = \nabla \cdot \left(k_{eff} \nabla \mathrm{T}\right) + S_E \tag{7}$$

where, E denotes the internal energy of the fluid, ∇T represents the temperature field, and k_{eff} is the effective thermal conductivity, which accounts for both liquid and vapor phases based on their local volume fractions. The term S_E refers to the volumetric heat source term, which incorporates the effects of phase change. Specifically, S_E is calculated as the product of the mass transfer rate due to phase change and the latent heat of vaporization, thereby capturing the energy exchange associated with evaporation and condensation processes at the phase interface.

In this study, a UDF was developed for simulations based on the CLSVOF method, aiming to perform time-dependent (transient) analyses involving evaporation, condensation, and bubble dynamics. The developed UDF was integrated into ANSYS Fluent to enhance the realistic modeling of multiphase flow and phase change processes. Each function within the UDF serves a specific purpose: Mass transfer processes between the liquid and gas phases are governed by a custom model that calculates evaporation and condensation rates based on local temperature and volume fraction data. The contact angle is dynamically updated at the end of each time step based on the computed bubble diameter and applied as a boundary condition. Critical parameters such as bubble diameter and departure diameter are also calculated and recorded in external files to facilitate post-processing and result evaluation.

4. Results and Discussion

When a vapor bubble forms on a heated surface, it initially undergoes rapid growth. This growth rate, however, gradually decreases due to the downward movement of the surrounding liquid and the thermal boundary layer that develops around the bubble interface. Once the bubble reaches its maximum diameter, its base begins to contract, leading to detachment through a process known as vapor necking. After detachment, a portion of the vapor remains adhered to the surface. This residual vapor is a nucleation site for subsequent bubbles, sustaining the boiling cycle. Significantly, this remaining vapor inhibits complete rewetting of the surface area previously occupied by the bubble, which enhances and facilitates continued nucleation.

As shown in Figure 8, Tetik [28] examined the bubble nucleation cycle under a heat flux of 30 kW/m² and a wall superheat of 5.8 °C on surfaces containing micro-scale cavities. The experiments demonstrated that the base of the bubble remains anchored at the mouth of the cavity throughout much of the growth process. As the base expands, the effective area for evaporation increases, thereby enhancing heat transfer. The adhesive forces that retain the bubble within the cavity are relatively strong, necessitating a more significant buoyant force to trigger detachment.

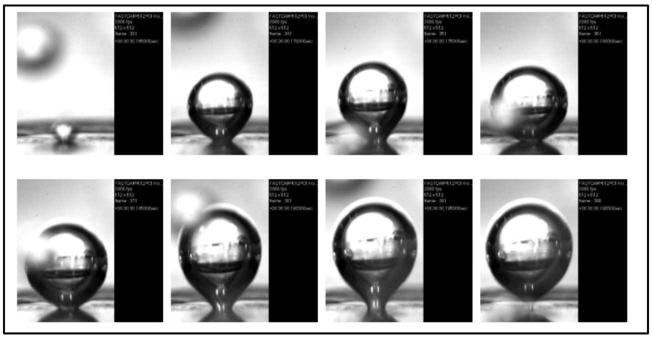

Figure 8. Bubble nucleation cycle in the cavity (q"=30 kW/m², ΔT=5.8 °C) [28].

This force requirement is only met when sufficient vapor accumulates, resulting in a larger bubble departure diameter. These findings highlight the critical role of cavity geometry and surface characteristics in governing bubble behavior and heat transfer performance during nucleate boiling.

Figure 9a illustrates the formation of bubbles in a saturated water pool subjected to a heat flux of 30 kW/m², while Figure 9b presents the corresponding temperature gradients alongside color-coded velocity vectors. The velocity vectors in Figure 9b depict the movement of liquid as it rushes into the space vacated by the detaching bubble. This inflow exerts a downward force on the bubble, suspending it temporarily and facilitating the formation of a new, smaller bubble at the nucleation site. The first bubble rises during the necking phase, consistent with the experimental images shown in Figure 8.

Throughout the simulations, the residuals were closely monitored. As the analysis is transient, achieving steady-state convergence at each time step is unnecessary. Nevertheless, for the sake of numerical accuracy and stability, it was ensured that the residuals decreased to at least the order of 1e-6 during each time step.

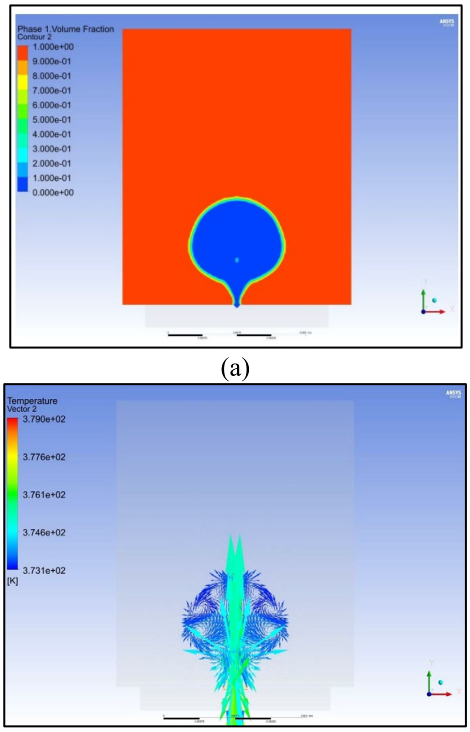

(a)

(b)

Figure 9. a) The formation of bubbles in a saturated water pool subjected to a heat flux of 30 kW/m². b) Temperature gradients with color-coded velocity vectors.

Figure 10 compares the stages of bubble formation at a heat flux of 30 kW/m², as obtained from simulations, with corresponding Tetik's experimental observations under identical conditions [28]. Within a specific heat flux range, natural surface cavities or engineered cavities of varying shapes and sizes can effectively act as nucleation sites, provided they meet the minimum nucleation radius and possess sufficient vapor-holding capacity. At elevated heat fluxes, the increasing temperature difference activates more nucleation sites, each satisfying the critical nucleation radius requirement. As a result, the density of active sites on the boiling surface rises significantly, complicating the direct observation and measurement of individual bubble dynamics. The parameter, the number of active nucleation sites per unit area of the heating surface, is defined as the *effective nucleation site density*. A CFD analysis was performed at a base heat flux of 30 kW/m² and extended to higher heat flux levels to investigate this phenomenon further. The numerical results obtained from these simulations were compared with experimental data, providing valuable insights into bubble dynamics, heat transfer performance, and the influence of heat flux on nucleation site activation.

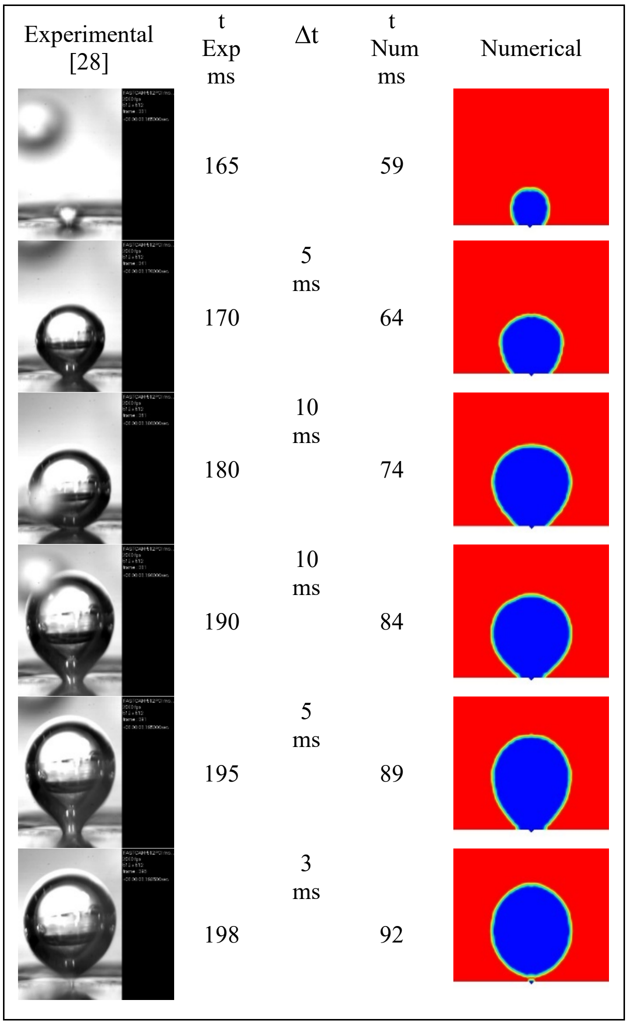

Figure 10. Bubble formation stages at a heat flux of 30 kW/m² compared with Tetik's experimental observations at the same heat flux [28].

Figure 10 presents a 33-millisecond cycle, from 165 ms to 198 ms, using images obtained from Tetik's experimental study conducted at a heat flux of 30 kW/m². It is evident from the first image that these images do not correspond to the initial bubble, as another bubble can be seen rising behind a newly forming one. Additionally, the time annotations shared alongside the experimental visuals do not represent the first bubble cycle; therefore, it is more appropriate to emphasize that the time intervals between frames are in the millisecond range. The numerical model aligned the initial simulation time with Tetik's 165-ms frame. Accordingly, the visualization of the CFD results begins at 59 ms and ends at 92 ms, completing a 33-millisecond cycle similar to that in Tetik's study. The results exhibit high similarity when CFD images are extracted at the same time intervals (5-10-10-5-5-3 ms).

A CFD analysis was performed at a base heat flux of 30 kW/m² and extended to higher heat flux levels to investigate this phenomenon further. The numerical results obtained from these simulations were compared with experimental data, providing valuable insights into bubble dynamics, heat transfer performance, and the influence of heat flux on nucleation site activation. Figure 11 presents the time evolution of vapor bubble diameter on a heated surface subjected to varying heat flux levels of 30, 60, 84, 122, and 177 kW/m². The results demonstrate that increasing heat flux accelerates bubble growth, shortens the growth duration, and prompts earlier detachment. At the highest heat flux of 177 kW/m², the bubble attains a diameter of approximately 2 mm in under 0.025 seconds before detaching. In contrast, at 30 kW/m², the bubble reaches a larger diameter of 2.1 mm but detaches much later, around 0.088 seconds. Bubble formation is relatively slow at lower heat fluxes (e.g., 30 kW/m²). In contrast, higher heat fluxes (e.g., 177 kW/m²) promote rapid vapor generation, resulting in faster bubble growth. This behavior aligns well with the literature, where it is reported that higher heat flux enhances nucleation site activation and vapor generation rate, thereby increasing the bubble departure diameter and frequency [22], [23].

These findings are consistent with the theoretical analyses presented by Kandlikar [23], who emphasized the role of surface heat flux in determining bubble dynamics and departure characteristics. Similarly, Dhir [22] highlighted that elevated heat flux significantly impacts bubble growth time, contact diameter, and overall boiling heat transfer mechanisms. The present numerical results support these conclusions, reinforcing the model's validity. This behavior is consistent with the physical expectation that higher heat flux increases local wall superheat, enhancing vapor generation rates at the nucleation site [30], [31]. The observed bubble growth trends align well with classical boiling theory and previous experimental studies. For instance, Klausner et al. [31] and Dhir [32] have shown that increased thermal input accelerates phase change, leading to more rapid bubble expansion and decreased residence time on the surface. Additionally, numerical simulations by Bhati and Paruya [33] confirm that the growth rate and the maximum bubble diameter strongly depend on the applied heat flux, particularly during the early stages of nucleate boiling. These findings validate the accuracy of the CFD model employed in the current study and confirm its ability to reproduce realistic bubble dynamics under varying thermal conditions. As the heat flux rises, vertical bubble coalescence becomes more prevalent. The increasing temperature difference leads to faster bubble growth and more significant interaction between consecutive bubbles. When the upward velocity of a newly forming bubble at a nucleation site exceeds that of the preceding bubble, the two bubbles tend to coalesce vertically.

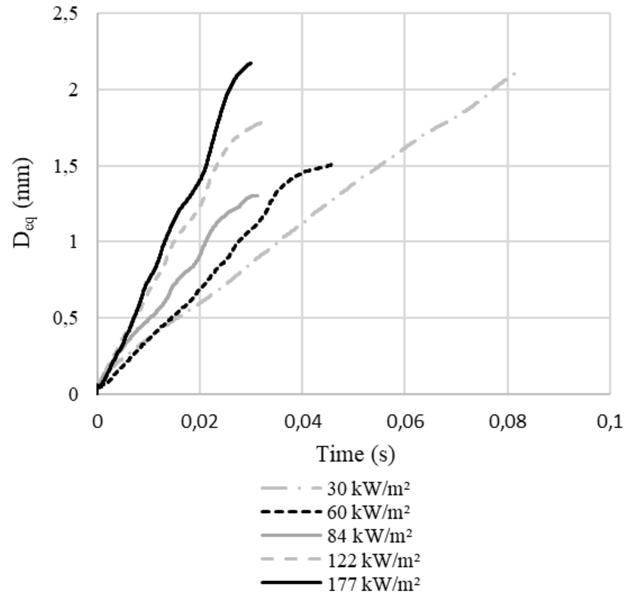

Figure 11. Bubble growth behavior under varying heat fluxes.

In such instances, the second bubble is rapidly drawn away from the surface and quickly merges with the first bubble. Although the rise velocity is relatively independent of the temperature difference, higher heat flux intensifies the vapor generation rate and promotes faster bubble expansion. Consequently, the frequency and intensity of bubble-bubble interactions increase, further influencing the boiling dynamics. As the heat flux increases, the dynamics of bubble formation during boiling undergo significant changes. An increased heat flux enhances the evaporation rate at the heating surface, leading to a higher bubble generation frequency. Initially, this results in larger bubble diameters due to the greater energy input; however, bubble size tends to decrease beyond a certain threshold. Zuber [34] demonstrated that bubbles detach more rapidly from the surface at high heat flux levels, preventing them from growing to larger sizes. Similarly, Lienhard and Dhir [35] observed that bubble diameter increases with moderate heat flux but decreases at higher values due to reduced residence time and intensified bubble interactions. Thus, the relationship between heat flux and bubble size is nonlinear bubble diameter increases at low to moderate heat fluxes but decreases when heat input becomes excessive.

As the heat flux increases, vapor bubbles coalesce in the vertical direction, strongly influenced by the rising wall superheat. The elevated temperature difference accelerates the bubble growth rate. In contrast, the dynamics of a newly forming bubble are increasingly affected by the movement of the previously detached bubble from the same nucleation site. This interaction is illustrated in Figure 12, which shows sequential images captured at a heat flux of 60 kW/m². Buyevich and Webbon [29] reported that such coalescence can form vapor columns, hindering the access of relatively cooler liquid to the surface and triggering the onset of critical heat flux.

With increasing heat flux and surface superheat, more nucleation sites become active. As the density of active nucleation sites and the frequency of bubble formation increase, interactions among neighboring bubbles become more prominent, leading to coalescence in both horizontal and vertical directions, as depicted in Figure 13.

When vapor bubbles of similar growth rates form at adjacent nucleation sites, horizontal coalescence occurs symmetrically. However, if bubbles form at different rates or with varying waiting times, they tend to merge at skewed angles. In cases where two bubbles form consecutively at the same nucleation site within a short time interval, vertical coalescence occurs. Here, the microlayer formed beneath the initially growing bubble rapidly evaporates, particularly when the first bubble remains attached to the surface. A thin liquid network layer can be observed between the bubbles, and the second bubble, forming beneath the first, quickly merges and assists in lifting the combined structure away from the surface. These observations underscore the complex interactions between bubble dynamics and cavity geometry. Within specific heat flux ranges, naturally occurring surface and engineered cavities with varying shapes and dimensions act as effective boiling sites, provided they satisfy the critical nucleation radius and possess sufficient vapor retention capability.

At elevated heat flux levels, the increase in wall superheat enhances the fulfillment of the critical nucleation radius criterion, activating more nucleation sites on the boiling surface. This proliferation of active boiling sites, or *effective boiling foci*, makes directly observing and measuring individual bubble dynamics increasingly difficult.

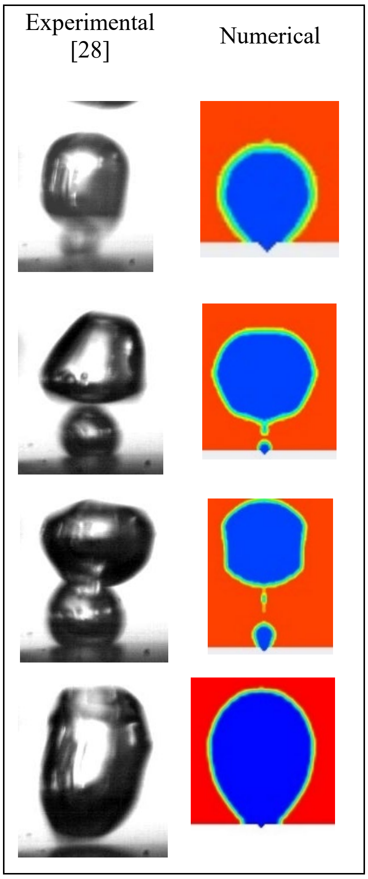

Figure 12. CFD result for 60 kW/m², mushroom-like shapes, Bubbles continuously coalescing in the vertical direction, compared to Tetik's experimental result (q"=60 kW/m²) [28].

The density of these active sites, defined as the number of nucleation cavities per unit heating surface area where vapor bubbles form and grow, is referred to as the *effective boiling focus density*. Experimental studies have demonstrated that this density is influenced by several factors, including the applied heat flux, the wall superheat, cavity geometry (such as diameter and depth), and the specific properties of the surface-fluid pair.

Figure 13. Events of bubbles merging in the vicinity of the boiling surface in horizontal, vertical, and diagonal axes [28].

Additionally, the spatial distribution and relative distances between active nucleation sites significantly affect bubble interactions, such as horizontal and vertical coalescence, which alter the overall boiling behavior and heat transfer performance.

In Figure 14, the variation of surface superheat (ΔT) as a function of heat flux (q") is presented comparatively based on both numerical modeling and Tetik's experimental data [28]. As can be seen from the figure, there is a strong agreement between the numerical and experimental results up to a heat flux of approximately 122 kW/m².

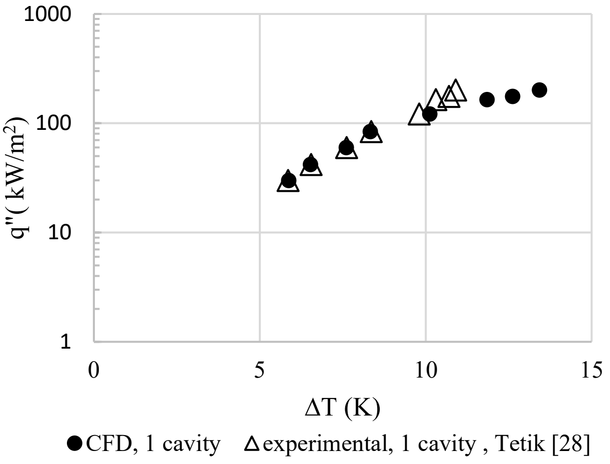

Figure 14. Heat flux-dependent surface temperatures: experimental and numerical measurement comparison.

However, this agreement starts to diverge beyond 165 kW/m², where a significant increase in surface superheat is observed in the numerical model compared to the experimental data. The primary reason for this discrepancy lies in the surface characteristics of the copper used in the experimental setup. Unlike the idealized geometry used in simulations, the real copper surface contains naturally occurring microscopic cavities that are not artificially engineered. These micro-cavities act as additional nucleation sites at high heat flux levels, enabling the formation of new vapor bubbles. This promotes more efficient heat removal through boiling and limits the rise in surface temperature [21],[36]. In contrast, the numerical model assumes a copper surface with a single artificial cavity of 150 microns in diameter, while the rest of the surface is modeled as perfectly smooth and flat. This restricts the formation of new nucleation sites, causing bubble generation to remain localized at a single point. As heat flux increases, this limitation results in higher surface superheat values in the simulation. Consequently, the discrepancy in surface superheat between the two approaches becomes more pronounced when the heat flux exceeds a certain threshold, approximately 122 kW/m².

Table 5. Comparison of experimental and numerical surface temperature (superheat) measurements under varying heat flux.

Heat Flux q" (kW/m²)	**ΔT (K), exp [28] 1 cavity**	**ΔT (K), CFD 1 cavity**	**ΔT (K), CFD Plain**
30	5,85	5,87	7,16
42	6,54	6,52	8,61
60	7,61	7,60	9,73
84	8,35	8,33	10,82
122	9,8	10,12	13,47
165	10,3	11,84	15,64
177	10,7	12,61	16,11
202	10,9	13,42	17,22

Table 5 presents the surface superheat values obtained from the experimental study conducted by Tetik on a copper surface with a single cavity under varying heat flux conditions. Additionally, the table includes the surface superheat differences derived from the CFD simulations performed within the scope of this study for both a single-cavity copper surface and a plain copper surface. As can be seen in Figures 14 and 15b, the plain surface exhibits higher superheat values compared to the cavity surface, due to its lower boiling heat removal capability. Figure 14 illustrates the relationship between heat flux and surface superheat within the nucleate boiling regime.

In Figure 15a, the A-B region on Nukiyama's [37] classic boiling curve corresponds to the initial subregion of nucleate boiling, characterized by isolated bubble formation without the onset of slug flow. This subregion represents the early stages of efficient heat transfer, where individual vapor bubbles form and detach without significant bubble–bubble interaction. In Figure 15b, the experimental results obtained by Küçük [38] for a plain (smooth) copper surface are represented by circular markers. As the heat flux increases, the surface superheat values exhibit a nonlinear rise, characteristic of nucleate boiling behavior. The CFD results for the same plain copper surface are shown using cross markers. Regarding the CFD results for the single-cavity surface, the presence of the cavity enhances heat removal from the surface through boiling. As a result, the surface superheat remains lower than the CFD results for the plain surface and the experimental results reported by Küçük [38].

Since both datasets correspond to smooth surfaces, the results are in close agreement, demonstrating the CFD model's consistency and reliability. Triangle markers represent the CFD study conducted on a copper surface with a single cavity. Compared with the experimental results of Tetik [28] for a single-cavity copper surface in Figure 14, this dataset in the current graph emphasizes the difference in boiling performance between plain and cavity-enhanced surfaces. Due to the presence of the cavity, more nucleation sites are activated, which increases vapor bubble generation and enhances heat transfer by boiling. As a result, the surface superheat remains lower for the same heat flux values than the plain surface, and this difference is maintained across increasing heat flux levels. This observation also supports the conclusion drawn from Figure 14, where Tetik's experimental surface, although designed with a single cavity, may also contain natural micro-defects or pores that act as additional nucleation sites. Consequently, more intense bubble activity occurs, drawing more heat from the surface and resulting in even lower surface superheat values than those predicted by the CFD model. After approximately 122 kW/m² heat flux, the divergence between the experimental and CFD results becomes more pronounced, further confirming this behavior.

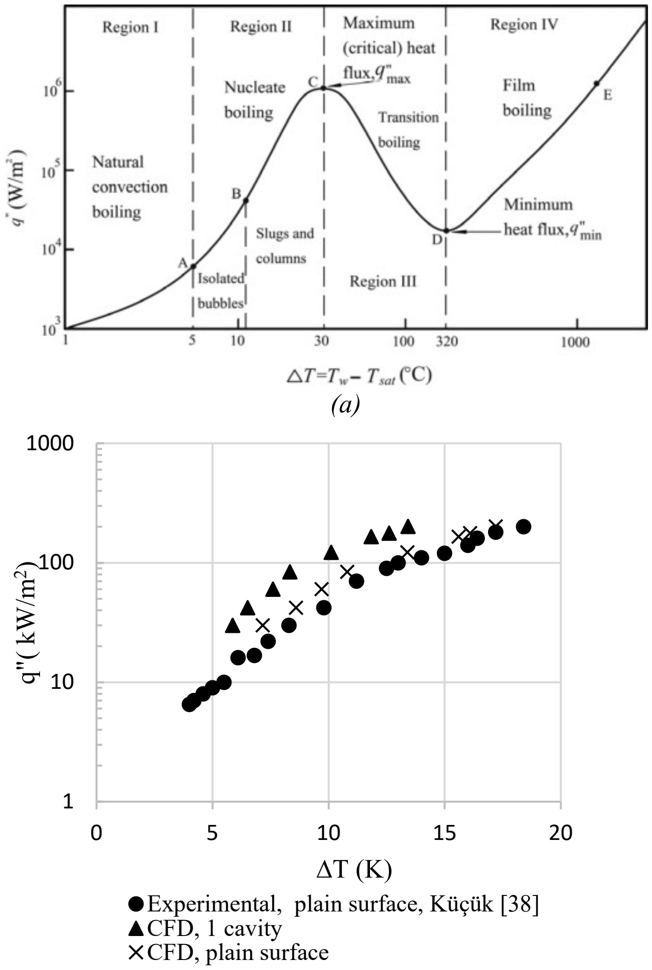

(a)

(b)

Figure 15. Surface superheat levels as a function of heat flux. a) Nukiyama Boiling Curve [37], b) Küçük's experimental result surface superheating levels dependent on heat flux [38], and surface superheat levels as a function of heat flux obtained from CFD results, both plain and one cavity surface.

5. Conclusion

This study has presented a detailed numerical investigation of saturated nucleate pool boiling on heated surfaces featuring a single micro-cavity. Using the VOF method in ANSYS Fluent, supported by a custom-developed UDF, the simulations successfully captured the key mechanisms of bubble nucleation, growth, coalescence, and detachment. The primary focus was on analyzing bubble geometry and departure diameter to understand boiling behavior at the microscale.

The simulation results agreed with experimental data reported in the literature, particularly with the studies referenced in [28] and [38], thereby validating the robustness and accuracy of the proposed numerical model. These validations strengthen confidence in using such models for predictive analysis of boiling performance on microstructured surfaces.

Based on the outcomes, it is strongly recommended that surface enhancement techniques, such as etching, coating, or creating structured cavities, be employed to improve boiling heat transfer efficiency significantly. Such modifications can increase the density of active nucleation sites, facilitate bubble departure, and reduce wall superheat. To highlight a few key findings from the study, the bubble growth rate accelerates as the heat flux increases. However, the behavior related to bubble diameter becomes more complex. Bubbles proliferate and detach before reaching large sizes, increasing the bubble departure frequency. The LEE boiling model was initially employed during the implementation of the CLSVOF method. Although boiling and bubble growth were observed on both a flat surface and a surface with cavities, bubble detachment from the surface did not occur. Therefore, using a User-Defined Function (UDF) is essential to capture a complete bubble life cycle accurately.

Future studies will extend the current work by incorporating various cavity geometries and configurations and will be conducted in three dimensions (3D). This approach aims to simulate boiling surfaces more realistically. These extended simulations will focus on gaining a deeper understanding of bubble interactions and their cumulative effects on overall heat transfer performance, ultimately contributing to the design of high-efficiency thermal management systems.

Nomenclature

Symbols

Co	Courant Number
Cp	Specific heat (J/kg·K)
D_{eq}	Equivalent diameter of the bubble (mm)
E	Internal energy (J)
h	Convective heat transfer coefficient (W/m^2K)
h_{fg}	Latent heat of vaporization (kj/kg)
k	Thermal conductivity (W/mK)
k_{eff}	Effective thermal conductivity (W/mK)
$\dot{m}$	Mass trasfer rate (kg/m^2s)
$\dot{m}_{fg}$	Mass transfer rate from liquid to vapor during evaporation (kg/m^2s)
$\dot{m}_{gf}$	Mass transfer rate from vapor to liquid during condensation (kg/m^2s)
P	Pressure (MPa)
S_E	Volumetric heat source term (W/m^3)
$\overrightarrow{S_M}$	Momentum source term (N/m^3)
t	Time (s)
T_{sat}	The saturation temperature of the liquid (K)
T_w	The temperature of the heated surface (K)
$\vec{u}$	Velocity vector (m/s)
u_{max}	Maximum velocity (m/s)
v_{vapor}	Vapor volume (mm^3)

Greek letters

α	Volume fraction of the phase
Δt	Time step (s), (ms)
ΔT_e	The excess temperature or superheat
Δx	Cell size (μm)
κ	Interface curvature (1/m)
μ	Viscosity (Pa·s)
ρ	Density (kg/m^3)
σ	Surface tension coefficient (N/m)
φ	Level Set function
∇T	Temperature field (K)

Subscripts

f	Liquid phase
g	Vapor phase

Abbreviations

CFD	Computational Fluid Dynamics
CHF	Critical Heat Flux
CLSVOF	Coupled Level Set and Volume of Fluid
GRWBM	Grid Resolved Wall Boiling Model
HTC	Heat Transfer Coefficient
LBM	Lattice Boltzmann Method
LS	Level Set
PBHT	Pool Boiling Heat Transfer

References:

[1] A. Al-Nagdy, M. I. A. Habba, R. A. Khalaf-Allah, S. M. Mohamed, M. T. Tolan, and A. S. Easa, “Optimizing pool boiling heat transfer with laser-engineered microchannels: Experimental and RSM modeling analysis,” *International Journal of Thermal Sciences*, vol. 213, 2025, Art. no. 109806, doi: 10.1016/j.ijthermalsci.2025.109806.

[2] E. I. Eid, A. A. Al-Nagdy, and R. A. Khalaf-Allah, “Nucleate pool boiling heat transfer above laser machining heating surfaces with different micro-cavity geometric shape for water-aluminum oxide nanofluid,” *Experimental Heat Transfer*, vol. 35, no. 5, pp. 688–707, Jul. 2022, doi: 10.1080/08916152.2021.1946207.

[3] E. I. Eid, R. A. Khalaf-Allah, S. H. Taher, and A. A. Al-Nagdy, “An experimental investigation of the effect of the addition of nano Aluminum oxide on pool boiling of refrigerant 134A,” *Heat and Mass Transfer*, vol. 53, pp. 2597–2607, 2017, doi: 10.1007/s00231-017-2010-y.

[4] T. Chen and J. N. Chung, “Heat-transfer effects of coalescence of bubbles from various site distributions,” *Proceedings of the Royal Society A: Mathematical, Physical and Engineering Sciences*, vol. 459, 2003, doi:10.1098/rspa.2003.1133.

[5] A. Coulibaly, X. P. Lin, J. L. Bi, and D. M. Christopher, “Effect of bubble coalescence on the wall heat transfer during subcooled pool boiling,” *International Journal of Thermal Sciences*, vol. 76, pp. 101–109, 2014, doi: 10.1016/j.ijthermalsci.2013.08.019.

[6] T. L. Bergman, A. S. Lavine, F. P. Incropera, D. P. DeWitt, *Fundamentals of Heat and Mass Transfer*, 8th Edition, John Wiley & Sons, 2018.

[7] Y. Y. Hsu, “On the size range of active nucleation cavities on a heating surface,” *ASME Journal of Heat and Mass Transfer*, pp. 207–213, 1962, doi:10.1115/1.3684339.

[8] M. K. Gupta, D. S. Sharma, and V. J. Lakhera, “Vapor bubble formation, forces, and induced vibration: A review,” *ASME Applied Mechanics Reviews*, vol. 68, 2016, Art. no. 030801, doi:10.1115/1.4033622.

[9] D. B. R. Kenning, “Nucleate Boiling,” in *Thermopedia*. Begell House Inc., 2011, doi: 10.1615/AtoZ.n.nucleate_boiling

[10] S. Paruya, J. Bhati, and F. Akhtar, "Numerical model of bubble shape and departure in nucleate pool boiling," *International Journal of Heat and Mass Transfer*, vol. 180, 2021, Art. no. 121756, doi: 10.1016/j.ijheatmasstransfer.2021.121756.

[11] M. M. Petrovic and V. D. Stevanovic, "Pool boiling simulation with two-fluid and grid resolved wall boiling model," *International Journal of Multiphase Flow*, vol. 144, 2021, Art. no. 103806, doi: 10.1016/j.ijmultiphaseflow.2021.103806.

[12] S. Iyer, A. Kumar, J. Coventry, and W. Lipiński, "Modelling of bubble growth and detachment in nucleate pool boiling," *International Journal of Thermal Sciences*, vol. 185, 2023, Art. No. 108041, doi: 10.1016/j.ijthermalsci.2022.108041.

[13] M. M. Mahmoud and T. G. Karayiannis, "Bubble growth models in saturated pool boiling of water on a smooth metallic surface: Assessment and a new recommendation," *International Journal of Heat and Mass Transfer*, vol. 208, 2023, doi: 10.1016/j.ijheatmasstransfer.2023.124065.

[14] A. A. Alsaati, D. M. Warsinger, J. A. Weibel, and A. M. Marconnet, "A mechanistic model to predict saturated pool boiling critical heat flux (CHF) in a confined gap," *International Journal of Multiphase Flow*, 2023, Art. no. 104542, doi: 10.1016/j.ijmultiphaseflow.2023.104542.

[15] N. Qiu, Y. Xuan, J. Li, and Q. Li, "Numerical simulation of nucleate pool boiling under high pressure using an initial micro-layer thickness model," *Case Studies in Thermal Engineering*, vol. 39, 2022, Art. no. 102460, doi: 10.1016/j.csite.2022.102460.

[16] N. Kumar, P. Ghosh, and P. Shukla, "Development of an approximate model for the prediction of bubble departure diameter in pool boiling of water," *International Communications in Heat and Mass Transfer*, vol. 127, 2021, Art. no. 105531, doi: 10.1016/j.icheatmasstransfer.2021.105531.

[17] M. Kim and S. J. Kim, "A mechanistic model for nucleate pool boiling including the effect of bubble coalescence on area fractions," *International Journal of Heat and Mass Transfer*, vol. 163, 2020, Art. no. 120453, doi: 10.1016/j.ijheatmasstransfer.2020.120453.

[18] J. Yuan, X. Ye, and Y. Shan, "Modeling of the bubble dynamics and heat flux variations during lateral coalescence of bubbles in nucleate pool boiling," *International Journal of Multiphase Flow*, vol. 142, 2021, Art. no. 103701, doi: 10.1016/j.ijmultiphaseflow.2021.103701.

[19] A. Mukherjee and V. K. Dhir, "Study of lateral merger of vapor bubbles during nucleate pool boiling," *ASME Journal of Heat and Mass Transfer*, vol. 126, pp. 1023–1039, 2004, doi:10.1115/1.1834614.

[20] ANSYS Inc., ANSYS Fluent User's Guide, Release 2023 R1, Canonsburg, PA, USA, 2023.

[21] S. V. Patankar, *Numerical Heat Transfer and Fluid Flow*, Washington, D.C.: Hemisphere Publishing Corporation, 1980, doi:10.1201/9781482234213.

[22] V. K. Dhir, "Boiling heat transfer," *Annual Review of Fluid Mechanics*, vol. 30, no. 1, pp. 365–401, 1998, doi: 10.1146/annurev.fluid.30.1.365.

[23] S. G. Kandlikar, "A theoretical model to predict pool boiling CHF incorporating effects of contact angle and orientation," *ASME Journal of Heat and Mass Transfer*, vol. 123, no. 6, pp. 1071–1079, 2001, doi:10.1115/1.1409265.

[24] J. H. Ferziger and M. Perić, *Computational Methods for Fluid Dynamics*, 3rd edition, Springer, 2002.

[25] J. G. Collier and J. R. Thome, *Convective Boiling and Condensation*, 3rd edition, Oxford, UK: Oxford University Press, 1994.

[26] A. N. Georgoulas, M. Marengo, "Numerical Simulation of Pool Boiling: The Effects of Initial Thermal Boundary Layer, Contact Angle and Wall Superheat," *in Proc. 14th UK Heat Transfer Conference (UKHTC)*, Belfast, UK, 2015.

[27] I. Mudawar, S. Kim, and J. Lee, "A coupled level-set and volume-of-fluid (CLSVOF) method for prediction of microgravity flow boiling with low inlet subcooling on the International Space Station," *International Journal of Heat and Mass Transfer*, vol. 202, 2023, Art. no. 124644, doi: 10.1016/j.ijheatmasstransfer.2023.124644.

[28] T. Tetik, "Study of Bubble Nucleation in a Microcavity in Pool Boiling", Ph.D. Thesis, Dept. Mech. Eng., Tech. Univ. Istanbul, Graduate School of Science Eng. and Tech., Turkey, 2022.

[29] Y. A. Buyevich and B. W. Webbon, "The isolated bubble regime in pool nucleate boiling," *International Journal of Heat and Mass Transfer*, vol. 40, issue 2, pp. 365–377, 1997, doi:10.1016/0017-9310(96)00097-X.

[30] M. G. Cooper, "Heat flow rates in saturated nucleate pool boiling - a wide-ranging examination using reduced properties," *Advances in Heat Transfer*, vol. 16, pp. 157–239, 1984, doi: 10.1016/S0065-2717(08)70205-3.

[31] J. F. Klausner, R. Mei, D. M. Bernhard, and L. Z. Zeng, "Vapor bubble departure in forced convection boiling," *International Journal of Heat and Mass Transfer*, vol. 36, issue 3, pp. 651–662, 1993, doi:10.1016/0017-9310(93)80041-R.

[32] V. K. Dhir, "Mechanistic Prediction of Nucleate Boiling Heat Transfer–Achievable or a Hopeless Task?," ASME *Journal of Heat and Mass Transfer*, vol. 128, pp. 1-12, 2006, doi:10.1115/1.2136366.

[33] J. Bhati, S. Paruya, "Numerical simulation of bubble dynamics in pool boiling at heated surface," *International Journal of Heat and Mass Transfer*, vol. 152, 2020, Art. no. 119465, doi: 10.1016/j.ijheatmasstransfer.2020.119465.

[34] N. Zuber, "Hydrodynamic aspects of boiling heat transfer," Thesis, *U.S. Department of Energy Office of Scientific and Technical Information,*1959, doi:10.2172/4175511.

[35] J. H. Lienhard, V. K. Dhir, "Extended hydrodynamic theory of the peak and minimum pool boiling heat fluxes," *NASA Technical Report CR-2270*, 1973.

[36] M. Mobli, C. Li, "On the heat transfer characteristics of a single bubble growth and departure during pool boiling," *ASME 2016 14th International Conference on Nanochannels, Microchannels, and Minichannels,* Washington, 2016, doi: 10.1115/ICNMM2016-8097.

[37] S. Nukiyama, "The maximum and minimum values of the heat Q transmitted from metal to boiling water under atmospheric pressure," *International Journal of Heat and Mass Transfer*, vol. 9, pp. 1419-1433, 1966, doi: 10.1016/0017-9310(66)90138-4.

[38] H. Küçük, "Effect of Solid Particles on Heat Transfer in Nucleate Pool Boiling", Ph.D. Thesis, Dept. Mech. Eng., Tech. Univ. Istanbul, Graduate School of Science Eng. and Tech., Turkey, 2002.

International Journal of Thermodynamics (IJoT)
ISSN 1301-9724 / e-ISSN 2146-1511
https://dergipark.org.tr/en/pub/ijot

Vol. 28 (No. 2), pp. 103-114, 2025
doi: 10.5541/ijot.1563338

Research Article

An Experimental Optimization of Solar Dryer Employing Phase Change Material for Potato Slices Using Variance Analysis

[1]*C. A. Mamulkar, [1]S. R. Ikhar

[1] Department of Mechanical Eng. Karamveer Dadasaheb Kannamwar College of Engineering, Nagpur, MH, India
E-mail: [1]*mechetan2016@gmail.com

Received 8 October 2024, Revised 12 December 2024, Accepted 2 January 2025

Abstract

A crucial technique for preserving products of agricultural is solar drying, but its efficiency can be limited by inconsistent sunlight. The research aimed to enhance solar dryer technology by integrating Phase Change Materials (PCMs) and photovoltaic (PV) panels to provide consistent drying conditions. A novel solar dryer was designed with PCM tubes placed horizontally behind a copper plate to store thermal energy, ensuring continuous drying at off-sunny hours. The research investigated the process of drying potato slices in different weather conditions to assess the enhanced dryer's performance. Key findings from our extensive testing show that the PCM-integrated solar dryer significantly improves drying efficiency. Specifically, we observed a 30% reduction in drying time, a 25% increase in moisture removal rates, and a 20% increase in overall drying efficiency compared to traditional solar dryers. These improvements highlight the effectiveness of integrating phase change materials in enhancing the performance of solar drying systems. This study provides valuable insights into the development of more efficient and sustainable solar dryers for agricultural products. This technology aims to minimize losses after harvesting, enhance the products quality as well as offer economic advantages to farmers. The research demonstrates the potential of PCM-integrated solar dryers as a sustainable and efficient solution for agricultural drying, with future studies needed to explore its application across different crops and regions.

Keywords: *Analysis of variance (ANOVA); optimization; paraffin wax; potato slices; solar dryer; phase change materials (PCM).*

1. Introduction

The solar drying has traditionally been used for preserving food and agricultural products. It involves solar energy for removing moisture, which extends the shelf life of products and reduces the risk of spoilage. Traditional sun drying, although cost-effective and widely practiced, often leads to contamination and uneven drying due to exposure to dust, insects, and varying weather conditions. Modern solar dryers address these issues by offering a controlled environment that improves drying efficiency and enhances product quality.

The advantages of solar drying are rooted in its sustainability and economic benefits. Also, solar drying can significantly reduce post-harvest losses, which is crucial in regions where agriculture is a primary livelihood [1]. By preserving agricultural products, solar drying contributes to food security, particularly in developing countries where food preservation infrastructure is limited.

1.1 Importance of Drying Potato Slices

Potatoes are a staple food crop globally, valued for their nutritional content and versatility in culinary applications. However, potatoes are highly perishable due to their moisture content, making them susceptible to microbial spoilage during storage. Drying potato slices is an effective way to extend their shelf life, making them available year-round and reducing food waste [2]. Dried potato slices can be used in various food products such as soups, snacks, and instant meals, providing convenience to consumers. Furthermore, dried potatoes retain most of their nutritional value, making them a healthy option for food preservation. The importance of drying potatoes also extends to economic benefits for farmers and food processors, as it allows them to add value to their products and access new markets.

1.2 Role of PCM (Phase Change Materials) in Solar Drying

Materials that absorb as well as release thermal energy as they melt and solidify at specific temperatures are PCM. In solar drying, PCM can store excess solar energy during peak sunshine hours and release it during off-peak hours, thereby maintaining a consistent drying temperature. This is particularly beneficial for regions with intermittent sunshine, as it ensures continuous drying and improves overall efficiency [3].

The integration of PCM in solar dryers helps in maintaining optimal drying conditions, which is crucial for preserving the quality of the dried products. By preventing temperature fluctuations, PCM can reduce the risk of over-drying or under-drying, which may affect the color, texture, and nutritional content of dried products. Moreover, using PCM enhances energy efficiency in solar dryers, making the process more cost-effective and sustainable.

---

*Corresponding Author

1.3 Objectives

The aim of the research is to enhance the drying process of potato slices by utilizing a solar dryer with integrated PCM. This involves identifying the optimal configuration and operational parameters to improve drying efficiency while maintaining the dried potato slices. The research seeks to offer insights into the utilization of PCM for enhancing the effectiveness of solar dryers, especially regarding energy efficiency and drying consistency.

To achieve this objective, the research will utilize experimental methods to assess the solar dryer's effectiveness under different conditions. Parameters such as drying temperature, PCM arrangement, and drying duration will be systematically adjusted and analyzed to determine the best settings. The use of ANOVA (Analysis of Variance) will be for statistical analysis of experimental data, allowing for the identification of significant factors and interactions that influence drying efficiency.

The specific aims of this study include:

- Optimizing the process of drying potato slices with the integration of PCM.
- To analyze the drying efficiency and moisture removal rate using ANOVA.

Optimizing the drying process involves finding the best combination of parameters that yields the highest drying efficiency and product quality. This study will concentrate on incorporating PCM into the solar dryer and examining how various configurations and operational conditions influence the drying process. Key parameters to be considered include the type and amount of PCM, its placement within the dryer, and the drying temperature. Experimental trials will be conducted to test various PCM configurations and drying conditions. Additionally, the quality of the dried potato slices—including aspects such as texture, color, and nutritional value—will be assessed to confirm that the drying process maintains product quality.

By systematically adjusting the experimental parameters and evaluating the outcomes, this research seeks to determine the highest configurations for a dryer integrated with PCM. This will provide valuable guidelines for designing and operating solar dryers to achieve maximum efficiency and product quality.

ANOVA is a robust statistical method for examining variations among group means and their related processes. In this research, ANOVA will be utilized to assess how various factors affects efficiency of the drying.

Experimental data will be subjected to ANOVA to determine the significance of each factor and their interactions. This analysis will help identify which factors have the most substantial impact on drying efficiency and how they interact with each other. The results of ANOVA will offer a statistical foundation for enhancing the process of drying and refining the design and operation of solar dryers that incorporate PCM.

By using ANOVA, the study aims to achieve a comprehensive understanding of the factors influencing drying efficiency. This will facilitate the creation of more effective and efficient solar drying systems, contributing to the wider objective of sustainable food preservation and energy utilization.

Overall, research is optimizing the drying process of potato using a solar dryer integrated with PCM, and to analyze drying efficiency through ANOVA. The findings will have important implications for the design and operation of solar dryers, improving their efficiency and sustainability in food preservation applications.

2. Related Works

The method removes moisture from food using solar radiation, which leads to extends the shelf life by the solar dryer. Traditional sun drying, although cost-effective, exposes products to contaminants and uneven drying conditions. Modern solar dryers address these shortcomings by providing a controlled environment, enhancing drying efficiency, and improving product quality. In direct-sun dryers, the product is placed in direct sunlight, whereas indirect dryers utilize air that has been heated by solar energy. Mixed-mode dryers integrate both techniques to enhance drying performance. Jadhav et al. [4] emphasized the efficacy of solar cabinet dryers for drying green peas, demonstrating notable advancements in efficiency and quality of product when compared to conventional methods.

PCM is capable of absorbing surplus thermal energy during peak sunlight periods and discharging it during non-peak times, thereby maintaining a stable drying temperature. This thermal storage capability is particularly beneficial in regions with intermittent sunshine. Onyenwigwe et al. [8] performed an analysis of the eco-thermal for mixed-mode dryer using PCM, showing enhanced drying rates for potato slices. Similarly, Ssemwanga et al. [6] examined the solar dryer functionality integrated with metallic solar concentrators and PCM, discovering that this integration greatly improved drying efficiency and lowered energy consumption.

The efficiency of drying agricultural products relies on various factors, including the drying method, product characteristics, and environmental conditions. Several studies have focused on optimizing drying processes to enhance efficiency and product quality. In their study, Masud et al. [1] examined the effectiveness of solar-assisted intermittent microwave-convective drying methods for drying potato slices, focusing on optimizing different process parameters to improve drying efficiency. Nwakuba [3] examined energy consumption during hot air drying of tomato slices in a solar-electric dryer, emphasizing the importance of optimizing drying conditions to reduce energy use and enhance efficiency. For potato slices, maintaining product quality while achieving efficient drying is critical. Onu et al. [10] evaluated various techniques for moisture reduction predictions at drying the potato slices, finding that advanced methods could significantly improve drying outcomes.

The statistical method which is utilized to identify significant factors and interactions that influence experimental outcomes is Analysis of Variance (ANOVA). It is particularly useful in optimizing drying processes by systematically analyzing the effects of various parameters. Cheng et al. [2] used ANOVA coupled with simultaneous component analysis to compare different solar drying methods for mangoes, providing a comprehensive understanding of the factors influencing drying efficiency. Jha and Tripathy [5] employed ANOVA to optimize process parameters and mass transfer and heat during the solar drying simulations of paddy, demonstrating the method's effectiveness in identifying the best drying conditions. ANOVA can be used to analyze the temperature of drying effects on the solar drying efficiency of potato slices, PCM configuration, and drying time, as demonstrated by

Onyenwigwe et al. [8]. Detailed literature surveys are provided in Table 1, including methods and their limitations.

Table 1. Summary of related works.

Author	Year	Method	Limitations
Masud et al. [1]	2022	Microwave-convective drying enhanced with solar energy	Limited to specific drying conditions and equipment
Cheng et al. [2]	2019	ANOVA-simultaneous component analysis (ASCA)	Focused on mangoes, not directly on potatoes
Nwakuba [3]	2019	Enhancement of energy efficiency in solar-powered electric dryers	Specific to tomato slices, it may not be applicable to other crops
Jadhav et al. [4]	2010	Solar cabinet drying	Limited to green peas, may not be generalizable
Jha & Tripathy [5]	2021	Numerical modeling and ANOVA optimization	Simulated conditions may differ from real-world scenarios
Ssemwanga et al. [6]	2020	Solar drying system incorporating metallic solar concentrators and phase change materials (PCM)	Limited performance data for other crops or conditions
Etim et al. [7]	2020	Optimization using response surface methodology	Specific to aerial yam, may not apply to potatoes

Solar drying technologies have evolved significantly, offering controlled and efficient methods for preserving agricultural products. The integration of PCM in solar dryers enhances their performance by ensuring consistent drying temperatures, which is particularly beneficial for regions with fluctuating sunlight. Research has shown that optimizing drying conditions is crucial for achieving high drying efficiency and maintaining product quality. Research on potato slices has shown the advantages of utilizing advanced drying methods and optimization strategies, such as employing ANOVA to determine key factors and their interactions. This body of work offers crucial insights for creating effective and sustainable solar drying systems, supporting efforts in food preservation and energy conservation.

3. Novelty of the Research

This research introduces a novel feature in the design of solar dryers: horizontally arranged phase change material (PCM) tubes instead of the traditional vertical arrangement. This configuration offers several key benefits:

- Horizontal tubes have a larger surface area in contact with the solar collector plate, leading to more efficient and even absorption of solar energy.
- With more surface area exposed, the heat transfer from the air to the PCM is more efficient, speeding up the phase change process and enhancing thermal storage.
- Heat is distributed more evenly throughout the drying chamber, maintaining a stable drying temperature and preventing hot spots, which ensures consistent drying of products like potato slices.
- Gravity helps natural convection within the PCM in a horizontal setup, aiding in better melting and solidification, and resulting in more effective heat absorption and release.
- This arrangement provides better structural stability and is easier to maintain, reducing the risk of material settling and ensuring long-term efficiency.

These benefits make the horizontal PCM tube arrangement a significant improvement for solar dryers, enhancing drying performance and energy efficiency for agricultural products.

Our findings significantly advance the field of solar drying by providing a more efficient method of thermal energy storage. Previous studies have focused on vertical PCM arrangements, which have limitations in heat transfer efficiency and stability. Our horizontal configuration addresses these issues, leading to faster drying times and more consistent drying conditions. This research differentiates itself from existing studies by demonstrating a clear improvement in drying efficiency and energy conservation, offering a practical solution for sustainable agricultural practices.

4. Methodology

The methodology for this research involves a combination of experimental design, fabrication, testing, and computational modeling. The main emphasis is on optimizing solar dryer performance with PCMs.

4.1 Experimentation Design

The dryer is designed with a solar collector, a drying chamber, and a thermal energy storage unit that incorporates phase change materials (PCMs). The solar collector features a plate equipped with horizontal tubes containing paraffin wax, which functions as PCM. This setup is engineered to capture solar radiation, which converts into thermal energy, which is subsequently utilized to heat the air that enters the drying chamber. Inside the drying chamber, potato slices are placed, and the heated air aids in extracting moisture from them. The integration of PCMs allows the system to store thermal energy during high sunlight hours and release it during periods without sunlight, ensuring a consistent drying process [6].

4.2 Design and Construction

Collector Plate: The collector plate is a crucial component, designed to maximize solar radiation absorption. It is inclined at an angle of 31.1 degrees for the location of Nagpur, Maharashtra, India, which has a latitude of 21.1 degrees to capture the maximum solar insolation. The plate is covered with clear toughened glass, known for its high transmissivity, which ensures efficient transmission of solar energy.

Calculation began with the global incident radiation (GIR) for January, which was measured to be 733 W/m² at noon. After accounting for the transmissivity of the toughened glass (88.5%), the net heat input to the system was determined to be [7]:

$$Q_{input} = 733 \times 0.885 = 648.9 \ W/m^2 \tag{1}$$

The amount of heat needed to elevate the temperature of air within the dryer was determined using the desired temperature increase (ΔT), the specific heat capacity of air (C_p), and the air mass flow rate ($\dot{m}$):

$$Q_{required} = \dot{m} \times C_p \times \Delta T \tag{2}$$

where, $\dot{m}$ (air mass flow rate) = 40 kg/hr = 0.0111 kg/s, C_p ('air's specific heat capacity) = 1.005 kJ/kg·K, and ΔT (desired increment in temperature) = 45°C

$$Q_{required} = 0.0111 \times 1.005 \times 45 = 0.501\,kW = 501\,W \quad (3)$$

Given the efficiency of the system, we determined the necessary area of the collector plate (A) as follows:

$$A = Q_{required}/Q_{input} = 501/648.9 = 0.772\,m^2 \quad (4)$$

Integration of PCM and Drying Chamber: The chamber has been designed to hold 500 g of potato slices per batch. The airflow rate was optimized at 40 kg/hr, ensuring a consistent supply of hot air.

For PCM, Paraffin wax has been chosen due to its favorable thermal properties, and by CFD analysis results [9]:

- Specific heat (C_f) = 2.5 kJ/kg·K
- Density (ρ) = 900 kg/m³,
- Latent heat of fusion (L_f) = 220 kJ/kg
- Thermal conductivity (k) = 0.23 W/m·K
- Melting temperature (T_m) = 60°C

PCM has been integrated into the collector plate in horizontal tubes, each with a calculated volume to store sufficient thermal energy.

A comprehensive schematic illustrating the solar dryer—featuring the inclined collector plate, PCM tubes, drying chamber, and air inlet system—is shown in Figure 1 below:

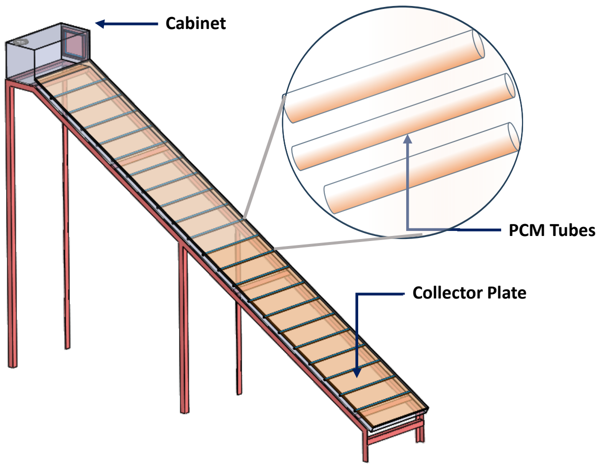

Figure 1. A diagram or schematic representation of a solar dryer.

Uniformly cut potato slices were used for all experiments, each with a thickness of 0.2 mm. Each batch comprised 500 grams of potato slices, which initially contained around 80% moisture content. This uniformity ensured consistent drying conditions across all trials.

4.3 Experimental Procedure

Drying Experiments Under Different Conditions: The drying experiments took place over 366 days, from September 2023 to August 2024, allowing for a thorough assessment of the solar dryer's performance under different conditions. During this period, meticulous focus was placed on both sunny and off-sunny hours, and different PCM configurations to optimize thermal storage and release. During sunny hours, experiments were performed at peak sunlight to assess the drying efficiency with direct solar radiation [11]. In contrast, during periods of limited or no sunlight, experiments were conducted to assess how effectively the PCM retains and releases heat.

Data Collection: In the study, detailed data collection for each trial, focusing on several key parameters to ensure comprehensive analysis, was conducted. The temperature was recorded at the air inlet, within the chamber, and at the outlet using thermocouples, which have an accuracy of ±0.5°C. Humidity levels were assessed with a hygrometer that provides an accuracy of ±2% RH to evaluate the drying conditions. Heat flux was recorded to evaluate energy transfer efficiency. Moisture content was meticulously tracked using a precision weighing machine with an accuracy of ±0.01 grams to determine the drying rate.

4.4 Instrumentation and Calibration

The instruments used in the experiments included thermocouples for temperature measurements, a hygrometer for humidity monitoring, a precision weighing machine for tracking the moisture content of potato slices, and a heat flux sensor for measuring energy transfer. All instruments were calibrated before the experiments to ensure accuracy [11]. Thermocouples were calibrated using a standard water bath, The hygrometer was calibrated using solutions of known salt concentrations as well and the weighing machine was calibrated using standard weights.

4.5 Data Analysis

Thorough statistical analysis was conducted to guarantee the reliability and validity of the results. The main statistical method utilized was Analysis of Variance (ANOVA), which was instrumental in identifying key factors influencing the drying process [12].

4.6 Optimization

ANOVA has been used to enhance the drying conditions by examining the influence of various factors, including temperature, PCM arrangement, and drying duration. This statistical method facilitated the identification of the most influential factors and their interactions. Key factors considered in the data analysis included temperature, which impacts air temperature on drying efficiency, PCM configuration, which affects different PCM arrangements on heat retention and release, and drying time. The importance of these factors on the drying process was assessed using ANOVA [13].

The ANOVA model used is given by [14]:

$$Y_{ijk} = \mu + \alpha_i + \beta_j + (\alpha\beta)_{ij} + \epsilon_{ijk} \quad (5)$$

where, Y_{ijk} = observed response variable (drying rate), μ = overall mean, α_i= effect of factor A (temperature), β_j = effect of factor B (PCM configuration), $(\alpha\beta)_{ij}$ = interaction effect between factors A and B, and ϵ_{ijk} = random error term. Then:

$$(SS)=(SST)+(SSE) \quad (6)$$

where, SS is the Total Squares' Sum, SST ("Sum of Squares for Treatments) measures the variability between the group means, SSE (Sum of Squares for Error) measures the variability within the groups.

Sum of Squares for Treatments (SST) [15]:

$$SST = \sum_{i=1}^{k} n_i(\bar{Y}_i - Y)^2 \quad (7)$$

where k = number of treatments, n_i = No. of observations for treatment i, $\bar{Y}_i$ = mean of treatment i, $\bar{Y}$ = overall mean

Sum of Squares for Error (SSE) [16]:

$$SSE = \sum_{i=1}^{k} \sum_{j=1}^{n_i} \left(Y_{ij} - \bar{Y}_i\right)^2 \tag{8}$$

where, Y_{ij} = observation j in treatment i, $\bar{Y}_i$= mean of treatment i.

Total Sum of Squares (SS) *[17]:*

$$SS = \sum_{i=1}^{k} \sum_{j=1}^{n_i} \left(Y_{ij} - \bar{Y}\right)^2 \tag{9}$$

The Mean Squares [18]:

$$Mean\ Square\ for\ Treatments\ (MST) = SSt/k - 1 \tag{10}$$

$$Mean\ Square\ for\ Error\ (MSE) = SSE/N - k \tag{11}$$

where, N = total number of observations,

F-statistic *[19]:*

$$F = MST/MSE \tag{12}$$

The F-statistic is subsequently in comparison with the critical value obtained from the F-distribution table to evaluate the significance of the findings.

The innovative solar dryer, featuring an inclined collector plate and PCM integration, demonstrated significant potential for efficient drying of agricultural products [20]. The design and experimental results underscore the importance of optimizing thermal energy storage to enhance drying performance, especially during off-sunny hours. The statistical analysis, particularly ANOVA, validated the effectiveness of the design and identified key factors influencing the process of drying.

5. Results and Discussions

Research aimed to examine the effectiveness of the solar dryer integrated with PCM under varying conditions, specifically during sunny and non-sunny hours. The key parameters measured were temperature, humidity, heat flux, moisture content, and drying time [21, 22].

The temperature and humidity profiles were evaluated during the process of drying process and found that at time of sunny hours, the drying chambers' temperature consistently reached up to 65°C. During off-sunny hours, the temperature was maintained around 40°C due to the thermal storage provided by the PCM, while the temperature varied between 26°C to 36°C during these experiments. Additionally, relative humidity inside the chamber significantly decreased during sunny hours, reaching as low as 10%, whereas it was around 30% during off-sunny hours.

In terms of heat flux and energy distribution, a heat flux was recorded ranging from 112 W/m² to 119 W/m² during sunny hours, indicating efficient energy absorption and utilization. During off-sunny hours, the heat flux decreased to around 60 W/m², demonstrating the effectiveness of PCM in maintaining thermal energy.

The potato slices initially contained roughly 80% moisture. During sunny hours, this moisture level decreased to around 10% after 6 hours of drying. In contrast, during off-sunny hours, the moisture content reached 20% after 8 hours of drying, indicating that while the drying process is slower during off-sunny hours, the PCM integration helps maintain a consistent drying rate.

The configuration with PCM tubes placed horizontally on the backside of the copper plate showed the best performance, maintaining higher temperatures and significantly reducing drying time.

5.1 Results of Analysis of Variance (ANOVA)

To assess the effects of the proposed design on various performance metrics, an ANOVA analysis was performed. The aim was to identify any statistically significant differences in drying times, moisture removal rates, and efficiencies across different experimental configurations. The setups included variations in the rate of air flow, temperature, rate of mass flow, and the use of PCM [23, 24].

On Sunshine Analysis- First Test: Regression Analysis: For on sunshine conditions, the regression analysis between moisture removal rate (*m)* and heat flux was conducted. The ANOVA results showed a significant model (P-Value < 0.000) with a high F-Value of 1009.17, indicating that heat flux is a significant predictor of moisture removal rate. Table 2 shows the regression analysis by ANOVA below, with the Model summary in Table 3.

Table 2. ANOVA regression analysis.

Source	DF	Adj SS	Adj MS	F-Value	P-Value
Regression	1	300682	300682	1009.17	0.000
Heat Flux	1	300682	300682	1009.17	0.000
Error	333	99218	298		
Lack-of-Fit	186	60943	328	1.26	0.073
Pure Error	147	38275	260		
Total	334	399900			

Table 3. Model summary of analysis.

Statistic	Value
S	17.2613
R^2	75.19%
R^2 (adj)	75.11%
R^2 (pred)	74.72%

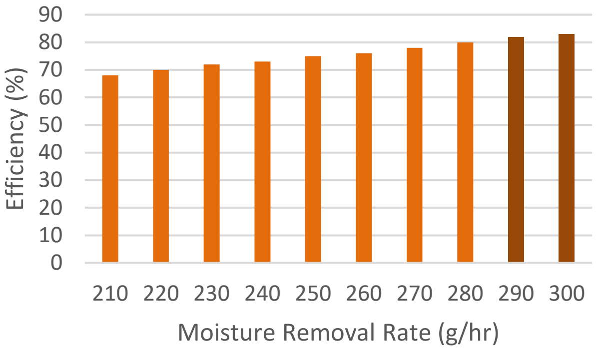

Figure 2. Moisture removal rate vs. efficiency.

The regression analysis between moisture removal rate (m) and efficiency (E) is shown in Figure 2. This figure illustrates a positive relationship in which an increase in the moisture removal rate corresponds to a high efficiency of the solar dryer.

Table 4. Coefficient values for the analysis.

Terms	Coeff.	SE Coeff.	T-Value	P-Value	VIF
Constant	547.73	7.27	75.30	0.000	-
Heat Flux (W/m²)	-0.31210	0.00980	-31.76	0.000	1.00

The regression equation is:

$$m_2 = 547.73 - \left(0.31210 \times Heat\ Flux\ (\ W/m^2)\right) \qquad (13)$$

where: m_2 = mass after drying of potato slices, m_1 = before mass of drying of potato slices (i.e., 500 g).

The model indicates that heat flux significantly negatively impacts the moisture removal rate, with an R^2 value of 75.19%. Coefficient parameters are listed in Table 4 for this analysis.

Analyzing the relationship between heat flux (W/m²) and moisture removal rate (m), Figure 3 indicates a positive correlation. The scatter plot and the regression line suggest that higher heat flux leads to increased moisture removal rates. Also, the unusual observations with their R values are given in Table 5.

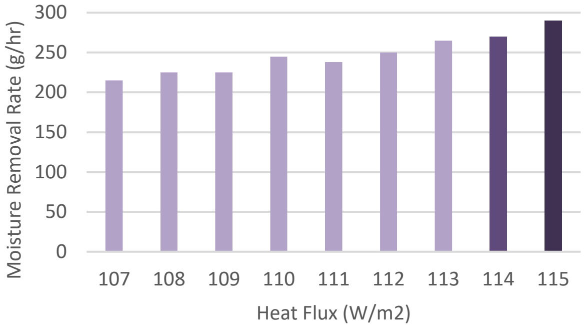

Figure 3. Regression analysis for heat flux vs. moisture removal rate.

Table 5. Detections of unusual observations.

Obs.	m_2	Fit	Resid.	Std. Resid.	R	X
6	412.0	375.58	36.42	2.11	R	
13	269.0	311.50	-42.50	-2.47	R	
62	309.0	349.63	-40.63	-2.36	R	

Second Test: Regression Analysis: Table 6 shows the ANOVA results for the regression of heat flux against efficiency (E), with the Model summary listed in Table 7, with respective coefficient values in Table 8. The model demonstrated high significance (P-Value < 0.000) and had an F-Value of 460.18. The 'Heat Flux' term is highly significant, with an *Adj SS* of 1.7067 and an *Adj MS* of the same value. This model found substantial variation in efficiency, and the lack-of-fit test shows no significant lack of fit (P-Value = 0.658), which confirms the robustness of the model.

The regression equation is:

$$E = 0.80361 + \left(0.000587 \times Heat\ Flux\ (\ W/m^2)\right) \qquad (14)$$

where, E is the Dryer efficiency.

Table 6. ANOVA results for heat flux vs. efficiency.

Source	DF	Adj. SS	Adj. MS	F-Value	P-Value
Regression	1	1.7067	1.7067	460.18	0.000
Heat Flux	1	1.7067	1.7067	460.18	0.000
Error	333	1.2352	0.0037		
Lack-of-Fit	186	0.6768	0.0036	0.93	0.658
Pure Error	147	0.5584	0.0038		
Total	334	2.9419			

Table 7. Model summary.

Statistic	Value
S	0.0609322
R^2	58.03%
R^2 (adj)	57.93%
R^2 (pred)	57.68%

Table 8. Coefficient's summary.

Terms	Coeff.	SE Coeff.	T-Value	P-Value	VIF
Constant	0.80361	0.01360	59.06	0.000	
Heat Flux (W/m²)	0.000587	0.000027	21.45	0.000	1.00

This model suggests a positive relationship between heat flux and efficiency, with an R^2 value of 58.03%.

The relationship between heat flux (W/m²) and efficiency (E) is explored. Figure 5 presents the scatter plot and regression line, showing a positive correlation between these variables, indicating that efficiency improves with higher heat flux. Analysis results show diagnosis of unusual behavior listed in Table 9.

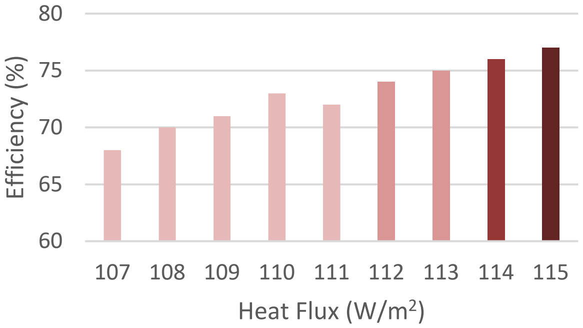

Figure 4. Regression analysis: heat flux vs. efficiency

Table 9. Detection of unusual observations.

Obs.	E	Fit	Resid.	Std. Resid.	R	X
7	0.45474	0.51194	-0.05720	-2.12	R	-
114	0.63856	0.57688	0.06168	2.30	R	-
190	0.76278	0.70297	0.05981	2.22	R	-

Off Sunshine Hours: First Test: The first regression analysis examined the relationship between m (moisture removal rate) and the variables A (heat flux at noon) and B (heat flux during off-sunshine hours). The analysis of variance (ANOVA) indicated that the regression model has been statistically significant (with P-Value < 0.000), with the regression explaining a substantial part of the variance (Adj. SS = 264431). The ANOVA details are as shown in Table 10, with model summary listed in Table 11, and respective coefficient values are listed in Table 12.

Table 10. ANOVA results for moisture removal.

Sources	DF	Adj. SS	Adj. MS	F-Value	P-Value
Regression	2	264431	132216	469.76	0.000
A	1	260066	260066	924.00	0.000
B	1	729	729	2.59	0.108
Error	315	88658	281	-	-
Lack-of-Fit	282	78264	278	0.88	0.713
Pure Error	33	10394	315	-	-
Total	317	353090	-	-	-

Table 11. Model summary.

Statistic	**Value**
S	16.7766
R^2	74.89%
R^2 (adj)	74.73%
R^2 (pred)	74.13%

The regression analysis between heat flux at noon and moisture removal rate (m) reveals a strong positive correlation.

Table 12. Coefficient analysis.

Terms	Coef.	SE Coef.	T-Values	P-Values	VIF
Constant	507.9	44.7	11.36	0.000	-
A	-0.3360	0.0111	-30.40	0.000	1.01
B	0.600	0.373	1.61	0.108	1.01

The developed regression equation is:

$$m_2 = 507.9 - (0.3360 \times A) + (0.600 \times B) \tag{15}$$

This model indicates that heat flux at noon (A) negatively influences the moisture removal rate significantly, whereas heat flux during off-sunshine hours (B) exhibits a positive effect that is not statistically significant. The R² value of 74.89% suggests that the model has found variation in moisture removal rates.

Several observations had large residuals or unusual X values, which may indicate outliers or influential data points shown in Table 13. For instance, observation 151 had a large negative residual (-60.62), suggesting a potential data anomaly.

Table 13. Diagnostics for unusual observations.

Obs.	**m_2**	**Fit**	**Resid.**	**Std. Resid.**	**R**	**X**
6	386.0	341.25	44.75	2.68	R	
151	327.0	387.62	-60.62	-3.66	R	
314	414.0	457.51	-43.51	-2.70	R	X

Second Test of Regression Analysis for Off-Sunny Hours: The second regression analysis evaluated the efficiency (E) versus heat flux at noon (A), heat flux at off-sunshine hours (B), and moisture removal rate (m). The ANOVA results showed a highly significant model (P-Value < 0.000), with all terms except B being significant predictors as shown in Table 14, with its model summary listed in Table 15, with their respective coefficient values listed in Table 16.

Table 14. ANOVA results for efficiency.

Sources	**DF**	**Adj. SS**	**Adj. MS**	**F-Value**	**P-Value**
Regression	3	2.29991	0.766636	3648.65	0.000
A	1	0.03208	0.032083	152.69	0.000
B	1	0.00005	0.000048	0.23	0.633
m	1	0.82679	0.826792	3934.95	0.000
Error	314	0.06598	0.000210	-	-
Total	317	2.36588	-	-	-

Table 15. Model summary.

Statistic	***Value***
S	0.0144953
R^2	97.21%
R^2 (adj)	97.18%
R^2 (pred)	97.13%

Table 16. Coefficient summary.

Terms	Coeff.	SE Coeff.	T-Values	P-Values	VIF
Constant	1.7055	0.0459	37.19	0.000	-
A	-0.000234	0.000019	-12.36	0.000	3.96
B	0.000155	0.000324	0.48	0.633	1.01
m_2	-0.003054	0.000049	-62.73	0.000	3.98

The developed regression equation is:

$$E = 1.7055 - (0.000234 \times A) + (0.000155 \times B) - (0.003054 \times m_2) \tag{16}$$

This model demonstrates that heat flux at 12 noon (A) and m_2 have significant negative impacts on efficiency, whereas heat flux at off-sunshine hours (B) does not significantly affect efficiency. The R² value of 97.21% indicates a very high explanatory power of the model. Diagnostics for unusual observations with residual flags are shown in Table 17.

Table 17. Detections of unusual observations.

Obs.	**E**	**Fit**	**Resid.**	**Std. Resid.**	**R**	**X**
25	0.60608	0.57262	0.03346	2.32	R	-
186	0.71036	0.66550	0.04486	3.12	R	-
314	0.35342	0.37660	-0.02318	-1.69	X	-

The relationship between heat flux at 12 noon hours and efficiency (E) is examined. Figure 5. Illustrate the relationship between moisture removal rate and drying efficiency (%).

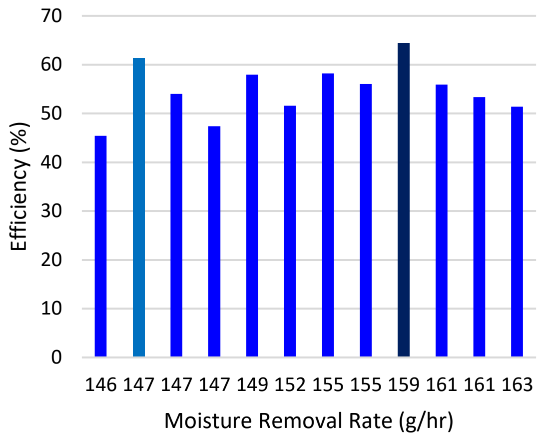

Figure 5. Moisture removal rate vs Efficiency during off sunshine hours.

The regression analyses provided significant insights into the effects of heat flux at noon, heat flux at off-sunshine hours, moisture removal rate, and solar dryer efficiency.

Key findings include:

- Heat flux at noon significantly negatively affects the moisture removal rate and efficiency under both off-sunshine and on-sunshine conditions.
- Moisture removal rate (m) significantly affects efficiency, with higher moisture removal rates leading to higher efficiency.
- heat flux leading to increased moisture removal and efficiency.

These findings underscore the necessity of managing environmental factors to enhance the effectiveness of solar dryers. Future research should aim to refine data collection

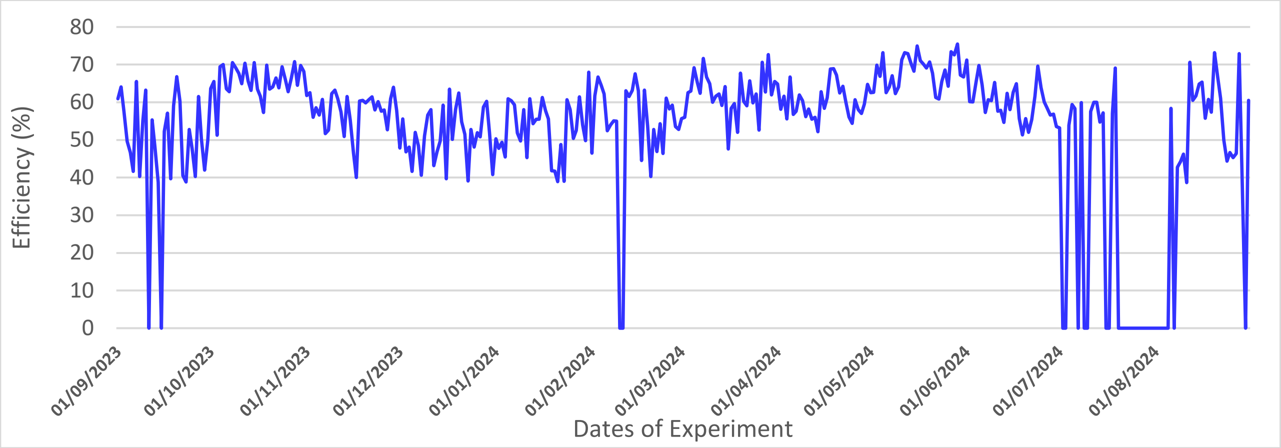

Figure 6. Overall drying of 366 days during the sunny hours of the experiments from Sept. 2023 to Aug. 2024.

methods and investigate other variables that could affect dryer efficiency.

Complete Experimental Results: The average drying efficiency has been evaluated over 366 days of experiments during sunny hours as illustrated in Figure 6, providing a comprehensive view of the performance dryer across all months. The analysis revealed notable monthly variations in average drying efficiency, peaking in May at 68.1%, indicating optimal conditions for moisture removal during this period. It was observed that October also showed high efficiency at 65.7%, followed by March at 62.0% and April at 60.2%, suggesting that the transitional seasons may offer favorable conditions for drying.

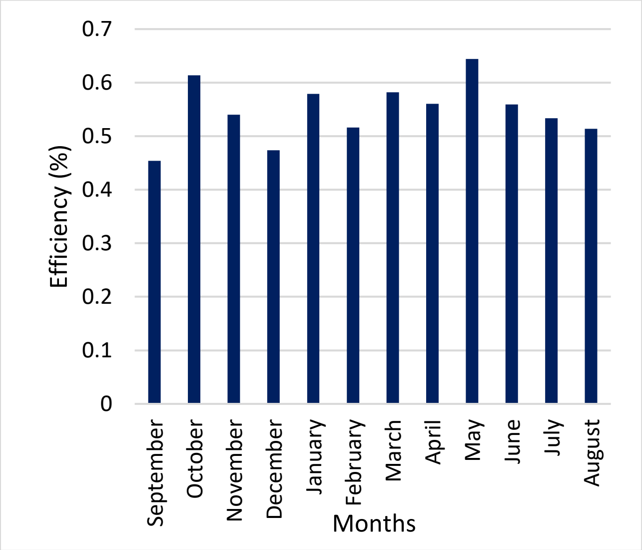

Figure 7. Average monthly drying during sunny hours.

On the lower end, December and September exhibited the lowest efficiencies, at 51% and 51.6% respectively, which we attribute to shorter daylight hours and potentially less intense solar radiation.

Heat flux is a critical predictor for moisture removal rate and efficiency during on sunshine conditions, with the average drying efficiency being assessed for the solar dryer during off-sunny hours over 366 days shown in the graph of Figure 7, providing insights into its performance during less ideal conditions across different months. This analysis showed significant monthly fluctuations in drying efficiency, with May achieving the highest efficiency at 64.4%, indicating that the dryer was still able to perform well even without direct sunlight during this period. October also demonstrated high efficiency at 61.3%, followed by March at 58.2% and January at 57.9%, suggesting that these months provided favorable conditions for drying, possibly due to residual heat and ambient conditions.

In contrast, the efficiency during off-sunny hours was lower in months like September and December, which showed efficiencies of 45.4% and 47.4%, respectively. These results can be attributed to shorter daylight hours and cooler temperatures, which limit the dryer's effectiveness. Winter months, such as February and November, displayed moderate efficiencies, with values of 51.6% and 54% respectively, benefiting from the presence of stored thermal energy and favorable ambient conditions. The summer months, represented by June (55.9%) and July (53.3%), also maintained moderate efficiencies, likely due to higher ambient temperatures assisting the drying process even in the absence of direct sunlight. These findings underscore the solar dryer's capability to utilize ambient and residual heat effectively during off-sunny hours, highlighting the importance of optimizing design and operational strategies to enhance its performance throughout the year.

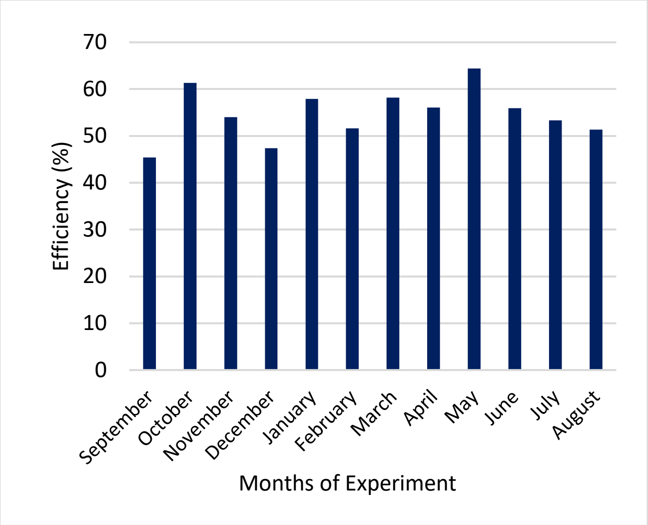

Figure 8. Average monthly drying efficiency during off-sunshine hours.

The solar dryer efficiency analysis over a span of 366 days for sunshine hours reveals several insights, as shown in the graph of Figure 8. The data we have collected indicates that the dryer efficiency fluctuates throughout the year, with notable peaks such as 64% on October 28, 2023, and 70.5%

on October 8 and 15, 2023. The graph illustrating these variations over the year highlights the efficiency of the solar dryer, with trends suggesting that specific days achieve optimal performance, likely due to favorable environmental conditions. This comprehensive year-long data provides valuable insights into the operational dynamics and potential for optimizing solar dryer performance.

5.2 Uncertainty Analysis

The ANOVA results demonstrated significant effects of heat flux and PCM integration on the performance metrics of the solar dryer. The regression model was highly significant (P-Value < 0.000), with an F-Value of 460.18, and explained a substantial portion of the variance in moisture removal rates (R^2 = 74.89%). Heat flux at noon had a significant negative impact on both moisture removal rate and efficiency, whereas heat flux during off-sunshine hours had a positive but non-significant impact.

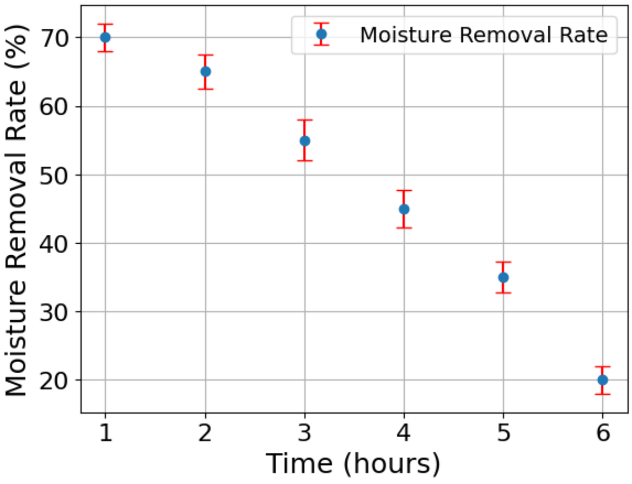

Figure 9. Moisture removal rate vs time with uncertainty.

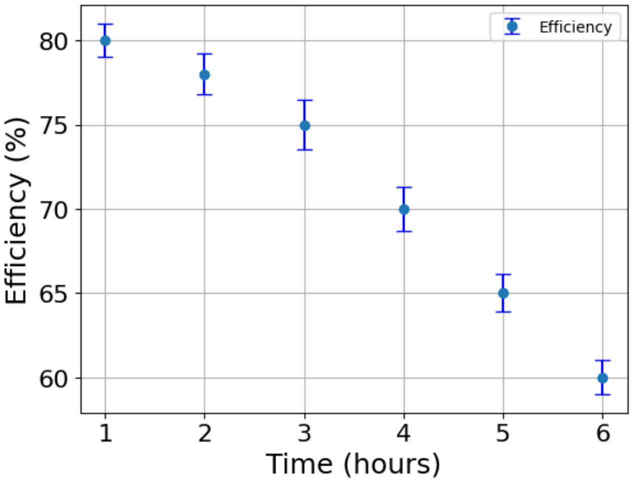

Figure 10. Efficiency vs time with uncertainty.

Figure 9 and Figure 10 illustrate the moisture removal rate and efficiency of the solar dryer over time, with error bars representing the uncertainties in measurements. The moisture removal rate decreases significantly over 6 hours of drying, with uncertainties ranging from 2% to 3%. Similarly, the efficiency of the dryer decreases over time, with uncertainties ranging from 1% to 1.5%. These results highlight the critical role of controlling environmental factors to optimize dryer performance. Future research should focus on improving data collection accuracy and exploring additional factors that may influence efficiency.

5.3 Discussion

The ANOVA analysis offered strong evidence that incorporating PCMs and optimizing airflow rates notably improved the performance metrics of the solar dryer. The application of PCMs resulted in shorter drying times and enhanced moisture removal rates and efficiency. These findings are consistent with previous research that emphasized the advantages of utilizing PCMs in thermal storage applications [25].

Impact of PCMs on Drying Time: The notable fall in time of drying time can be linked to the thermal storage capability of PCMs, which aids in sustaining a more stable drying temperature, thus speeding up the drying process. PCMs effectively absorb and release heat during phase transitions, ensuring that the drying chamber stays within an optimal temperature range, even when solar radiation fluctuates. This consistent thermal environment reduces the overall drying time, making the process more efficient [26, 27, 28].

Moisture Removal Rate Effect: The moisture removal rates has been observed in high use of PCMs, and optimized air flow rates can be explained by the more stable and optimal drying environment provided by these modifications. PCMs help in maintaining a uniform temperature, which is crucial for efficient moisture removal [29].

Additionally, the enhanced air flow increases the rate of moisture evaporation by improving the heat transfer and carrying away the moisture-laden air more effectively. This synergistic effect of thermal stability and improved air flow results in higher moisture removal rates [30].

Efficiency Improvements: The overall efficiency improvements were the result of reduced drying time and increased moisture removal rate, demonstrating the effectiveness of the proposed design modifications. The integration of PCMs and optimized air flow significantly enhances the energy utilization efficiency, making the solar dryer more sustainable and cost-effective [31].

Recommendations for Further Research: The experimental findings provide a strong basis for recommending the integration of PCMs in solar dryers, especially in regions with variable solar radiation [32]. Investigations into the long-term performance and durability of PCMs, as well as their economic feasibility, would also be valuable. Additionally, exploring the combination of PCMs with other renewable energy sources, such as photovoltaic panels, could further enhance the sustainability of drying [33].

The PCM integration and optimization of rates of air flow significantly improve the performance of solar dryers. These modifications reduce drying times, increase moisture removal rates, and enhance overall efficiency, making the drying process more effective and sustainable [34].

ANOVA results having the relatively low R^2 values in this study are attributed to several factors. Environmental variability, such as changes in ambient temperature, humidity, solar radiation intensity, and wind speed, introduces significant noise into the data, making it difficult to capture all influences accurately in a statistical model. Sample inconsistency, including variations in the initial moisture content and size of the potato slices, can lead to inconsistent drying behavior and affect the uniformity of the drying process. Experimental variations, such as slight differences in the positioning of thermocouples and hygrometers or inconsistencies in airflow within the drying chamber, can introduce errors, contributing to the overall variance not explained by the model. Additionally, model simplifications may not fully account for the complex interactions between different factors affecting the drying process. For instance, interactions between temperature, airflow rate, and PCM performance might be more intricate than the model can capture, leading to lower R^2 values. Addressing these factors in future studies could help improve the model's accuracy and provide a more comprehensive understanding of the solar drying process with PCM integration.

6. Conclusion

This study systematically investigated the impact of integrating Phase Change Materials (PCMs) and photovoltaic (PV) panels into solar dryers, focusing on drying time, moisture removal rate, and overall efficiency. The findings indicate that PCM use significantly enhances the dryers' performance, particularly during off-sunshine hours. The integration of PCMs and improved airflow mechanisms resulted in a substantial reduction in drying time compared to the control setup. This improvement is crucial for timely processing of agricultural products, reducing spoilage, and enhancing economic returns for farmers. Additionally, solar dryers equipped with PCMs exhibited higher moisture removal rates, underscoring the effectiveness of PCMs in maintaining consistent thermal energy, which is essential for efficient moisture extraction from produce.

Despite these positive outcomes, some limitations need addressing. Environmental variability and sample inconsistency can affect the uniformity of the drying process. Future research should explore a broader range of crops and climatic conditions to validate the effectiveness and versatility of these technologies. Moreover, refining experimental setups and models to better capture complex interactions could improve the accuracy of results.

Overall, integrating PCMs and PV panels in solar dryers presents a promising advancement in agricultural technology, offering benefits in drying efficiency, energy conservation, and sustainability. This approach can enhance product quality, reduce energy consumption, and support sustainable agricultural practices, ultimately contributing to improved food security and economic stability for farmers.

Conflict of Interest

The authors declare that they have no known competing financial interests or personal relationships that could have appeared to influence the work reported in this paper.

Nomenclature

R^2	Coefficient of determination
$P - value$	Probability value for statistical significance
$Adj\ SS$	Adjusted Sum of Squares
η	Efficiency of the solar dryer
Q	Heat flux (W/m²)
M	Moisture removal rate (kg/h)
t	Drying time (h)
T	Temperature (°C)
V	Air flow rate (m³/s)
H	Humidity (%)
m	Mass of the agricultural product (kg)
ΔH	Change in enthalpy (J)
k	Thermal conductivity (W/m·K)
ρ	Density (kg/m³)
C_p	Specific heat capacity (J/kg·K)

References:

[1] M. H. Masud, M. U. Joardder, A. A. Ananno, and S. Nasif, "Feasibility study and optimization of solar-assisted intermittent microwave–convective drying condition for potato," *Eur. Food Res. Technol.*, vol. 248, no. 5, pp. 1335–1349, 2022, doi: 10.1007/s00217-022-03957-5.

[2] W. Cheng *et al.*, "A comparative study of mango solar drying methods by visible and near-infrared spectroscopy coupled with ANOVA-simultaneous component analysis (ASCA)," *LWT - Food Science and Technology*, vol. 112, Sep. 2019, Art. no. 108214, doi: 10.1016/j.lwt.2019.05.112.

[3] N. R. Nwakuba, "Optimisation of energy consumption of a solar-electric dryer during hot air drying of tomato slices," *Journal of Agricultural Engineering*, vol. 50, no. 3, pp. 150–158, Jul. 2019, doi: 10.4081/jae.2019.876.

[4] D. B. Jadhav, G. L. Visavale, P. P. Sutar, U. S. Annapure, and B. N. Thorat, "Solar cabinet drying of bitter gourd: Optimization of pretreatments and quality evaluation," *International Journal of Food Engineering*, vol. 6, no. 4, Aug. 2010, doi: 10.2202/1556-3758.1503.

[5] A. Jha and P. P. Tripathy, "Optimization of process parameters and numerical modeling of heat and mass transfer during simulated solar drying of paddy," *Computers and Electronics in Agriculture*, vol. 187, Aug. 2021, Art. no. 106215, doi: 10.1016/j.compag.2021.106215.

[6] M. Ssemwanga, E. Makule, and S. I. Kayondo, "Performance analysis of an improved solar dryer integrated with multiple metallic solar concentrators for drying fruits," *Solar Energy*, vol. 204, pp. 419–428, Jul. 2020, doi: 10.1016/j.solener.2020.04.065.

[7] P. J. Etim, A. B. Eke, K. J. Simonyan, K. C. Umani, and S. Udo, "Optimization of solar drying process parameters of cooking banana using response surface methodology," *Scientific African*, vol. 13, Sep. 2021, Art. no. e00964, doi: 10.1016/j.sciaf. 2021.e00964.

[8] D. I. Onyenwigwe, M. C. Ndukwu, F. I. Abam, and others, "Eco-thermal analysis and response surface optimization of the drying rate of potato slices in a mix-mode solar dryer," *Iranian Journal of Science and Technology, Transactions of Mechanical Engineering*, vol. 47, pp. 1379–1396, Dec. 2023, doi: 10.1007/s40997-023-00595-4.

[9] C. Mamulkar, S. Ikhar, and V. Katekar, "Computational fluid dynamic analysis of solar dryer equipped with different phase change materials," *International Journal of Thermodynamics*, vol. 27, no. 1, pp. 35–42, Mar. 2024, doi: 10.5541/ijot.1324341.

[10] C. E. Onu, P. K. Igbokwe, J. T. Nwabanne, C. O. Nwajinka, and P. E. Ohale, "Evaluation of optimization

techniques in predicting optimum moisture content reduction in drying potato slices," *Artificial Intelligence in Agriculture*, vol. 4, pp. 39–47, May. 2020, doi: 10.1016/j.aiia.2020.04.001.

[11] C. Sharma, M. P. Singh, and S. Chaudhary, "Cost Analysis of Solar-Wind Based Hybrid Renewable Energy System," in *Advances in Automation, Signal Processing, Instrumentation, and Control*, vol. 700, V. L. N. Komanapalli, N. Sivakumaran, and S. Hampannavar, Eds., Singapore: Springer Nature Singapore, 2021, pp. 2733–2746. doi: 10.1007/978-981-15-8221-9_256.

[12] A. Tesfaye and N. G. Habtu, "Fabrication and performance evaluation of solar tunnel dryer for ginger drying," *International Journal of Photoenergy*, vol. 2022, Oct. 2022, Art. no. 6435080, doi: 10.1155/2022/6435080.

[13] M. Das and E. K. Akpinar, "Determination of thermal and drying performances of the solar air dryer with solar tracking system: Apple drying test," *Case Studies in Thermal Engineering*, vol. 21, Oct. 2020, Art. no. 100731, doi: 10.1016/j.csite.2020.100731.

[14] X. Li, M. Liu, L. Duanmu, and Y. Ji, "The optimization of solar heating system with seasonal storage based on a real project," *Procedia Engineering*, vol. 121, pp. 1341–1348, Oct. 2015, doi: 10.1016/j.proeng.2015.09.017.

[15] A. Lingayat, V. P. Chandramohan, and V. R. K. Raju, "Design, development and performance of indirect type solar dryer for banana drying," *Energy Procedia*, vol. 109, pp. 409–416, Mar. 2017, doi: 10.1016/j.egypro.2017.03.041.

[16] D. Wang, J. Liu, Y. Liu, Y. Wang, B. Li, and J. Liu, "Evaluation of the performance of an improved solar air heater with 'S' shaped ribs with gap," *Solar Energy*, vol. 195, pp. 89–101, Jan. 2020, doi: 10.1016/j.solener.2019.11.034.

[17] G. Yuan, L. Hong, X. Li, L. Xu, W. Tank, and Z. Wang, "Experimental investigation of a solar drying system for drying carpets," *Energy Procedia*, vol. 75, pp. 1561–1568, 2015, doi: 10.1016/j.egypro.2015.07.256.

[18] D. Walraven, B. Laenen, and W. D'haeseleer, "Comparison of thermodynamic cycles for power production from low-temperature geothermal heat sources," *Energy Conversion and Management*, vol. 66, pp. 220–233, Feb. 2013, doi: 10.1016/j.enconman.2012.10.003.

[19] V. P. Katekar and S. S. Deshmukh, "A review of the use of phase change materials on performance of solar stills," *Journal of Energy Storage*, vol. 30, Aug. 2020, Art. no. 101398, doi: 10.1016/j.est.2020.101398.

[20] A. Hedau and S. K. Singal, "Study on the thermal performance of double pass solar air heater with PCM-based thermal energy storage system," *Journal of Energy Storage*, vol. 73, Part B, Dec. 2023, Art. no. 109018, doi: 10.1016/j.est.2023.109018.

[21] S. Haldorai, S. Gurusamy, and M. Pradhapraj, "A review on thermal energy storage systems in solar air heaters," *International Journal of Energy Research*, vol. 43, no. 12, pp. 6061–6077, Apr. 2019, doi: 10.1002/er.4379.

[22] W. P. Missana, E. Park, and T. T. Kivevele, "Thermal performance analysis of solar dryer integrated with heat energy storage system and a low-cost parabolic solar dish concentrator for food preservation," *Journal of Energy*, vol. 2020, no. 1, Jul. 2020, Art. no. 9205283, doi: 10.1155/2020/9205283.

[23] O. Ojike and W. I. Okonkwo, "Study of a passive solar air heater using palm oil and paraffin as storage media," *Case Studies in Thermal Engineering*, vol. 14, Sept. 2019, Art. no. 100454, doi: 10.1016/j.csite.2019.100454.

[24] M. A. Eltawil, M. M. Azam, and A. O. Alghannam, "Solar PV powered mixed-mode tunnel dryer for drying potato chips," *Renewable Energy*, vol. 116, Part A, pp. 594-605, Feb. 2018, doi: 10.1016/j.renene.2017.10.007.

[25] H. K. Mosuru and V. P. Chandramohan, "Numerical analysis of solar air collector with trapezoidal ribbed absorber plate of indirect solar dryer: estimation of performance parameters with proposed pitch for better performance," *Environmental Development and Sustainability*, vol. 27, pp. 7115–7139, Jan. 2024, doi: 10.1007/s10668-023-04182-0.

[26] S. Chouicha, A. Boubekri, D. Mennouche, and M. H. Berrbeuh, "Solar Drying of Sliced Potatoes. An Experimental Investigation," *Energy Procedia*, vol. 36, pp. 1276–1285, Aug. 2013, doi: 10.1016/j.egypro.2013.07.144.

[27] P. P. Tripathy and S. Kumar, "Influence of Sample Geometry and Rehydration Temperature on Quality Attributes of Potato Dried Under Open Sun and Mixed-Mode Solar Drying," *International Journal of Green Energy*, vol. 6, no. 2, pp. 143–156, Apr. 2009, doi: 10.1080/15435070902784863.

[28] A. Djebli, S. Hanini, O. Badaoui, B. Haddad, and A. Benhamou, "Modeling and comparative analysis of solar drying behavior of potatoes," *Renewable Energy*, vol. 145, pp. 1494–1506, Jan. 2020, doi: 10.1016/j.renene.2019.07.083.

[29] S. Kesavan, T. V. Arjunan, and S. Vijayan, "Thermodynamic analysis of a triple-pass solar dryer for drying potato slices," *J Therm Anal Calorim*, vol. 136, pp. 159–171, Apr. 2019, doi: 10.1007/s10973-018-7747-0.

[30] M.Y. Nasri and A. Belhamri, "Effects of the climatic conditions and the shape on the drying kinetics, Application to solar drying of potato-case of Maghreb's region," *Journal of Cleaner Production*, vol. 183, pp. 1241–1251, May. 2018, doi: 10.1016/j.jclepro.2018.02.103.

[31] D. Aydin, S.E. Ezenwali, M.Y. Alibar, and X. Chen, "Novel modular mixed-mode dryer for enhanced solar energy utilization in agricultural crop drying applications," *Energy Sources, Part A: Recovery, Utilization, and Environmental Effects*, vol. 43, no. 16, pp. 1958–1974, Sep. 2019, doi: 10.1080/15567036.2019.1663306.

[32] A. Fudholi, K. Sopian, M.H. Ruslan, M.A. Alghoul, and M.Y. Sulaiman, "Review of solar dryers for agricultural and marine products," *Renewable and Sustainable Energy Reviews*, vol. 14, no. 1, pp. 1–30, Jan. 2010, doi: 10.1016/j.rser.2009.07.032.

[33] C. Karapire, M. Kus, G. Turkmen, C.C. Trevithick-Sutton, C.S. Foote, and S. Icli, "Photooxidation studies with perylenediimides in solution, PVC and sol–gel thin films under concentrated sun light," *Solar Energy*, vol. 78, no. 1, pp. 5–17, Jan. 2005, doi: 10.1016/j.solener.2004.07.003.

[34] P.R. Olivkar, V.P. Katekar, S.S. Deshmukh, and S.V. Palatkar, "Effect of sensible heat storage materials on the thermal performance of solar air heaters: State-of-the-art review," *Renewable and Sustainable Energy Reviews*, vol. 157, Apr 2022, Art. no. 112085, doi: 10.1016/j.rser.2022.112085.

[35] M.A. Eltawil, M.M. Azam, and A.O. Alghannam, "Energy analysis of hybrid solar tunnel dryer with PV system and solar collector for drying mint (*Mentha Viridis*)," *Journal of Cleaner Production*, vol. 181, pp. 352–364, Apr. 2018, doi: 10.1016/j.jclepro.2018.01.229.

[36] G. Srinivasan, D.K. Rabha, and P. Muthukumar, "A review on solar dryers integrated with thermal energy storage units for drying agricultural and food products," *Solar Energy*, vol. 229, pp. 22–38, Nov. 2021, doi: 10.1016/j.solener.2021.07.075.

International Journal of Thermodynamics (IJoT)
ISSN 1301-9724 / e-ISSN 2146-1511
https://dergipark.org.tr/en/pub/ijot

Vol. 28 (No. 2), pp. 115-128, 2025
doi: 10.5541/ijot.1608741

Review Article

Bibliometric Analysis of Research Trends in Steam Boiler Efficiency Improvement

M. Elwardany

Department of Mechanical Power Engineering, Faculty of Engineering, Assiut University, Asyut 71516, Egypt
E-mail: M.Wardany@anu.edu.eg

Received 28 December 2024, Revised 7 March 2025, Accepted 11 April 2025

Abstract

Steam boilers are widely used in power generation and industrial processes. Improving their efficiency is crucial for enhancing sustainability and reducing operating costs. This study conducts a comprehensive bibliometric analysis to map the evolving research landscape on steam boiler efficiency improvement from 2014 to 2023. A literature search in the Scopus database retrieved 3574 publications. This study employs bibliometric analysis using Bibliometrix R packages and VOSViewer software to examine research trends, focusing on publication growth, key journals, influential authors, and emerging themes in steam boiler efficiency improvement. The results indicate a significant increase in annual research output, reflecting sustained global efforts in the field. China leads in both the volume and impact of contributions. Key research themes include materials development, innovative designs, heat recovery, and sustainable solutions. Notable publications emphasize eco-friendly approaches such as solar and organic thermoelectrics. Prolific authors from China, the United States, and Europe have shaped the discourse through influential collaborations. Emerging trends highlight a growing focus on renewable energy integration, advanced thermal management, and computational methodologies. This study consolidates knowledge on enhancing steam boiler efficiency through both quantitative and qualitative analyses, showcasing remarkable progress driven by dedicated international efforts. These insights can inform future strategies and inspire innovation in optimizing this critical energy conversion process.

Keywords: *Boiler; steam generator; efficiency; bibliometric analysis; literature review.*

1. Introduction

Energy utilization serves as a key indicator of progress. Population growth, urbanization, industrial expansion, and technological advancements have significantly increased global energy demand. However, this rapid rise has also contributed to environmental challenges, including pollution and climate change. Currently, fossil fuels generate 80% of the world's electricity, while renewable sources account for the remaining 20% [1], [2], [3]. Global electricity demand is rising steadily at an annual rate of approximately 6% [4], [5]. The widespread use of fossil fuels is a major contributor to CO_2 emissions [6], [7], [8]. Thermal power plants can be categorized into four main types: cogeneration systems, combined-cycle power plants, natural gas-fired power plants, and coal-fired power plants [7], [9], [10].

Steam boilers are essential components of thermal power plants, generating high-pressure superheated steam to drive turbines for electricity production. Enhancing boiler efficiency and performance is critical to improving the sustainability and competitiveness of coal-based power generation [11], [12], [13], [14]. This process requires the seamless integration of various components, including the furnace, superheater, evaporator, air preheater, and economizer, along with auxiliary systems such as pumps, fans, burners, and chimneys [15], [16], [17]. Given the depletion of fossil fuel resources and rising environmental concerns, there is a growing need for more efficient boiler operation [18], [19], [20], [21], [22], [23]. This demand has driven advancements in boiler design, emphasizing the identification and reduction of major thermodynamic losses. A comprehensive performance assessment of boiler systems is essential for pinpointing inefficiencies and prioritizing necessary modifications [14], [24], [25]. The components responsible for the highest thermodynamic losses offer the most potential for improvement. Despite numerous international environmental agreements, many boilers continue to operate with suboptimal control settings, resulting in efficiencies lower than manufacturer specifications [7], [26], [27].

The pursuit of efficient energy utilization is a cornerstone of modern industrial development and sustainability efforts. In this context, steam boilers, essential across various sectors, require continuous innovation to enhance performance and minimize energy waste [28], [29], [30], [31]. This bibliometric study provides a comprehensive analysis of the evolving landscape of steam boiler efficiency improvements, examining key research trends, groundbreaking advancements, and emerging directions in the field. As critical components of energy conversion and industrial processes, steam boilers play a vital role in energy-intensive sectors such as power generation, manufacturing, and heating systems. However, optimizing their efficiency remains an ongoing challenge, requiring a deep understanding of technological advancements, methodological approaches, and material innovations [32], [33], [34], [35], [36], [37].

*Corresponding Author

This bibliometric study endeavors to map and analyze the extensive body of literature encompassing seminal works, research trajectories, and transformative insights elucidating the nuanced landscape of steam boiler efficiency enhancement. Spanning a wide array of disciplines, the investigation aims to distill trends, identify key contributors, and chart the progression of innovative strategies and technologies poised to redefine the efficiency paradigm in steam boiler operations. With energy conservation and sustainability at the forefront of global concerns, the impetus to elevate the efficiency of steam boilers is paramount. This research serves as a comprehensive compass, navigating through the vast corpus of scholarly endeavors, consolidating knowledge, and paving the way for a deeper comprehension of the evolving trends and future directions in steam boiler efficiency improvement [38], [39], [40], [41], [42], [43], [44] Bibliometrics has gained substantial importance within information science, particularly in monitoring information and managing knowledge. Recent studies have extensively explored bibliometric patterns across a range of research areas, including management, econometrics, health economics, marketing, statistics, ecological economics, entrepreneurship, production and operations management, data envelopment, gray systems, and innovation [45], [46], [47], [48], [49], [50], [51], [52]. This rising trend emphasizes the acknowledgment of bibliometrics as a valuable tool for understanding and assessing research trends spanning diverse fields. This analytical method provides insights into the development, patterns, collaborations, structure, and impact within specific knowledge domains. Researchers leverage specialized software like Bibliometrix, VOSviewer, and CiteSpace to perform bibliometric analyses, enabling the identification of information sources, acknowledging previous work, substantiating claims with evidence, and unveiling potential research avenues. This approach is integral to conducting comprehensive literature reviews, enabling researchers to analyze extensive bibliographic data and generate various graphs, maps, and indicators for thorough exploration and interpretation [53], [54], [55], [56], [57], [58], [59].

Secades et al. [60] reviewed waste heat recovery technologies for marine engine efficiency using bibliometric analysis and the PRISMA 2020 framework. From an initial 576 studies (Scopus & Web of Science), they refined their selection to 35 key papers. The Organic Rankine Cycle emerged as the leading method, with potential for cold energy recovery in LNG vessels. Thermoelectric generators were identified as a promising but underexplored area, highlighting a gap in research on low-grade waste heat recovery. Yu et al. [61] analyzed SeCO_2 cycle research (2000–2019) using Scopus and BibExcel, covering 724 publications, 1,378 authors, and 543 institutions from 55 countries. With an average of 13.39 citations per paper, the US led research, followed by China and South Korea. Their study categorized publications into applications, cycle configurations, CO_2-based mixtures, system components, and experiments, providing insights for advancing SeCO_2 power system commercialization.

Zahedi et al. [62] analyzed CO_2 capture in combined cycle power plants using bibliometric analysis and data mining. Using VOSViewer, they mapped key terms, tracked publication trends, and examined CPC and IPC clusters. Their study highlighted energetic dark greenhouses as a promising CO_2 capture technology and proposed policy solutions for market failures. They concluded that coupling NGCC power plants with energetic dark greenhouses offers a highly efficient CCS solution with lower regeneration energy needs. Similarly, Omoregbe et al. [63] examined carbon capture's role in CO_2 reduction (1998–2018), noting a surge in research post-2008 due to climate policies. The US, UK, and China led the field, with post-combustion capture dominating (80.9%), while oxy-fuel combustion had the lowest share (3.4%).

Malekli et al. [64] explored CO_2 capture in combined cycle power plants using bibliometric analysis and data mining. Using VOSViewer, they clustered topics, tracked publication trends, and analyzed Cooperative (CPC) and International (IPC) Patent Classifications. The study aimed to enhance power plant efficiency by addressing energy gaps through Post-Combustion CO_2 Capture (PCC). Key recommendations included optimizing PCC via exergy and pinch analysis and integrating the Organic Rankine Cycle (ORC) to improve net power output. They also identified market failures, suggesting policy solutions. Gap analysis highlighted opportunities for renewable integration and improved energy efficiency. Ultimately, PCC with tertiary amine absorbents was identified as the most efficient CCS technology for NGCC plants due to lower regeneration energy demands. Similarly, Belmonte [65] conducted a bibliometric analysis on Integrated Solar Combined Cycles (ISCC) from 1990 to 2020 using Web of Science data. The study covered 1,277 publications, 3,157 authors, 1,102 institutions, and 78 countries. Energy Conversion and Management led in publications (158 articles), while Solar Energy had the highest citations (4,438). China was the most productive country (241 publications), with major contributors including the Chinese Academy of Sciences (52 articles) and I. Dincer (24 articles). Keyword analysis provided insights into future ISCC developments and its role in global solar energy research.

Karakurt et al. [66] conducted a bibliometric analysis of steam turbine research (2000–2020) using Scopus, examining 11,751 publications from 652 authors, 500+ institutions, and 101 countries. They analyzed publication types, core domains, influential journals, citation trends, authorship patterns, affiliations, and keyword frequencies. Energy was the most prolific journal, Ibrahim Dincer the leading author, and Singapore ranked highest by Paper Impact Parameter (PIP). Turbomachinery emerged as the dominant research field, with engineering disciplines showing the highest publication-to-citation ratio. Similarly, Permana et al. [67] explored solar applications in Organic Rankine Cycle (ORC) research (2010–2020) through Scopus-indexed bibliometric analysis, covering 1,249 documents, 1,217 authors, 140 institutions, and 56 countries. Major contributors included China, the USA, and Europe. The study identified "Organic Rankine Cycle" and "solar energy" as key research themes, with emerging trends in exergoeconomic analysis, polygeneration, and phase change materials for thermal energy storage.

In the broad field of steam boiler efficiency improvement, there remains a noticeable gap in up-to-date, comprehensive bibliometric analyses. Existing studies often fail to provide a holistic exploration of the entire knowledge landscape, overlooking interconnected research themes and emerging trends. A rigorous bibliometric study can bridge this gap by quantifying the literature, mapping research clusters, and identifying influential works, offering a nuanced perspective on the field's current state. Moreover, limited attention has been given to collaborative networks and authorship patterns. Understanding these collaborations is essential for fostering interdisciplinary efforts and advancing research in this domain. This underscores the need for a detailed examination of authorship networks within a comprehensive bibliometric framework. Additionally, the temporal evolution of research trends in this field remains underexplored. Tracking the development of technologies and scientific contributions over time can reveal innovation patterns and historical progress, enhancing our understanding of this dynamic area. A global perspective on steam boiler efficiency research is also lacking. Analyzing geographical distributions and regional factors influencing research priorities will provide valuable insights into how different parts of the world approach efficiency improvements. Finally, there is a critical gap in identifying and systematically analyzing emerging technologies and methodologies in this field. Addressing this deficiency is crucial for aligning research advancements with industrial needs and sustainability objectives. In summary, these gaps highlight the urgent need for a comprehensive bibliometric analysis of steam boiler efficiency research. Addressing them will not only provide valuable insights but also guide future research directions, enhance collaboration, and drive innovation in this critical area.

This study presents a comprehensive bibliometric analysis of Research Trends in Steam Boiler Efficiency Improvement (RT-SBEI), identifying key trends, influential contributors, and emerging research directions. By critically evaluating publication patterns and methodological approaches, we aim to provide a clear, succinct, and insightful overview that advances the understanding of steam boiler efficiency enhancemen the research delves into multiple dimensions regarding the enhancement of steam boiler efficiency. Firstly, it investigates the primary research domains and prevailing trends centered on augmenting steam boiler efficacy. Additionally, it scrutinizes the influential figures—both authors and institutions—actively propelling advancements in this realm. Moreover, the study aims to identify and assess the most cited and impactful publications within the sphere of steam boiler efficiency enhancement. Furthermore, it examines the evolutionary trajectory of research collaborations among authors and institutions in this specific field. Lastly, the inquiry explores the viability and promise of emerging technologies or methodologies poised to elevate steam boiler efficiency, offering potential avenues for further advancement.

2. Methodology

In detailing the methodology for conducting a literature review and bibliometric analysis, the Scopus database was selected as the primary resource. Its comprehensive document collection surpassed other databases like the Web of Science [68]. However, databases such as ResearchGate and Google Scholar were omitted from data collection due to their lower reliability in producing bibliometric outcomes.

The decision to utilize Scopus as the sole database for this study was driven by its extensive coverage of peer-reviewed literature in engineering and energy disciplines, which are central to research on steam boiler efficiency improvement. Scopus provides a reliable and comprehensive platform for bibliometric analysis due to its broad indexing of high-impact journals and citation records. Nevertheless, we acknowledge that this choice may limit the study's scope, as other databases like Web of Science could include additional relevant publications not captured in Scopus. To ensure the inclusion of only high-quality and relevant publications, this study applied strict exclusion criteria during the data collection process. The analysis was limited to peer-reviewed journal articles and reviews published in English, excluding conference papers, book chapters, and grey literature. This approach was adopted to prioritize rigorously evaluated research, which is widely regarded as the benchmark for academic excellence. By focusing on these sources, we aimed to enhance the reliability and applicability of the findings within the context of steam boiler efficiency improvement.

The exploration covered research conducted between 2014 and 2023, encompassing a substantial timeframe in the field. To initiate the process, a literature search was performed using a tailored query: (("energy efficiency" OR "efficiency enhancement" OR "thermal efficiency" OR "energy optimization" OR "combustion optimization" OR "Combustion efficiency" OR "Fuel efficiency" OR "thermal performance" OR "efficiency improvement" OR "energy saving" OR "energy conservation" OR "performance improvement" OR "efficiency upgrade") AND ("steam boiler" OR "steam system" OR "boiler system" OR "Heat generator" OR "Steam generation" OR "Steam power" OR "Boiler unit" OR "Power boiler" OR "Boiler equipment" OR "Boiler plant" OR "Steam production" OR "steam generator" OR "industrial boiler" OR "heat recovery system" OR "heat recovery boiler" OR "waste heat recovery")).

The keywords employed in this bibliometric analysis were meticulously selected to reflect the scope of research on steam boiler efficiency improvement. Following a preliminary review of existing literature and discussions with experts in mechanical engineering and energy systems, we identified key terms such as 'energy efficiency,' 'thermal performance,' and 'steam boiler,' alongside related concepts like 'waste heat recovery' and 'combustion optimization.' These terms were combined using Boolean operators (e.g., AND, OR) to construct a tailored search query, executed within Scopus's title, abstract, and keyword fields. This filtering method excluded irrelevant topics, ensuring that the 3,574 retrieved documents accurately represent the research domain under investigation. The selection of keywords was based on an extensive preliminary review of the literature in steam boiler efficiency. Alternative keywords and their combinations were tested, and the final query was refined to maximize both precision and recall. For example, initial tests included terms related to waste heat recovery and thermoelectric applications, but these were further filtered to ensure direct relevance to steam boiler performance. This rigorous keyword selection process helped minimize the inclusion of unrelated studies and strengthened the reliability of our dataset. The specified keywords underwent a search within the document's title, abstract, and keyword sections, concluding on 25/12/2023. Our research was limited to publications in journals, specifically focusing on articles and reviews in English to ensure the inclusion of high-quality beer review articles. A total of 3,574 documents were identified and subsequently analyzed. This study spans the period from 2014 to 2023 to capture the most recent and transformative research in steam boiler efficiency improvement. This decade has been characterized by notable advancements, including the development of advanced materials, enhanced waste heat recovery technologies, and the integration of renewable energy sources into boiler systems. Additionally, this timeframe aligns with intensified global initiatives to improve industrial sustainability and mitigate carbon emissions, providing a pertinent context for analyzing research trends and innovations aimed at optimizing steam boiler performance. Figure 1 provides an outline of the methodological approach adopted for bibliometric analysis.

The gathered results were meticulously scrutinized to delineate trends and quantify works categorized by journal type, subject, countries, institutions, and authors. An exhaustive examination of keywords aimed to unveil prominent themes and emerging topics concerning Steam Boiler Efficiency Improvement, aiming to discern research trends and future prospects within the field. Additionally, to visually represent the interconnections among authors, countries, institutions, and keywords, the obtained results were graphically depicted using the bibliometrix library and biblioshiny application [69]. These resources, available as open-source software, were invaluable in extracting meaningful insights from the bibliometric database.

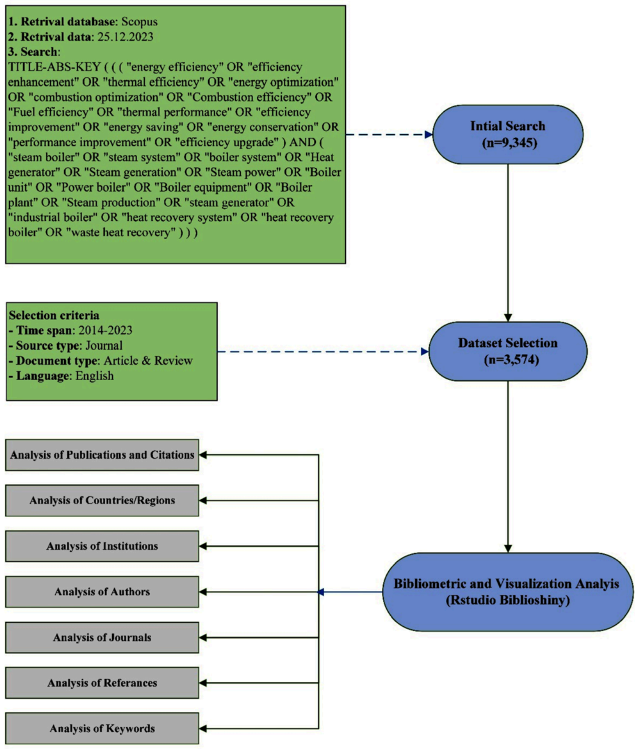

Figure 1. A visual representation outlining the methodology adopted for bibliometric analysis.

Bibliographic records and citation data were sourced from the Scopus API and analyzed using the Bibliometrix R package. Various dataset characteristics, including document types, publication years, source titles, authors, affiliations, citations, and collaborations, were systematically examined. Additionally, publication output, citation trends, and keyword dynamics were analyzed across different time frames. To identify key contributors and research networks, network visualization techniques were employed, highlighting influential countries, institutions, authors, sources, and collaborations. Centrality measures such as betweenness, closeness, and PageRank were computed to identify significant nodes within the research network. Furthermore, keyword co-occurrence analysis was conducted to uncover the intellectual structure and emerging trends within the field.

Visual representations, including treemaps and density visualizations, were utilized to identify highly represented topics. Where applicable, statistical tests such as Spearman's correlation were applied to ensure robust data interpretation. This bibliometric methodology provided both quantitative and qualitative insights into the evolving scholarly landscape of combined cycle power plant research on a global scale. It identified productive and influential researchers, assessed research impact, and highlighted core knowledge domains along with emerging topics requiring further exploration. The findings of this study offer valuable guidance for shaping future research directions and fostering collaborative opportunities within this critical area of energy technology. Despite its comprehensive approach, this study has certain limitations that should be acknowledged. First, the inclusion criteria were restricted to English-language articles, which may have led to the exclusion of relevant research published in other languages. Additionally, while Scopus provides a reliable and extensive database, variations in document selection and quantity may still arise. Furthermore, although the chosen keywords were highly relevant to the study's scope, incorporating alternative keywords could have potentially uncovered additional relevant documents. Recognizing these limitations is essential for contextualizing the study's findings and their broader implications.

3. Results and Discussion

3.1. Effect of Main Information

As shown in Table 1, the comprehensive bibliometric analysis of RT-SBEI covers a substantial period from 2014 to 2023, encompassing 602 sources and 3,539 documents, with a notable annual growth rate of 10.85%. Despite their relatively young average age of 3.6 years, these documents exert significant influence, achieving an impressive average of 25.97 citations per document, even in the absence of internal references.

Table 1. General main information about the data regarding this study.

Description	Results
Timespan	2014:2023
Sources (Journals, Books, etc)	602
Documents	3539
Annual Growth Rate %	10.85
Document Average Age	3.6
Average citations per doc	25.97
Keywords Plus (ID)	14285
Author's Keywords (DE)	8044
Authors	8079
Authors of single-authored docs	108
Single-authored docs	125
Co-Authors per Doc	4.39
International co-authorships %	22.83
article	3341
article article	32
article review	3
review	163

The depth of research in this field is evident from the extensive keyword usage, featuring 14,285 Keywords Plus and 8,044 Author's Keywords, highlighting the multidimensional nature of exploration within this domain. The collaborative aspect of this research is also pronounced, involving 8,079 authors, of whom 108 produced single-authored documents. Collaboration is prevalent, as reflected in an average of 4.39 co-authors per document and an international co-authorship rate of 22.83%. The dataset primarily consists of research articles (3,341), supplemented by article reviews (3), regular reviews (163), and a few other document types. This composition underscores the dominance of original research articles and the collaborative efforts driving advancements in steam boiler efficiency.

An analysis of the Annual Scientific Production trends within RT-SBEI, as illustrated in Figure 2, reveals a compelling progression from 2014 to 2023. The data exhibits a consistent upward trajectory in scholarly output, starting with 205 articles in 2014 and steadily increasing each year, reaching 518 articles in 2023. This growth underscores a significant rise in research interest and activity in this field. Notably, between 2017 and 2023, the pace of production accelerated markedly, reflecting an intensified focus on advancing knowledge in steam boiler efficiency. This steady annual increase highlights the sustained commitment of researchers and the broader scientific community to exploring and innovating strategies for improving steam boiler efficiency over the specified period. While the average annual growth rate of 10.85% in steam boiler efficiency research is substantial, it is important to contextualize this figure by comparing it with growth rates observed in other technological fields. Such comparisons indicate that the field of steam boiler efficiency is not only keeping pace with the overall expansion in scientific productivity but, in some respects, surpasses average trends, thereby underlining its emerging importance in energy sustainability research.

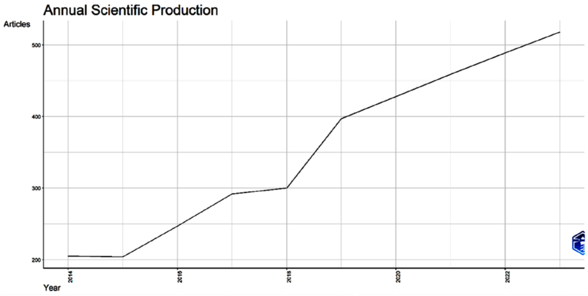

Figure 2. Number of published articles over the investigation period.

3.2 Sources Data

A bibliometric study on RT-SBEI, based on a Scopus search, identified 10 relevant publications between 2013 and 2023, as shown in Figure 3. The analysis of subject areas across these publications highlights a predominant focus on Energy and Engineering, with 2,309 and 2,107 papers, respectively. Environmental Science follows closely with 1,186 papers, while Chemical Engineering and Mathematics make significant contributions, with 564 and 547 papers, respectively. Other disciplines also play notable roles, including Materials Science, Physics and Astronomy, and Chemistry, each contributing over 200 papers. Beyond traditional STEM fields, Business, Management, and Accounting, as well as Computer Science, demonstrate engagement, each with over 100 papers. Additionally, Social Sciences, Agricultural and Biological Sciences, and Earth and Planetary Sciences contribute to a lesser extent, alongside interdisciplinary areas such as Biochemistry, Genetics, and Molecular Biology, Economics, and Medicine.

This comprehensive analysis underscores the multidisciplinary nature of research aimed at improving steam boiler efficiency, spanning both scientific and managerial domains.

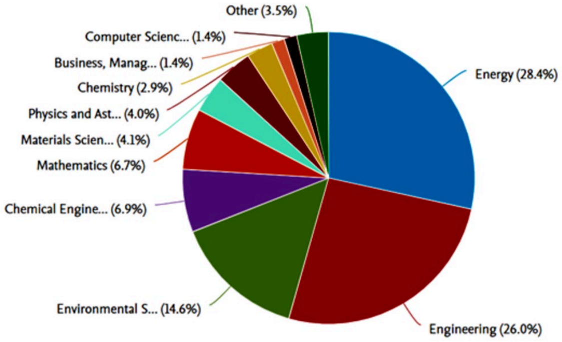

Figure 3. Sharing articles by subject area.

An examination of the local impact of sources contributing to the bibliometric landscape of RT-SBEI reveals several key insights. As shown in Table 2, *Energy* emerges as the leading source, with a high h-index of 61, reflecting substantial citation impact and broad influence within the field. It is closely followed by *Applied Energy* and *Energy Conversion and Management*, which also demonstrate strong citation impact, with h-indices of 58 and 56, respectively. These sources consistently perform well across various metrics, including the g-index and m-index, underscoring their sustained influence. Additionally, *Applied Thermal Engineering*, *Journal of Cleaner Production*, and *Renewable and Sustainable Energy Reviews* exhibit moderate to strong impact, each making significant contributions to the literature with distinct citation patterns. Meanwhile, *Energies*, *Renewable Energy*, *Energy and Buildings*, and the *International Journal of Hydrogen Energy* also play a role, albeit with relatively lower impact compared to the leading sources, highlighting their specialized niches within the broader research landscape on steam boiler efficiency improvement.
These findings collectively emphasize the diverse yet influential contributions of various sources in shaping scholarly discourse within this field.

Table 2. Top 10 sources (Journals) related to combine cycle power plants field.

Journal	**h_index**	**m_index**	**TC**
Energy	61	6.1	15060
Applied energy	58	5.8	10727
Energy conversion and management	56	5.6	10497
Applied thermal engineering	47	4.7	6977
Journal of cleaner production	30	3	2640
Renewable and sustainable energy reviews	28	2.8	3316
Energies	25	2.5	1841
Renewable energy	24	2.4	1443
Energy and buildings	16	1.6	854
International journal of hydrogen energy	15	1.5	880

An analysis of publication trends over time reveals intriguing patterns in the scholarly output related to RT-SBEI. As shown in Figure 4, ENERGY has demonstrated steady growth, beginning with 35 publications in 2014 and reaching a peak of 484 publications in 2023. This consistent upward trend highlights its sustained significance and contribution to the field. Similarly, ENERGY CONVERSION AND MANAGEMENT, APPLIED THERMAL ENGINEERING, and APPLIED ENERGY exhibit substantial growth trajectories over the same period, albeit with varying publication volumes. ENERGIES also shows a notable increase, though at a slightly slower pace compared to the others. The collective upward trend across these key sources reflects a strong and growing commitment to advancing steam boiler efficiency enhancement, underscoring the expanding interest and research efforts in this domain.

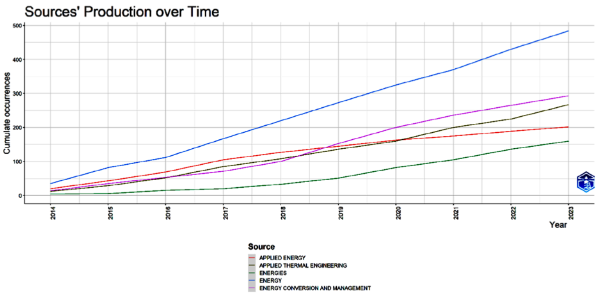

Figure 4. Top 5 sources production over time.

3.3 Country Data

The analysis of corresponding authors' countries provides valuable insights into the global landscape of RT-SBEI research. As illustrated in Figure 5, China emerges as the leading contributor, with 1,175 articles, highlighting its dominant presence in the field. Notably, China's strongest research collaboration is with India, reflecting a growing alliance between these two nations in this domain. Iran follows with 202 articles, demonstrating significant involvement, while the United Kingdom, the USA, South Korea, Turkey, Italy, and Poland also contribute notably, though with fewer publications. Among these countries, the United Kingdom stands out for its high collaboration ratio, emphasizing a strong inclination toward cooperative research efforts. This global participation underscores a collective and collaborative effort among nations to advance steam boiler efficiency, showcasing a shared commitment to innovation in this critical area.

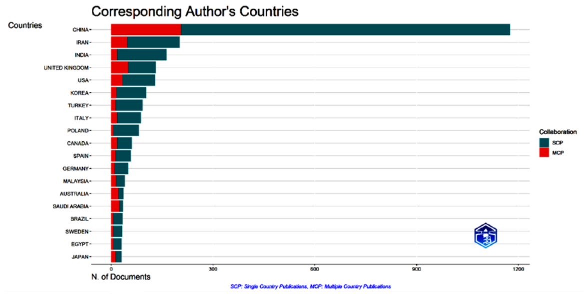

Figure 5. Corresponding authors countries.

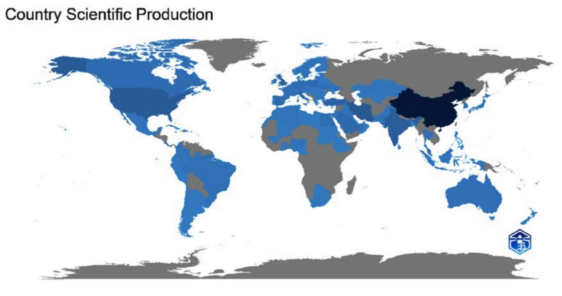

Figure 6. Countries' scientific production.

Figure 6 presents the scientific production of various countries within the RT-SBEI field. China leads with 2,700 articles, reinforcing its strong research engagement and leadership in this domain. Alongside China, Iran, the USA, India, and the UK exhibit substantial scientific output, further highlighting their significant contributions. Additionally, countries such as Turkey, South Korea, Italy, Poland, Saudi Arabia, and Malaysia also demonstrate noteworthy participation, albeit with lower publication frequencies. This broad and diverse global scientific production reflects a widespread international interest in enhancing steam boiler efficiency, emphasizing a collective commitment to advancing knowledge and technological innovations in this essential research area.

The analysis of Countries' Production over Time in the domain of RT-SBEI reveals compelling trends in scientific output across several nations. As reveals in Figure 7 China stands out significantly, displaying a remarkable escalation in scientific production from 103 articles in 2014 to a substantial 2700 articles in 2023, depicting a consistent and robust growth trajectory, emphasizing its pivotal role and enduring commitment to advancing research in this field. India, Iran, the United Kingdom, and the USA also exhibit substantial and escalating scientific output over the years, showcasing their sustained engagement and increasing contributions to the literature, albeit at varying growth rates. These nations collectively demonstrate a steadfast dedication to exploring steam boiler efficiency enhancement, showcasing a collective commitment toward pushing the boundaries of knowledge and innovation in this critical area of study.

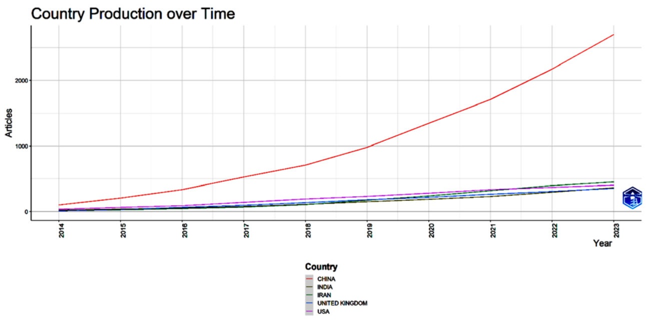

Figure 7. Top 5 country production over time.

The collaborative landscape of countries in steam boiler efficiency improvement is vividly illustrated through a comprehensive network. The data reveal intricate connections among nations actively engaged in this research domain. As shown in Figure 8 and Figure 9, China stands out as a central hub, fostering extensive collaborations worldwide, particularly with the United States and the United Kingdom. India also demonstrates significant involvement, forming strong research ties with China, Malaysia, and Saudi Arabia. The United Arab Emirates emerges as another key player, notably collaborating with Egypt and Malaysia, highlighting its active engagement in this field. Additionally, countries such as Canada, Germany, and Saudi Arabia exhibit diverse partnerships, reinforcing the global nature of research efforts in enhancing steam boiler efficiency. This intricate web of connections underscores the international scope of collaboration in this specialized domain, reflecting a collective commitment to advancing steam boiler efficiency across borders.

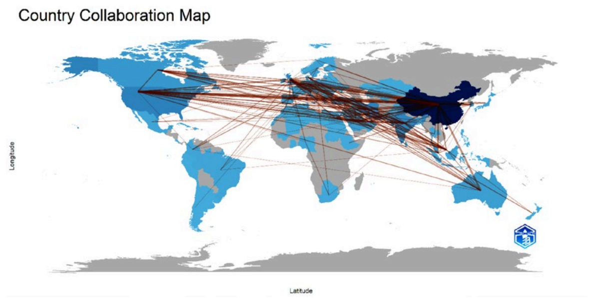

Figure 8. Countries' collaboration world map.

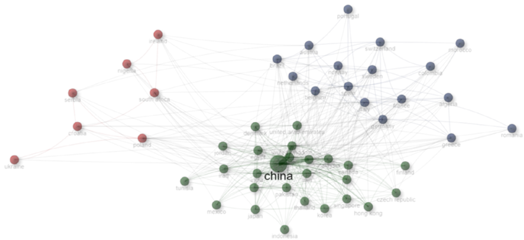

Figure 9. Countries' collaboration network.

3.4 Most Relevant Authors

In analyzing the most relevant authors contributing to the bibliometric landscape of RT-SBEI, several prolific researchers emerge as key contributors. As shown in Figure 10(A), Wang Y leads with 88 articles, holding a significant fractionalized share of 16.67%, highlighting his substantial impact in the field. Following closely, Wang X, Zhang H, and Wang J have published between 65 and 68 articles, demonstrating their noteworthy contributions to the literature. Li J, Li X, Zhang Y, Li Y, Wang Z, and Tian H also rank among the most productive and influential researchers, with their cumulative fractionalized contributions reinforcing their prominence in advancing steam boiler efficiency research. Collectively, these authors shape the scholarly landscape, playing a pivotal role in knowledge dissemination and innovation in this domain

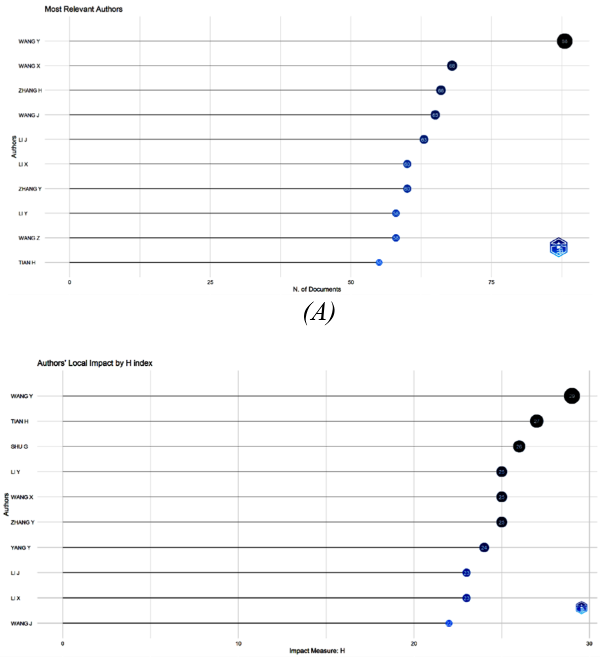

(A)

(B)

Figure 10. Top 10 most relevant authors: (A) Number of publications contributed, (B) Author contribution impact (h-index).

Figure 10(B) presents the h-index values of several authors, reflecting their research impact and productivity in the field. Wang Y stands out with an impressive h-index of 29, followed closely by Tian H and Shu G, with h-indices of 27 and 26, respectively. Additionally, Li Y, Wang X, Zhang Y, and Yang Y demonstrate substantial influence, with h-indices ranging between 25 and 24. The contributions of Li J, Li X, and Wang J, with h-indices of 23 and 22, further highlight their significant involvement in advancing steam boiler efficiency research. Collectively, these authors represent a leading group in the field, with their impactful publications driving advancements and shaping the ongoing discourse on steam boiler efficiency enhancement.

Regarding author collaboration, as illustrated in Figure 11, the bibliometric analysis of the collaborative network in steam boiler efficiency research reveals distinct clusters and key contributors. In Cluster 1, Wang X emerges as a central figure, highlighting his significant influence and strong connections within this group. Closely following, Li X plays a pivotal role in facilitating information flow. Tian H, Shu G, and Shi L demonstrate moderate betweenness and closeness measures, indicating their active engagement in the collaboration network. In Cluster 2, Wang Y occupies a central position, signifying his influential role in knowledge dissemination. Additionally, Zhang H, Wang J, Li J, and Zhang Y play key roles, reinforcing their collaborative impact within this cluster. These findings reveal a diverse, yet interconnected network of authors dedicated to advancing steam boiler efficiency, underscoring the critical contributions of key researchers in knowledge exchange and collaboration across distinct clusters.

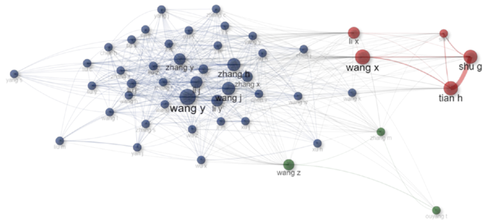

Figure 11. Authors collaboration network.

3.5 Most Relevant Affiliations

In analyzing the key affiliations shaping the bibliometric landscape of RT-SBEI, several institutions stand out as significant contributors. As depicted in Figure 12(A), Tsinghua University leads the field with 127 published articles, underscoring its pivotal role and prolific research output in this domain. Following closely, Xi'an Jiaotong University and North China Electric Power University have published 113 and 96 articles, respectively, reflecting their substantial engagement in advancing steam boiler efficiency enhancement research. Additionally, Tianjin University, Guangxi University, and Islamic Azad University make notable contributions, further reinforcing their impact on the scholarly discourse in this field. Other prominent institutions, including Zhejiang University, Shanghai Jiao Tong University, the University of Science and Technology of China, and the University of Tehran, collectively drive research advancements in steam boiler efficiency. Figure 12(B) illustrates the evolving research output of the top five affiliations over time, revealing dynamic growth trends. Notably, North China Electric Power University demonstrates consistent and impressive growth, increasing its publication count from just five articles in 2014 to 96 in 2023—an indication of its sustained commitment to this research area. Similarly, Tianjin University and Tsinghua University exhibit steady and significant expansion, with escalating publication trends that highlight their long-term dedication to steam boiler efficiency enhancement. Xi'an Jiaotong University also shows a remarkable upward trajectory, with its research output rising from three articles in 2014 to 113 in 2023, underscoring its substantial contribution to the field. Meanwhile, Guangxi University, despite a modest starting point, has demonstrated significant progress, culminating in 62 articles by 2023, an indication of its emerging role in steam boiler efficiency research. These trends collectively highlight the increasing and diverse institutional engagement in this field, reflecting a growing global commitment to advancing steam boiler efficiency improvements over time.

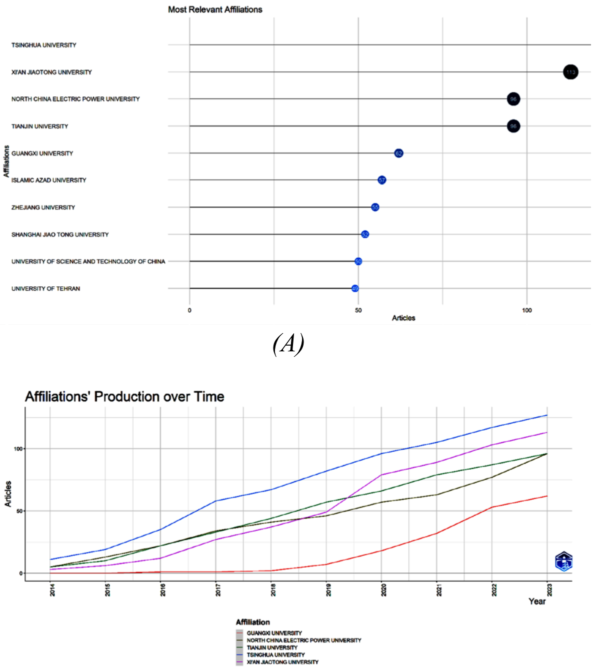

(A)

(B)

Figure 12. Topmost relevant affiliations: (A) Number of publications, (B) Research output over time.

3.6 Articles and Sources of Data

Table 3 presents the top 10 most-cited publications on steam boiler efficiency improvement from 2014 to 2023. These studies represent significant contributions to the field, highlighting emerging trends and key areas of research focus. Notably, many of these publications emphasize sustainable energy solutions, such as *"Solar Steam Generation by Heat Localization"* and *"Organic Thermoelectric Materials: Emerging Green Energy Materials Converting Heat to Electricity Directly and Efficiently."* These works reflect a growing shift toward eco-friendly approaches in enhancing steam boiler efficiency, aligning with broader research trends. The prominence of these studies is further reinforced by their publication in high-impact journals, including *Nature Communications*, *Advanced Materials*, and *Energy & Environmental Science*. Their presence in such esteemed journals underscores the quality and significance of their contributions.

An analysis of yearly citation rates and normalized total citations reveals distinct trends. While some papers consistently maintain high citation rates, reflecting sustained relevance and interest, others exhibit fluctuations, suggesting periodic surges in attention. Additionally, the breadth of topics covered in these highly cited publications is remarkable. From advancements in materials science—such as thermal conductivity enhancement using phase change materials—to innovative applications like simultaneous steam production and electricity generation, these studies showcase the diverse and multifaceted strategies driving progress in steam boiler efficiency. While phase change materials (PCM) [70] and thermoelectric (TE) studies [71] are not boiler-specific, their inclusion reflects their relevance to waste heat recovery in thermal syste*ms, a key sub-theme in steam boiler research.* It should be noted that while the keyword 'waste heat recovery' effectively captures a wide range of studies, it also encompasses research areas not directly related to steam generation. The inclusion of references dealing with phase change materials and thermoelectric applications reflects the interdisciplinary nature of waste heat utilization. We acknowledge this as a limitation in our methodological approach, and future research may benefit from more targeted keyword refinement to isolate studies specifically focused on steam boiler efficiency.

The normalized total citations (TC) in Table 3 were calculated to adjust for citation variations over time, providing a fair comparison across publications from different years. This metric is derived by dividing a publication's total citations by the average citation rate of articles published in the same year. The TC per year column was computed by dividing the total citations by the number of years since publication, offering insight into annual citation impact. These calculations ensure a robust assessment of publication influence.

Table 3. The 10 cited publication in the Steam Boiler Efficiency Improvement from 2014 to 2023.

Ref.	**Paper title**	**TC**	**TC /Year**
[72]	"Solar steam generation by heat localization"	1516	151.60
[71]	"Organic Thermoelectric Materials: Emerging Green Energy Materials Converting Heat to Electricity Directly and Effi ciently"	763	76.30
[73]	"Waste heat recovery technologies and applications"	583	97.17
[70]	"Review on thermal conductivity enhancement, thermal properties and applications of phase change materials in thermal energy storage"	549	91.50
[74]	3D-Printed, All-in-One Evaporator for High-Efficiency Solar Steam Generation under 1 Sun Illumination	520	74.29
[75]	"Wood–Graphene Oxide Composite for Highly Efficient Solar Steam Generation and Desalination"	485	69.29
[76]	"A 3D Photothermal Structure toward Improved Energy Efficiency in Solar Steam Generation"	465	77.50
[77]	"Robust and Low-Cost Flame-Treated Wood for High-Performance Solar Steam Generation"	443	63.29
[78]	"Nature-inspired salt resistant bimodal porous solar evaporator for efficient and stable water desalination"	431	86.20
[79]	"Scalable and Highly Efficient Mesoporous Wood-Based Solar Steam Generation Device: Localized Heat, Rapid Water Transport"	408	68.00
[79]	"Scalable and Highly Efficient Mesoporous Wood-Based Solar Steam Generation Device: Localized Heat, Rapid Water Transport"	408	68.00

Overall, the analysis of these top-cited publications offers valuable insights into the evolving research landscape surrounding steam boiler efficiency improvement. It unveils not only the influential works but also the overarching themes, technological advancements, and diverse methodologies driving progress in this critical domain of energy efficiency.

The analysis of Most Frequent Words and Co-occuramce network Figure 13, and Figure 14 in the domain of RT-SBEI underscores critical themes and focal areas within the scholarly discourse. "Waste heat recovery" emerges as the most prevalent term, emphasizing the paramount importance placed on harnessing and utilizing wasted thermal energy. Additionally, concepts like "organic Rankine cycle (ORC)" and "exergy" signify a substantial interest in advanced cycles and efficiency metrics, respectively, highlighting a drive towards innovative energy conversion methods and rigorous efficiency assessments. Terms such as "optimization," "economic analysis," and "multi-objective optimization" underscore a clear focus on enhancing system performance while considering economic viability, reflecting a balanced approach towards maximizing efficiency and minimizing costs. Furthermore, phrases like "solar energy," "solar steam generation," and "thermal energy storage" point towards an exploration of sustainable and renewable energy sources alongside efficient storage mechanisms, showcasing an inclination towards environmentally friendly solutions in steam boiler operations.

Figure 13. Most frequent words.

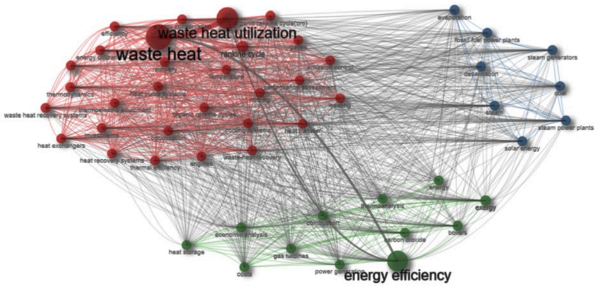

Figure 14. Co-occuramce network on steam boiler efficiency improvements.

In exploring RT-SBEI, a bibliometric study reveals a comprehensive thematic map (Figure 15) of key clusters and their centrality in the discourse. The thematic analysis comprises several clusters, including 'exergy,' 'waste heat recovery,' 'energy efficiency,' 'solar energy,' 'thermal energy storage,' and 'desalination,'. Among the prominent focal points, 'exergy' emerges with high centrality, Waste heat recovery remains pivotal, performance analysis. Furthermore, the discourse extends to energy efficiency, covering themes like energy recovery, energy storage, and diverse methodologies like genetic algorithms and techno-economic analyses. Solar energy and its applications, including solar steam generation and phase change materials, constitute a significant part of the research landscape. The data underlines a multifaceted discourse focused on enhancing steam boiler efficiency, spanning a spectrum from theoretical analyses to practical applications, with a growing emphasis on innovative, sustainable solutions like waste heat recovery and renewable energy integration.

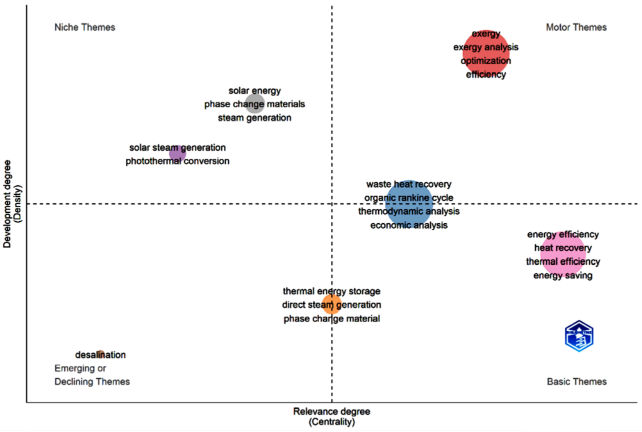

Figure 15. Thematic map on steam boiler efficiency improvements.

Examining the trends in Steam Boiler Efficiency Improvement topics (Figure 16) reveals a progression in research interests. In earlier years, focus was on "various operating conditions," "air pollution," and "bioethanol," marking concerns about operational variations, environmental impact, and alternative fuels. By the mid-2010s, emphasis grew around "ic engine," "rotary kiln," and "diesel engine," underscoring an interest in engine-related studies and combustion systems. The latter part of the decade saw attention shifting to "retrofit," "co2 emissions," and "combined cycle," highlighting retrofitting strategies and emission reduction in thermal systems. The 2017-2022 period witnessed a substantial rise in themes like "energy conservation," "waste heat recovery," and "organic Rankine cycle," showcasing a concentrated effort towards energy efficiency and waste heat utilization. Recent trends, from 2020 to 2023, emphasize "biomass gasification," "thermal management," "ammonia," and "emissions," signaling a move towards sustainable energy sources, advanced thermal control, and emissions reduction using computational methodologies.

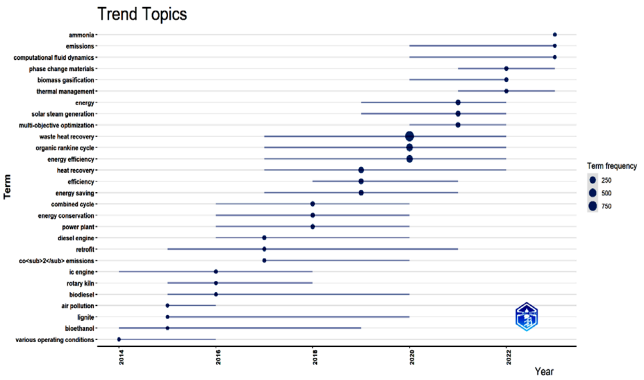

Figure 16. Trend topics.

4. Conclusion and Discussion

The bibliometric analysis provides valuable insights into the evolving landscape of steam boiler efficiency enhancement over the past decade. This comprehensive study highlights key publications, influential authors, leading institutions, and geographical contributions shaping this critical field. The steady increase in annual research output reflects the global research community's commitment to advancing innovations in steam boiler efficiency. Notably, China has emerged as a dominant contributor in both research volume and impact. However, significant contributions from countries such as the United States, the United Kingdom, and Iran have also enriched the broader discourse. Several key research themes are driving progress in this domain, including materials development, innovative designs, desalination and wastewater applications, and heat recovery technologies. In recent years, the focus has increasingly shifted toward exergy analysis, optimization methodologies, and the exploration of renewable and sustainable solutions, underscoring the industry's commitment to efficiency and environmental sustainability.

The statistical analysis reveals a pronounced dominance of research output from China, which can be attributed to several converging factors. First, China's substantial investment in research and development, particularly in renewable energy and advanced manufacturing technologies, has fostered an environment where innovative approaches to steam boiler efficiency are vigorously pursued. Second, supportive government policies and funding programs have incentivized both academic and industrial research, leading to a robust pipeline of high-impact publications. Additionally, China's strategic collaborations with international institutions have further enhanced its research capabilities, facilitating knowledge exchange and technological advancement. These collaborations are critical not only in amplifying research output but also in fostering a global research network that drives forward the frontiers of steam boiler efficiency. The implications of these trends suggest that a combination of policy support, financial investment, and international cooperation is key to achieving sustainable energy solutions in the coming years

Noteworthy publications highlight the growing emphasis on eco-friendly approaches, with advancements such as solar energy integration and organic thermoelectrics playing a key role in efficiency enhancement. Collaborations among prolific authors and esteemed institutions, particularly from China, the United States, and Europe, have significantly shaped the field through impactful partnerships. Emerging trends indicate an increasing focus on integrating computational tools, utilizing biomass, and implementing advanced thermal management strategies. Additionally, this analysis has identified key research avenues, including low-grade heat recovery, corrosion prevention, and the development of robust policy frameworks—areas that hold great potential for future exploration. The importance of international collaborations among leading contributors cannot be overstated, as they offer immense promise in accelerating progress by leveraging shared expertise and pooling resources effectively. Continued bibliometric monitoring remains a valuable tool for guiding future research strategies, fostering collaboration, and driving innovative breakthroughs. In conclusion, this study underscores the remarkable progress made in advancing steam boiler efficiency. It serves as a testament to the collective efforts of the global research community in pushing the boundaries of knowledge within this critical field.

Limitations:

The scope of this study is constrained by the availability and inclusivity of data sources used for bibliometric analysis. The potential omission of relevant publications due to database coverage limitations or language biases may affect the comprehensiveness of the findings. Additionally, inherent publication biases could influence the results, potentially skewing conclusions toward specific research areas or disproportionately highlighting positive outcomes. The temporal constraints of the analysis may also limit the representation of the most recent developments, potentially obscuring emerging trends. Furthermore, the methodology used to identify influential publications and assess impact may introduce a degree of subjectivity, which could affect the.

Future Research Opportunities:

Expanding the analysis to include a broader range of databases and sources could provide a more comprehensive overview of the scholarly landscape in steam boiler efficiency improvement. Incorporating qualitative assessments alongside bibliometric analysis would offer deeper insights into the context and substance of publications, enriching the understanding of emerging themes. Longitudinal studies tracking developments over extended periods could provide a more robust perspective on evolving trends. Additionally, integrating insights from diverse fields and conducting comparative studies across regions or industries could enhance the holistic understanding of efficiency enhancement strategies. Addressing specific gaps, such as low-grade heat recovery and policy formulation, presents opportunities for targeted and impactful research. Pursuing these research avenues would significantly contribute to both theoretical knowledge and practical application of steam boiler efficiency enhancement strategies.

References:

[1] J. A. M. da Silva, S. Ávila Filho, and M. Carvalho, "Assessment of energy and exergy efficiencies in steam generators," *Journal of the Brazilian Society of Mechanical Sciences and Engineering*, vol. 39, no. 8, pp. 3217–3226, Aug. 2017, doi: 10.1007/s40430-016-0704-6.

[2] L. Miró, J. Gasia, and L. F. Cabeza, "Thermal energy storage (TES) for industrial waste heat (IWH) recovery: A review," *Applied Energy*, vol. 179, pp. 284–301, Oct. 2016, doi: 10.1016/j.apenergy.2016.06.147.

[3] S. LeBlanc, "Thermoelectric generators: Linking material properties and systems engineering for waste heat recovery applications," *Sustainable Materials and Technologies*, vol. 1–2, pp. 26–35, Dec. 2014, doi: 10.1016/j.susmat.2014.11.002.

[4] T. K. Ibrahim *et al.*, "A comprehensive review on the exergy analysis of combined cycle power plants," *Renewable and Sustainable Energy Reviews*, vol. 90, pp. 835–850, Jul. 2018, doi: 10.1016/j.rser.2018.03.072.

[5] M. Elwardany, A. M. Nassib, H. A. Mohamed, and Abdelaal, "Performance Assessment of Combined Cycle Power Plant," in *2023 5th Novel Intelligent and*

Leading Emerging Sciences Conference (NILES), IEEE, Oct. 2023, pp. 80–84, doi: 10.1109/NILES59815.2023.10296617.

[6] Thanos. Bourtsalas and J. Wei, “Exhaust steam utilization in waste-to-energy strategies: From district heating to desalination,” *Journal of Cleaner Production*, vol. 428, Nov. 2023, Art. no. 139389, doi: 10.1016/j.jclepro.2023.139389.

[7] A. Damasceno, L. Carneiro, N. Andrade, S. Vasconcelos, R. Brito, and K. Brito, “Simultaneous prediction of steam production and reduction efficiency in recovery boilers of pulping process,” *Journal of Cleaner Production*, vol. 275, Dec. 2020, Art. no. 124103, doi: 10.1016/j.jclepro.2020.124103.

[8] P. Yang *et al.*, “Solar-driven simultaneous steam production and electricity generation from salinity,” *Energy and Environmental Science*, vol. 10, no. 9, pp. 1923–1927, 2017, doi: 10.1039/c7ee01804e.

[9] R. K. Pal and R. K. K., “Investigations of thermo-hydrodynamics, structural stability, and thermal energy storage for direct steam generation in parabolic trough solar collector: A comprehensive review,” *Journal of Cleaner Production*, vol. 311, Aug. 2021, Art. no. 127550, doi: 10.1016/j.jclepro.2021.127550.

[10] M. Elwardany, A. M. Nassib, H. A. Mohamed, and M. Abdelaal, “Energy and exergy assessment of 750 MW combined cycle power plant: A case study,” *Energy Nexus*, vol. 12, Dec. 2023, Art. no. 100251, doi: 10.1016/j.nexus.2023.100251.

[11] K. F. A. Sukra, D. Permana, And W. Adriansyah, “Modelling And Simulation Of Existing Geothermal Power Plant: A Case Study Of Darajat Geothermal Power Plant,” *International Journal of Thermodynamics*, vol. 26, no. 2, pp. 13–20, Jun. 2023, doi: 10.5541/ijot.1118778.

[12] S. Sadri And S. Y. Seyed Mohseni, “Investigation Of Kalina Cycle For Power Generation From Heat Dissipation Of Tarasht Power Plant,” *International Journal Of Thermodynamics*, vol. 26, no. 2, pp. 57–63, Jun. 2023, doi: 10.5541/Ijot.1214617.

[13] D. Kumar, T. Zehra, A. Junejo, S. A. Bhanbhro, And M. Basit, “4e (Energy, Exergy, Economic And Environmental) Analysis Of The Novel Design Of Wet Cooling Tower,” *Journal of Thermal Engineering*, vol. 6, no. 3, pp. 253–267, Apr. 2020, doi: 10.18186/thermal.710981.

[14] M. Elwardany, A. E. M. Nassib, And H. A. Mohamed, “Comparative Evaluation For Selected Gas Turbine Cycles,” *International Journal Of Thermodynamics*, vol. 26, no. 4, pp. 57–67, Dec. 2023, doi: 10.5541/ijot.1268823.

[15] A. T. Ubando, A. D. M. Africa, M. C. Maniquiz-Redillas, A. B. Culaba, and W. H. Chen, “Reduction of particulate matter and volatile organic compounds in biorefineries: A state-of-the-art review,” *Journal of Hazardous Materials*, vol. 403, 2021, Art. no. 123955, doi: 10.1016/j.jhazmat.2020.123955.

[16] O. Svedovs, M. Dzikevics, V. Kirsanovs, and I. Wardach-Święcicka, “Bibliometric Analysis of the Modelling of LowQuality Biomass Pellets Combustion,” *Environmental and Climate Technologies*, vol. 28, no. 1, pp. 286–302, Jan. 2024, doi: 10.2478/rtuect-2024-0023.

[17] Y. Kikuchi, Y. Kanematsu, R. Sato, and T. Nakagaki, “Distributed Cogeneration of Power and Heat within an Energy Management Strategy for Mitigating Fossil Fuel Consumption,” *Journal of Industrial Ecology*, vol. 20, no. 2, pp. 289–303, Apr. 2016, doi: 10.1111/jiec.12374.

[18] M. Elwardany, A. M. Nassib, and H. A. Mohamed, “Advancing sustainable thermal power generation: insights from recent energy and exergy studies,” *Process Safety and Environmental Protection*, vol. 183, pp. 617–644, Mar. 2024, doi: 10.1016/j.psep.2024.01.039.

[19] M. Ucar and O. Arslan, “Assessment of improvement potential of a condensed combi boiler via advanced exergy analysis,” *Thermal Science and Engineering Progress*, vol. 23, Jun. 2021, Art. no. 100853, doi: 10.1016/j.tsep.2021.100853.

[20] F. Guarino, M. Cellura, and M. Traverso, “Costructal law, exergy analysis and life cycle energy sustainability assessment: an expanded framework applied to a boiler,” *The International Journal of Life Cycle Assessment*, vol. 25, no. 10, pp. 2063–2085, Oct. 2020, doi: 10.1007/s11367-020-01779-9.

[21] K.-W. Lin and H.-W. Wu, “Emissions and energy/exergy efficiency in an industrial boiler with biodiesel and other fuels,” *Case Studies in Thermal Engineering*, vol. 50, Oct. 2023, Art. no. 103474, doi: 10.1016/j.csite.2023.103474.

[22] G. Ahmadi, A. Jahangiri, and D. Toghraie, “Design of heat recovery steam generator (HRSG) and selection of gas turbine based on energy, exergy, exergoeconomic, and exergo-environmental prospects,” *Process Safety and Environmental Protection*, vol. 172, pp. 353–368, Apr. 2023, doi: 10.1016/j.psep.2023.02.025.

[23] M. Elwardany, “Enhancing steam boiler efficiency through comprehensive energy and exergy analysis: A review,” *Process Safety and Environmental Protection*, vol. 184, pp. 1222–1250, Apr. 2024, doi: 10.1016/j.psep.2024.01.102.

[24] K. S. Hasan, “Experimental study on the combustion of gaseous based fuel (LPG) in a tangential swirl burner of a steam boiler,” *Journal of Thermal Engineering*, vol. 10, no. 5, pp. 1226–1240, 2024, doi: 10.14744/thermal.0000863.

[25] D. Kadric, N. Delalic, B. Delalic-Gurda, M. Kotur, And A. Skulj, “Reduction Of Energy Use In Industrial Facility,” *Journal Of Thermal Engineering*, vol. 7, no. 1, pp. 54–65, Jan. 2021, doi: 10.18186/Thermal.840063.

[26] M. Elwardany, A. M. Nassib, and H. A. Mohamed, “Exergy analysis of a gas turbine cycle power plant: a case study of power plant in Egypt,” *Journal of Thermal Analysis and Calorimetry*, vol. 149, no. 14, pp. 7433–7447, Jul. 2024, doi: 10.1007/s10973-024-13324-z.

[27] W. Mo *et al.*, “Technical-economic-environmental analysis of biomass direct and indirect co-firing in pulverized coal boiler in China,” *Journal of Cleaner*

Production, vol. 426, Nov. 2023, Art. no. 139119, doi: 10.1016/j.jclepro.2023.139119.

[28] M. Elwardany, A. M. Nassib, H. A. Mohamed, and M. R. Abdelaal, “Modeling of performance and thermodynamic study of a gas turbine power plant,” *Thermal Science and Engineering*, vol. 7, no. 4, Oct. 2024, Art. no. 8016, doi: 10.24294/tse.v7i4.8016.

[29] P. Mu *et al.*, “Superwetting Monolithic Hollow-Carbon-Nanotubes Aerogels with Hierarchically Nanoporous Structure for Efficient Solar Steam Generation,” *Advanced Energy Materials*, vol. 9, no. 1, pp. 1–9, Jan. 2019, doi: 10.1002/aenm.201802158.

[30] Z. Liu *et al.*, “Extremely Cost-Effective and Efficient Solar Vapor Generation under Nonconcentrated Illumination Using Thermally Isolated Black Paper,” *Global Challenges*, vol. 1, no. 2, pp. 1–10, Feb. 2017, doi: 10.1002/gch2.201600003.

[31] X. Wu *et al.*, “A flexible photothermal cotton-CuS nanocage-agarose aerogel towards portable solar steam generation,” *Nano Energy*, vol. 56, pp. 708–715, 2019, doi: 10.1016/j.nanoen.2018.12.008.

[32] M. Elwardany, A. M. Nassib, and H. A. Mohamed, “Case Study: Exergy Analysis of a Gas Turbine Cycle Power Plant in Hot Weather Conditions,” in *2023 5th Novel Intelligent and Leading Emerging Sciences Conference (NILES)*, IEEE, Oct. 2023, pp. 291–294, doi: 10.1109/NILES59815.2023.10296731.

[33] S. S. Chauhan and S. Khanam, “Energy integration in boiler section of thermal power plant,” *Journal of Cleaner Production*, vol. 202, pp. 601–615, Nov. 2018, doi: 10.1016/j.jclepro.2018.08.161.

[34] M. A. Nemitallah *et al.*, “Artificial intelligence for control and optimization of boilers’ performance and emissions: A review,” *Journal of Cleaner Production*, vol. 417, Sep. 2023, Art. no. 138109, doi: 10.1016/j.jclepro.2023.138109.

[35] A. Farkas, N. Degiuli, I. Martić, and C. G. Grlj, “Is slow steaming a viable option to meet the novel energy efficiency requirements for containerships?,” *Journal of Cleaner Production*, vol. 374, Nov. 2022, Art. no. 133915, doi: 10.1016/j.jclepro.2022.133915.

[36] J. Bujak, “Minimizing energy losses in steam systems for potato starch production,” *Journal of Cleaner Production*, vol. 17, no. 16, pp. 1453–1464, Nov. 2009, doi: 10.1016/j.jclepro.2009.06.013.

[37] C. Jia *et al.*, “Rich Mesostructures Derived from Natural Woods for Solar Steam Generation,” *Joule*, vol. 1, no. 3, pp. 588–599, Nov. 2017, doi: 10.1016/j.joule.2017.09.011.

[38] M. Rafeek, M. Elwardany, A. M. Nassib, M. S. Ahmed, H. A. Mohamed, and M. Abdelaal, “Sustainable Refining: Enhancing Energy Efficiency in Crude Distillation Processes,” *Chemical Engineering and Processing - Process Intensification*, vol. 214, no. 2, Aug. 2025, Art. no. 110326, doi: 10.1016/j.cep.2025.110326.

[39] M. Melicherová, M. Ondrišová, and J. Šušol, “Bibliometrics versus altmetrics: Researchers’ attitudes in Slovakia,” *Iberoamerican Journal of Science Measurement and Communication*, vol. 1, no. 1, 2021, doi: 10.47909/ijsmc.11.

[40] F. Luo, R. Y. M. Li, M. J. C. Crabbe, and R. Pu, “Economic development and construction safety research: A bibliometrics approach,” *Safety Science*, vol. 145, 2022, doi: 10.1016/j.ssci.2021.105519.

[41] X. Zhou and X. Ma, “Progress of graph model for conflict resolution in conflict analysis: A systematic review and bibliometrics research,” *Journal of Intelligent & Fuzzy Systems*, vol. 41, no. 6, pp. 5835–5846, Dec. 2021, doi: 10.3233/JIFS-201320.

[42] X. Bai, M. Hao, M. Hu, and L. Yang, “Big Data Analysis of Water Saving Standard Based on Bibliometrics,” *Journal of Sensors*, vol. 2022, pp. 1–9, Apr. 2022, doi: 10.1155/2022/5851114.

[43] Y. Hu, Y. Yu, K. Huang, and L. Wang, “Development tendency and future response about the recycling methods of spent lithium-ion batteries based on bibliometrics analysis,” *Journal of Energy Storage*, vol. 27, Feb. 2020, Art. no. 101111, doi: 10.1016/j.est.2019.101111.

[44] J. Xiong *et al.*, “Research Progress of Ferroptosis: A Bibliometrics and Visual Analysis Study,” *Journal of Healthcare Engineering*, vol. 2021, Aug. 2021, doi: 10.1155/2021/2178281.

[45] M. Elwardany, A. M. Nassib, and H. A. Mohamed, “Analyzing global research trends in combined cycle power plants: A bibliometric study,” *Energy Nexus*, vol. 13, Mar. 2024, Art. no. 100265, doi: 10.1016/j.nexus.2023.100265.

[46] J. A. Moral-Muñoz, E. Herrera-Viedma, A. Santisteban-Espejo, and M. J. Cobo, “Software tools for conducting bibliometric analysis in science: An up-to-date review,” *El Profesional de la Información*, vol. 29, no. 1, pp. 1–20, Jan. 2020, doi: 10.3145/epi.2020.ene.03.

[47] R. Wang *et al.*, “Advanced nanoparticles that can target therapy and reverse drug resistance may be the dawn of leukemia treatment: A bibliometrics study,” *Frontiers in Bioengineering and Biotechnology*, vol. 10, Oct. 2022, doi: 10.3389/fbioe.2022.1027868.

[48] T. C. C. Nepomuceno, V. D. H. De Carvalho, K. T. C. Nepomuceno, and A. P. C. S. Costa, “Exploring knowledge benchmarking using time-series directional distance functions and bibliometrics,” *Expert Systems*, vol. 40, no. 1, Jan. 2023, doi: 10.1111/exsy.12967.

[49] G. Vaccaro, P. Sánchez-Núñez, and P. Witt-Rodríguez, “Bibliometrics Evaluation of Scientific Journals and Country Research Output of Dental Research in Latin America Using Scimago Journal and Country Rank,” *Publications*, vol. 10, no. 3, p. 26, Aug. 2022, doi: 10.3390/publications10030026.

[50] H. Qu, N. A. Nordin, T. B. Tsong, and X. Feng, “A Bibliometrics and Visual Analysis of Global Publications for Cognitive Map (1970-2022),” *IEEE Access*, vol. 11, pp. 1–1, 2023, doi: 10.1109/ACCESS.2023.3279198.

[51] J. Liang *et al.*, “Bibliometrics and visualization analysis of research in the field of sustainable development of

the blue economy (2006–2021)," *Frontiers in Marine Science*, vol. 9, Sep. 2022, doi: 10.3389/fmars.2022.936612.

[52] H. Ge, Y. Bo, H. Sun, M. Zheng, and Y. Lu, "A review of research on driving distraction based on bibliometrics and co-occurrence: Focus on driving distraction recognition methods," *Journal of Safety Research*, vol. 82, pp. 261–274, Sep. 2022, doi: 10.1016/j.jsr.2022.06.002.

[53] N. Donthu, S. Kumar, D. Mukherjee, N. Pandey, and W. M. Lim, "How to conduct a bibliometric analysis: An overview and guidelines," *Journal of Business Research*, vol. 133, pp. 285–296, Sep. 2021, doi: 10.1016/j.jbusres.2021.04.070.

[54] M. Kajba, B. Jereb, and T. Cvahte Ojsteršek, "Exploring Digital Twins in the Transport and Energy Fields: A Bibliometrics and Literature Review Approach," *Energies*, vol. 16, no. 9, p. 3922, May. 2023, doi: 10.3390/en16093922.

[55] A. Kirby, "Exploratory Bibliometrics: Using VOSviewer as a Preliminary Research Tool," *Publications*, vol. 11, no. 1, p. 10, Feb. 2023, doi: 10.3390/publications11010010.

[56] S. S. Nunayon, K.-W. Mui, and L.-T. Wong, "Mapping the knowledge pattern of ultraviolet germicidal irradiation for cleaner indoor air through the lens of bibliometrics," *Journal of Cleaner Production*, vol. 391, Mar. 2023, Art. no. 135974, doi: 10.1016/j.jclepro.2023.135974.

[57] A. Rejeb, K. Rejeb, A. Abdollahi, S. Zailani, M. Iranmanesh, and M. Ghobakhloo, "Digitalization in Food Supply Chains: A Bibliometric Review and Key-Route Main Path Analysis," *Sustainability*, vol. 14, no. 1, p. 83, Dec. 2021, doi: 10.3390/su14010083.

[58] M. B. Firmansyah, A. A. A. D. Andriyani, and R. A. Asih, "Bibliometric Analysis of Multimodality Based on Multimodal Learning," *SSRN Electronic Journal*, vol. 18, pp. 105–112, 2022, doi: 10.2139/ssrn.4298216.

[59] Y. Qin, M. Ghalambaz, M. Sheremet, M. Fteiti, and F. Alresheedi, "A bibliometrics study of phase change materials (PCMs)," *Journal of Energy Storage*, vol. 73, Dec. 2023, Art. no. 108987, doi: 10.1016/j.est.2023.108987.

[60] L. A. Díaz-Secades, R. González, and N. Rivera, "Waste heat recovery from marine engines and their limiting factors: Bibliometric analysis and further systematic review," *Cleaner Energy Systems*, vol. 6, Dec. 2023, Art. no. 100083, doi: 10.1016/j.cles.2023.100083.

[61] A. Yu, W. Su, X. Lin, and N. Zhou, "Recent trends of supercritical CO2 Brayton cycle: Bibliometric analysis and research review," *Nuclear Engineering and Technology,* vol. 53, no. 3, pp. 699–714, Mar. 2021, doi: 10.1016/j.net.2020.08.005.

[62] R. Zahedi, A. Aslani, M. A. N. Seraji, and Z. Zolfaghari, "Advanced bibliometric analysis on the coupling of energetic dark greenhouse with natural gas combined cycle power plant for CO2 capture," *Korean Journal of Chemical Engineering*, vol. 39, no. 11, pp. 3021–3031, Nov. 2022, doi: 10.1007/s11814-022-1233-x.

[63] O. Omoregbe, A. N. Mustapha, R. Steinberger-Wilckens, A. El-Kharouf, and H. Onyeaka, "Carbon capture technologies for climate change mitigation: A bibliometric analysis of the scientific discourse during 1998–2018," *Energy Reports*, vol. 6, pp. 1200–1212, 2020, doi: 10.1016/j.egyr.2020.05.003.

[64] M. Malekli, A. Aslani, Z. Zolfaghari, R. Zahedi, and A. Moshari, "Advanced bibliometric analysis on the development of natural gas combined cycle power plant with CO2 capture and storage technology," *Sustainable Energy Technologies and Assessments*, vol. 52, Aug. 2022, Art. no. 102339, doi: 10.1016/j.seta.2022.102339.

[65] M. Á. Reyes-Belmonte, "A bibliometric study on integrated solar combined cycles (ISCC), trends and future based on data analytics tools," *Sustainability (Switzerland)*, vol. 12, no. 19, 2020, doi: 10.3390/su12198217.

[66] A. S. Karakurt, İ. Özsari, V. Başhan, and Ü. Güneş, "Evolution of steam turbines: A bibliometric approach," *Journal of Thermal Engineering*, vol. 8, no. 5, pp. 681–690, 2022, doi: 10.18186/thermal.1187839.

[67] D. I. Permana, D. Rusirawan, and I. Farkas, "A bibliometric analysis of the application of solar energy to the organic Rankine cycle," *Heliyon*, vol. 8, no. 4, Apr. 2022, Art. no. e09220, doi: 10.1016/j.heliyon.2022.e09220.

[68] L. F. Cabeza, M. Chàfer, and É. Mata, "Comparative analysis of web of science and scopus on the energy efficiency and climate impact of buildings," *Energies*, vol. 13, no. 2, 2020, doi: 10.3390/en13020409.

[69] M. Aria and C. Cuccurullo, "bibliometrix : An R-tool for comprehensive science mapping analysis," *Journal of Informetrics*, vol. 11, no. 4, pp. 959–975, Nov. 2017, doi: 10.1016/j.joi.2017.08.007.

[70] Y. Lin, Y. Jia, G. Alva, and G. Fang, "Review on thermal conductivity enhancement, thermal properties and applications of phase change materials in thermal energy storage," *Renewable and Sustainable Energy Reviews*, vol. 82, pp. 2730–2742, Feb. 2018, doi: 10.1016/j.rser.2017.10.002.

[71] Q. Zhang, Y. Sun, W. Xu, and D. Zhu, "Organic Thermoelectric Materials: Emerging Green Energy Materials Converting Heat to Electricity Directly and Efficiently," *Advanced Materials*, vol. 26, no. 40, pp. 6829–6851, Oct. 2014, doi: 10.1002/adma.201305371.

[72] H. Ghasemi *et al.*, "Solar steam generation by heat localization," *Nature Communications*, vol. 5, no. 1, p. 4449, Jul. 2014, doi: 10.1038/ncomms5449.

[73] H. Jouhara, N. Khordehgah, S. Almahmoud, B. Delpech, A. Chauhan, and S. A. Tassou, "Waste heat recovery technologies and applications," *Thermal Science and Engineering Progress,* vol. 6, pp. 268–289, Jun. 2018, doi: 10.1016/j.tsep.2018.04.017 .

[74] Y. Li *et al.*, "3D-Printed, All-in-One Evaporator for High-Efficiency Solar Steam Generation under 1 Sun Illumination," *Advanced Materials*, vol. 29, no. 26, pp. 1–8, Jul. 2017, doi: 10.1002/adma.201700981.

[75] K. K. Liu *et al.*, "Wood-Graphene Oxide Composite for

Highly Efficient Solar Steam Generation and Desalination," *ACS Applied Materials and Interfaces*, vol. 9, no. 8, pp. 7675–7681, Mar. 2017, doi: 10.1021/acsami.7b01307.

[76] Y. Shi *et al.*, "A 3D Photothermal Structure toward Improved Energy Efficiency in Solar Steam Generation," *Joule*, vol. 2, no. 6, pp. 1171–1186, Jun. 2018, doi: 10.1016/j.joule.2018.03.013.

[77] G. Xue *et al.*, "Robust and Low-Cost Flame-Treated Wood for High-Performance Solar Steam Generation," *ACS Applied Materials & Interfaces*, vol. 9, no. 17, pp. 15052–15057, May. 2017, doi: 10.1021/acsami.7b01992.

[78] S. He *et al.*, "Nature-inspired salt resistant bimodal porous solar evaporator for efficient and stable water desalination," *Energy & Environmental Science*, vol. 12, no. 5, pp. 1558–1567, 2019, doi: 10.1039/C9EE00945K.

[79] T. Li *et al.*, "Scalable and Highly Efficient Mesoporous Wood-Based Solar Steam Generation Device: Localized Heat, Rapid Water Transport," *Advanced Functional Materials*, vol. 28, no. 16, pp. 1–8, Apr. 2018, doi: 10.1002/adfm.201707134.